Sapienza University, Tor Vergata University, National Institute for Astrophysics, Italian Space Agency
Astronomy, Astrophysics and Space Science PhD Program

The electromagnetic coupling between Jupiter and its moons during the Juno mission: discoveries and analysis of the Jovian Infrared Auroral Mapper (JIRAM) observations

Doctoral Dissertation of:
Alessandro Moirano

Supervisor:
Alessandro Mura

Co-Supervisor:
Giuseppe Piccioni

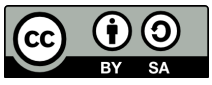

Abstract

The present thesis investigates the electromagnetic interaction between the Galilean moons and Jupiter, which is usually called *satellite-ionosphere coupling*. This interaction can occur in planetary systems with a magnetosphere that is large enough to include the orbit of the moon(s). The magnetic field of the Jupiter is rooted in the ionosphere and entangles the plasma (that is: a gas made by ions and electrons) of the whole magnetosphere: as a consequence, a system of plasma waves and currents transfers the Jovian rotation to magnetosphere, which tends to rigidly corotate with Jupiter. This plasma is ultimately supplied by the constant volcanic activity on Io, the innermost of the Galilean moons. Indeed, the Ionian surface is coated by frozen SO_2 originating from Io's volcanoes: this sublimates due to the solar radiation and contributes, together with the gases ejected by the volcanoes, to Io's atmosphere, which is subsequently lost into the Jovian magnetosphere and ionized by collisions with the magnetospheric particles. A dense plasma cloud, called *Io Plasma Torus*, is thus produced around Io's orbit, and the plasma diffuses from here towards the rest of the magnetosphere. Due to the fast rotation of Jupiter (one sidereal Jovian day lasts about 10 hours), the Galilean moons are thus constantly overtaken by the magnetospheric plasma, and hence they represent an obstacle to the plasma flow. This produces a local perturbation around the satellites, whose details depends on the plasma environment, the local magnetic field and the characteristic of the moons. At Jupiter, the typical conditions near Io, Europa and Ganymede - the three innermost Galilean moons - allow the propagation of field-aligned plasma modes known as *Alfvén waves*. These modes transmit the perturbation from the satellites to the planetary ionosphere, which takes between a few minutes to half an hour, depending on the considered moon and its longitude in Jupiter's frame. Near the Jovian ionosphere, the Alfvén waves partially transfer their energy to the electrons, which are accelerated into the Jovian ionosphere. Here, the electron precipitation trigger a chain of reactions with the atmospheric particles and generates

an auroral emission, which, in the case of the satellite-ionosphere coupling, is called *satellite auroral footprint* (or just *footprint*).

Since 2016, the Juno mission has been flying around Jupiter in highly eccentric, polar orbits. Thanks to the spacecraft orbit geometry, the high spatial resolution of its Jovian InfraRed Auroral Mapper (JIRAM) has been delivering images of the polar regions of Jupiter with an unprecedented level of spatial detail. Among its observations, JIRAM reports several detection of the footprint of Io, Europa and Ganymede. The observations performed by JIRAM have revealed new details in the structure of the footprint emissions: a chain of regularly-spaced patches of emission is consistently found along the track of the footprint of Io, Europa and Ganymede. The features of this new structure - named *sub-dots* - can not be fully explained by current models of the satellite-ionosphere coupling. Instead, we suggest that the high intensity of the electron precipitation associated with the footprint can trigger an ionospheric feedback, which can shape the morphology of the auroral emission. This feedback process has only been applied to the terrestrial magnetosphere so far, but the order of magnitude adaptation from Earth to Jupiter shown in Chapter 5 agrees with JIRAM observations.

In the last chapter of this thesis, the position of the Io footprint is used to determine the state of the Io Plasma Torus. Indeed, the Alfvén waves speed - and hence their travel time - depends on both the magnetic field magnitude and the plasma density. Therefore, the position of the footprint can be compared with the position predicted by a model of Jupiter's magnetic field and of the Io Plasma Torus, to determine the plasma content of the latter. This represents a new method to constrain the conditions of the Io torus, whose monitoring is fundamental to understand the interplay between Io's atmosphere, the torus and the Jovian magnetosphere. We shows that the position of the Io footprint can indeed be used to quantitatively detect episodes of variability in the Io torus. As Juno-JIRAM has been gathering observation for about 6 years, this represents a unique source of information on the plasma source of the Jovian magnetosphere. Therefore, we derived the torus conditions using all the available

observations of JIRAM. To further improve the quality of the results, the torus states derived from JIRAM are used to simulate the radio occultations of the Io torus performed by Juno during each spacecraft closest approach to Jupiter. We conclude that the Io Plasma Torus was in a denser and hotter state compared to Voyager 1, on average. Nevertheless, large density and temperature fluctuations have often been observed to occur over a few week or months. Similar variations have already been documented in literature, but not satisfactorily explained yet. It is even still debated if such variability is caused either by variations in the plasma supply from Io, or by external factors. At present, no theoretical model is available to compare with the variability reported in this thesis. The Juno dataset obtained by combining the Io footprint position and the radio occultations represents an important survey of the plasma conditions around Io, hence it can be used to constrain future models of the Io Plasma Torus.

Preface

This work is the summary of the last three years of my professional life. Although at times it felt as a chore - I bet many researchers and student can relate to this perception - I wanted a meaningful thesis, something a little beyond a collection of my publications and works. Indeed, the electromagnetic interaction between planets and moons is a subject that is rarely mentioned at any level of the university curriculum, and people are often astonished by the discovery of this interaction and its manifestation as aurorae on the surface of the planet. The main driver of this thesis is represented by the Juno mission around Jupiter and one of its instruments, the Jovian Infrared Auroral Mapper (JIRAM): it has been providing us the most detailed images of the polar region of Jupiter, where its continuous, powerful aurora can be observed. For this reasons, I wanted this manuscript to fulfil two tasks: being a comprehensive reference where newcomers can start their travel into the planet-satellite electromagnetic interaction and showing the most updated results I have been able to obtain by looking at the auroral emission associated with the Galilean moons at Jupiter. I hope the reader will find this work useful as I intended to be. At least, a little bit.

Acknowledgements

I like to think about this thesis as a collective effort, which has been put together by my hands. This makes very difficult to properly thank all the people who contributed, as I have to take into account all the different types of support I've received to get here. I'll try my best with the following non-ordered list, but if you, the reader, do not recognize yourself here and we met at some point, you have my thanks too.

To my partner, who has supported me since we met, encouraging me in pursuing my objectives while keeping me on the right path. The last three year would have been very different without you.

To my family, and especially to my parents, who invested in my future since I was a baby and keep supporting me nowadays.

To my supervisors, who took the risks of getting a stranger onboard. I hope it paid off.

To all past and present friends, who left me something that contributed to my personality, helped when it was needed or just shared something with me. I'd like to thanks you one by one, but this page is obviously too short. I'm bringing all of you in my heart.

To the people I've worked with in the last years, for the scientific and professional development I got, and for making an amazing mission to Jupiter.

To all the projects that put a huge effort in making scientific material publicly available to everyone at no cost for the users. This thesis would have been crippled without you.

Contents

List of Figures

List of Tables

List of Acronyms

CHAPTER 1

Introduction

Jupiter holds some physical records among the planet of the Solar System, namely it is the biggest - with a radius $R_J = 71492$km - and its rotation period is the shortest - 9.925 hr. Its magnetic field is about four orders of magnitude stronger than the terrestrial one, which makes the Jovian magnetosphere the biggest object in the whole System (besides the Solar magnetosphere). Four main moons orbit the magnetosphere of Jupiter (from inside out: Io, Europa, Ganymede and Callisto, also called *Galilean moons*), and they also hold records, like Ganymede, which is the only moon with its own intrinsic magnetic field, and Io, which is the most volcanically active body in the Solar System. The large amount of gaseous material supplied by the volcanism on Io - mainly sulfur dioxide SO_2 - is dispersed around its orbit, dissociated and ionized by charge-exchange reactions and electron impacts with magnetospheric particles (Bagenal and Dols, 2020). The Iogenic charged particles are accelerated towards rigid corotation with Jupiter by the fast-rotating planetary magnetic field, and form a torus-shaped cloud called *Io Plasma Torus* (IPT). Under the influence of the centrifugal force, the plasma [1] slowly diffuses from Io's orbit away from Jupiter, forming a *plasmadisk*

[1] For the purpose of this thesis, a plasma can be intuitively defined as a gaseous ensemble of charged particles - ions and electrons - that is globally neutral. The most noticeable difference between a neutral gas and a plasma is that particles in neutral gases interact with each other by "cue ball"-like pairwise collisions, while in plasmas each

that rotates around Jupiter. The magnetic field of Jupiter is dominated by a dipole moment titled by about 10° with respect to the spin axis, but higher orders are to be considered near the planetary surface[2]. At distances greater than Io's orbit (5.9 R_J) along the equator, the electric currents in the plasmadisk generate an induced magnetic field that is comparable with the internal one. The result is the stretching of the magnetic field lines near the equator and the overall inflation of the Jovian magnetosphere. In Fig. 1.1 we show a sketch of the Jovian magnetosphere. The magnetic field is rooted into the planetary ionosphere, therefore the Iogenic plasma and the Jovian ionosphere are ultimately magnetically connected. This *Magnetosphere-Ionosphere* (M-I) coupling is carried by a current system that transfers angular momentum from the planet and accelerates the plasma, whose centrifugal force ultimately inflates the geometry and size of the whole magnetosphere. A consequence of the powerful electromagnetic environment of the Jovian magnetosphere is the constant precipitation of electrons into the atmosphere and the resulting presence of auroral emissions coming from around the polar regions of the planet.

The morphology of Jupiter's aurorae is rather complex, but it can be roughly divided into four regions. An example of how the Jovian aurora looks like in the *Ultraviolet* (UV) and *Infrared* (IR) is shown in Fig. 1.2. The UV image of the northern hemisphere was acquired from the *Space Telescope Imaging Spectrograph* (STIS) onboard the *Hubble Space Telescope* (HST) in November 1998, while the IR image comes from the 22^{th} passage of the Juno spacecraft over the southern pole in September 2019. Both images show the same features, and different small-scale details can be ascribed to the different resolutions and vantage points between the two instruments. The *main emission* encompasses the magnetic pole of Jupiter like a bright ribbon a few thousand kilometers wide. The main emission is always

particle is affected by the electromagnetic field generated by all the other particles. This substantial difference gives raise to a large variety of waves that can be excited and are specific to plasmas, as can be found in any textbook of plasma physics (e.g: Krall and Trivelpiece (1973)).

[2]Being gaseous, Jupiter does not have a solid surface to refer to. Instead, the 1 bar pressure level is usually referred to as *the surface*.

active, but its location, intensity and shape can change over time. The main emission is magnetically mapped to an equatorial region at about 30 R_J from Jupiter, but it can change as a result from the compression and expansion of the magnetosphere under the action of the Solar Wind. Inside the main emission, there is the *polar emission*, which appears patchy and highly variable. This region is mapped to the outer magnetosphere and the magnetotail, where the variability of the Solar Wind highly affects the dynamics of the magnetosphere. Between the main emission and the magnetic shell connected to Io's orbit it is possible to observe the *diffuse emission*, which is usually associated with the radial motion of plasma driven by the centrifugal force between Io's orbit and 30 R_J. Lastly, the orbital motion of the Galilean moon is associated with their auroral *Footprint* (FP), which can be identified as a bright spot moving in Jupiter's frame and followed by a fading *Footprint Tail* (FPT). The footprints are the final result of the so-called *Satellite-Ionosphere* (S-I) coupling. Indeed, Io, Europa, Ganymede and Callisto orbit around Jupiter at about 18, 14, 11 and 8 km/s, while the plasma flows at ∼74, 98, 150, and 200 km/s at their respective orbit. Therefore, the moons act as obstacles against the plasma that constantly overtakes them (the plasma flow is faster than the orbital velocity of the Galilean satellties), and they constantly perturb the flow around them. This local perturbation generates plasma and magnetic field oscillations that propagate away from the moon. In particular, the *Alfvén waves* are transverse oscillations that travel along the magnetic field and that can accelerate electrons into the atmosphere along their way: this ultimately produce auroral emission, although the details of the physical processes that drives the auroral precipitation is still investigated. The emission associated with the footprints of Io, Europa and Ganymede will be the main source of data of this work. As for Callisto, only one observation, performed by the HST, is currently available (Bhattacharyya et al., 2018). The Callisto footprint is expected to be very close to (if not overlapping) the main emission and its perturbation weaker than the other three moons (Saur et al., 2013), therefore its detection is much more challenging, even from *in situ* observations. In this thesis, Callisto will not be analyzed, as

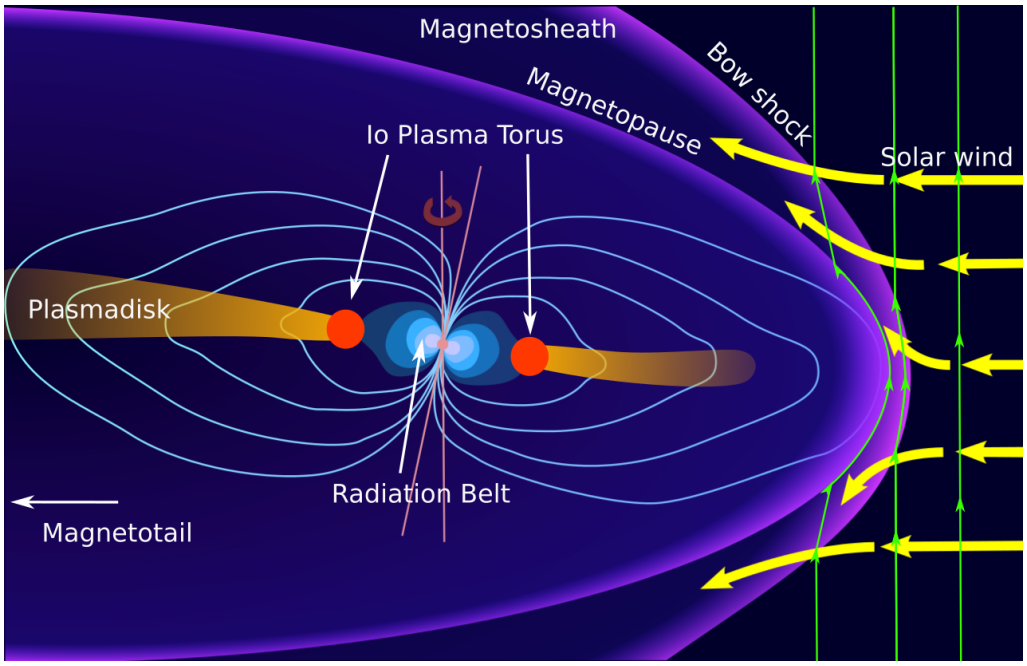

FIGURE 1.1: Sketch of the Jovian magnetosphere. The green and light blue lines are the Solar and Jovian magnetic field lines, respectively. The orange area near the equator is dominated by the Iogenic plasma diffusing from Io's orbit outwards and forming the *plasmadisk* and the *magnetotail* current sheet. The inner purple area is the Jovian *magnetosphere*, while black area on the right is the *interplanetary medium* dominated by the solar wind. The Solar wind is slowed down from supersonic to subsonic flow in the *bow shock* and "coats" the Jovian magnetosphere with a region of turbulent flow called *magnetosheath*. The inner purple line is the *magnetopause*, that is: the imaginary boundary that separates the region connected to the planetary magnetic field from the Solar wind, connected with the stellar magnetic field. The planetary magnetic field is inflated near the magnetic equator because of the centrifugal force of the plasmadisk. The contour levels close to Jupiter represent the *radiation belt*. Retrieved and adapted from commons.wikimedia.org. Credits to NASA/JPL, Public domain, via Wikimedia Commons.

we do not have additional record of the Callisto footprint.

Jupiter is also nowadays the most explored Outer Planets, with two dedicated orbiter missions (Galileo from 1995 to 2003 and Juno since 2016) and two more in the next future (Juice, launched in 2023, and Europa Clipper, expected to launch in 2024), in addition to the flybys performed by

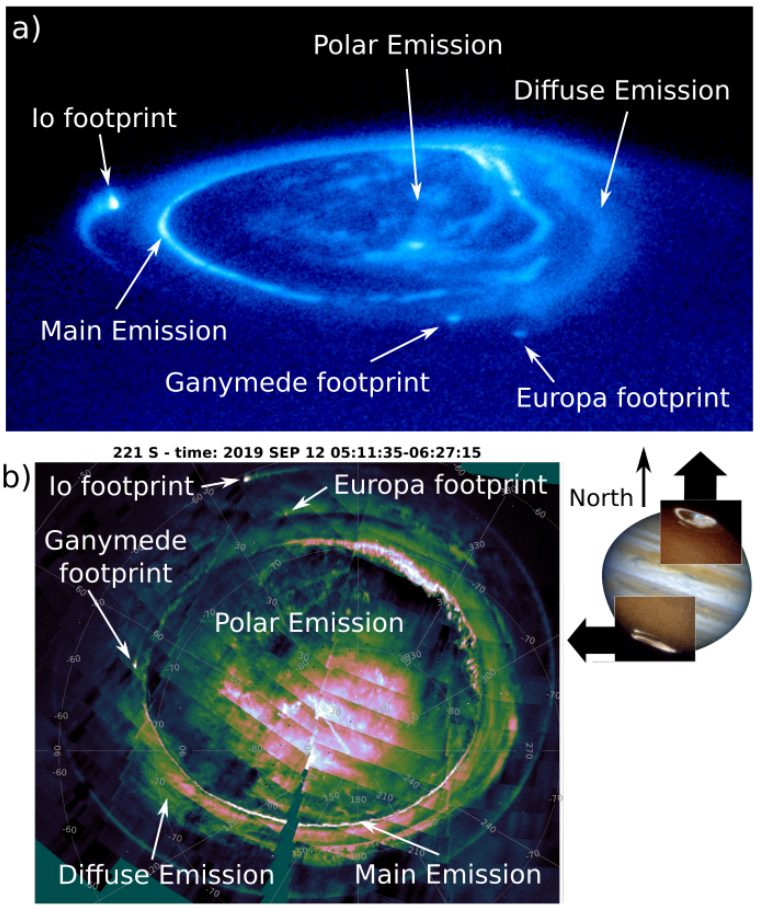

FIGURE 1.2: *(a)* Observation of the northern aurora in the UV band by the HST-STIS instrument on November 26^{th} 1998. The image shows the auroral footprints of Io, Europa and Ganymede, as well as the principal features of all the aurora. *(b)* Observation of the southern aurora in the IR band by Juno-JIRAM on September 12^{th} 2019, showing the same features of panel *(a)*. The different level of details is due to the different resolution of the images. The FOV of JIRAM is too narrow to observe the whole polar region at a single time, thus the IR image is obtained from the tesselation of a one-hour long acquisition of several shots. The image of the UV aurora and Jupiter are retrieved from commons.wikimedia.org. Credits to NASA/JPL, Public domain, via Wikimedia Commons.

Pioneer 10 and 11, Voyager 1 and 2, Cassini, Ulysses and New Horizons. The large wealth of data provided by these missions, together with Earth-based observations, has gradually been improving our understanding of the Jovian System since the 1970s. The Juno mission (Bolton et al., 2017) is currently orbiting Jupiter in highly eccentric polar orbits, and at the time of writing it is about halfway its Extended Phase (about 50 revolutions around Jupiter). Among its scientific goals, Juno investigates the interior structure of Jupiter (Iess et al., 2018), its atmosphere, its magnetosphere (Bagenal et al., 2017) and - especially in the Extended Phase - the Galilean moons. By looking at the temporal position of Juno in the Jupiter exploration timeline, its observations are fundamental to compare and complement the past ones, but they are also fundamental in lying the ground for the future missions. The payload and orbit of Juno are designed to thoroughly investigate the magnetosphere of Jupiter. Thanks to the high eccentricity of the orbit, Juno is as far as $\sim$100 R_J from Jupiter during the *Apojove* (AJ), while it gets as close as $\sim$0.07 R_J ($\sim$5000 km) from the planet surface during the *Perijove* (PJ), thus it explores different magnetospheric regions at various distances. Besides, the spacecraft crosses the magnetic shells connected to the orbits of the Galilean satellites at least twice each orbit, thus it can directly probe the region of the magnetosphere involved in the S-I coupling. The payload includes particle detectors for ions and electrons (the *Jupiter Energetic particle Detector Instruments* (JEDI) (Mauk et al., 2017) and the *Jovian Auroral Distributions Experiment* (JADE) (McComas et al., 2017)), an infrared imager and spectrometer (the *Jovian InfraRed Auroral Mapper* (JIRAM) Adriani et al. (2017)) and an *UltraViolet Spectrograph* (UVS) (Gladstone et al., 2017) to observe the aurora, a *MAgnetic Field investigation* (MAG) (Connerney et al., 2017) and antennas for the investigation of plasma waves (Waves; Kurth et al. (2017)). All these instruments are able to measure directly or indirectly the quantities involved in the S-I coupling, such as magnetic and electric field fluctuations, electron and ion energy distributions and densities, as well as the intensity and location of the auroral emissions.

In this thesis, the S-I coupling will be examined from the observations of the satellite footprints of Io, Europa and Ganymede. The main bulk of the

data comes from the infrared observations of the JIRAM instrument onboard Juno, thanks to the work performed with the JIRAM team at the *Insititute of Space Astrophysics and Planetology* (IAPS), a department of the *National Intitute for Astrophysics* (INAF) in Italy. Furthermore, ultraviolet imaging from HST and Juno-UVS represents additional source of data - mostly used as comparison - thanks to the collaboration with the UVS team and the Laboratory for Planetary and Atmospheric Physics (LPAP, under the STAR institute in Belgium). Lastly, the radio-occultations obtained from the radio tracking signal of the spacecraft are also used (thanks to the Radio Science and Planetary Exploration Laboratory of the University of Bologna), as they are sensitive to the plasma and can then be used to monitor the Io Plasma Torus. The leading role of JIRAM in the next chapters is mainly motivated by its high spatial resolution. Indeed, the JIRAM imager recorded new undocumented details of the structure of the footprint. Furthermore, the precise determination of the footprint position can be used as a calibration tool for ground based observations or a constraint for other observations. Lastly, the periodic monitoring of the footprints, together with JIRAM high resolution, is used to infer the plasma conditions at the moons and its variations, as the local perturbation that ultimately produces the emission depends on the plasma parameters around the moons. In the next chapters, it will be shown the role of JIRAM in improving our current understanding of the S-I coupling and the monitoring of the Jovian magnetosphere. Indeed, on one side, the high resolution of the instrument has led to the discovery of a new, unexplained auroral feature, which shed light onto the role of the ionosphere in the S-I coupling; on the other, the ability of monitoring the conditions of the IPT - which is the major plasma source of the whole magnetosphere - is fundamental to constrain models and confirm or challenge previous observations of the Io torus and its variability. This latter topic is particularly thorny, as it involves the interplay among the material supply from Io to the IPT, and from the IPT to the Jovian magnetosphere. To further complicate the issue, the role of external factor such as the solar wind are still debated and poorly modelled. In summary, this thesis summarize the recent results in two areas of the Jovian magnetosphere: improving

the understanding of the S-I coupling with JIRAM new discoveries, and help monitoring the conditions of the IPT, as major plasma source of the magnetosphere.

Chapter 2 introduces the general structure of the Jovian magnetosphere, with more in-depth details on the region from Io's orbit to Ganymede's. A brief description of the M-I coupling can also be found at the end of the same chapter. Chapter 3 describes the theory of the S-I coupling, with an introduction on low-frequency waves in magnetized plasmas. Chapter 4 introduces the Juno mission and its payload, with focus on JIRAM and the radio instrumentation, whose data are used to complement the infrared observations from JIRAM in the last chapter. Chapter 5 shows one of the new discoveries on the footprints of Io, Europa and Ganymede from JIRAM; indeed, a small-scale structure with typical size of 200-300 km has been detected near the footprints. This structure is hardly explained by the current understanding of the S-I coupling, thus we suggest new candidate processes to explain JIRAM observations. Chapter 6 shows how the position of the Io footprint can be used to constrain the plasma distribution near the satellite and what information we have retrieved so far from the footprint position on the conditions of the Io torus during the Juno mission.

CHAPTER 2

The Jovian Magnetosphere

This chapter introduces the general structure of the Jovian magnetosphere, with additional details on the region from Io's orbit to Ganymede's, which is fundamental to understanding the processes underlying the Satellite-Ionosphere (S-I) *coupling. The S-I coupling itself can be interpreted as a specific case of Magnetosphere-Ionosphere* (M-I) *coupling, that is: the ensemble of electromagnetic processes that transfers energy and angular momentum between a planet and its magnetosphere. Therefore, the M-I coupling will be briefly and qualitatively introduced as well, so that the understanding of the S-I coupling will naturally follow in the next chapter.*

The Jovian magnetosphere is the region of space around Jupiter where the motion of charged particles is affected by the planetary magnetic field. The magnetosphere does not extend indefinitely, because, at some point, the role of the Solar magnetic field becomes dominant (see Fig. 1.1); hence, the magnetosphere represents a limited space, with quite well physically defined boundaries. Indeed, the supersonic flow of the Solar wind is abruptly slowed down near the Jovian magnetosphere, forming a structure called *bow shock*. Downstream of the bow shock, the Solar wind forms the *magnetosheath*, which encases the magnetosphere and where the plasma and the magnetic field are highly turbulent. The boundary between the region permeated by

the Solar magnetic field and the planetary one is called *magnetopause*, which marks the limits of the magnetosphere. Historically, the magnetosphere of Jupiter is subdivided into three main regions, according to the physical processes that determines the dynamics of the particles and the geometry of the magnetic field (Dessler, 1983):

- the *inner magnetosphere* extends from the Jovian surface up to Io's orbit at about 6 R_J. The geometry of the magnetic field is determined by the internal source, which is believed to be a system of electrical currents flowing in the deep atmosphere of Jupiter (Russell, 1993). The internal magnetic field is dominated by the dipole moment, which is tilted by about 10° toward ∼200° West longitude, and beyond 1-2 R_J from the surface the field can be approximated by a pure dipole for most purposes. Nevertheless, by looking at the surface magnetic field (e.g: Connerney et al. (2018, 2022)), it is clear that higher order moments are also present, which must be taken into account between the planetary surface and 1-2 R_J above it. At the time of writing, the most updated model for the internal field is the *Juno Reference Model through Perijove 33* (JRM33), which is based on the magnetometer data acquired during Juno's prime mission up to orbit 33 (Connerney et al., 2022). According to JRM33, the internal magnetic field is described by a 30-degree spherical harmonic expansion, although the coefficients are currently determined up to order 18 (or 13, if stricter confidence is needed). The magnetospheric material is supplied by Io and diffuses mostly from its orbit outwards, therefore the plasma density in the inner magnetosphere is quite low. At 2-3 R_J, the magnetosphere is dominated by high energy particles, trapped by the magnetic field and forming a radiation environment similar to the terrestrial Van Allen belt (Bolton et al., 2002).

- the *middle magnetosphere* lies between ∼6 R_J and 30-50 R_J, where the Iogenic plasma flows almost azimuthally near the equator and carries currents, generating an external magnetic field superimposed to the one generated by the internal source. The external field has a

droplet-like geometry, with the tip toward Jupiter (Connerney et al., 1981, 2020; Nichols et al., 2015), therefore the total field is radially stretched near the equator (see Fig. 1.1). This is the region where Io, Europa and Ganymede orbit, hence the origin of the S-I coupling lies there. As the details of the coupling is strongly affected by the plasma properties (as explained in chapter 3), more in-depth details will be presented in sections 2.1 and 2.2.

- the *outer magnetosphere* extends from 30-50 R_J up to the magnetopause. The changes in the Solar wind pressure strongly affect the spatial and temporal variability of this region, which does not exhibit the same approximate axi-symmetry of the middle and inner magnetosphere. Moreover, the outer magnetosphere traditionally includes the *magnetotail*, which extends for thousands of R_J in the anti-sunward direction.

In the present thesis, only the part of the magnetosphere from inside Io's orbit to Ganymede's are thoroughly described (i.e: from ∼4-5 R_J to ∼15 R_J) in order to introduce the particle and magnetic environment at the orbit of the Galilean moon used in this study. Therefore, the next sections are dedicated to the description of the plasma environment near Io, Europa and Ganymede.

2.1 The Io Plasma Torus

As anticipated in Chapter 1, the main source of material in the Jovian magnetosphere is Io, the most active volcanic body in the Solar System. The origin of the volcanism on Io is in the tidal stress and heating caused by the orbital resonance with the other moons (Peale et al., 1979). Io hosts different type of volcanic activity, like plumes, lava flows, eruptions and calderae (see Lopes and Williams (2015); Lopes et al. (2023) and reference therein), and each of them provide different proportions of gas, dust and heat. Moreover, each type of activity exhibits variability, potentially associated with the

tidal resonance with the other satellites (de Kleer et al., 2019). The details of the material supply from Io to the magnetosphere are still highly debated (Bagenal and Dols, 2020; Roth et al., 2020) and different types of compounds are injected into the Jovian magnetosphere by different chains of processes. Nevertheless, the supply of material from Io can be roughly divided into two main steps, that is: the mass loading of Io's atmosphere and the dispersion of atmospheric material into the Jovian magnetosphere.

Sulfur dioxide (SO_2) is the main constituent of Io's atmosphere[1] and it is mainly provided by sublimation from the surface, where it is deposited by the volcanic activity. It appears that only a small fraction of the atmospheric SO_2 is provided by direct outgassing. Instead, sodium chloride (NaCl) is mainly injected into the atmosphere directly by volcanic outgassing (Roth et al., 2020). The different atmospheric loading of these two compounds - sublimation vs outgassing - leads to important observational differences. Indeed, sodium - derived from dissociation of NaCl - is a better indicator of volcanic activity than SO_2 (e.g.: Yoneda et al. (2010)). Sulfur dioxide is quite steadily produced by sublimation, which is caused by the solar radiation: as a result, this compound is distributed nearly uniformly in Io's atmosphere, while NaCl appears more patchy (Roth et al., 2020). In both cases, the possibility of injecting material directly into the magnetosphere is very unlikely. McDoniel et al. (2019), using a Monte Carlo simulation, showed that a large plume is able to form an extended cloud above the plume, which can be an important source of plasma. Nevertheless, this event does not directly produce plasma, but only neutrals; moreover, the location of the plume on Io's surface strongly impacts the interaction with the magnetospheric environment and, thus, the effective production of such a cloud. Lastly, strong volcanic outbursts are expected to be rare: about one every $\sim$ a few years, although we currently lack sufficient monitoring of Io's volcanic activity to properly determine the occurrence of these events.

[1]The discovery of Io's atmosphere dates back to 1973 with the Pioneer 10 flyby, and another milestone of its exploration happened in 1979 with the Voyager 1 flyby, which revealed the presence of volcanism, an SO_2 atmosphere and the presence of hot, gaseous sulfur dioxide above the volcanic region of Loki Patera. More details about the discovery of the atmosphere of the Galilean moons can be found in McGrath et al. (2004).

The losses from Io's atmosphere into the Jovian magnetosphere can occur following three channels (Bagenal and Dols, 2020):

- *Mass Loading* The collisions with the magnetospheric electrons ionize and dissociate the atmospheric compounds, thus producing sulfur and oxygen ions, and, proportionally to their abundance, also sodium and chlorine ions. Additionally, photoionization contributes to about 10-15% of the total ionization rate. Because this channel produces new ions, it can be referred to as *mass loading*. The ions are nearly at rest in Io's frame, therefore they are "picked up" by the planetary magnetic field. The ions are then accelerated to the bulk plasma flow and start the gyromotion typical of charged particles in a magnetic field.

- *Momentum Loading* Charge-exchange reactions due to ion-neutral collisions do not change the total number of ions around Io. Indeed, this reaction moves electrons from the neutrals to the ions (hence the name *charge-exchange*): this ionizes the neutrals, and neutralize the ions, thus no net charge is added or subtracted to the system. There are two important consequences to this process. The first is that the "new" ion is picked up by the magnetic field and accelerated, in the same way as an ion produced by electron impact. The second is that the "old" neutralized ion is not "tied" to the magnetic field anymore. Therefore, the centrifugal force generated by the pickup acceleration is not offset by the magnetic tension, and the neutralized ion is launched away from Jupiter. Due to the momentum transfer with no net ion production, this channel can be referred to as *momentum loading*.

- *Atmospheric Sputtering* Collisions with ions and electrons can transfer momentum between the magnetospheric plasma and Io's atmosphere without ionization, nor charge-exchange reaction. After enough collisions, the neutral particle can escape the atmosphere: this can be called *atmospheric sputtering*.

The final result of the atmospheric loss from Io is the formation of a neutral banana-shaped cloud near Io [2] and a toroidal plasma cloud called the *Io Plasma Torus* (IPT), whose major radius can be considered the orbit of Io (Fig. 2.1). The structure of the IPT is determined by the physical processes occurring within it, namely: ion pickup, centrifugal confinement and diffusive equilibrium, radial transport, and physical chemistry (Bagenal and Dols, 2020), here briefly described:

- *Ion Pickup* The collisions between the neutral cloud and the magnetospheric electrons produce new ions that, right after being produced, move at nearly the same speed of the cloud, i.e: at Keplerian speed. Around Io's orbit, this speed is far lower than the rigid corotation at the angular speed of Jupiter. Therefore, the new ion experiences an electric field due to its motion relative to the magnetic field, and it is "picked up" (i.e: accelerated). This produces an ion gyro-motion (Warnecke et al., 1997), which heats the newly produced plasma. In addition, the electric field produces a drift[3], so that in the end the bulk speed of the new ions is the speed of the magnetospheric plasma.

- *Centrifugal Confinement and Diffusive Equilibrium* Plasmas tend to be confined by magnetic fields, so that any motion perpendicular to the field is strongly inhibited. Instead, the plasma is free to move along the field lines, therefore the dynamics of a magnetized plasma can be assimilated to an ensemble of beads sliding along wires (that is: the magnetic field lines). In a fast rotating magnetosphere, where the plasma experiences a strong centrifugal acceleration, the plasma is thus confined near the farthest point from the rotation axis along

[2]Sometimes, it is also referred to as *neutral torus*: this should be used to refer to the neutrals along Io's orbit, and not to the high concentration of neutrals surrounding Io. Moreover, the sodium environment in the outer magnetosphere is sometimes also referred to as "neutral cloud", although it should be more appropriate to call it *neutral nebula*; the literature also uses *Mendillodisk* to refer to that environment, after Mendillo et al. (1990). In the context of the present thesis, where the outer magnetosphere is not investigated, I will refer to the dense neutral environment near Io as *neutral cloud*, while the distribution of neutrals along Io's orbit will be called *neutral torus*.

[3]The so-called E×B drift; e.g: Krall and Trivelpiece (1973).

the magnetic field lines (Hill et al., 1974). The plane passing through these points is called *centrifugal equator* (Fig. 2.2), and, in a tilted dipolar-like magnetic field, it can be estimated as two-third between the spin equator and the magnetic equator [4,5]. The centrifugal equator is also the region where the plasma density is usually the highest (Bagenal and Sullivan, 1981). The plasma pressure opposes the centrifugal confinement, hence the plasma content gradually decreases away from the centrifugal equator. As the pressure is proportional to the temperature, the vertical (i.e: field-aligned) structure of the IPT is an indication of the plasma temperature. The precise determination of the plasma distribution along field lines requires also to take into account the mirror force - which is relevant only for particles whose velocity satisfies $v_\perp \neq v_\parallel$[6] - and the ambipolar potential - which arise from the charge separation between the ions and the electrons, the former being heavier, and hence more strongly affected by the centrifugal force (Bagenal and Sullivan, 1981; Mei et al., 1995).

- *Radial Transport* Iogenic material is detected throughout the whole Jovian magnetosphere, which implies some form of radial transport. This is believed to occur via centrifugally-driven flux tube interchange (Hill et al., 1981), which is similar to the Rayleigh-Taylor instability that occurs between two fluids of different density in a gravity field. Indeed, the flux tubes at Io's orbit are heavier than the outer flux tubes, hence the effective gravity - dominated by the centrifugal force and pointing outwards - replaces lightly-loaded flux tubes outside Io's orbit with the heavily-loaded tubes of the IPT. At present, this model predicts typical timescales for radial transport that are much shorter

[4]If the plasma is particularly hot, or if there is a large scatter in the particle pitch angle (i.e: the angle between the velocity of the particle and the magnetic field), then the magnetic mirror force competes with the centrifugal force: this moves the confinement toward the magnetic equator (Hill et al., 1974).

[5]For clarity, the magnetic equator crosses the magnetic field lines at their farthest point from the *center* of Jupiter. This should not be confused with the definition of centrifugal equator, which crosses the magnetic field lines at their farthest point from the *spin axis* of Jupiter

[6]The perpendicular and parallel directions are referred to the local magnetic field.

than the ∼20-80 days derived from observations (e.g: Tsuchiya et al. (2018)), and therefore it is not consistent with the large mass retained in the IPT. Moreover, a fraction of the plasma supplied at Io's orbit diffuses inward (see Fig. 2.3) at a rate about 50 times slower than the outward diffusion: the mechanism underlying this inward diffusion is still unknown. At present, the radial transport is an active area of research that is being addressed by both observations (Bagenal and Kivelson, 2019; Bagenal et al., 2018) and modeling efforts (Hiraki et al., 2012).

- *Physical Chemistry* Due to the high density of the IPT, collisions are not negligible, and they cause the reactions that ultimately affect the source and loss of particles and energy. The modeling of the physical chemistry in the IPT presents several challenges. First, the cross section of excitation, ionization, dissociation and charge exchange reactions are not agreed upon or even determined, in some cases. Second, the physical chemistry has to be determined self-consistently with the diffusive transport to account for spatial and temporal variations. Over the last three decades, physical chemistry models improved consistently, with better database for the chemical reactions, as well as the inclusion of radial, azimuthal and temporal variation of the torus (Copper et al., 2016; Delamere et al., 2004, 2005; Nerney et al., 2017; Steffl et al., 2008; Tsuchiya et al., 2019; Yoshioka et al., 2018).

Voyager 1, being the first spacecraft to fly *inside* the IPT, perhaps represents one of the most important milestones in the exploration of the torus. Indeed, its trajectory was near the centrifugal equator and brought the spacecraft as close as less than 5 R_J from Jupiter's center: the radial structure of the torus was probed for the first time. Since then, the IPT has been divided into three radially distinct regions by their composition, density and temperature (Fig. 2.3): the outer warm torus, the ribbon and the inner cold disk.

- *The Warm Torus* The outer region of the IPT contains about 90%

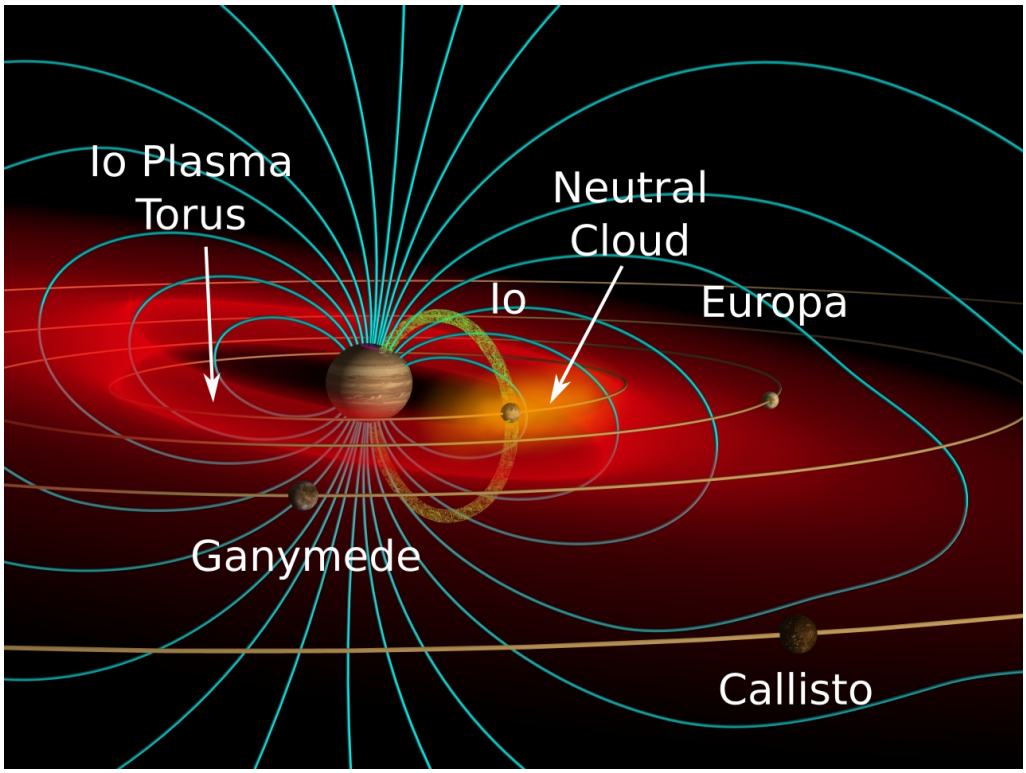

FIGURE 2.1: Graphical representation of the Jovian inner and middle magnetosphere. The light blue lines are the magnetic field lines, the yellow lines the orbit of Io, Europa, Ganymede and Callisto (from inside out). The intensity of the red color represents the plasma density, while the yellow glow around Io is the neutral cloud. The yellow tube connecting Io with Jupiter represents the current tube, at the feet of which auroral emission are observed. Retrieved and adapted from commons.wikimedia.org, credits to John Spencer.

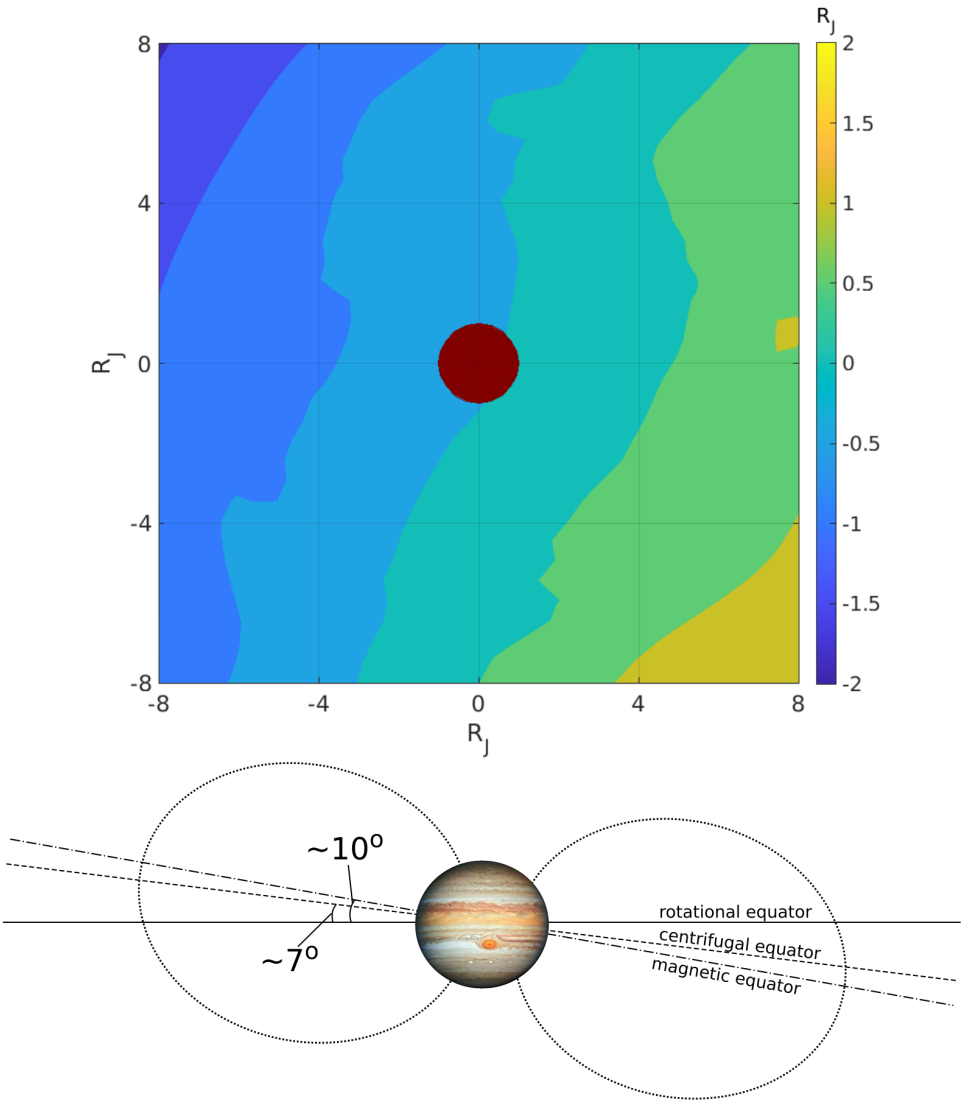

FIGURE 2.2: Top: contour plot representing the distance of the centrifugal equator from the rotational equator in Jupiter's rotating frame, in units of Jovian radii. The red spot in the center represents Jupiter. Bottom: sketch comparing the position of the rotational, magnetic and centrifugal equators (continuous, dash-dotted and dashed line, respectively). The position of the centrifugal equator in the inner magnetosphere is approximately 2/3 the angle between the magnetic and centrifugal equators (Hill et al., 1974). The angle between the magnetic dipole moment of Jupiter and the spin axis is ∼10° (Connerney et al., 2022), hence the centrifugal equator is tilted by ∼7°.

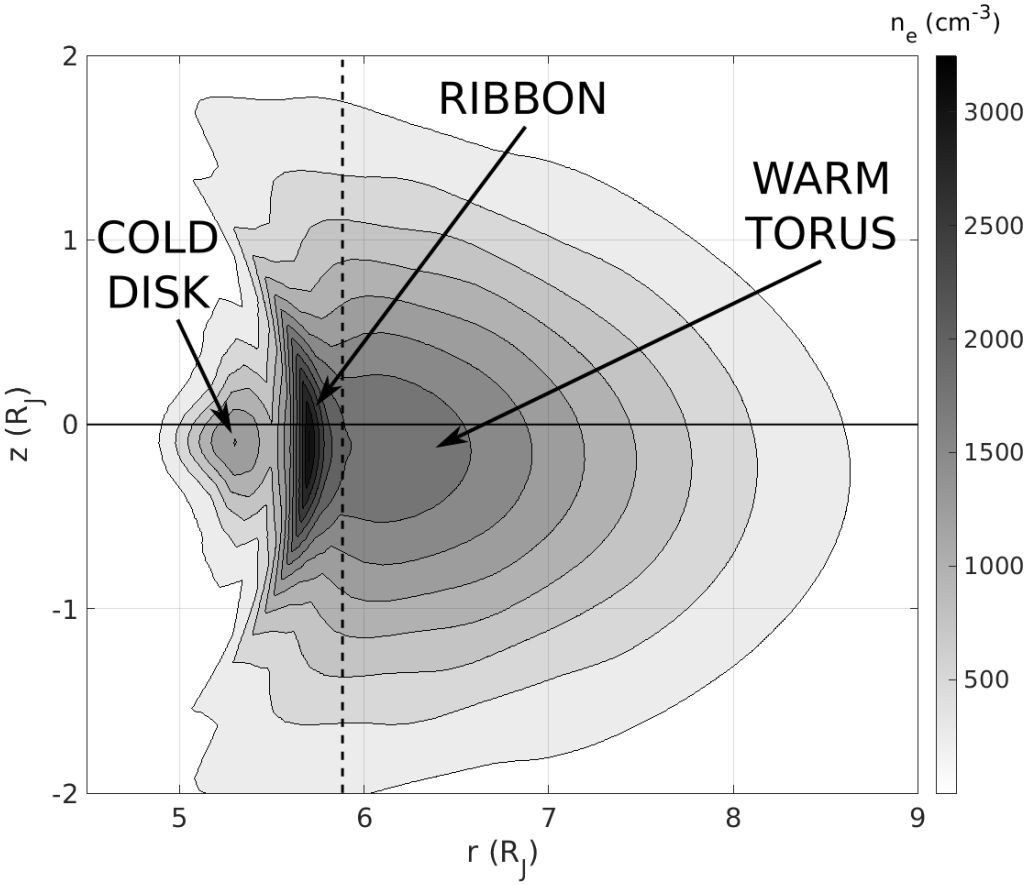

FIGURE 2.3: Electron density profile of the Io Plasma Torus, modeled using the diffusive equilibrium model by Bagenal and Sullivan (1981) (see section 6.1.1 for more details). $z = 0$ is the rotational equator; the vertical dashed line is the radial distance of Io's orbit. The three regions are characterized by different compositions, density and temperature. This latter parameter determines the vertical extension of each region: the higher the temperature, the thicker the region. The radial extension is determined by the plasma diffusion transversal to the magnetic field. The convex shape of the torus is due to the geometry of the magnetic field, which constrains the plasma distribution.

of the torus mass. The ion temperature is 60-100 eV, while electrons are at $\sim$ 5 eV. The warm torus scale height is about 1-1.5 R_J along the magnetic field lines, while is extends radially from 6 R_J - where the electron density at the centrifugal equator n_{e0} is 2000-2500 particles/cm^3 - to 8-9 R_J - where $n_{e0} \sim 100$ particles/cm^3 [7]. About 90% of the ions are oxygen (O^+ and O^{2+}) and sulfur (S^+, S^{2+} and S^{3+}) supplied by Io, O^+ and S^{2+} being the most abundant. Protons are $\leqslant$10%, and they likely originate from the Jovian ionosphere. The neutral clouds around Io also provides a few percent of sodium and chlorine ions (Na^+ and Cl^+, Küppers and Schneider (2000)). Traces of carbon (C^{2+}) are also detected (Feldman et al., 2004). As plasma diffuse from Io's orbit to Europa's, it expands, but instead of cooling down, the plasma heats up to a few hundreds of eV at Europa's orbit (9.4 R_J). The underlying process is still unknown, but it might be associated with a radially-increasing presence of hot electrons at a temperature of 50-100 eV. This hot electron population affects the relative abundances of the ions, which have higher ionization states as the plasma diffuse outwards. The hot electrons usually represent about 0.2-0.3% of the total electron contents, and they increase to a few percent at 9 R_J; moreover, the occurrence of a strong mass loading event can increase the hot electron fraction (Yoshioka et al., 2018). Unfortunately, the origin of these hot electrons is still undetermined.

- *The Ribbon* Just inside Io's orbit, between 5.6 and 5.9 R_J there is a narrow, high density region, with a vertical thickness similar to the warm torus. This region, called *ribbon*, potentially represents the inner boundary of the warm torus; nevertheless, it is usually described aside due to several differences with the outer region. Indeed, the ribbon exhibits a temperature similar to the warm torus, but with a more pronounced non-Maxwellian tail in the energy particle distribution [8]. Furthermore, while the plasma flow in the warm torus is very close

[7] To simplify the notation, particle density will be just written as cm^{-3} hereafter.
[8] This is considered a signature for pickup processes, described earlier in this section.

to corotation, the flow in the ribbon lags by ∼5% behind. Lastly, the electron density of the ribbon can be higher than 3000 cm^{-3}, while the composition is dominated by O^+, S^+ and, to a lesser extent, S^{2+}. These characteristics suggest that the ribbon might be the region where plasma is mainly produced from Io's neutral cloud and then diffused outward and inward into the warm torus and the cold disk, respectively.

- *The Cold Disk* Inward of the ribbon, the temperature of ions and electrons steeply drops to ∼1 eV; consequently, the plasma is more tightly confined and forms a ∼0.2 R_J-thick disk, with a typical electron density of 1000-1500 cm^{-3} (Herbert et al., 2008). The cold disk is located between 4.7 and 5.6 R_J. The details of the inward diffusion of material from Io's orbit are still poorly understood. Modeling efforts (Cowee et al., 2005) showed that the molecular ion SO_2^+ may be involved in the supply of mass and energy in the cold disk, but the spatial and temporal distribution of molecular ions in the IPT is still poorly constrained.

To conclude the description of the IPT, both spatial and temporal variations have to be introduced. The relevance of this last topic is related to two long-lasting question on the Jovian magnetosphere, that is: *(a)* how the IPT variability is related to the Iogenic source (e.g Roth et al. (2020)) and *(b)* how the whole Jovian magnetosphere is affected by changes in the torus (e.g: Bonfond et al. (2013)). A proper answer to this question requires to continuously monitor the IPT, the neutral cloud and Io; the auroral emissions on Jupiter are another fundamental tool, as they reflect processes occurring in the magnetosphere. The variability of the IPT can be classified into four category, namely: System III variations, System IV variations, local time asymmetry and temporal variability.

- *System III Variations* These are longitudinal variations associated with the asymmetry of the Jovian magnetic field (Chenette et al., 1974). The name derives from the System III frame of reference, in

which the planetary magnetic field is static. This frame of reference rotates around Jupiter's spin axis with a period of 9 hours, 55 minutes and 30 seconds and it is considered the main Jupiter frame nowadays[9]. The electron density and temperature of the IPT exhibit a ∼5% and ∼10% longitudinal variation respectively (Steffl et al., 2006), which are explained by heating due to plasma waves and longitudinal variations of the mirror ratio of the magnetic field (i.e: the ratio of the equatorial magnetic field to the field at the surface) (Hess et al., 2011a).

- *System IV Variations* These are longitudinal changes of the relative abundances of O^+, S^+, S^{2+} and S^{3+}; such modulation drifts at a speed 1-5% slower than System III (Kaiser and Desch, 1980; Steffl et al., 2006). The System IV periodicity seems to be related to the presence of hot electrons in the IPT (Hess et al., 2011b; Steffl et al., 2008) and to plasma sub-corotation near $6R_J$ (Copper et al., 2016). Furthermore, the period of System IV varies over time and it seems to shorten towards System III periodicity during and following strong mass loading events (Tsuchiya et al., 2019).

- *Local Time Asymmetry* The geometric barycenter of the IPT appears displaced towards the dawn side of Jupiter by about 0.2 R_J from Jupiter's center (Morgan, 1985; Schneider and Trauger, 1995); moreover, the torus is brighter at its dawn sector than at dusk. A candidate explanation is the presence of a dawn-dusk electric field, which originates in the plasma flow along the magnetotail (Barbosa and Kivelson, 1983). Based on the near-Earth observations performed by the Hisaki telescope, it was suggested that the local time asymmetry can be affected by the variable supply of material from the IPT to the magnetosphere (Brown and Bouchez, 1997), as well as to the compression of the whole magnetosphere caused by the variable solar wind pressure (Murakami et al., 2016).

[9]For sake of completeness, System I and II are based on the motion of the clouds near the equator and the poles, respectively, and they correspond to a period of 9h 50m 30s and 9h 55m 40s. Indeed, because Jupiter is a gaseous planet, its atmosphere has a differential rotation, which is slower at the poles than the equator (Dessler, 1983).

- *Temporal Variability* This last type of variability is associated with the variable supply of material from Io and the neutral cloud to the IPT. In principle, the plasma variations can originate either within or outside the torus. The former case is usually associated with the volcanic activity on Io, and in particular with strong eruptions and plumes. For example, both the Cassini and Galileo spacecraft detected a dust and plasma enhancement in 2000 (Delamere et al., 2004; Krüger et al., 2003; Steffl, 2004), which overlapped the increased activity of the Tvashtar volcano (Milazzo et al., 2005). In 2015, Hisaki continuously monitored the IPT conditions after another major mass loading event, potentially associated with the eruption of Kurdalagon Patera (de Pater et al., 2017). The understanding of the volcanically-driven temporal variability is a challenging endeavor that is still incomplete today. Indeed, strong events such as the above-mentioned ones are quite rare - once every ∼10 years - and unpredictable. Moreover, a full understanding of their effects on the IPT requires monitoring both the plasma, the neutral cloud and Io itself over several weeks or months: at present day, a similar dataset of simultaneous observations is still limited. Changes in the IPT content might also be ascribed to external causes. Indeed, global reconfiguration of the magnetosphere can drive injection of electrons from the outer part of the magnetosphere (Louarn et al., 2014); this, in turn, might affect the density and temperature of the torus, and hence the interaction with the neutral cloud and Io's atmosphere (Morgenthaler et al., 2022a). Unfortunately, no in-depth studies or clear evidence of these processes are available at present.

The overall variability of the IPT is given by the interplay between the above-mentioned types of variability. For example, the System III and System IV variations create a beat modulation of the IPT composition with a period of ∼29 days (Steffl et al., 2008). Moreover, the local time asymmetry appears to increase during periods of intense mass loading of the IPT (Brown and Bouchez, 1997), with the dawn ansa of the torus moving dawnwards. Observations performed by Hisaki suggest that the solar wind

compression of the magnetosphere can increase the dawn-dusk electric field, and therefore the local time asymmetry as well (Murakami et al., 2016).

2.2 The Magnetosphere from Europa to Ganymede

The IPT extends up to 8-9 R_J from Jupiter, that is: just inside Europa's orbit at 9.4 R_J. Therefore, the torus described in the previous section is the plasma environment between the first two Galilean moons (from inside out), while the magnetospheric features from Europa to Ganymede are described in this section.

The material in the plasmadisk from Europa's orbit outwards mainly comes from the IPT and, to a far lesser extent, from the interaction of the plasmadisk with Europa's neutral cloud (Bagenal and Dols, 2020), which is composed mainly by oxygen (Burger et al., 2010; Plainaki et al., 2018). Additionally, Europa shows the presence of water plumes (Roth et al., 2014), which is an additional source of oxygen and hydrogen. At about 8 R_J and outwards, the plasma density drops considerably with respect to Io's orbit, where the typical electron density is a few thousand cm^{-3}: at Europa, the electron density is about 150 cm^{-3}, while at Ganymede is <10 cm^{-3} (Dougherty et al., 2017). In the same regions, the radial transport speed increases from 0.5-2 km/s to 3-10km/s at Europa and Ganymede, respectively (Bagenal and Delamere, 2011). For comparison, at Io, the radial flow speed is only ∼0.1 km/s. The results of the decreasing density - which implies lower collisional rates between the particles - and the increasing radial transport speed is an effective "freezing" of the plasma composition[10]. Furthermore, the proton mixing ratio, which is less than 10% in the IPT, is usually 10-15% between 9 and 15 R_J (Bodisch et al., 2017).

[10]There is a radially-increasing fraction of hot electrons with typical temperature of a few hundreds electronvolts: this slightly favors the presence of O^{2+} and S^{3+} at the cost of O^+, S^+ and S^{2+}. Nevertheless, this radial variation of the ion composition is far less extreme than the one observed in the three regions of the IPT.

A puzzling behavior of the plasma is its heating as it is transported outwards. Indeed, assuming a dipolar magnetic field, the volume of a flux tube increases with the radial distance from the center of the planet as L^3, where L is the McIlwain L-parameter (e.g: Bagenal and Delamere (2011)). Moreover, if the plasma expands adiabatically as it diffuses outwards, the quantity $PV^\gamma \sim PL^{3\gamma}$ should be conserved (P is the plasma pressure, V the flux tube volume and γ the ratio specific heats). The temperature T in an adiabatic transformation is related to the pressure by $T = CP^{\frac{(\gamma-1)}{\gamma}}$ (C is a constant): if $\gamma > 1$ - as is the case for a monatomic gas, for which γ=5/3 - then the temperature increases/decreases as the pressure increases/decreases. By combining the above-mentioned adiabatic relations, one can expect the temperature to decrease with increasing radial distance as $T \sim V^{1-\gamma} \sim L^{3(1-\gamma)} = L^{-2}$ for a monatomic gas. Instead, the plasma temperature increases from 20-90 eV in the warm torus (Bagenal and Dols, 2020; Dougherty et al., 2017) to ∼180 eV at Europa's orbit and to ∼400 eV at Ganymede's (Bagenal and Delamere, 2011; Dougherty et al., 2017). Theoretical studies proposed that the heating is caused by *magnetohydrodynamics* (MHD) turbulence, which essentially heats the plasma by wave-particle interaction (Ng et al., 2018; Saur, 2004b). It was suggested (Bagenal and Delamere, 2011) that the underlying energy source for the heat might reside either in the planetary rotation - which is the main source of energy for most of the magnetospheric processes at Jupiter - or in the solar wind.

The magnetic field in the middle magnetosphere is due to the currents inside Jupiter - the *internal* field - and to the currents flowing in the plasmadisk around the planet - the *external* field. The internal field is introduced at the beginning of section 2 and, from Io's orbit to Ganymede's, can be approximated by a dipole field. In the middle magnetosphere, the plasmadisk current that produces the external field flows mostly azimuthally, with a small radial component. The two current components - azimuthal and radial - distort the dipolar magnetic field lines. The azimuthal component introduces a radial magnetic field above and below the plasmadisk according to Ampère's law Eq.A.13 (see Fig. 1.1 and 2.4), and the magnetosphere appears inflated with respect to a magnetosphere without a centrifugally-

confined, dense plasmadisk. Similarly, the radial component bends the magnetic field lines counterclockwise, as seen from the North pole. The precise determination of the magnetic field is fundamental to constrain the source of auroral phenomena and, in general, to map the various magnetospheric regions to the Jovian surface (or the other way around). Indeed, as it will be explained in section 2.3, the magnetospheric plasma is coupled with the planetary ionosphere by a system of currents flowing along the magnetic field. The electrons associated with these currents precipitate onto the atmosphere, where they can trigger reactions whose emission (i.e: the aurora) can be detected, for example, in the IR and UV bands with imaging and spectroscopic techniques (Broadfoot et al., 1979; Drossart et al., 1989). Therefore, it is possible to determine the location of various magnetospheric processes by looking at the aurora on the surface of Jupiter and, in general, of a planet, and using a magnetic field model to trace the location of the emission to the magnetosphere. Alternatively, if the position of the source is known - such as a moon - it is possible to predict the position of the associated emission, if there is any, and to test the validity of magnetospheric models.

The internal magnetic field of Jupiter appears quite stable over time. There are secular variations of this field detected by comparing nearly 50 years of observations, from Pioneer 10 in 1973 to Juno, although they are more prominent around the equator than in the polar regions (Moore et al., 2019). Moreover, by comparing Juno data with Voyager 1 (1979) and Ulysses (1992), it has been suggested that the dipole moment exhibits a precession of $\sim 0.1^\circ/\mathrm{yr}$ (Connerney et al., 2023). Although these variations are important for comparing datasets from different epochs and for long-term orbiter missions, they occur on a much longer timescale than the variations of the external field. Indeed, the azimuthal component of the plasmadisk current can vary by about 10% over a few weeks, and the radial component even by a factor 2 over the same period (Connerney et al., 2020): this affects the bending and stretching of the magnetic field in the middle magnetosphere, and hence the magnetosphere-ionosphere mapping. In the present thesis, the bulk of the data presented comes from the Juno epoch, which spans

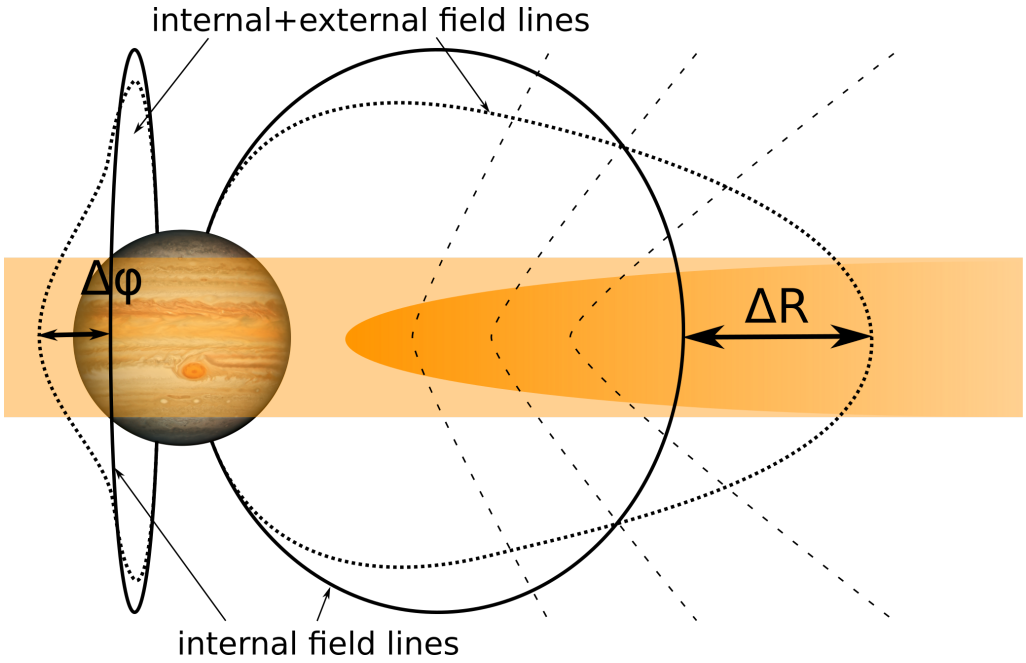

FIGURE 2.4: Sketch of the effect of the external field on the magnetic field geometry. The continuous lines represent the field due to the internal source only, the dotted lines the field the lines resulting from the superposition of the external field generated by the current in the plasmadisk (represented by the orange area). The lines on the left show the azimuthal bending $\Delta\phi$, while the lines on the right the radial stretching ΔR. The radial contribution of the external field is represented by the dashed lines. The image of Jupiter is retrieved from Wikimedia Commons (credits to NASA/JPL, Public domain, via Wikimedia Commons).

about 7 years of observations. Thus, the variations of the external field are expected to be more important than the $\sim 0.7°$ of cumulative drift[11] of the internal magnetic field, which will be considered constant (in Jupiter's frame) in the rest of this work.

The models of the external magnetic field can be divided into two categories: empirical and physical. Empirical models derive the field from a parametric current annular disk characterized by its shape (inner and

[11]This is the drift since the arrival of Juno at Jupiter and, hence, it is an upper limit that applies when comparing the oldest Juno data from August 2016 with the most recent ones. If one compares observations acquired closer in time, then the dipole drift will be proportionally smaller.

outer radii, and thickness), orientation and current density. The parameters are then tuned so that the resulting field matches the magnetic field measurements. Examples of this approach are the Voyager 1- and 2-based CAN81 model (Connerney et al., 1981) and the Juno-based Con2020 model (Connerney et al., 2020). These models are quite straightforward to code. Connerney et al. (1981) and Edwards et al. (2001) suggested an analytical approximation to derive the magnetic field in the current-free region above and below the plasmadisk, as well as in the inner magnetosphere: this makes the computation of the field very fast. Near and inside the plasmadisk, instead, it is necessary to perform a numerical integration[12]. The drawback of empirical models is that they adjust the plasmadisk current to fit the observations, disregarding the physical processes that drive the current in the first place. An additional conceptual step is then needed to derive a physical understanding of the dynamics of the plasmadisk. On the contrary, physical models derive the current distribution in the magnetosphere by solving a system that involves all the forces acting on the magnetospheric plasma (e.g: Caudal (1986); Nichols (2011); Nichols et al. (2015)). Indeed, by looking at Eq.A.7, the $\vec{J} \times \vec{B}$ force in the momentum equation balances the divergence of the pressure tensor ($\nabla \cdot \mathbf{P}$) and the plasma inertia forces ($n\partial_t \vec{U} + n(\vec{U} \cdot \nabla)\vec{U} = nd\vec{U}/dt$). In plasma physics the pressure is often considered a tensor represented by a 3×3 matrix instead as a scalar quantity, which is the case in fluid dynamics. Indeed, the pressure of a plasma represents its energy density, which is the macroscopic average of the kinetic energy of the particles. In a magnetized plasma, the particles are forced to gyrate perpendicularly to the magnetic field by the Lorentz force, but they are unimpeded along the filed lines. Thus, the speed of the particles along the field can be different from the speed of their gyrating motion (i.e: $v_\parallel \neq v_\perp$) and, hence, the pressure force exerted by the plasma in the two direction can be different (i.e: $p_\parallel \neq p_\perp$). Therefore, the pressure has to be represented by a matrix, which, in a frame with the z axis along the

[12]A toolbox for computing both the internal and external magnetic field at Jupiter has been recently published (Wilson et al., 2023) and it is available at: https://lasp.colorado.edu/mop/missions/juno/community-code/.

magnetic field, takes the form

$$\mathbf{P} = \begin{bmatrix} p_\perp & 0 & 0 \\ 0 & p_\perp & 0 \\ 0 & 0 & p_\parallel \end{bmatrix} \tag{2.1}$$

The plasmadisk current can be obtained by projecting the momentum conservation equation Eq.A.7 perpendicularly to the magnetic field (Nichols et al., 2015):

$$\vec{J_\perp} = \frac{\hat{b}}{B} \times \left[\rho_m \frac{d\vec{U}}{dt} + \nabla p_\perp + (p_\parallel - p_\perp)(\hat{b} \cdot \nabla)\hat{b} \right] \tag{2.2}$$

where $\hat{b}$ is the unit vector along the magnetic field, ρ_m the mass density of the plasma and $(\hat{b} \cdot \nabla)\hat{b}$ is the curvature of the magnetic field. The three terms in Eq.2.2 are the plasma inertia - which is due to the centrifugal motion - the pressure gradient and the pressure anisotropy current. Eq. 2.2 is coupled with the Ampère law Eq. A.13, so that it is possible to obtain the magnetic field from a differential equation. To solve this equation it is necessary to input the plasma pressure ($p_\parallel$ and $p_\perp$), density (ρ_m) and velocity ($\vec{U}$). The major advantage of physical models is that they allow us to understand which contribution in Eq. 2.2 is more relevant in determining the plasmadisk current: for example, Nichols et al. (2015) reported that inside ∼20 R_J the dominant contribution is the $\nabla p_\perp$ term, between 20 and 50 R_J is the pressure anisotropy $(p_\parallel - p_\perp)(\hat{b} \cdot \nabla)\hat{b}$, and outside 50 R_J is the centrifugal force. On the other side, the main drawback is that the magnetic field resulting from a physical model is as reliable as the plasma parameters of pressure, density and velocity plugged in Eq. 2.2, which may introduce deviations with the measurement of the magnetic field. In this thesis, it is necessary to have the most reliable magnetic field model, in order to have a precise mapping between the position of the moons and the Jovian surface where auroral emission is observed. On the other hand, the physical investigation of the origin of the plasmadisk currents is not a goal of the present study. For this reason, the analysis and results presented here will mostly use the magnetic field derived from an empirical approach; more

specifically, the most commonly used models will be Juno-based JRM33 (internal field) and Con2020 (external field) (Connerney et al., 2020, 2022; Wilson et al., 2023).

2.3 Magnetosphere-Ionosphere Coupling

In a planetary magnetosphere, the motion of the charged particles is affected by the magnetic field of the planet itself. If no magnetic field is present, the plasma motion is governed by Kepler's laws, hence it orbits around the planet with the Keplerian angular speed $\omega_K = \sqrt{GM_P/r^3}$, M_p being the mass of the planet and r the distance from its center. On the other side, the presence of a planetary magnetic field considerably affects the motion of the charged particles. Indeed, a fundamental principle of plasma physics is the so-called *Alfvén theorem* or *frozen-in-flux* theorem (Alfvén, 1942, 1943), which states that, under ideal conditions [13] , the flux of magnetic field through any given surface in a plasma is constant [14] . In other, more intuitive words, the magnetic field can be considered as a "mesh" that "entangles" the plasma: any motion of the plasma correspond to a motion of the magnetic "mesh" and vice versa [15] . In a planetary system, the

[13] An *ideal plasma* is defined according to the *ideal Ohm's law*, Eq. A.9, which is an approximation of the *generalized Ohm's law*, Eq. A.8. The applicability of the approximated version depends on the time-scales and length-scales involved, as well as on the relative contribution between the plasma pressure and the magnetic pressure $B^2/8\pi$, but in space plasmas it holds very well in most of the cases.

[14] Another description is that the magnetic field is advected by the plasma, which can be obtained by plugging the ideal Ohm's law Eq. A.9 into Faraday's equation Eq. A.12. Alternatively, one can consider that two volumes of plasma crossed by the same magnetic field line at a given time t_0 remain on the same line under ideal conditions for $t > t_0$.

[15] Although this metaphor likely helps one's imagination, it can be misleading and, in general, proper care should be used when deriving deductions based on this conceptualization. Indeed, the idea of "mesh" derives from the idea of magnetic field *lines* and therefore the magnetic field is often believed to "move" under the motion of the plasma as a result of the frozen-into-flux theorem. Counter-examples to that description are symmetric systems such as a uniform or an axially-symmetric system, for which the idea of moving field lines is ill posed. More properly, the motion of plasma perpendicularly to a background magnetic field induces electrical currents, which in turn generate an induced magnetic field (Ferraro, 1937). The sum of the background and the induced fields give the "illusion" that the magnetic field lines are advected with the flow.

magnetic field "entangles" the plasma in the magnetosphere, but also at the ionosphere, therefore the two environments are ultimately connected by the magnetic field. The ionosphere, in turn, is coupled with the atmosphere by ion-neutral and electron-neutral collisions, which exerts a drag force that makes the ionosphere corotate with the planet at an angular speed Ω_P. The atmosphere is thus coupled with the magnetosphere: energy and angular momentum are transferred between the planet and its magnetosphere, so that the plasma is accelerated towards rigid corotation with the planet itself. This is provided by the electric currents flowing between the two environments. Indeed, consider a dipolar magnetic field aligned with the planetary spin axis and a magnetospheric plasma that is sub-corotating at $\omega_M < \Omega_P$ (Fig. 2.5), so that there is a velocity shear between the magnetosphere and the ionosphere. Thanks to the frozen-in-flux theorem, this velocity shear bends the magnetic field and introduces a magnetic shear stress between the magnetosphere and the ionosphere [16] . This makes the ionosphere slow down to an angular velocity ω_I between ω_M and Ω_P, which results from the magnetic stress on the upper ionosphere and the collisional atmospheric drag at its bottom. At the ionosphere, the plasma-neutral relative motion and the collisions drive a system of ionospheric currents - perpendicular to the magnetic field - as electron and ions collide with the neutrals at different rates, thus they generate a current [17] . In the upper layers of the ionosphere, the collisions become less and less important, hence the currents can flow only along the magnetic field [18] . These *field aligned currents* (FACs) are closed in the magnetosphere, where the bending of the magnetic field can generate a current perpendicular to the magnetic field, according to Ampère's law. Thanks to this current, there is a $\vec{J} \times \vec{B}$ force in Eq. A.7 that accelerates the magnetospheric plasma. The current keeps flowing until there is no relative motion between the ionosphere and the

[16] See the Maxwell stress tensor in Eq. A.7 for its mathematical expression.

[17] Indeed, the last term in Eq. A.2 is now non-zero, which results in a net current.

[18] By looking at Eq.A.14, it is clear that, if the collision frequencies $\nu_i, \nu_e \to 0$, then $\sigma_\parallel \to \infty$ and $\sigma_P, \sigma_H \to 0$, hence $\vec{J} = \sigma_\parallel \vec{E}_\parallel$. Therefore, a fully magnetized, collisionless plasma can be considered a perfect conductor along the magnetic field, and a dielectric in the perpendicular direction.

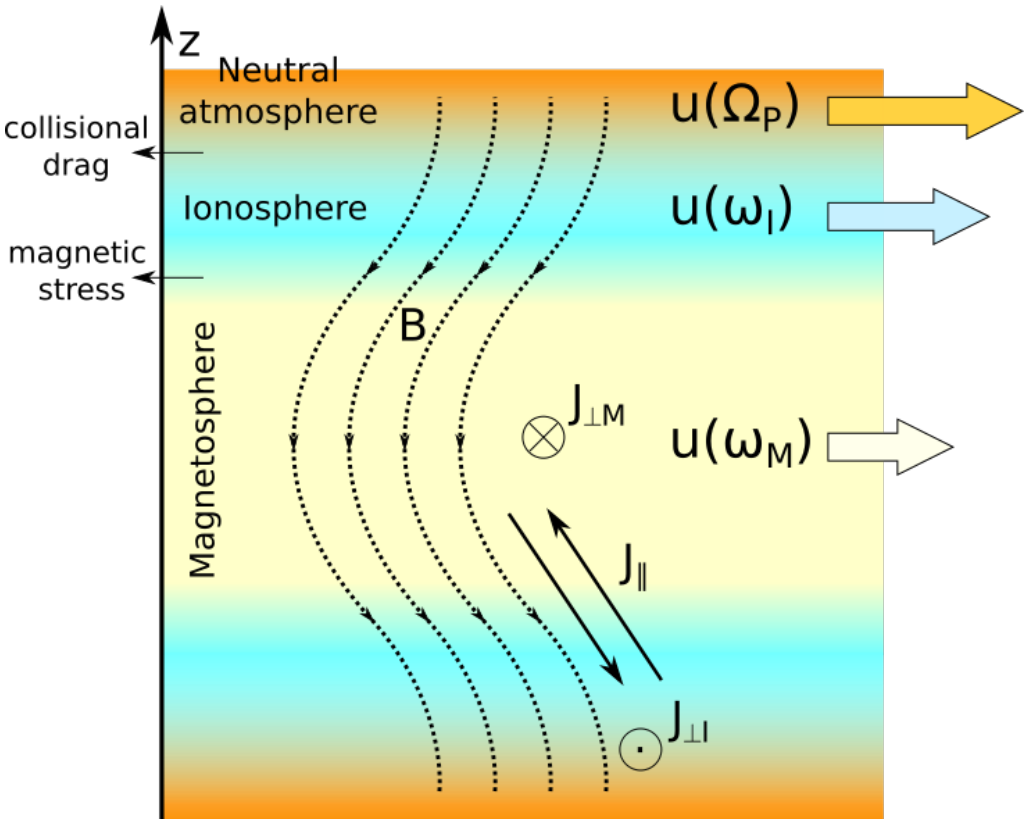

FIGURE 2.5: Sketch of the Magnetosphere-Ionosphere coupling in cylindrical projection. This is obtained by mapping a magnetic shell (that is: the magnetic field lines whose farthest point from Jupiter's center is at a given distance from the planet itself) on a plane. Hence, the top and bottom sides correspond to Jovian surface at the northern and southern hemispheres, respectively. The magnetosphere is sub-corotating at angular speed $\omega_M < \Omega_P$. The ionosphere is expected to move with angular velocity ω_I, which is determined by the neutral drag acting on its bottom and by the magnetic stress acting on its top. The black dotted lines represent the magnetic field. The black arrows represent the flow of the field aligned currents, which are closed by the ionospheric current $J_{\perp,I}$ and the magnetospheric current $J_{\perp,M}$.

neutral atmosphere, that is: until the magnetospheric corotation is restored.

To summarize, the presence of the magnetic field changes qualitatively the orbital motion of plasma around the planet. Indeed, if no magnetic field is present, the angular speed decreases as $r^{-3/2}$, according to Kepler laws.

On the other side, with a magnetic field, the angular speed is constant and equal to the planetary angular speed. This requires a transfer of energy and angular momentum between the planet and its magnetosphere, which is carried by currents. In order for the M-I coupling to be efficient, three conditions must be satisfied (Dessler, 1983):

1. the atmosphere must have an efficient vertical transport of momentum for transferring it to the ionosphere (planet-atmosphere coupling).

2. high ionospheric conductivity (atmosphere-ionosphere coupling).

3. the ideal Ohm's law Eq. A.9 must be applicable (ionosphere-magnetosphere coupling).

Additionally, the magnetic tension $F_M = \frac{(\vec{B}\cdot\nabla)\vec{B}}{4\pi}$ (see Eq.A.7) in the magnetosphere must be strong enough to counterbalance the centrifugal force $F_c = \rho\Omega_P^2 r$ of the corotating plasma (ρ being the plasma mass density). This condition can be satisfied in the inner region of a magnetosphere (the so-called *plasmasphere*), where the magnetic field is strong enough, but it cannot extend indefinitely towards the outer regions. Indeed, for a dipole field, the magnetic tension can be re-written $F_M = \frac{B^2}{4\pi}(\hat{b}\cdot\nabla)\hat{b} = \frac{B^2}{4\pi}\frac{1}{R_c}$, where R_c is the curvature radius of the magnetic field and $\hat{b} = \vec{B}/|\vec{B}|$. At the equator, $B \sim r^{-3}$ and $R_c = r/3$ lead to $F_M \sim r^{-7}$. Thus, beyond a certain distance, the magnetic tension is not strong enough to confine the plasma, which drifts outwards. This triggers a positive feedback: as the drifting plasma moves to higher distances, it conserves its angular momentum and loses angular velocity, hence it is sub-corotating. Currents are set up to accelerate the plasma toward corotation: they increase the centrifugal force, which in turn enhances the radial drift of the plasma. Because the magnetic field magnitude decreases with the distance from the planet as r^{-3}, the magnetospheric currents must increase in order for the $\vec{J}\times\vec{B}$ force in Eq. A.7 to effectively accelerate the plasma. This is not possible indefinitely, as there is finite conductivity in the ionosphere, thus limiting the maximum

current [19] . As a result, the outer region of the magnetosphere does not corotate rigidly with the planet, and the magnetic field is advected in a spiral-like pattern (Khurana et al., 2004).

[19]This further highlight the importance of the second conditions for the M-I coupling: the higher the conductivity, the farther from the planet the corotation can be supported.

CHAPTER 3

Satellite-Ionosphere Coupling

This chapter describes the physics involved in the S-I coupling, that is: the chain of physical processes that transmit the perturbation in the plasma flow around the moons up to the planetary ionosphere. As the perturbation is propagated by waves that are typical of magnetized plasmas, a brief introduction on the low-frequency plasma modes is provided in section 3.1.

Now that the M-I is introduced as the ensemble of processes that transfer energy and angular momentum between a planet and its magnetospheric plasma by electric currents, it is easier to understand how the S-I coupling can be considered as a specific case of M-I coupling. Indeed, natural satellites orbit around planets at Keplerian angular speed ω_K, which, in general, is different than the corotation speed at the angular speed Ω_P of the planet. More precisely, most of the moons in the Solar System orbit beyond the corotation radius, that is: the distance where $\omega_K = \Omega_P$ [1] . Hence, the moons represent a local source of sub-corotation, which the magnetosphere counteracts by arranging a current system between the natural satellite

[1]For example, the terrestrial Moon orbits at about 60 R_E (1 R_E = 6371 km is the Terrestrial radius), while the corotation radius is ∼6.5 R_E; at Saturn and Jupiter, the innermost major satellites Mimas and Io orbits at 3.2 R_S (1 R_S = 58232 km is the Saturnian radius) and 5.9 R_J, respectively, and the corotation radius is ∼2 planetary radii for both planets.

and its proximity, and the planetary ionosphere. In the following, it is assumed that the orbital speed of the moon is smaller than the corotation speed of the plasma at the orbits of the satellites. Furthermore, consider a satellite that orbits completely within a planetary magnetosphere and that the plasma flow is mainly azimuthal at the satellite. At the Earth, the Moon is connected to the planetary magnetic field only when it orbits through the magnetotail, where the flow is predominantly radial, while the major moons of Jupiter and Saturn are always well within the magnetosphere. Hence, the theory of the present section strictly applies to cases like Jupiter and Saturn, and not like Earth. Moreover, in the remainder of the present chapter, the Io-Jupiter coupling will be used to introduce and explain the physics of the S-I coupling, as it is the most investigated from both the theoretical and observational points of view. The fundamentals of the Io-Jupiter electromagnetic interaction can be quite straightforwardly applied to Europa and Ganymede. At Callisto the local interaction with the Jovian magnetosphere may occasionally be different from the other three Galilean moons, due to the radial variations of plasma parameters: this is expected to decrease the Poynting flux (i.e: the energy transfer) between Jupiter and Callisto (Saur et al., 2013). At Saturn, it is suggested that the local interaction of Enceladus, Dione and Rhea may be strong enough to generate a significant Poynting flux, possibly through a process similar to the one that is found at Jupiter (Saur et al., 2013).

Early[2] models of the S-I coupling at Jupiter did not consider the presence of the high density IPT, nor of Io's atmosphere, neither of which had been detected. Therefore, assuming that the density of the Jovian magnetosphere is very low and that Io is an atmosphere-less, conducting satellite, Piddington and Drake (1968) and Goldreich and Lynden-Bell (1969) proposed the so-called "unipolar inductor" model. According to this model, Io, the Jovian magnetic field, and the planetary ionosphere can be considered as the components of a resistive circuit. Indeed, Io behaves like a conducting body moving in a magnetic field, therefore it can be considered as a DC

[2]That is, before the Voyager 1 fly-by of Jupiter in 1979.

electric potential generator; the low density magnetospheric plasma is a perfect conductor along and a dielectric across the magnetic field, hence it can be viewed as a resistance-free transmission line along the field; near Jupiter's surface, the high density of the ionosphere and the presence of neutral particles introduce a finite conductivity, hence it can be considered the resistive load of the circuit. Later, Io's ionosphere was introduced in the model as well, and it can be considered as an additional resistance in parallel to the Jovian ionosphere (Saur et al., 2004). According to the unipolar inductor model, the currents are field-aligned and thus no force is exerted on the plasma by the $\vec{J} \times \vec{B}$ force in Eq. A.7. Therefore, the energy is transferred between Jupiter and Io, with no contribution to the magnetospheric plasma. Moreover, the Io-Jupiter current system reacts almost immediately to changes in the conductivity of the ionosphere: the electromagnetic field propagate at the speed of light, and thus the Io-Jupiter current system takes only a couple seconds to reach a new steady state. As it will be clear by the end of this chapter, the discovery of the dense IPT by Voyager 1 in 1979 has radically changed the picture of the S-I coupling at Jupiter. Indeed, the inclusion of a dense plasma environment around Io implies that the current is no more field-aligned, thus a force is exerted on the plasma. Moreover, the relative speed between Io and the IPT continuously generates a plasma flow perturbation around the moon, similarly to a river passing around a pier of a bridge. This triggers a specific plasma mode, called *Alfvén wave* (Alfvén, 1942), which carries the currents that mediate the Io-Jupiter coupling. The speed of these waves decreases with the plasma density and, in general, is lower than the speed of light. Consequently, current variations due to conductivity changes take several minutes to propagate between Io and Jupiter: during such a time interval, Io continues along its orbit, and the "updated" current cannot close at the satellite: the result is that the S-I electromagnetic coupling cannot be considered a static state, but rather a "snapshot" of various physical processes that transmits the local sub-corotation near Io up to the Jovian ionosphere (e.g: Delamere et al. (2003)).

Before explaining the details of the current understanding of the S-I

coupling at Jupiter, the reader might find the brief recap on the propagation of long-wavelength, low frequency modes in magnetized plasmas given in the next section useful. This is fundamental to the electromagnetic S-I coupling, as one of these modes - the already-mentioned Alfvén waves - carries the currents between Jupiter and Io, and thus it mediates the S-I coupling. After that, the next three sections are dedicated to the details of the local interaction, the far-field propagation and the auroral emission of the S-I coupling, respectively, assuming Io as an example.

3.1 Low-Frequency Plasma Modes in Magnetized Plasmas

The following section is an introduction to low-frequency waves in magnetized plasmas, part of which can be found in many textbooks (e.g: Chandrasekhar (1961); Krall and Trivelpiece (1973); Pucelle and Segre (2014)). These waves fulfill a key role in the S-I coupling, and in the M-I coupling in general, therefore it is fundamental to understand which modes are excited by the Jovian satellites and how they mediate the planet-moon interaction.

Consider a uniform plasma permeated by a uniform magnetic field. The response of the plasma to any form of perturbation can be derived from the MHD equations Eq. A.5[3], A.7 and A.12. These three equations do not form a closed system, and an equation for the energy balance is needed. A simple yet general choice to include the plasma response to heat transfer is a polytropic law

$$Pn^{-N} = constant \tag{3.1}$$

where n is the plasma density. The value of the polytropic index N determines the type of thermodynamic process occurring to the plasma (e.g: $N = 0$ corresponds to a isobaric process, $N = 1$ to an isothermal one). In the following, it will be assumed $N = \gamma$, where γ is the heat capacity ratio, corresponding to an adiabatic process. In Eq.3.1 it is assumed that the

[3]Here, it is assumed that there is no source or sink of particles, i.e: $S = L = 0$.

pressure is isotropic, i.e: $p_\perp = p_\parallel$ in Eq. 2.1. If the pressure anisotropy cannot be neglected, it is possible to derive two polytropic equations from Eq. 2.1 and 3.1, one for $p_\perp$ and one for $p_\parallel$ (Chew et al., 1997). Nevertheless, without loss of generality and for sake of simplicity, it will be here assumed that the pressure is isotropic.

To show the small-amplitude plasma modes that can be excited, Eq. A.5, A.7, A.12 and 3.1 are linearized, which is obtained by substituting

$$\begin{aligned} \vec{B} &\rightarrow \vec{B}_0 + \vec{B}_1 \\ n &\rightarrow n_0 + n_1 \\ P &\rightarrow P_0 + P_1 \\ \vec{V} &\rightarrow \vec{V}_0 + \vec{V}_1 \end{aligned} \tag{3.2}$$

where the subscript "0" refer to the static equilibrium fields, and "1" to the perturbed quantities. It is assumed that $Q_1 << Q_0$ for each quantity in Eq. 3.2, so that each term of the order Q_1^2 or higher can be neglected; moreover, it is also assumed that the plasma is initially at rest, hence $\vec{V}_0 = 0$. To solve the system of equations, a wave-like solution of the form $\sim exp[i(\vec{k}\cdot\vec{r} - \omega t)]$ can be found. By substituting this solution into the system and rearranging, another system of equations can be obtained for the three components of the velocity:

$$\Big[\omega - \frac{(\vec{k}\cdot\vec{B}_0)^2}{4\pi\rho_0}\Big]\vec{V}_1 = \tag{3.3}$$
$$= \Big\{\Big[\frac{\gamma P_0}{\rho_0} + \frac{B_0^2}{4\pi\rho_0}\Big]\vec{k} - \frac{(\vec{k}\cdot\vec{B}_0)^2}{4\pi\rho_0}\vec{B}_0\Big\}(\vec{k}\cdot\vec{B}_0) - \frac{(\vec{k}\cdot\vec{B}_0)(\vec{V}_1\cdot\vec{B}_0)}{4\pi\rho_0}\vec{k}$$

where $\rho_0 = n_0\overline{m}$, $\overline{m}$ being the average ion mass. If the z axis is parallel to the equilibrium magnetic field $\vec{B}_0$, and $\vec{k}$ is in the $x-z$ plane and forms an angle θ with B_0, than the equation above corresponds to the following eigenvalue problem:

$$\begin{bmatrix} \omega^2 - k^2V_A^2 - k^2C_s^2sin^2\theta & 0 & -k^2C_s^2sin\theta cos\theta \\ 0 & \omega^2 - k^2V_A^2cos^2\theta & 0 \\ -k^2C_s^2sin\theta cos\theta & 0 & \omega^2 - k^2C_s^2cos^2\theta \end{bmatrix} \begin{bmatrix} V_x \\ V_y \\ V_z \end{bmatrix} = 0 \tag{3.4}$$

where

$$V_A = \sqrt{\frac{B_0^2}{4\pi\rho_0}} \tag{3.5}$$
$$C_s = \sqrt{\frac{\gamma P_0}{\rho_0}}$$

are the *Alfvén speed* and the *sound speed*, respectively. Eq. 3.4 can be solved if the determinant is zero, that is:

$$(\omega^2 - k^2 V_A^2 cos^2\theta)[\omega^4 - \omega^2 k^2 (V_A^2 + C_s^2) + k^4 V_A^2 C_s^2 cos^2\theta] = 0 \tag{3.6}$$

The dispersion relation Eq. 3.6 has three independent solutions, which correspond to three different plasma waves.

The first solution of Eq.3.6 is

$$\omega = k V_A cos\theta \tag{3.7}$$

whose eigenvector is $[0 \quad V_y \quad 0]$. This mode corresponds to a so-called *shear Alfvén wave* propagating at an angle θ from the background magnetic field. This mode is characterized by $\vec{k}\cdot\vec{V_1} = \vec{B_0}\cdot\vec{V_1} = 0$, and by $\rho_1 = 0$ and $P_1 = 0$, which means that Alfvén waves are transversal oscillation of the magnetic field with no density, nor pressure perturbation. Furthermore, the Alfvén waves cannot propagate perpendicularly to the magnetic field.

The other two solutions are given by

$$\omega = k V_{f,s} \tag{3.8}$$
$$V_{f,s} = \left\{ \frac{1}{2}[V_A^2 + C_s^2 \pm \sqrt{(V_A^2 + C_s^2)^2 - 4V_A^2 C_s^2 cos^2\theta}] \right\}$$

where V_f and $V_s \leq V_f$ are the *fast* and *slow magnetosonic modes*, whose eigenvectors have the form $[V_x \quad 0 \quad V_z]$. To understand the nature of these two waves, consider a cold plasma, i.e: $C_s << V_A$[4]: in this case, $V_f = V_A$, and

[4]The ratio $(C_s/V_A)^2$ is also known as *plasma β parameter*, which also corresponds to the thermal-to-magnetic pressure ratio

$$\beta = \frac{C_s^2}{V_A^2} = \frac{8\pi P_0}{B_0^2} \tag{3.9}$$

As the pressure is reasonably expected to be proportional to the temperature, the cold plasma approximation corresponds to $\beta << 1$.

the wave propagates perpendicularly to the magnetic field ($\theta = 0$) - contrary to an Alfvén wave - as a compressional wave. The slow mode, instead, propagates at $V_s = C_s$ along the magnetic field, and $V_s = 0$ perpendicularly to it, therefore it corresponds to a sound wave traveling along the magnetic field.

In the S-I interaction, the Alfvén waves have the primary role to carry the currents of the coupling. The role of the fast and slow modes in the S-I coupling is expected to be secondary or even negligible (Jacobsen et al., 2007), although more modeling and observational effort would be needed to properly determine their effect. In the following, some generalization to the dispersion relation of the Alfvén waves Eq. 3.7 will be presented, as they are expected to play a significant role in the S-I coupling at Jupiter, while the other two modes will not be covered.

Relativistic correction The dispersion relation for the relativistic Alfvén speed is obtained from the continuity and mass equations A.1, A.2, Faraday's equation A.12, and Ampère's equation A.13. In the latter, the displacement current proportional to $\partial\vec{E}/\partial t$ must be retained. Assuming a plasma made by electrons e and an ion species i, the linearization Eq.3.2 leads to the generalization of the dielectric matrix Eq.3.4 (Krall and Trivelpiece, 1973)

$$\boldsymbol{\varepsilon} = \begin{bmatrix} \varepsilon_1 & +i\varepsilon_2 & 0 \\ -i\varepsilon_2 & \varepsilon_1 & 0 \\ 0 & 0 & \varepsilon_3 \end{bmatrix} \tag{3.10}$$

where

$$\varepsilon_1 = 1 + \frac{\omega_{pe}^2}{\Omega_e^2 - \omega^2} + \frac{\omega_{pi}^2}{\Omega_i^2 - \omega^2} \tag{3.11}$$

$$\varepsilon_2 = \frac{\Omega_e}{\omega}\frac{\omega_{pe}^2}{\Omega_e^2 - \omega^2} - \frac{\Omega_i}{\omega}\frac{\omega_{pi}^2}{\Omega_i^2 - \omega^2} \tag{3.12}$$

$$\varepsilon_3 = 1 - \frac{\omega_{pe}^2}{\omega^2} - \frac{\omega_{pi}^2}{\omega^2} \tag{3.13}$$

$\Omega_{e,i}$ and $\omega_{pe,i}$ are the cyclotron and plasma frequencies for electrons and ions respectively:

$$\Omega_{e,i} = \frac{q_{e,i}B}{m_{e,i}c} \tag{3.14}$$

$$\omega_{pe,i} = \sqrt{\frac{4\pi n_{e,i} q_{e,i}^2}{m_{e,i}}} \tag{3.15}$$

One of the solutions obtained by approximating the dispersion relation derived by the dielectric Eq.3.10 to low-frequency modes[5] is the relativistic generalization of the shear Alfvén waves dispersion relation Eq. 3.7:

$$\omega = k \frac{V_A}{\sqrt{1 + \frac{V_A^2}{c^2}}} cos\theta \tag{3.16}$$

In the Jovian case, the relativistic correction must be considered for Alfvén waves propagating between the planetary ionosphere and the IPT and the plasmadisk, as the strong magnetic field and low plasma density both increase the Alfvén speed up to a considerable fraction (>95-99%) of the speed of light.

Dispersive correction: inertial and kinetic effects The derivation of the dispersion relations of the Alfvén waves is limited to the validity regime of the MHD equations, that is: the timescale involved must be longer than the plasma and cyclotron frequencies and the length-scale longer than the particle gyroradius and the Debye length $\lambda_D = \sqrt{\frac{1}{4\pi n_0 q_e^2} \frac{T_e T_i}{T_e + T_i}}$. In order to properly determine the plasma behavior at small scales, it is necessary to resort to a kinetic approach[6](Lysak and Lotko, 1996; Lysak and Song, 2003). Consider again a uniform plasma in a uniform magnetic field, as at the beginning of this section, but instead of assuming that the perturbation satisfies the MHD criteria of long timescales and length-scales, assume that (1) the magnetic pressure dominates the plasma pressure (*cold plasma* or

[5]Waves with frequency $\omega < \Omega_i$; for a general ion i, $\Omega_i < \Omega_e$.

[6]A proper introduction to kinetic theory of plasmas would probably detract attention from the main points, and it is not reported (nor necessary) in the present work. In brief, the MHD approach considers a plasma as a continuous medium, subject to both the fluid and Maxwell's equations, while the kinetic approach considers the plasma as an ensemble of particles subject to mutual electromagnetic interaction. With this approach, the thermodynamic quantities (e.g: density and temperature) and the dielectric properties of the plasma are statistically derived from its particle distribution function. Although the kinetic approach could be considered more "physically sound", the MHD equations can be derived from the kinetic theory, thus the two methods are broadly consistent. Furthermore, the computation complexity needed by the kinetic approach is usually higher than in MHD, which implies that it can be applied only to simpler systems.

low-β approximation), (2) $V_A << c$[7] and (3) that wavelength is smaller than the Debye length. In this case the dielectric assume the form (Lysak and Lotko, 1996; Lysak and Song, 2003)

$$\boldsymbol{\varepsilon} = \begin{bmatrix} \frac{c^2}{V_A}\frac{1-\Gamma_0(\mu_i)}{\mu_i} - \left(\frac{k_\parallel c}{\omega}\right)^2 & \frac{k_\parallel k_\perp c^2}{\omega^2} \\ \frac{k_\parallel k_\perp c^2}{\omega^2} & \frac{\Gamma_0(\mu_e)}{k_\parallel^2\lambda_D^2}(1+\xi Z(\xi)) - \left(\frac{k_\perp c}{\omega}\right)^2 \end{bmatrix} \tag{3.17}$$

where $\mu_{e,i} = k_\perp^2\rho_{e,i}^2$ ($\rho_{e,i} = m_{e,i}v_{e,i\perp}/q_{e,i}B$ is the electron/ion gyroradius), $\xi = \omega/k_\parallel v_{e\,th}$ ($v_{e\,th} = \sqrt{2T_e/m_e}$ is the electron thermal velocity), Γ_0 the modified Bessel function and Z the plasma dispersion function (Fried and Conte, 1961). The $\parallel$ and $\perp$ symbols refer to the parallel and perpendicular direction with respect to the magnetic field. The dispersion relation obtained in two different regimes is particularly illustrative of the physics involved:

- *Hot electrons* The thermal speed on the electrons is larger than the phase speed of the wave, that is: $v_{e;th} >> \omega/k \rightarrow \xi << 1$ in Eq. 3.17. In this case the dispersion relation is

$$\omega^2 = k_\parallel^2 V_A^2(1 + k_\parallel^2\rho_i^2 + k_\perp^2\rho_s^2) \tag{3.18}$$

  where $\rho_s = T_e m_i/q_e^2B^2$. The waves associated with Eq. 3.18 are called *Kinetic Alfvén Waves* (KAW), and the relevant parameters for the wave propagation are the electron pressure and the ion cyclotron radius.

- *Cold electrons* The thermal speed on the electrons is smaller than the phase speed of the wave, that is: $v_{e;th} << \omega/k \rightarrow \xi >> 1$ in Eq. 3.17. In this case the dispersion relation is

$$\omega^2 = k_\parallel^2 V_A^2 \frac{1 + k_\perp^2\rho_i^2}{1 + k_\perp^2\lambda_e^2} \tag{3.19}$$

  where $\lambda_e = c/\omega_{pe}$ is the electron skin depth. The waves associated with Eq. 3.19 are called *Inertial Alfvén Waves* (IAW), and the relevant parameter for the wave propagation is the electron inertia.

[7] Actually, the inclusion of the relativistic correction is straightforward, as it consists in a factor $[1 + (V_A^2/c^2)]^{-\frac{1}{2}}$, with V_A from Eq.3.5.

The main difference in the kinetic approach is that Eq. 3.18 and 3.19 are the dispersion relation of dispersive waves, that is $\partial\omega/\partial k \neq 0$, and the speed of the wave depends on its wavelength. In other words, the different wavelengths excited by a perturbation propagate at different speed, when kinetic and/or inertial effect are important. For this reason, it is possible to generally refer to the full dispersion relation derived from the dielectric Eq. 3.17 as the *Dispersive Alfvén Waves* (DAW) relation.

At the orbits of the Galilean satellites, the plasma density is higher by a factor $\sim 10^2$ and the magnetic field intensity lower by a factor $\sim 10^3$ than above the Jovian ionosphere. Therefore the ion cyclotron radius of the ions $\rho_i \sim B^{-1}$ is expected to be large near the satellites, while the the electron skin depth $\lambda_e \sim n_e^{-1}$ small. On the other side, above the ionosphere, the electron inertia dominates over the kinetic effects (Jones and Su, 2008; Su et al., 2006). The main interest on the DAW for the S-I coupling at Jupiter is not mainly related to the determination of the dispersion relation, but rather to the field-aligned electric field associated with the waves, which may play a key role in accelerating the auroral electrons (Damiano et al., 2019; Hess et al., 2010a) (see section 3.3).

3.2 Local Magnetosphere-Ionosphere Interaction

Early models of the Io-magnetosphere local interaction are introduced at the beginning of Chapter 3. The problem was tackled by Piddington and Drake (1968) and Goldreich and Lynden-Bell (1969) considering Io as a conductor moving in a magnetic field: the Hall effect produces a charge separation on the sides of the moon, thus it can be regarded as a voltage generator - hence the name "unipolar inductor". A fundamental hypothesis of the unipolar inductor model is the presence of low density plasma between Io and Jupiter to carry the S-I coupling currents: in this case, any change in the currents propagates at the speed of light and the satellite-magnetosphere-ionosphere can be considered as a quasi-stationary electric circuit made by a generator

and a resistive load.

The discovery of the IPT by Voyager 1 considerably affected - and complicated - the subsequent modeling efforts of the S-I coupling. Indeed, (1) the mass and momentum loading between Io and the IPT (section 2.1) must be considered to determine the currents generated at Io, and (2) the electric field that drives the S-I-mediating currents propagates at approximately the Alfvén speed Eq.3.5, which in the IPT is much smaller than the speed of light ($v_A \lesssim 10^{-3}c$ (Kivelson et al., 2004)). Hence, any perturbation in the currents near Io takes several minutes to reach Jupiter and back; over that time window, Io moves by about ~ 5 Io radii (1 R_{Io} = 1822 km). Therefore, the currents cannot form a closed loop at Io, and the satellite and Jupiter's ionosphere are not coupled - not in the same sense as in the unipolar inductor model. Rather, Io acts as a perturbation in the plasma flow of the IPT, and the amplitude is determined by the details of the local interaction. The perturbation then propagates according to the properties of the magnetospheric plasma until it reaches Jupiter, where ionospheric currents are finally driven to counterbalance the plasma velocity perturbation (see sections 3.3 and for more details on the far-field propagation). Until the perturbation reaches Jupiter, the conductivity of the planet is not relevant, which is a major difference with the unipolar inductor model, where the Jovian conductivity is the limiting factor of the current. An exception can occur when Io is farthest from the centrifugal equator, where the plasma density is low: in this case $V_A \to c$, thus it is possible for the perturbation to propagate fast enough to form a loop closed at the moon itself, and the unipolar inductor model can be used.

The currents at Io are generated by several phenomena. There is a *pick-up current* associated with the generation of new ions, given by (Goertz, 1980)

$$\vec{J}_{pu} = \sum_i m_i \dot{n}_i c^2 \frac{\vec{E}}{B^2} \tag{3.20}$$

where $\dot{n}_i$ is the ion-electron creation rate, which is determined by the physical chemistry associated to the mass loading of the IPT (section 2.1). Additionally, there are the *Pedersen* and *Hall currents* (Eq. A.15) of Io's

ionosphere. Indeed, these are driven by the electric field seen in Io's frame $\vec{E}_{Io} = -\vec{v}_{rel} \times \vec{B}_{Io}$ (Eq. A.9), where $\vec{v}_{rel} = \vec{\Omega}_J \times \vec{r}_{Io} - \vec{v}_{Io}$, $\vec{r}_{Io}$ and $\vec{v}_{Io}$ are Io's position and velocity, respectively. This current is mostly directed away from Jupiter. Lastly, the ionospheric current leads to a charge accumulation on Io's sides: this drives a *polarization current*, which takes the form (Goertz, 1980):

$$\vec{J}_p = \frac{c^2}{4\pi V_A^2} \frac{d\vec{E}}{dt} \tag{3.21}$$

These currents are mostly perpendicular to the magnetic field, and they cannot extend indefinitely away from Io. For example, the currents associated with the Pedersen and Hall conductivities need the presence of the collisions in the Ionian ionosphere, thus far away from Io the currents can only flow along the magnetic field. The current given by the sum of Eq. 3.20, 3.21 and A.15 must satisfy the current continuity Eq. A.6, and thus FACs has to be introduced, which are given by (Goertz, 1980; Neubauer, 1980; Saur et al., 2004)

$$\vec{J}_A = \Sigma_A \nabla \cdot \vec{E} \frac{\vec{B}}{B} \tag{3.22}$$

where $\Sigma_A = (\mu_0 V_A)^{-1}$, μ_0 is the magnetic permeability.

The currents and conductivities near Io determine the electric field, which in turn affects the plasma flow in proximity of the satellite. In particular, the degree of influence of the local interaction on the plasma flow can be quantified by the factor

$$\alpha = \frac{E_1}{E_0} = \frac{2\Sigma_A}{\Sigma_P + 2\Sigma_A} \tag{3.23}$$

where Σ_P is the height-integrated Pedersen conductivity of Io's ionosphere, $\vec{E}_0 = \vec{E}_{Io} = -\vec{v}_{rel} \times \vec{B}_{Io}$ and $\vec{E}_1$ is the electric field associated with Io's currents (Saur et al., 2013). This factor represents the strength of the local satellite-magnetosphere interaction, and it determines both the amount of plasma entering Io's atmosphere and the flow perturbation (Saur et al., 2004). The case $\alpha = 1$ corresponds to an insulating moon, therefore the plasma flows unperturbed and impinges directly onto the surface/atmosphere. On the contrary, the case $\alpha = 0$ corresponds to a perfectly conducting moon,

with the plasma flow fully diverted along the sides of the satellite. According to the estimate performed by Saur et al. (2013), the interaction strength at Io is expected between 0.04 and 0.37, depending on the local plasma conditions, which are a function of the magnetic latitude of Io. Indeed, the pickup current Eq. 3.20 depends on the local production of ion-electron pairs due to the physical chemistry, while the polarization current Eq. 3.21 and the FACs Eq. 3.22 depend on the Alfvén speed, which in turn is determined by the magnetic field and plasma density. For comparison, the strength at Europa, Ganymede and Callisto is 0.15-0.94, 0.21-0.91 and 0.0-0.98, respectively. Such a large interval for α is due the three outer moons periodically crossing the plasmadisk, thus greatly increasing their interaction strength in those occasions.

As a last remark on the local interaction, it's worth noticing that the strength of the local interaction may have a qualitative effect on the propagation of the Alfvén waves far from Io. Jacobsen et al. (2007) simulated the S-I coupling in the case of weak and strong local interaction at Io, and concluded that the strong interaction leads to non-linear evolution of the Alfvén waves. This in turn affects both the morphology and intensity of the coupling currents, hence it might also determine the details of the auroral emission associated with the S-I coupling at Jupiter.

3.3 Far-Field Propagation

The perturbation generated by the local interaction generates plasma modes such as the Alfvén waves Eq. 3.7 and the magnetosonic modes Eq. 3.8 that propagates away from Io. Additionally, the ionospheric currents driven at Io by the relative motion with the plasma of the IPT (section 3.2) has to be closed, thus they feed a system of FACs. In this section the chain of physical processes that transfers the perturbation up to the Jovian ionosphere is introduced. To this end, several topic has to be covered: (1) how the plasma modes propagates in the Jovian magnetosphere and how they can carry currents; (2) which frequencies/wavelengths can propagate

and how the inhomogeneity of the magnetic field and plasma affects the reflection/transmission of waves; (3) how the S-I coupling can accelerate electrons into the planetary atmosphere with high enough energy to explain the associated auroral emission.

A powerful tool to investigate the propagation of disturbances in a fluid medium is the *method of characteristics*, which are surfaces (or lines, in 2D problems) along which a perturbation travels (Landau and Lifschitz, 1987). The characteristics are obtained by casting the MHD equations in Appendix A in a new coordinate frame given by the so-called Elsässer variables (Elsasser, 1950; Magyar et al., 2019)

$$\vec{z}^{\pm} = \vec{v}_{rel} \pm \vec{V}_A \tag{3.24}$$

where $\vec{v}_{rel}$ is the plasma velocity in Io's frame. Although the characteristics are usually employed to investigate supersonic flows and shock formation, their validity is more general (Landau and Lifschitz, 1987). Indeed, they represent the region of space that can be affected by a perturbation, thus they express a cause-effect relation that can be also applied to subsonic flows.

At Io, the satellite-plasma relative speed v_{rel} is ∼57 km/s, the Alfvén speed is ∼200 km/s and the sound speed is ∼30 km/s. Therefore, the problem in question is the one of sub-Alfvénic, supersonic plasma flow past an object, which corresponds to a plasma β parameter < 1 in Eq. 3.9. Under such conditions, the fast magnetosonic mode Eq. 3.8 propagates faster than the plasma flow speed in Io's frame, hence its amplitude is expected to decrease as r^{-2} from Io, and its contribution to the far-field propagation is negligible. The slow magnetosonic waves, which can be seen as sound waves propagating along the magnetic field, propagate slower than the Alfvén waves, and in the limit $\beta \to 0 \Rightarrow C_s \to 0$, hence they disappear. Moreover, the magnetosonic modes do not carry currents along the magnetic field, but rather perpendicular to it (Jacobsen et al., 2007; Siscoe, 1983). Therefore, only the Alfvén waves can effectively mediate the S-I coupling; indeed, assuming again that the wavevector $\vec{k}$ has components (k_x, 0, k_z) as

in section 3.1, the current can be written (Siscoe, 1983)

$$\vec{J_1} = \frac{iB_0}{4\pi\omega}[k^2(v_{1x})_{f,s}\hat{y} + k_z(v_{1y})_A(-k_z\hat{x} + k_x\hat{z})] \tag{3.25}$$

where $(v_{1x})_{f,s}$ and $(v_{1y})_A$ are the velocity perturbations associated with the magnetosonic and Alfvénic modes, respectively; the imaginary factor i implies that the current is out-of-phase by 90° with respect to the magnetic field and velocity perturbation. It is easy to see that

$$\vec{J}_{1\parallel} = \frac{iB_0}{4\pi\omega}k^2(v_{1y})_A sin\theta cos\theta = -\frac{i}{4\pi}k(B_{1y})_A sin\theta \tag{3.26}$$

where the above equation shows the parallel current in terms of the velocity or magnetic field perturbation. Hence, the propagation of FACs requires and oblique propagation, that is: $\theta \neq 0$ (recall that for $\theta = 90°$ the Alfvén waves do not propagate).

The characteristics of the Alfvén waves are given by Eq.3.24 (Magyar et al., 2019; Saur et al., 2004), hence their wavefront forms an angle with the magnetic field - which can be called *Mach-Alfvén angle*

$$\alpha_{MA} = tan^{-1}(v_{rel}/V_A) \tag{3.27}$$

The currents carried by the Alfvén waves are parallel to the characteristics: this is another major difference with the unipolar inductor model, which expects the currents to be field aligned. In Fig. 3.1, a sketch of the Alfvén and slow magnetosonic characteristics is shown. The currents are fed by FACs above Io's ionosphere, which arise to close the currents at Io, as explained in the previous section. The Alfvén characteristics in the context of the S-I coupling are usually refer to as *Alfvén wings* (Drell et al., 1965)[8], and form a tubular surface over which the currents flow.

[8]A small historical note here. The theory of the Alfvén wings, which was originally developed by Drell et al. (1965), dates back to before the discovery of the IPT in the '70s by Kupo et al. (1976). At those times, it was intended to estimate the dissipation of kinetic energy of an artificial satellite flying in the terrestrial magnetosphere due to the generation of Alfvén waves. Drell et al. (1965) also suggested that the resulting currents can be "sent back" to the satellite in order to supply the propulsion. At present, the author is not aware of any development of such technology. The idea was adapted to

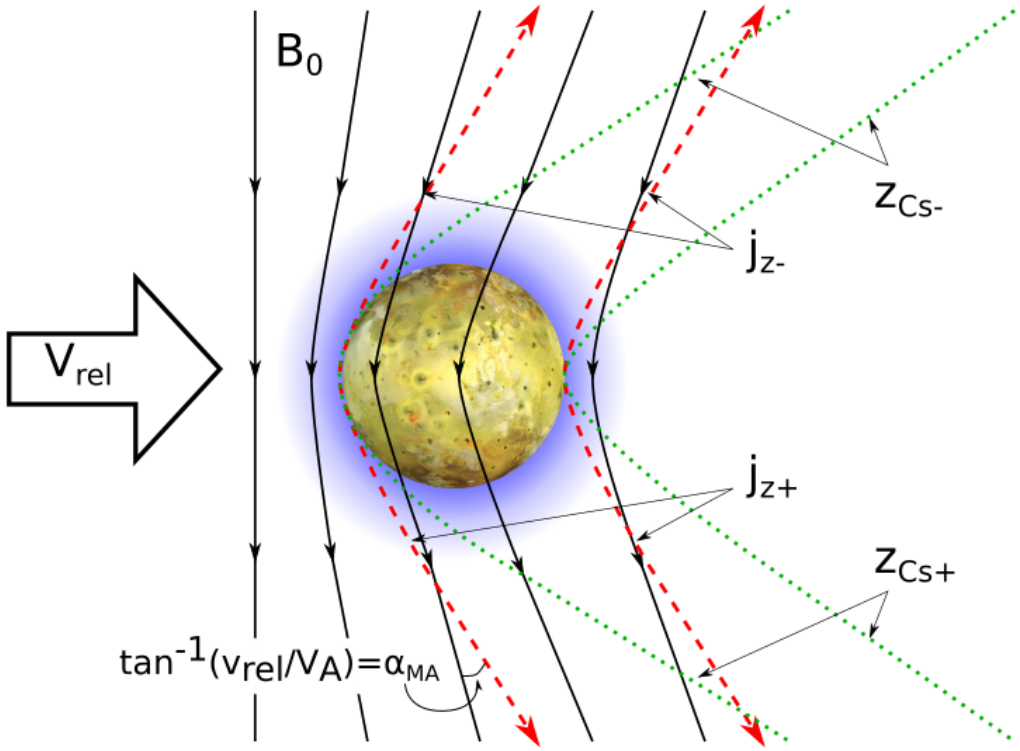

FIGURE 3.1: Sketch of the Alfvén characteristics (j_{z-} and j_{z+}, dashed red lines) and the slow magnetosonic characteristics (z_{Cs-} and z_{Cs+}, dotted green lines). The path of the currents is tilted with respect to the magnetic field by an angle $\alpha_{MA} = tan^{-1}(v_{rel}/V_A)$, where v_{rel} is the Io-plasma relative speed. The magnetosonic characteristics are more tilted than the Alfvénic ones because the speed of sound is lower than the Alfvén speed. The blue halo represents Io's ionosphere. The image of Io is retrieved from Wikimedia Commons (credits to NASA/JPL, Public domain, via Wikimedia Commons).

So far, the variation of magnetic field and density in the Jovian magnetosphere have not been taken into account. In section 2.1 it is shown that the plasma density at Io's orbit is one-two orders of magnitude higher than the density above the Jovian ionosphere, while the magnetic field magnitude is weaker by three orders of magnitude. This requires the relativistic correction Eq. 3.16 in the high-latitude magnetosphere, where the Alfvén speed is nearly the speed of light. As $V_A \approx c >> v_{rel}$ the angle α_{MA} in Eq.3.27 becomes small, and the currents are nearly field aligned. It's worth mentioning that the decrease of the Mach-Alfvén angle implies a reduction of the field-aligned component of the current Eq.3.26, which can be counterbalanced by a decrease of the wavelength (i.e: an increase of k) and/or by an increase of the wave amplitude. Another consequence of the non-uniformity of the magnetosphere is the formation of gradients in the Alfvén speed profile. A model electron density, magnetic field magnitude and Alfvén speed profile are depicted in Fig. 3.2. While the magnetic field magnitude is not expected to have sharp variations (middle panel), the plasma density exhibits strong gradients around the IPT and near the Jovian ionosphere, whose electron density is expected to peak at about 10^5 cm^{-3} and have a typical scale height of $\sim 10^3$ km (e.g: Mendillo et al. (2022)). These density variations are mirrored in the Alfvén speed profile (bottom panel). It's worth noticing that the inclusion of inertial effects Eq. 3.19, which are relevant near Jupiter, can form additional sharp gradients (for example, see Su et al. (2006)).

The transmission and reflection coefficients of waves at any Alfvén speed gradient depend on the relative size between the parallel wavelength of the wave $\lambda_{\parallel}$ and the size of the gradient L. In general, the energy of the reflected wave is given by (Hess et al., 2010a)

$$R = \Big(\frac{dln(n)}{2dx}dx\Big)^2 \tag{3.28}$$

the Io case to explain the observed radio emission (Marshall and Libby, 1967), and also mentioned as an alternative to the unipolar inductor model by Goldreich and Lynden-Bell (1969), if the diffusion of the magnetic field across Io is faster that the Alfvén waves in reaching the Jovian ionosphere and back. Only in the Eighties, after the discovery of the dense IPT, Neubauer (1980) developed a full non-linear theory of the Alfvén wings for the Io-Jupiter coupling.

where $n = c/V_A$ is the refractive index. For long wavelengths $L << \lambda_{\parallel}$, the transition between the IPT and the high-latitude magnetosphere can be considered as a discontinuity, hence the reflection coefficient is given by the Fresnel's equation for a normally-incident wave

$$R_D = \left(\frac{n_{IPT} - n_{HL}}{n_{IPT} + n_{HL}}\right)^2 \tag{3.29}$$

where $n_{IPT} >> 1$ and $n_{HL} \approx 1$ are the refractive index in the IPT and in the high-latitude magnetosphere, respectively. For long wavelengths, $R_D \approx 1$ and the waves are almost completely trapped within the torus. In the opposite case, $L >> \lambda_{\parallel}$ and the WKBJ approximation (Brillouin, 1926; Jeffreys, 1925; Kramers, 1926; Wentzel, 1926) leads to

$$R_{WKBJ} = \int_0^L \left(\frac{dln(n)}{2dx}\delta x\right)^2 \frac{dx}{\delta x} \tag{3.30}$$

which gives $R_{WKBJ} \to 0$ for $\delta x \to 0$, hence short wavelengths can escape the IPT and their reflection is negligible. From Eq. 3.29 and 3.30 it is clear that long and short wavelengths are expected to exhibit a completely opposite behavior at the density gradient of the IPT.

The precise details of the wavelengths excited by the S-I coupling along the Io flux tube are still unknown, but it can be assumed that Io injects a wave packet centered at a $\lambda_{\parallel,inj} = 2R_{Io}$. The initial wave packet spectrum then spreads into shorter wavelengths by a turbulent cascade - a process called *filamentation*. Therefore, the spectrum extends between the injection wavelength $\lambda_{\parallel,inj}$ and the dissipation wavelength, which is given by the ion skin depth $\lambda_i = c/\omega_{pi}$. Additionally, the compressional modes can also lead to filamentation, and the resulting waves corresponds to a wave packet centered at λ_i. The results by Hess et al. (2010a) show that only <20% of the energy of the injected wave packet can escape the torus, while the power transmitted outside the IPT by turbulent and compressional filamentations is 50% and 90% respectively, which matches the prediction based on Eq. 3.29 and 3.30 pretty well.

The reflection of Alfvén waves also occurs at the Jovian ionosphere,

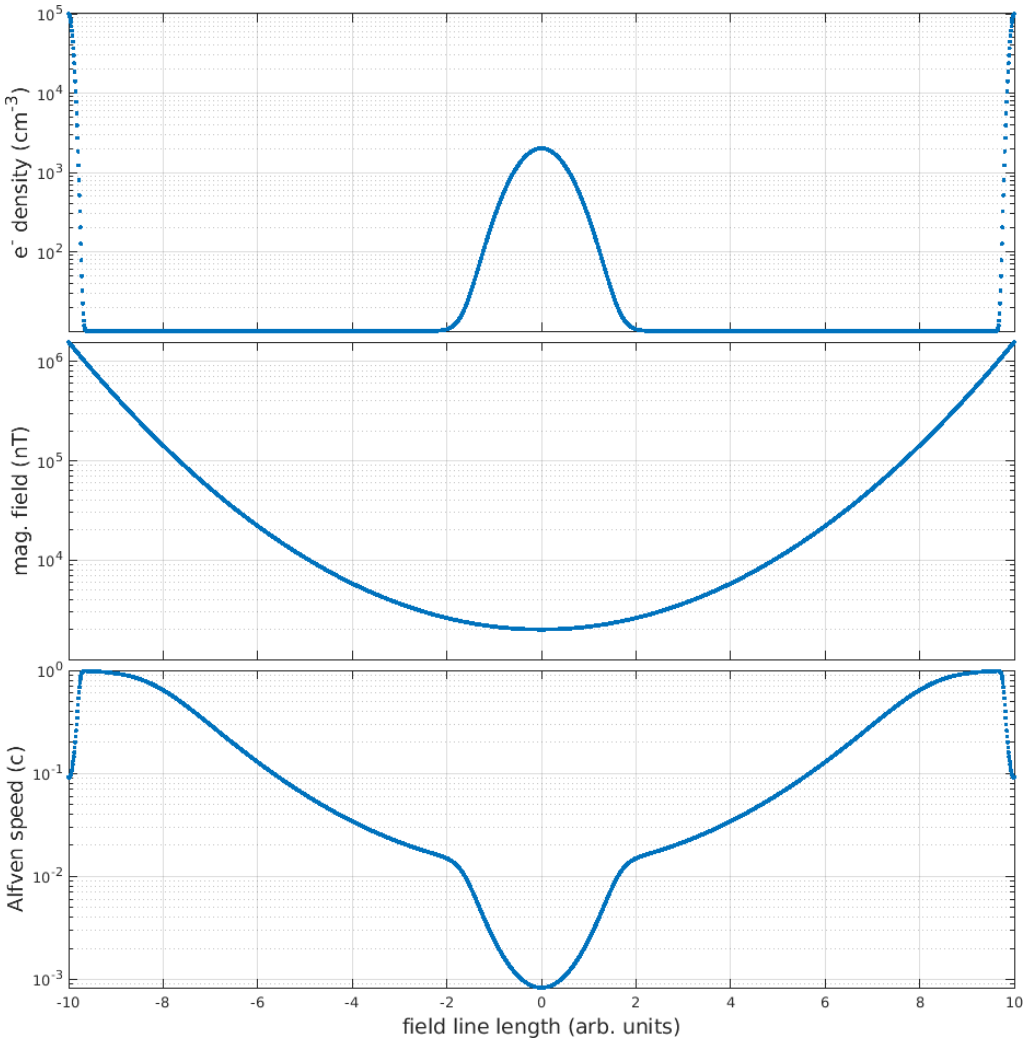

FIGURE 3.2: Electron density (top), magnetic field magnitude (middle) and relativistic Alfvén speed (bottom) along a magnetic field line. The IPT is centered at zero, while the high density at ±10 represents the northern and southern Jovian ionosphere, respectively. The sharp density gradients at $\sim \pm 1$ and above the ionosphere introduce gradients in the Alfvén speed, which can lead to partial wave reflection.

where the reflection coefficient is expected to be (Gurnett and Goertz, 1981)

$$R_{iono} = \left(\frac{\Sigma_P - \Sigma_A}{\Sigma_P + \Sigma_A}\right) \tag{3.31}$$

where Σ_A is the same as in Eq. 3.22 and Σ_P is the Pedersen conductivity σ_P (Eq. A.14) integrated over the vertical extension of the ionosphere. Assuming the Alfvén speed $V_A \approx c$, the ion density at the ionosphere $n_i \approx 10^5$ cm^{-3}, the surface magnetic field magnitude $B \approx 10^{-3}$ T and that the ionosphere is a ∼1000 km-thick uniform layer, then $\Sigma_A \approx 3 \cdot 10^{-3}$ S and $\Sigma_P \approx 16$ S (Smith, 2006). Therefore, $R_{iono} \approx 1$ and the Alfvén waves are almost completely reflected.

The presence of density gradients at the IPT and the ionosphere leads to a complex pattern of wave reflection and transmission. A sketch of the Alfvén wings that includes their reflection and transmission at each gradient is shown in Fig. 3.3. Alfvén waves are launched at Io (blue lines), whose wavefront, in Io's frame, form a Mach-Alfvén angle that is larger in the IPT than in the high-latitude magnetosphere due to the low Alfvén speed: this explains the different tilt of the blue line in the IPT region compared to the high-latitude one. The Alfvén wing between Io and the ionosphere is usually referred to as *Main Alfvén wing* (MAW). The wave is partially reflected at the density gradient: the reflected wave (green dashed line) travels within the torus up to the gradient towards the opposite hemisphere, where, again, it is partially reflected. The transmitted wave travels at nearly the speed of light towards the Jovian ionosphere, where it bounces back (continuous green line). When the reflected wave reaches the density gradient of the torus from the ionosphere, it is also partially reflected (purple line). The Alfvén wing originating from a reflection is called the *Reflected Alfvén wing* (RAW). Thus, there is an exponentially complex pattern of Alfvén waves bouncing back and forth between the gradients. As it will be illustrated in section 3.4, the auroral emission associated with the S-I coupling mirrors the pattern of the Alfvén wings.

The pattern depicted in Fig. 3.3, although useful to understand the shape of the characteristics, is only consistent with the ideal case of a weak perturbation (Saur et al., 2004). This corresponds to a weak local interaction,

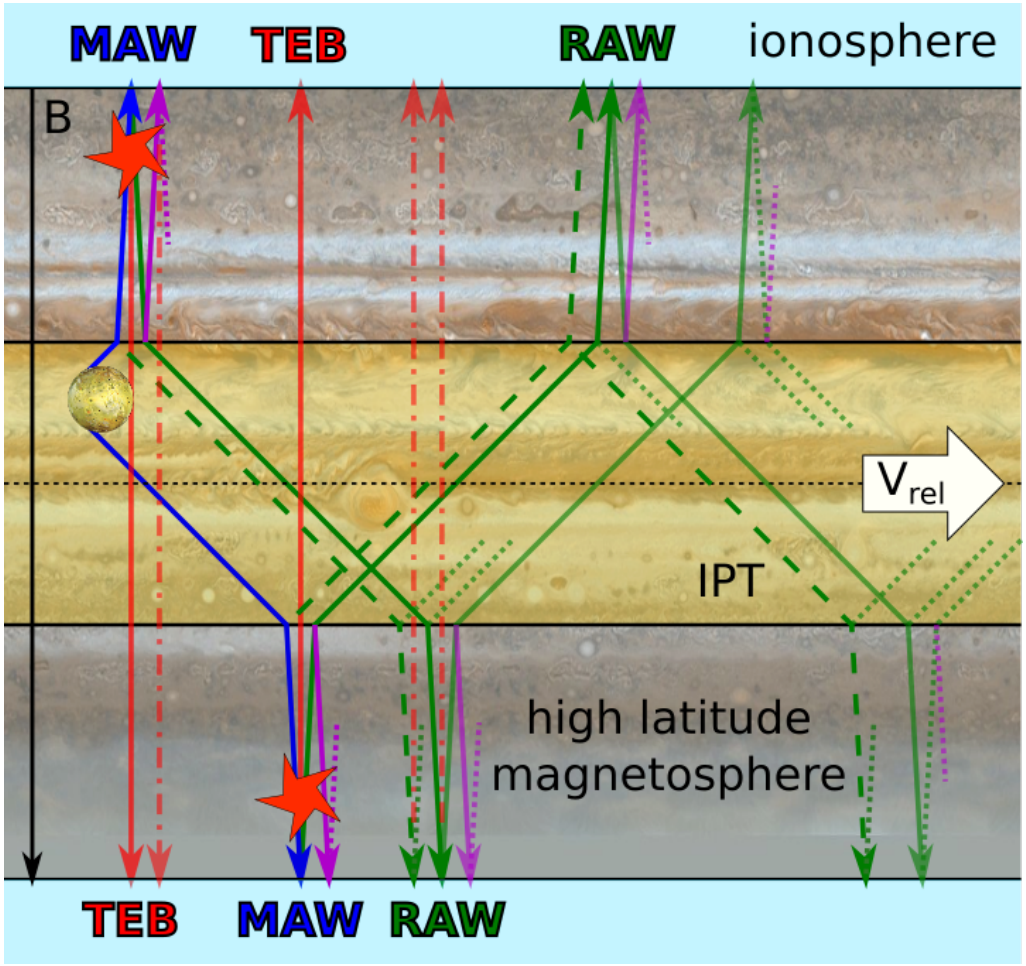

FIGURE 3.3: Diagram of the Alfvén wings in cylindrical projection. The blue lines represent the Alfvén wings coming directly from Io, called *main Alfvén wings*. The green and purple lines represent the characteristics of the *reflected Alfvén wings*. The red lines represent the trajectory of field-aligned electron beams (called *Trans-hemispheric Electron Beam*) that are excited above the ionosphere (at the red stars) by the Alfvén waves. The background projection of Jupiter and Io were retrieved from commons.wikimedia.org (credits to NASA/JPL, Public domain, via Wikimedia Commons).

that is $\alpha \approx 1$ in Eq.3.23, which in turn implies that the Alfvén conductance is much greater than the Pedersen conductance at Io. In this case, the characteristics Eq. 3.24 can be computed by the equilibrium fields of Eq. 3.2, because the perturbations are small. On the other side, the strong local interaction case $\alpha \approx 0$ (that is: $\Sigma_A << \Sigma_P$) requires the characteristics to be evaluated using the full perturbed fields. As explained in section 3.2, the interaction strength at Io is expected to range from a quite high strength, when Io is farthest from the centrifugal equator (α=0.04, $\Sigma_P >> \Sigma_A$), to an intermediate situation, when Io is at the centrifugal equator (α=0.37, $\Sigma_P \gtrsim \Sigma_A$). The strength of the local interaction also determines if the RAW returns back at Io or rather more downstream. This is crucial: in the former case, the local interaction is affected by the reflection at the torus or ionospheric density gradient, and the non-linear interaction between the MAW and the RAW must be considered, while in the latter there is no influence from the RAW and the interaction is strictly local. A sketch showing the shape of the wings in the two cases is shown in Fig. 3.4. To understand the relation between the interaction strength and the closure of the characteristics at Io, one has to compare the travel time t_A required for an Alfvén wave to travel from Io to the Jovian ionosphere and back, and the time t_c required by the magnetic field to cross the interaction region around Io. These two times are given by

$$t_A = \int_{z^\pm} \frac{dl}{V_A(l)} \tag{3.32}$$

$$t_c = \int_S \frac{ds}{v_{rel}(s)} \tag{3.33}$$

where $z^\pm$ is an Alfvén characteristic, S a streamline crossing the interaction region, l and s are the coordinates along the characteristic and the streamline, respectively. Depending on the centrifugal latitude of Io, t_A ranges between $\sim$400 s and $\sim$1000 s (Hinton et al., 2019; Moirano et al., 2023). Assuming weak interaction, Eq. 3.33 can be approximated by $t_c = L_{int}/v_{rel}$, and the flow is little affected by the local interaction, thus v_{rel}=57 km/s is given by the relative motion between the IPT and Io. L_{int} is the size of the interaction region along the streamline S, which can be approximated

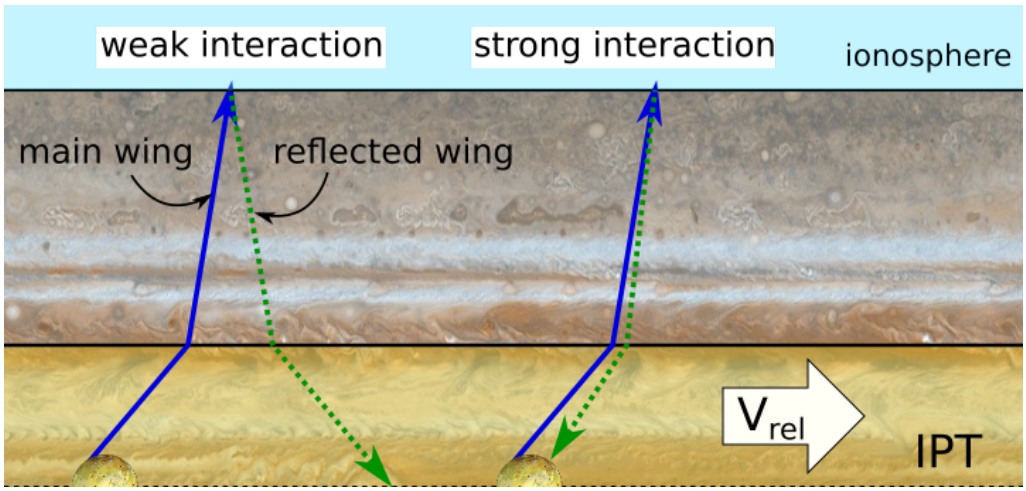

FIGURE 3.4: Diagram of the Alfvén wings in cylindrical projection, showing the qualitative comparison between the weak and strong local interaction. In the weak interaction case, the characteristics are computed with the equilibrium fields in Eq.3.2 and the two-way Alfvén travel time (Eq. 3.32) between Io and Jupiter is longer than the time required by the magnetic field to cross the local interaction region (Eq. 3.33). On the other side, in the strong interaction case, the perturbed field has to be taken into account. Furthermore, the crossing time likely increases due to the slowing down of the flow near Io, therefore the reflected characteristic close at Io. For a more detailed view, see the simulations in Fig. 2 of Jacobsen et al. (2007). The background projection of Jupiter and Io were retrieved from commons.wikimedia.org (credits to NASA/JPL, Public domain, via Wikimedia Commons).

by $L_{int} \approx 4R_{Io}$ (Saur et al., 2004). This leads to $t_c \approx$130 s $< t_A$, and the RAW cannot close at Io. Increasing the interaction strength slows the plasma flow near Io, therefore $v_{rel}(\alpha = 1) > v_{rel}(\alpha < 1)$, which implies that $t_c(\alpha = 1) < t_c(\alpha < 1)$. The slower plasma speed near Io and the inclusion of realistic model for the local interaction (Saur, 2004a; Saur et al., 2002), together with the use of the perturbed field to compute the Alfvén wings, leads to a longer crossing time, which is expected to be of the order of a few thousands seconds. Therefore, it is expected that the shape of the Alfvén wings is determined by a condition that is intermediate between the strong and weak interaction cases.

At this point, it should be further clear that, in general, the S-I coupling

cannot be simply reduced to a quasi-static electrical circuit. Although the unipolar inductor model is a good approximation when the coupling reacts quickly, the S-I interaction should be considered a quasi-steady structure made by "snapshots" of the local perturbation while it propagates in the magnetosphere. As an example of this viewpoint, Delamere et al. (2003) developed a model of the Io-Jupiter coupling based on momentum-transfer, and it separate the coupling into three phases: (1) decrease of plasma momentum due to the collisions with Io's atmosphere and to the generation of new ions, (2) momentum transfer within the torus and (3) weak coupling with Jupiter. These three phases can be considered as three temporal steps for the propagation of the initial perturbation, or as three regimes that are present at the same time at different locations. During phase 1 and 2 there is no coupling with the planet, which occurs only in phase 3, when (or where) currents and electron precipitation into the ionosphere are driven.

Delamere et al. (2003) called the above-mentioned phase 3 'weak coupling', because of the mechanism driving the electrons and currents into the Jovian ionosphere. Indeed, they assumed that the low density of the high-latitude plasma leads to the formation of quasi-static field-aligned electric potentials, but the lack of current carriers forbids an efficient coupling, thus the wording 'weak'. An alternative explanation for the coupling with the planet is mentioned at the end of section 3.1: the inclusion of kinetic-inertial effect in the propagation of the Alfvén waves generates magnetic-field-aligned electric field that can drive the electron precipitation. The "parallel potentials" model such as the one suggested by Delamere et al. (2003) and the "dispersive Alfvén" model are radically different. Indeed, the precipitating electrons are accelerated from a few eV up to several tens of keV. If this acceleration is driven by a static field-aligned potential, then the precipitating electron will all exhibit nearly the same energy. On the other side, if the acceleration is driven by wave-particle interaction, then the acceleration is determined by the time the electric field of the wave interacts with the electrons, which depends on the power spectrum of the wave. For a broadband wave spectrum, this implies that the acceleration is variable for each electron, and the resulting electron energy spectrum is broadband

as well. Regarding the Jovian aurora - not only the emission due to the S-I coupling - both models are required in different regions. Indeed, the particle measurements performed onboard Juno revealed the presence of precipitation due to both mono-energetic electrons (signature of the parallel potentials) and broadband spectra (signature of the Alfvénic activity) (Mauk et al., 2020). In the specific case of the S-I coupling, the acceleration appears to be almost always Alfvénic (Sulaiman et al., 2020). Therefore, in the last part of this section, the electron acceleration driven by Alfvén waves will be introduced in more detail, while the parallel potential model is not discussed[9].

The ongoing quest for the physical mechanism underlying the electron acceleration into the ionosphere is mainly motivated by observational constraints. Indeed, the Galileo spacecraft recorded beams of high-energy electrons near Io (Frank and Paterson, 1999); the Juno spacecraft have also been reporting electron energy distributions along the Io magnetic shell with a significant contribution up to ∼a few keV (Mauk et al., 2020; Szalay et al., 2020b). Radio emissions near the electron cyclotron frequency are detected above the Jovian ionosphere: these are most likely caused by the so-called *Cyclotron Maser Instability* (CMI)(Wu, 1985), which requires field-aligned electrons accelerated up to a few keV. Lastly, the auroral emission associated with the satellites (see section 3.4) also needs kiloelectronvolts of energy to trigger the ionospheric reactions and to explain the observed brightness. For comparison, the bulk of the electrons in the IPT have a temperature of ∼5 eV, and the hot electrons (see section 2.1) of 50-100 eV, therefore they cannot be responsible for the above-mentioned observations. Furthermore, although the temperature seems to increase at higher latitudes (Thomas and Lichtenberg, 1997), it does not reach the above-mentioned order of magnitude of a few keV. This suggests that there is an accelerating mechanism, which is expected to occur above the Jovian ionosphere between 1 and 2 R_J from the surface.

[9]The interested reader can check the following works and references therein on the parallel potential models: Delamere et al. (2003); Ergun et al. (2009); Hill and Vasyliūnas (2002).

A candidate explanation for the broadband acceleration due to the Alfvén wave-particle interaction relies on retaining the dispersive correction introduced at the end of section 3.1. Jones and Su (2008) simulated the Alfvén wave propagation generated by Io considering both the kinetic and inertial regimes Eq. 3.18 and 3.19, as both can have an associated field-aligned electric field. The two regimes each dominate in different regions: the kinetic correction is more important in the IPT, while the inertial regime dominates at high latitudes. Furthermore, it is suggested that the kinetic correction is not sufficient to sustain the electron acceleration, while the inertial correction at high latitude is compatible with the energy budget of the coupling. Therefore, in the following, only the inertial regime Eq. 3.19 will be considered. The field-aligned electric field can be deduced from the polarization of the field itself, which can be obtained by (Lysak and Song, 2003) $\boldsymbol{\varepsilon} \cdot \vec{E} = 0$, where $\boldsymbol{\varepsilon}$ is given in Eq.3.17:

$$\frac{E_\parallel}{E_\perp} = \frac{k_\parallel k_\perp \lambda_e^2}{1 + k_\perp^2 \lambda_e^2} \tag{3.34}$$

where $\parallel$ and $\perp$ are referred to the magnetic field and λ_e is the electron inertial length. Using the Faraday equation Eq.A.12, the polarization can be written in term of the magnetic field (Lysak, 1998):

$$\frac{E_\perp}{B_\perp} = V_A \sqrt{(1 + k_\perp^2 \rho_i^2)(1 + k_\perp^2 \lambda_e^2)} \tag{3.35}$$

where ρ_i is the ion gyroradius. Notice that $k_\perp \| E_\perp \perp B_\perp$. These two equations can be combined into an equation for the field-aligned electric field:

$$E_\parallel = k_\perp k_\parallel V_A \lambda_e^2 \sqrt{\frac{(1 + k_\perp^2 \rho_i^2)}{(1 + k_\perp^2 \lambda_e^2)}} B_\perp \tag{3.36}$$

In Eq.3.36, it can be noticed that a parallel electric field can arise from perpendicular fluctuations of the magnetic field, which are a feature of the Alfvén waves. Furthermore, the wave vector requires an oblique propagation, that is $k_\parallel \neq 0$ and $k_\perp \neq 0$. This is conceptually similar to Eq. 3.26, although that equation is not derived with the dispersive corrections.

According to models (Hess et al., 2010a; Jones and Su, 2008), the electric field Eq. 3.36 between 0.5 and 1.5 R_J from the Jovian surface is expected to be two order of magnitude higher than in the IPT. The efficiency of the energy transfer to the particles depends on the wavelength. Hess et al. (2010a) suggests that long wavelengths ($\lambda_\parallel \approx 2\ R_{Io}$) have very low efficiency (0.05%). A wave packet described by a broadband spectrum of wavelengths between the $\lambda_\parallel \approx 2\ R_{Io}$ and λ_i - the inertial length of the ions - have instead an efficiency up to 10%, and the short wavelength ($\lambda_\parallel \approx \lambda_i$) reach up to 100%. This estimate agrees with the energy deposition derived from the auroral emission (Gérard et al., 2006) and with *in-situ* measures of the Poynting flux (Sulaiman et al., 2023). The oscillating nature of Eq.3.36 implies that there must be an interaction that transfers energy from the wave to the particles. Such interaction cannot be resonant (e.g: Landau damping), as the phase speed of the waves is nearly the speed of light, while the speed of the particles is lower. Hess et al. (2007) suggests that long wavelengths act as large potential wells that accelerate the electrons, which acquire enough field-aligned speed - thanks to the width of the potential - to escape the acceleration region before the wave changes phase. An interesting consequence of this interpretation is that, with respect to the ionosphere, the electrons can be accelerated by both the outward- and inward-propagating waves, and that the acceleration can occur in both directions, depending on the wave phase seen by the electrons (Hess et al., 2010a). The presence of high-energy field-aligned electron beams traveling from above the ionosphere at one hemisphere towards the opposite have already been observed (Frank and Paterson, 1999) and invoked to explain structures in the auroral emission of the satellite (Bonfond et al., 2008). In Fig. 3.3, the acceleration region - which is expected to be formed wherever the Alfvén waves propagate at high-latitudes - is marked with red stars, and the path of the field-aligned *Trans-hemispheric Electron Beams* (TEBs) is represented by red arrows. As it will be further illustrated in section 3.4 and chapter 6, the auroral emission associated with the TEB, alongside with the MAW and RAW emissions, is fundamental to interpret and derive information on the S-I coupling.

3.4 Auroral Emission: the Footprints

The precipitation of high energy electrons into the upper layers of the Jovian atmosphere generates a variety of phenomena that represent the last step of the S-I coupling. These can be observed over a large interval of wavelengths, from radio to X-ray, each of which involves different physical processes[10].

Radio emissions from Jupiter were discovered in 1955 (Burke and Franklin, 1955), and Bigg (1964) discovered the correlation between the modulation of these radio emissions and Io's orbital phase, well before the Voyager 1 era[11]. Radio waves are emitted by the gyrating high-energy electrons precipitating into the planet, thus they can be considered cyclotron radiation. The mechanism responsible for this emission is called *Cyclotron Maser Instability* (CMI) (Louis et al., 2019; Wu, 1985), which requires (a) electrons with ∼keV of energy, (b) that the electron population increases as a function of the perpendicular speed, and (c) that the electron plasma frequency Eq.3.15 is lower than their cyclotron frequency Eq. 3.14 (Louis et al., 2019). This last condition can be approximately expressed as $\sqrt{m_e c^2/m_i V_A^2} \approx \sqrt{m_e/m_i} << 1$ at high latitudes. This process can be view as a wave-particle interaction that is able to amplify the radio waves near the cyclotron frequency (Sprangle et al., 1977): the radio waves are seen by the electrons as an oscillating electric field, which groups the electrons together in a portion of their gyro-orbit. If the frequency of the waves is slightly higher than the electron gyrofrequency, then the phase slippage between the electrons and the radio waves requires the electron energy to decrease, and thus, for energy conservation, the wave energy to increase. Radio emission are beamed, that is: they are emitted in a cone centered along the magnetic field. This is a strong observational constraint, as these waves can be detected only when the source is pointing towards the receiver. Furthermore, because the source location is not easily determined by radio observations, there is a degeneracy

[10]For a detailed review of the Jovian aurorae at various wavelengths, see Badman et al. (2015) and Bhardwaj and Gladstone (2000).

[11]Interestingly, the decametric radio emission from Jupiter is the only one in the Solar System with a frequency that exceeds the terrestrial ionospheric cutoff, so that it can be observed from ground (Badman et al., 2015).

with the opening of the beaming cone (Hue et al., 2023).

The precipitation of electrons into the ionosphere has a remarkable effect on the atmospheric chemistry, as it is able to produce ionization and excitation of the atmospheric H and H_2. When an electron with a few keV of energy enter the atmosphere, the ionization cross section of the hydrogen is larger than the excitation cross section (Grodent, 2015): this produces a large amount of secondary electrons that are responsible for further ionization and, when their energy decreases to a couple hundreds of eV thanks to the inelastic collisions, to excitation. The effect of the electron precipitation can be observed from the IR to the UV wavelengths. Molecular hydrogen ions can be produced by four reactions (Tao et al., 2011):

$$H_2 + e^{-*} \rightarrow H_2^+ + 2e^- \tag{3.37}$$

$$H_2 + h\nu \rightarrow H_2^+ + e^- \tag{3.38}$$

$$CH_4 + h\nu \rightarrow H_2^+ + e^- + products \tag{3.39}$$

$$H_2 + H^+ \rightarrow H_2^+ + H \tag{3.40}$$

Among these reactions, only Eq. 3.37 and 3.40 are significant for the auroral emission, as the energy input of the precipitating electron greatly exceeds the solar photoionization, at least locally. The H_2^+ molecule reacts very efficiently with the H_2, almost at every collision (Miller et al., 2020); the reaction produces 1.74 eV of extra energy, which is largely retained by the resulting H_3^+ as internal energy:

$$H_2^+ + H_2 \rightarrow H_3^{+*} + H \tag{3.41}$$

The internal energy of the H_3^{+*} is radiated in the infrared. The first evidence of IR auroral emission associated with the orbital motion of Io was recorded by the ProtoCAM of NASA's Infrared Telescope Facility (Connerney et al., 1993), and it was ascribed to the formation of H_3^{+*} after the electron precipitation due to the S-I coupling of Jupiter with Io. A few years later, Clarke et al. (1996) and Prangé et al. (1996) reported the first observations by HST of the Io-related emission in the UV, while the detection of the emission

associated with Europa and Ganymede had been discovered later (Clarke et al., 2002). The emission spectrum of the H_3^{+*} does not show electronic line transitions; the pure rotational spectrum is also not observed, nor in space, nor in laboratory. This leaves the changes in the vibrational and roto-vibrational states of the molecule as the only possible path to radiate the internal energy [12], which occurs in the IR wavelengths. The H_3^+ is lost by two main types of reaction (Badman et al., 2015; Tao et al., 2011):

$$\begin{aligned} H_3^+ + e^- &\rightarrow H_2 + H \qquad (3.42)\\ &\rightarrow H + H + H \\ H_3^+ + C_X H_Y &\rightarrow C_X H_{Y+1}^+ + H_2 \qquad (3.43)\\ &\rightarrow C_X H_{Y-1}^+ + 2H_2 \end{aligned}$$

$$(3.44)$$

where $C_X H_Y$ can be any hydrocarbon, such as methane (CH_4), acetylene (C_2H_2) and ethylene (C_2H_4). At Jupiter, the hydrocarbons dominate below the homopause, which is located at an altitude of about 500 km in the auroral regions (Sinclair et al., 2020), therefore no emission is expected to be observed below that. Above 500 km, the main loss of H_3^+ is due to dissociative recombination with electrons. The rate of destruction of the H_3^+ is crucial to properly interpret the auroral observations. Indeed, the roto-vibrational states are continuously excited by collisions with the ionospheric hydrogen (Tao et al., 2011), thus the H_3^+ keeps emitting until it is destroyed. As a rough estimate, the H_3^+ concentration can be computed by

$$\frac{d[H_3^+]}{dt} = -r[H_3^+][e^-] \qquad (3.45)$$

[12]The H_3^+ ion is quite peculiar and determining its characteristics has been proving challenging. For example, the triangular symmetry of the molecule forbids a permanent molecular dipole, hence there should be no IR transition. Nevertheless, vibrations can introduce a transient vibrationally-induced dipole, which leads to rotationally-driven emission and can explain the detection of forbidden IR lines. Furthermore, the lifetime of the H_3^+ can vary by orders of magnitude depending on the plasma conditions, from minutes or hours for planetary atmospheres, to years for the interstellar medium. For a thorough review on the H_3^+ in astronomy, see Miller et al. (2020).

where r is the recombination rate (e.g: Sundström et al. (1994)). According to Eq. 3.37 and 3.41, each H_3^+ ion produce one electron, thus $[e^-] = [H_3^+] = X$ and the equation can be solved to obtain

$$X(t) = \frac{X_0}{\frac{t}{\tau} + 1} \tag{3.46}$$

where X_0 is the initial concentration of H_3^+ and $\tau = (X_0 r)^{-1}$ can be considered as a characteristic time. Eq.3.46 has two important consequences. First, assuming that the intensity of the auroral emission is proportional to the concentration, it is possible to estimate τ, which is a degenerate measure of the recombination rate and the concentration, from auroral observations. Secondly, a high H_3^+ density decreases faster than a low one, as the characteristic time τ depends on the initial concentration. At the feet of the Alfvén wings generated by the S-I coupling, the electron precipitation is intense, hence the characteristic time is short and the emission is strong where - and only where - the electron precipitation is significant. Therefore, from the observational point of view, the morphology of the auroral emission is not smeared as the footprint moves relative to Jupiter, and it can be used to track the energy and particle deposition into the ionosphere (Tao et al., 2011).

The visible and UV auroral emission are expected to come from similar phenomena, that is: the photon emission from hydrogen excited by the collisions with the precipitating electrons. While the Jovian aurora is probably mostly observed in the UV than in any other wavelength, there are only a handful of observations in the visible range. The reason for this discrepancy might be two-fold. Indeed, due to observational constraints, the planetary albedo makes the day-side observations challenging, while the night-side can be investigated only by deep space missions. On the other side, the solar UV radiation is absorbed by the hydrocarbons, thus the day-side contrast is better in this latter range. Moreover, the physical process behind the visible aurora is the same as in the UV, therefore the same (or very similar) physical understanding is expected. The precipitating electrons excite both H_2 and H, which emit mainly in the Lyman and Werner bands,

and in the Lyman α bands, respectively (Badman et al., 2015). Continuum emission is also expected to contribute to the total emission (Grodent, 2015). The observations in the visible wavelengths are suggested to originate from the Balmer lines of the hydrogen (Bhardwaj and Gladstone, 2000; Gladstone et al., 2007).

The atmospheric composition and the mechanism that accelerates the electrons into the ionosphere determine the vertical extension of the auroral emission - sometimes called *auroral curtain*. Qualitatively speaking for both the IR and UV bands, the higher the precipitating electron energy, the more it penetrates into the atmosphere and the more secondaries it produces, which leads to a deeper and brighter emission[13] (Tao et al., 2011). Therefore, it is possible to infer the energy spectrum of the precipitating electrons from the shape and size of the auroral curtain by comparing the observations with the curtain predicted by an atmospheric model and different energy spectra (Bonfond et al., 2009). The X-ray emission from Jupiter is known since the early '80s, but the physical investigation of its origin and its association with the aurora started only in the mid '90s (Badman et al., 2015), and involved the presence of highly ionized oxygen ions precipitating into the atmosphere, potentially of Iogenic origin. Moreover, electron bremsstrahlung spectra are observed at Jupiter, which can be an additional source of X-rays.

The last part of this section introduces the morphology of the auroral footprint of the satellites as seen in the IR, but the same features are also observed in the UV[14]. In section 3.3 it is explained that the currents of the S-I coupling flows along the Alfvén wings - whose shape is determined by the plasma and magnetic field properties - that the Alfvén wings are reflected

[13]For the IR emission, there is actually a balance between the increasing electron energy and the increasing depth of penetration (Watanabe et al., 2018). Indeed, if the electron is too fast, it gets lost below the methane homopause, where the H_3^+ is immediately destroyed, with little time to produce ionization and dissociation - and thus there is no IR emission.

[14]As mentioned earlier, the observations in the visible are quite few, especially compared with the IR and UV. Nevertheless, as the origin of the UV and visible emission is similar - hydrogen de-excitation after electron precipitation - their morphology is also expected to be similar.

at density gradients, and that auroral electrons are accelerated above the ionosphere. As the electrons are accelerated along the magnetic field and the travel time between the acceleration region and the ionosphere is negligible with respect to the propagation time from the satellites, the position of the auroral footprints depends essentially on the shape of the Alfvén wings and its reflections. At Jupiter, the $\sim 10^\circ$ tilt between the rotational axis and magnetic dipole defines a centrifugal equator tilted by about $\sim 7^\circ$ around which the plasma is confined, hence the satellites wiggle up and down in the high density plasma around the centrifugal equator[15]. The result is the longitudinal variation of the Alfvén wings as the satellites orbit the planet. Examples of the Io footprint at various longitudes are reported in Fig. 3.5. The main feature is the emission associated with the foot of the MAW, which is usually called the *Main Alfvén wing* (MAW) *spot*. Similarly, the emission coming from the reflections is called the *Reflected Alfvén wing* (RAW) *spot*. It is worth noticing that the brightness of the RAW appears quite faint, thus even the detection of one reflection can be challenging. A leading feature can be observed upstream of the MAW spot, which is suggested to be caused by field-aligned electrons accelerated from the opposite hemisphere, thus it is called the *Trans-hemispheric Electron Beam* (TEB) *spot*. This last spot can be observed upstream or downstream of the MAW spot, depending on the longitude of the satellite. Indeed, consider the situation in Fig. 3.5, panel (a) - Io is north of the centrifugal equator. In this configuration, the northern Alfvén wing is shorter than the southern one, thus the local perturbation reaches Jupiter first in the North than in the South. As the electrons of the TEB take only a few seconds from North to South (Hess et al., 2010b), the associated emission occurs upstream of the MAW spot. The spatial separation between these three spots can be estimated from the simple geometry of Fig. 3.5, assuming a uniform magnetic field and plasma velocity v_{rel}. If t_N and t_S are the northward and southward Alfvén travel

[15]See section 2.1 and Fig. 2.2 for the definition of centrifugal equator. A brief explanation is also reported in the Glossary section B.

time respectively, then:

$$D_{MT}^{N,S} = (t_{N,S} - t_{S,N})v_{rel} \tag{3.47}$$

$$D_{TR}^{N,S} = (t_{N,S} + t_{S,N})v_{rel} \tag{3.48}$$

$$D_{MR}^{N,S} = 2t_{S,N}v_{rel} \tag{3.49}$$

The above equations imply that (1) the MAW and TEB spots overlap when $t_N = t_S$, that is: when Io is at the centrifugal equator; (2) the MAW-RAW distance is at a minimum when the Alfvén travel time towards the opposite hemisphere is at a minimum as well; (3) the TEB-RAW distance is quite stable, as t_N and t_S are nearly out of phase as function of the satellite's longitude, and it exhibits one minimum and one maximum (Hinton et al., 2019). Despite the similar morphology between the case on top of panel (a) of Fig. 3.5 and the one in panel (b), it is possible to use Io's longitude to determine the correspondence with the configuration of the Alfvén wings: in the case of Io, the moon is expected to be near the center of the centrifugal equator at $\sim$20° and $\sim$200° System III longitude, while it is farthest from it at $\sim$110° and $\sim$290°.

Two other features have to be introduced: the *Footprint Tail* (FPT) and the *sub-dots*. The FPT is referred to the fading emission that is observed trailing from the MAW spot, and thus it is magnetically mapped downstream of Io. By looking at panel (b) of Fig. 1.2, the reader can see a long arc of emission trailing from the Io footprint and extending for nearly 360° in longitude. The physical processes that can explain this morphology are still debated. One explanation (e.g: Hill and Vasyliūnas (2002)) suggests that the sub-corotating plasma in Io's wake drives a current system in order to return to corotation, much like the classical M-I coupling introduced in section 2.3. Alternatively, it is suggested (e.g: Hess et al. (2010b); Jacobsen et al. (2007)) that the complex pattern of reflection of Alfvén waves in the magnetospheric cavity and in the IPT can explain the *Io Footprint Tail* (IFPT) length. Bonfond et al. (2017b) showed that, under rather crude approximations, the two models similarly depend on the same set of parameters, thus a comparison with the observations cannot settle the investigation. Furthermore, both models predicts an e-fold decay of the tail

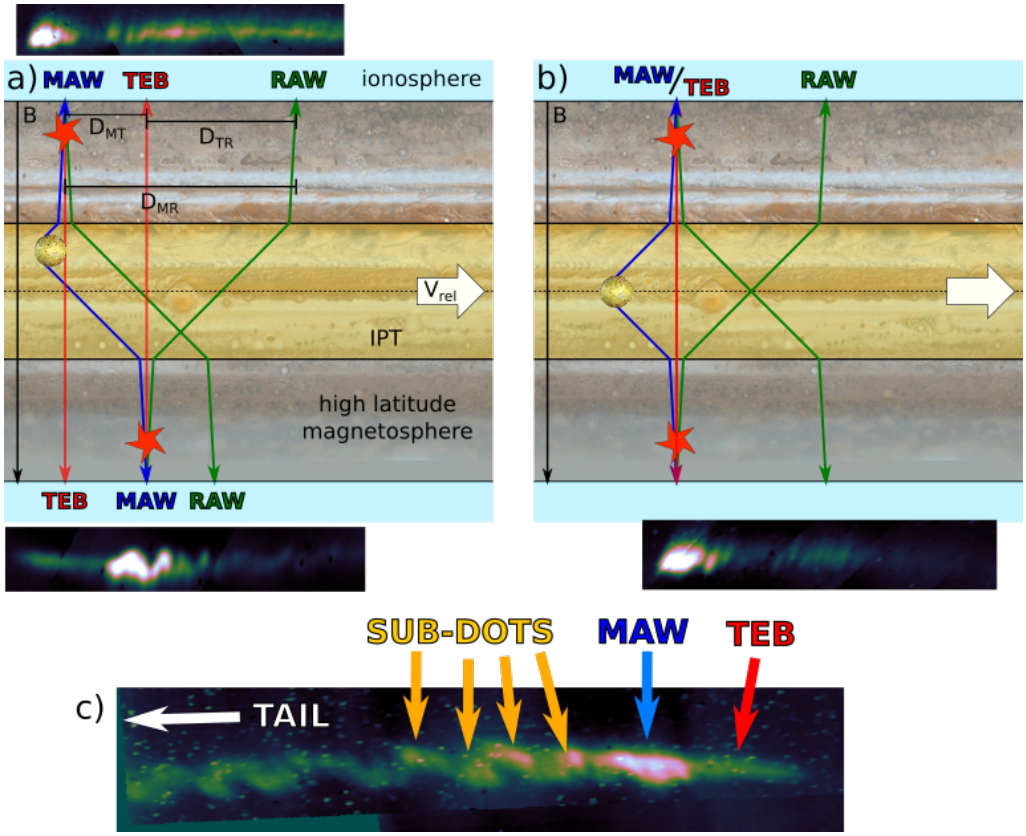

FIGURE 3.5: Scheme of the Alfvén wings, simplified with respect to Fig. 3.3. The blue, green and red arrows are the *Main Alfvén wing* (MAW), *Reflected Alfvén wing* (RAW) and *Trans-hemispheric Electron Beam* (TEB), respectively. At the foot of each reflection, a *spot* is usually observed. The red stars represent the acceleration regions. The images of the Io footprint are acquired by Juno-JIRAM in the IR band. D_{MT}, D_{TR} and D_{MR} are the spatial separation between the three features (see text for details). Panel (c) shows the details of the small-scale sub-dots observed by JIRAM. The background projection of Jupiter and Io were retrieved from commons.wikimedia.org (credits to NASA/JPL, Public domain, via Wikimedia Commons).

of about 20-40°, while both IR and UV observations reported much longer extensions (Bonfond et al., 2017b; Mura et al., 2018). In contrast, both Europa and Ganymede exhibit a much shorter tail, which appears in good agreement with the above-mentioned models. It is possible that the presence of the IPT, with its dynamics and chemistry, creates a specific environment to support the tail emission, although the details are still being investigated.

The sub-dots, which are shown in panel (c) of Fig. 3.5, are the only satellite-related auroral feature that has been observed only in the IR so far (Mura et al., 2018), due to the small scale of this feature. Indeed, they extends for ∼200-300 km and they are spaced by ∼300 km, and, at present, only the Juno-JIRAM infrared imager has been able to capture this level of spatial detail. It is reasonable to believe that a similar morphology could be observed in UV, as the electron precipitation triggers both the UV and IR emissions, but this has not been observed yet. The sub-dots represent the latest observational discovery on the satellite-induced auroral emission at Jupiter, hence their origin can be currently considered under investigation. As part of the author's PhD work has been performed on this topic, the full details of the analysis and the candidate physical explanations are given in section 5.

CHAPTER 4

The Juno Era

This chapter is dedicated to the general introduction of the Juno mission, with particular focus on the IR instrument JIRAM and its observations, which are the backbone of the work presented in this thesis. Additionally, the specifications of the radio instruments used by the gravity experiment will be briefly described as well, the latter being used for the radio occultations of the Io Plasma Torus (IPT)*: these represent an additional source of data used in the last part of this thesis (chapter 6).*

The Juno spacecraft (Bolton et al., 2017) has been launched in 2011 and it reached Jupiter in August 2016. The mission carries 8 science instruments, plus the radio antenna that is used for both navigation and science: this payload is designed to investigate the interior, the atmosphere and the magnetospheric environment of Jupiter (see panel *a* of Fig. 4.1). The polar orbit of the spacecraft is highly eccentric, with a perijove every ∼53 days. This geometry has several advantages. Firstly, and perhaps most importantly, the orbital geometry allows the spacecraft to largely avoid the radiation belts, whose intensity peaks at ∼1-2 R_J from the surface (see panel (*c*) of Fig. 4.1). Therefore, Juno is able to approach Jupiter up to a few thousands km from the cloud top by squeezing between the planet and the radiation belts near the perijoves, without its instrumentation

being damaged. The high eccentricity of the orbit allows to observe the magnetosphere from the Jovian surface up to - or close to - the magnetopause. The polar geometry represents a unique vantage point to observe the poles, which are a challenging target from Earth. The polar regions are extremely fascinating from the atmospheric and magnetospheric point of views. Indeed, as the Jupiter is a gaseous, fast-spinning planet, swirling phenomena and vortices are expected to determine the atmospheric structure around the poles (e.g: the polar hexagon observed at Saturn (Godfrey, 1988)). Juno discovered the presence of the so-called *polar cyclones* (Adriani et al., 2018), which form a stable structure made by a central cyclone surrounded by several equally-sized vortices[1]. Moreover, the magnetic field lines of the magnetosphere are closed near the magnetic poles, which are displaced from the rotational poles by about 10°: here intense auroral emission can be detected (even from Earth), and its location is determined by the region of the magnetosphere where the M-I-coupling - or S-I-coupling, for the satellite footprints - currents originate. As the spin axis of Jupiter form an angle of nearly 90° with its orbital plane, the Jovian aurorae can be only observed at a slanted angle; furthermore, as the magnetic dipole is tilted with respect to the spin axis, the aurorae cannot be observed when they are on the night side of Jupiter. The southward apsidal precession of Juno's trajectory in Fig. 4.1 is designed to make the spacecraft crossing the plasmadisk at a gradually closer distance from Jupiter. The precession has been continuing during the extended mission of Juno, which has allowed the flybyes of Ganymede and Europa so far, as well as the probing of the plasmadisk up to the outermost part of the IPT. Lastly, Juno's orbit also precedes from dusk to dawn (see panel *b* of Fig. 4.1): this allows to observe the Jupiter system at different local times; moreover, the syncronism between the dusk-dawn precession and the 53-day period of the orbit makes the spacecraft to perform observations at equally-spaced longitudes.

At the time of writing, six instruments onboard Juno out of eight have recorded measurements associated to the S-I coupling. Indeed, Juno crosses

[1]The number of cyclones is usually 6 in the South pole and 9 in the North pole, although an additional circumpolar vortex is sometimes observed.

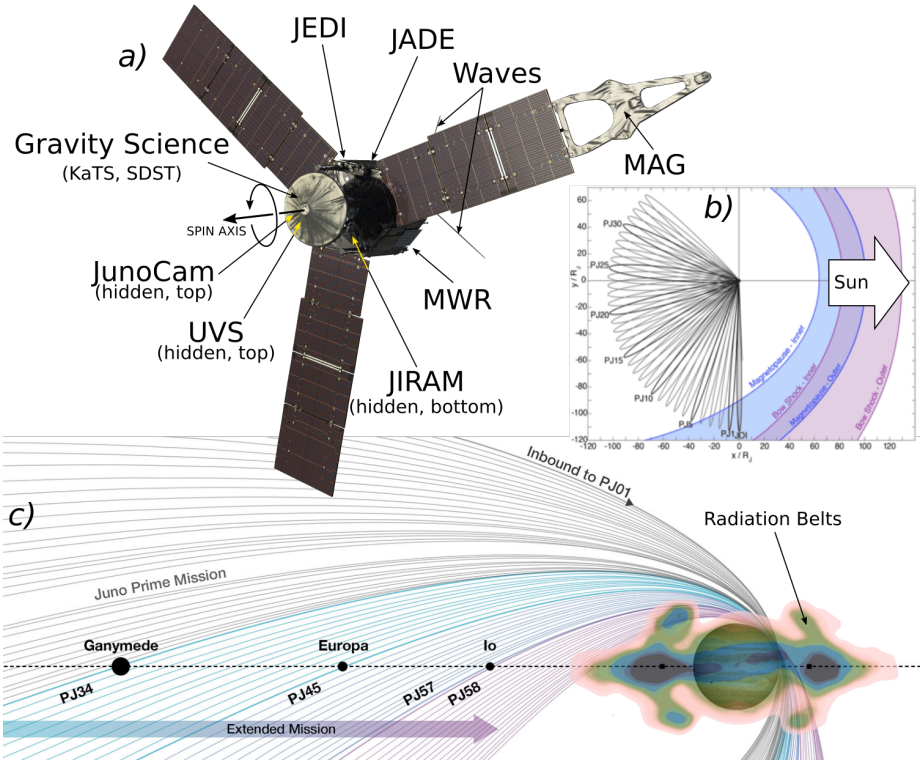

FIGURE 4.1: *(a)* Juno's scientific payload, made by 8 instruments and the radio antenna, used for both navigation and the measurements of the gravity field. JunoCam and UVS are hidden by the antenna, while JIRAM is not visible, as it is on the other side of the spacecraft. See the list of acronyms for the full name of each instrument. *(b)* Polar projection of Juno's trajectory showing the dusk-dawn precession of the orbit. Retrieved from Bolton et al. (2017). *(c)* Meridional projection of Juno's trajectory, showing the apsidal precession that moves the apojove more and more southwards as the mission goes on. The grey lines between the inbound/PJ 1 orbit and PJ 34 correspond to the the Prime Mission, the coloured orbits to the Extended Mission, during which Juno has been performing close flybyes of Ganymede, Europa and Io. Notice that Juno's orbit is designed to avoid the radiation belts as much as possible, while passing very close to the planet during the perijoves. The images were retrieved and adapted from commons.wikimedia.org (credits to NASA/JPL, Public domain, via Wikimedia Commons).

the magnetic shell of each of the Galilean moons at least twice per orbit[2], therefore the particle detectors (JADE and JEDI) and the field instruments (MAG and Waves) can measure currents and plasma waves caused by the S-I coupling. Due to the local nature of those measurements (i.e: particles and fields can be detected only at the location of the spacecraft), acquiring data directly from the MAW is quite challenging. Indeed, Juno must intercept the Alfvén wings, which has a cross section of a few R_{Io} at Io's orbit - corresponding to a few thousands km - and of only a couple hundreds of km near the Jovian ionosphere. Moreover, the shape of the Alfvén wings depends on the plasma distribution along the magnetic shell connected to the orbit of each moon, the magnetic field geometry and magnitude, and the local interaction strength. The uncertainty in these quantities makes the MAW crossing challenging to plan in advance, and only a small handful of such crossings has been observed so far (Sulaiman et al., 2020; Szalay et al., 2020b).

The other two instrument that have detected evidence of the S-I coupling so far are JIRAM and UVS, which are able to observe the IR and UV auroral emission - including the footprints - when the spacecraft passes over the poles. JIRAM is an imager and a spectrometer, and UVS is an imaging spectrograph[3], therefore the two instruments are not limited by the position of the spacecraft like JEDI, JADE, MAG and Waves, but rather by its pointing. Indeed, Juno is a spin-stabilized spacecraft that rotates at 2 rpm, with JIRAM and UVS pointing radially. Therefore, the spacecraft aims these two instruments approximately at the same location every 30 s. UVS is equipped with a flat scan mirror that allows for the pointing to move up and down from the spin plane by up to 30°, therefore the instrument

[2]"At least" because the wiggling of the magnetic field caused by the tilt of the dipole with respect to the spin axis can lead to multiple shell crossings during either the inbound or outbound leg of each orbit.

[3]Notice that there is a substantial difference between the two types of instruments. JIRAM is an imager *and* a spectrometer: the imager uses a band-pass filter, thus the images display the brightness integrated over the wavelengths of the filter. UVS, instead, is an imaging spectrograph that record the wavelength of each measured photon, therefore it is possible to obtain a spatial image of the aurora at a given UV wavelength, or integrated over a selected range of wavelengths.

does not have to always aim directly at the source. On the contrary, JIRAM is not equipped with such device. Both instrument are equipped with a de-spinning mirror, which allow to target-lock the instrument and increase the exposure time without smearing the image. JIRAM and UVS can thus acquire multiple images of the footprints over an extended time during each PJ. Moreover, as the footprints are quite bright even when compared with the main emission, their detection is quite straightforward. The *Io Footprint* (IFP) has been observed at nearly each orbit, thanks to the absence of other emission near the foot of Io's magnetic shell. The *Europa Footprint* (EFP) and *Ganymede Footprint* (GFP), although they are consistently observed, sometimes they can be outshined by the main emission and the diffuse emission, thus making their detection impossible. The two instrument have complementary capabilities, besides the different wavelengths. Indeed, JIRAM lacks the flat scan mirror and thus has tight observational constrains, but it has a high angular resolution of $\sim 0.01°$, which corresponds up to a few kilometers at the Jovian surface. On the other hand, the higher pointing freedom of UVS compared to JIRAM allows a more spatially and temporally extended monitoring of the footprint and the aurora.

The backbone of the present work is the dataset of the JIRAM observations of the Io, Europa and Ganymede footprints. The unprecedentedly high spatial resolution of the instrument has revealed new details of the morphology of the footprint which needs to be explained. Moreover, in order to support data analysis in the Extended Mission phase of Juno - especially the crossing of the IPT and the Io flyby - the position of the IFP is used to constrain the plasma properties at the orbit of the moon. This represents a new technique that allows to quantitatively infer the state of the Io torus[4]. The UVS data are used as a comparison to the results obtained from JIRAM, when possible, or to broaden the IR dataset, when needed. In this thesis,

[4]Other methods to investigate the IPT use spectroscopic observations - especially in the UV and visible wavelengths - radio occultations and particle detectors. The former is usually the most employed, as long observational campaigns can be performed from Earth, while the latter two require an *in-situ* probe.

UVS data are not personally processed by the author, but they are either retrieved from the literature or processed by the UVS team. Additionally, the radio occultations of the IPT are used as an independent source of data to constrain the state of the torus. Therefore, the specifications of JIRAM and the gravity instruments are described in section 4.1 and 4.2, respectively. The two following sections are intended as an overview of the instruments and to report the most important specifications of these tools for the type of analysis presented in this thesis, while the new results obtained in the past three years on the S-I coupling at Jupiter are reported in chapter 5 and 6.

4.1 The Jovian Infrared Auroral Mapper

JIRAM (Adriani et al., 2017) is a modified Schmidt telescope, which allows for a compact solution to be mounted on Juno. The instrument was built by Selex ES (now Leonardo) under an *Italian Space Agency* (ASI) contract and the scientific responsibility of INAF-IAPS, and it is composed by an imager and a spectrometer (see panel (c) in Fig. 4.2). The imager detector is made by 270×438 pixels, and it is covered by two band-pass filters: the M filter, which operates between 4.300 and 5260 μm, and can be used to observe the thermal emission from the deep atmosphere, and the L filter, which operates in the range 3.165-3.745 μm, where the auroral H_3^+ emission lines have an optimal contrast against the sunlit atmosphere of Jupiter. The images obtained in each band have 128×438 pixels, which leaves 14 opaque pixels between the two filter. Although in principle JIRAM can acquire data with both filters simultaneously, the exposure time required for an optimal *Signal-to-Noise Ratio* (SNR) by the M filter for the atmosphere is much shorter than the exposure needed for auroral observations (∼10 ms versus 1 s), hence in practice it is not possible to perform both observations at the same time. Due to fast angular speed of Juno of ∼12° s^{-1}, the presence of the de-spinning mirror to compensate the spacecraft spin is mandatory for the observations with the L filter. Notice that the JIRAM mirror can lock onto a specific target for up to 1.1 s, therefore the auroral

observation are performed close to the specification limits of the instrument[5]. The spectrometer slit is co-located with the M filter, and it is made by 256 spatial pixels, each of which has 336 channels that can record the IR spectrum between 2 and 5 μm, with a gap between 3.7 and 3.8 μm. The spectral sampling is $\sim$9 nm/channel. JIRAM has a beam splitter that sends about 70% of the incoming light into the spectrometer, and the remainder 30% into the imager. In the works reported in chapter 5 and 6, only the images acquired with the L band filter will be used: these show the IR emission of the H_3^+ ion (see section 3.4) caused by electron precipitation from the magnetosphere. As the electron precipitation is ultimately driven by magnetospheric processes, the observation of the aurorae can be used to constrain the physical understanding of such processes.

Since the first images captured by JIRAM, it has been clear the presence of an unexpected interference, whose intensity is higher than the H_3^+ auroral emission (see the example in Fig. 4.3). This effect seems to be caused by stray light coming from the junction between the M and L filters, and it is significant only when Jupiter is in the *field of view* (FOV) of the M filter. The interference does not uniformly affect the image, but gradually decrease from the junction. In order to remove the signal of the interference, a simple method has been developed (Mura et al., 2017): the noise is modelled as

$$N(x, y) = A(x)exp\Big(- \frac{y}{B}\Big) + C \tag{4.1}$$

where x and y are the columns and rows of the detector, respectively. The value of A and C can be determined by fitting the raw data of each image, while B appears rather constant over the dataset. This technique, despite its

[5]Unfortunately, at the time of writing, the de-spinning mirror has not been working properly since PJ 43: this severely hinders the possibility of further auroral observations. As the mirror is fundamental for the spectrometer, the team decided to suspend the auroral observations and preserve the instrument as much as possible for the Io flyby. Although this sounds like bad news, it is worth noticing that JIRAM was supposed to work for the first 8-10 orbits. Indeed, the instrument was added to the Juno mission at a late stage of the proposal, thus its electronics is not protected by the anti-radiation vault like other instruments. Therefore, in the end, JIRAM actually has been going beyond its expected lifetime, and the atmospheric observations with the M filter, which is less affected by the missing mirror, are still performed nowadays.

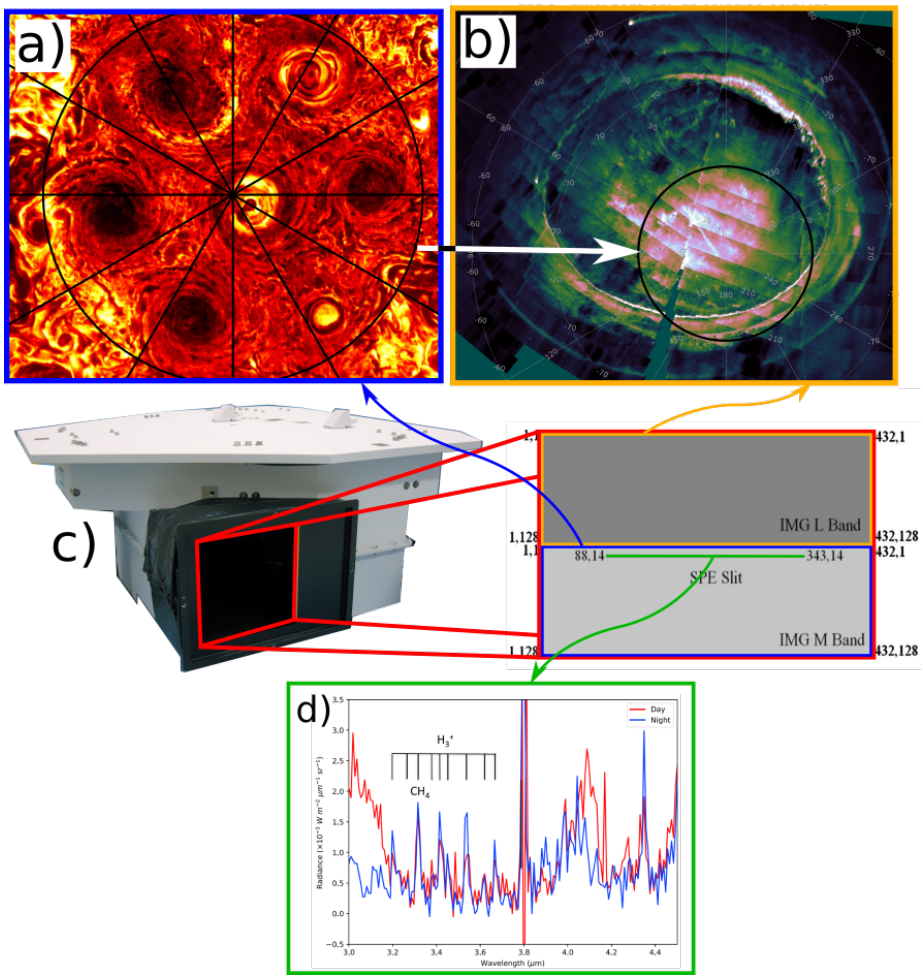

FIGURE 4.2: JIRAM and the three types of measurements it is able to perform. *(a)* Example of the polar cyclones at the South pole, observed with the M-band imager. *(b)* Example of the southern aurora, observed with the L-band imager (the image is the same as in Fig. 1.2). The black circle points out the region where the polar cyclones are found. *(c)* JIRAM (left) and the layout of the filters and the spectrometer slit position (right). *(d)* Example of the spectra observed by JIRAM (retrieved from Dinelli et al. (2017)).

simplicity, allows to recover the morphology of the auroral emission without greatly affecting the brightness, except near the filter junction, where the interference is too strong and the correction suppresses any signal. For this reason, the first 35 rows from the M filter are usually removed. The work reported in the present thesis uses the position and the morphology of the footprints to draw scientific conclusions, therefore the uncertainty on the brightness due to the correction is not relevant.

Besides the stray light, JIRAM data must be processed to remove the dead pixels and the so-called *odd-even difference*, which is a different average brightness of the odd columns of the detectors with respect to the even ones. This can be seen in the top image of Fig. 4.3 as vertical stripes, which are due to the detector acquiring odd and even columns asynchronously.

4.2 The Radio Instruments

Juno's *high-gain antenna* (HGA) is used for both communication with the spacecraft and scientific objectives, such as measuring the gravity field of Jupiter (e.g: Iess et al. (2018)) and performing radio occultations of the IPT (e.g: Moirano et al. (2021a); Phipps et al. (2021)). In chapter 6, we are interested in determining the plasma content of the IPT, hence we use the data of the radio occultations of the IPT, as they are sensitive to the electron content of the torus. The details of the processing from the radio data to the IPT electron distribution is given in section 6.3.1, to support the data analysis of the final chapter, while this section presents only the specifications of the instrument. The instrumentation includes two subsystems - the *Small Deep Space Transponder* (SDST) and the *Ka-band Translator System* (KaTS) - which are used to establish the *two-way dual link* between the stations of the *Deep Space Network* (DSN) on Earth and Juno (see Fig. 4.4). Indeed, the gravity measurements are obtained near the perijoves by tracking the spacecraft motion, which is affected by the gravity field of Jupiter. To this end, it is necessary to measure the Doppler shift in the radio communications due by the relative motion between Juno and

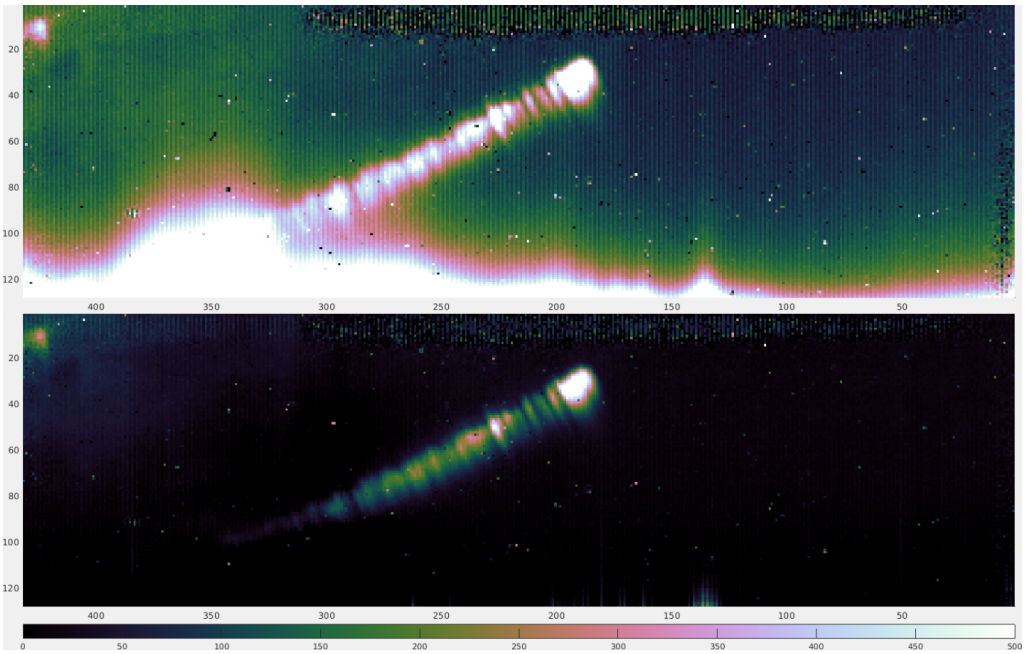

FIGURE 4.3: Image of the IFP acquired at the southern hemisphere by JIRAM during PJ 13. The top image shows the raw data, which is affected by several noises, most notably the bright interference near the junction with the M filter (around row 120). The processed image is reported in the bottom image: notice that the correction of the interference greatly suppress the signal near at the bottom of the image. Therefore, the footprint tail was not particularly short in that occasion, but rather it is not visible in the image due to the correction. The colorbar reports photon counts. To properly compare the two images, the same colorbar is applied, which results in the interference and the MAW spot being saturated.

the tracking *Deep Space Station* (DSS) on Earth. In realty, the frequency of the radio link is shifted by both dispersive (i.e: frequency-dependent, such as the crossing of plasma) and non-dispersive effects (like the Doppler shift), therefore a multi-frequency link is required to separate the two types of contributions (Bertotti et al., 1993; Mariotti and Tortora, 2013). In the case of Juno, the two main frequencies are in the X and Ka bands (hence the naming *dual link*). The details on the relation between the frequency shift and the plasma content of the IPT are presented in section 6.3.1. The tracking of the spacecraft is performed using a *two-way link*, which consists

of a signal sent from the DSS to Juno and then back to Earth, as shown in Fig. 4.4. This allows to improve the precision - as there is practically no power, nor technological complexity constrains - and to avoid offsets and drifts that usually affect the ultrastable oscillators mounted on spacecraft designed to support one-way links.

The usual procedure used for the radio tracking involves two uplink radio signals from the ground station in the X (7.153 GHz) and Ka bands (34.367 GHz), respectively (Asmar et al., 2017). The two signals are processed onboard Juno by the SDST and KaTS, respectively, which slightly shift the incoming frequencies to avoid interference between the uplink and the downlink[6]: the downlink frequencies are thus 8.404 GHz and 32.085 GHz in the X and Ka bands, respectively. It's worth noticing that the only station with the Ka uplink capability is the DSS 25 at Goldstone, California: when that station is not in view of the spacecraft, two X band uplink signals are used, one of which is converted into the Ka band by the SDST for the downlink, at a frequency of 32.088 GHz.

[6]The conversion is obtained by a multiplying factor called *turnaround ratio* or *transponder ratio*.

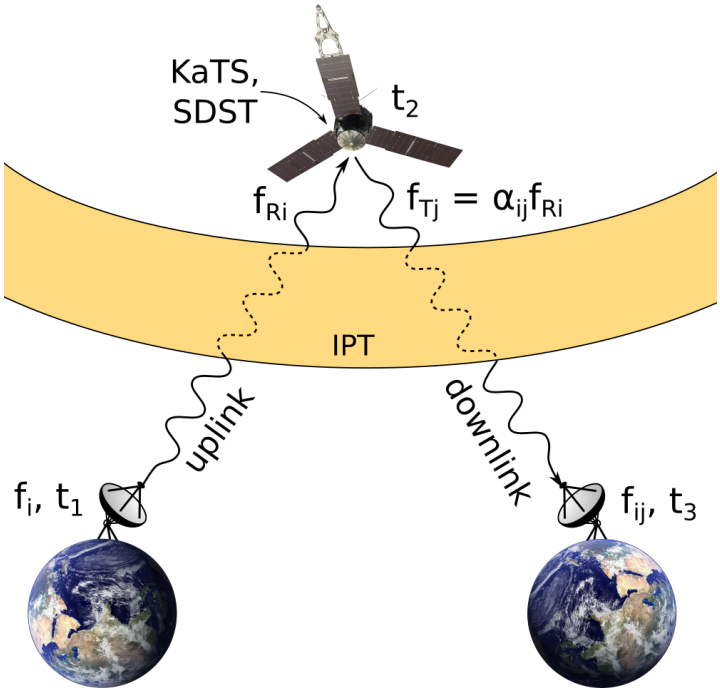

FIGURE 4.4: Sketch of the Juno 2-way radio occultations. The radio signal with frequency f_i is sent from the ground station at time t_1 and received with frequency f_{Ri} by the spacecraft at time t_2. The frequency shift $f_{Ri} - f_i$ is caused by the dispersive property of the plasma. The frequency of the received signal is converted to f_{Tj} by the KaTS/SDST systems according to the turnaround ratio α_{ij} in order to avoid interference between the uplink and downlink signals. Then, the signal is sent back to Earth. At time t_3, the signal f_{ij} is received by the ground station, with another frequency shift $f_{ij} - f_{Tj}$.

CHAPTER 5

Small-Scale Structure of the Satellite Footprints: the *Sub-dots*

This chapter describes a newly-discovered small-scale structure observed in the footprint tail of Io, Europa and Ganymede by JIRAM. These observations have been made possible thanks to the unprecedented spatial resolution of the JIRAM L-band imager. This structure - called sub-dots *- appears inconsistent with the pattern of reflection of the Alfvén wings illustrated in section 3.3. Instead, we suggest that the sub-dots are caused by a ionospheric feedback that drives field aligned currents/Alfvén waves from the Jovian ionosphere towards the magnetosphere.*

[1] As mentioned at the end of section 3.4, the advent of JIRAM at Jupiter brought new discoveries on the auroral emission associated with the Galilean moon since the first orbit (Mura et al., 2018). One of these is the presence of a small-scale periodic structure observed downstream of the MAW spot associated with the footprint of Io, Europa and Ganymede (see Fig. 3.5 and 5.1). This structure is named *sub-dots*, in order to avoid confusion with the MAW, RAW and TEB *spots* and for their smaller size compared to these latter. The sub-dots are consistently observed in the IFPT and *Ganymede*

[1]Chapter 5 reports the results published in Moirano et al. (2021b).

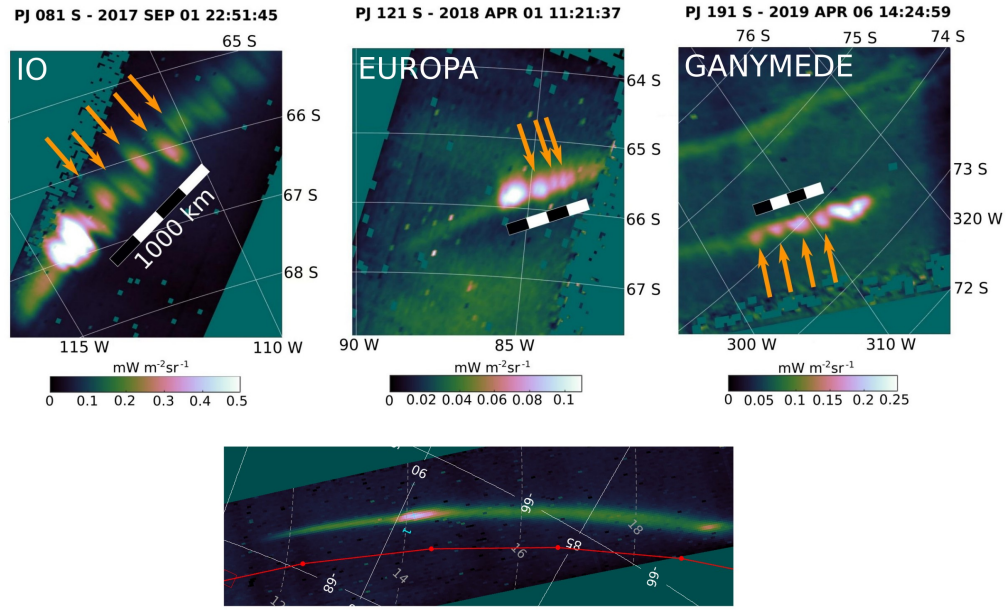

FIGURE 5.1: *Top*: examples of the Io, Europa and Ganymede footprints (from left to right) observed by JIRAM and showing the sub-dots substructure, highlighted by the orange arrows. Adapted from Fig. 1 of Moirano et al. (2021b). *Bottom*: example of the smooth tail of the Europa footprint, not showing the sub-dots structure.

Footprint Tail (GFPT), while sometimes the *Europa Footprint Tail* (EFPT) appears as a smooth, nearly uniform auroral arc. For this reason, there are more than double the observations of the GFPT showing the sub-dots than the EFPT, despite the fact that the former occurs closer to the main emission of Jupiter and thus it is more difficult to observe than the latter. The reason for the double appearance of the EFPT might lie in the weaker local interaction at Europa compared with Io and Ganymede, as it will be explained in section 5.2.

The dataset used to investigate the sub-dots includes images gathered between PJ 1 and 30; the number of orbits with available data for each footprint at both hemispheres is shown in Table 5.1. The larger number of observations obtained at the southern hemisphere compared to the northern one is due to Juno's orbit. Indeed, as illustrated in Fig. 4.1, the semimajor

axis of the trajectory has a southward precession, hence the PJ of the spacecraft comes close and closer to the North pole of Jupiter as the mission goes on. As the speed of the spacecraft is at maximum near the perijove, this means that Juno flies faster over the North pole than on the opposite hemisphere. Moreover, the spacecraft is also closer to Jupiter when it is over the North pole, which implies that JIRAM can observe a narrower portion of the Jovian surface. The two factors make the pointing of JIRAM more difficult in the North hemisphere than in the southern one, hence the reduced number of observations. The spatial resolution of the images is between 15 and 55 km pixel^{-1} in the Northern hemisphere and between 40 and 110 km pixel^{-1} in the southern one: at least two pixels are required to resolve a feature, thus JIRAM is able to identify structures with a typical size between 30 and 110 km in the North and between 80 and 220 km in the South.

Table 5.1: Number of PJs showing the sub-dots structure, from PJ 1 to 30.

	North	South
Io	6	16
Europa	1	3
Ganymede	2	9

The next parts of this section shows the morphological and dynamical characteristics of the sub-dots (section 5.1) and gives a potential physical explanation of the sub-dots generation (section 5.2).

5.1 Characteristics of the Sub-dots

The characterization of the sub-dots is given by their morphology and their dynamics. In order to quantitatively determine any potential variability of the sub-dots, we select an image of each footprint for each polar overflight by Juno, when available. Then the position of the sub-dots is retrieved in each image as (X,Y,Z) triplets and the Euclidean distance d between pairs of consecutive sub-dots is calculated. It's worth noticing that the difference

between the Euclidean distance d and the spherical distance $D = \Delta\psi R$ [2] - where $\Delta\psi$ is the angular separation - is ∼0.2 m for d ∼300 km, which is the typical distance between the sub-dots. The difference is far smaller than the JIRAM resolution, therefore the Euclidean distance is an acceptable approximation. The average distance $< d >$ between the sub-dots is then calculated with its associated standard deviation σ_d; this uncertainty reflects the variability of the sub-dots distance, not the uncertainty due to the instrumental resolution. The longitudinal distribution of the inter-sub-dots distance is reported in Fig. 5.2, where each point correspond to the average $< d >$ obtained from a single orbit. Lastly, for each hemisphere, we computed the typical mean distance λ_{hemi}, obtained as the average of all the average distances $< d >$. At the North, $< d >$ is between ∼130 and 560 km, with a mean λ_N=224±93 km. The shortest distance is observed when Io, Europa and Ganymede are around 250°: this might suggest a potential longitudinal modulation, although the scarcity of observation at the northern hemisphere forbids a robust statistical analysis. At the South, the distance ranges from ∼200 to 500 km, with a mean λ_S=323±89 km.

Contrary to the distance between the MAW, RAW and TEB spots, whose relative distance is a function of the longitude of the satellite (Bonfond et al., 2017a), the distance between the sub-dots is not dependent on the position of the satellites. Indeed, the data in Fig. 5.2 were fitted with a simple sinusoidal function (not shown), but the residuals did not improved with respect to a constant function. Furthermore, the relative distance between the MAW, RAW and TEB spots is a function of the Alfvén travel time (see Eq. 3.47, 3.48 and 3.49), which is different among Io (4-14 minutes), Europa (4-20 minutes) and Ganymede (9-35 minutes) (Hue et al., 2023; Moirano et al., 2023). Hence, the distance between the spots associated with the

[2] As Jupiter is an oblate spheroid, its polar radius (R_p = 66854 km) is shorter than its equatorial radius (R_J = 71492 km). Therefore, to estimate the spherical distance from this formula, it is necessary to compute the radius corresponding to the latitude θ where the footprint is observed:

$$R = \sqrt{R_p^2 + \frac{R_J^2 - R_p^2}{1 + \frac{R_J^2}{R_p^2} tan^2\theta}} \tag{5.1}$$

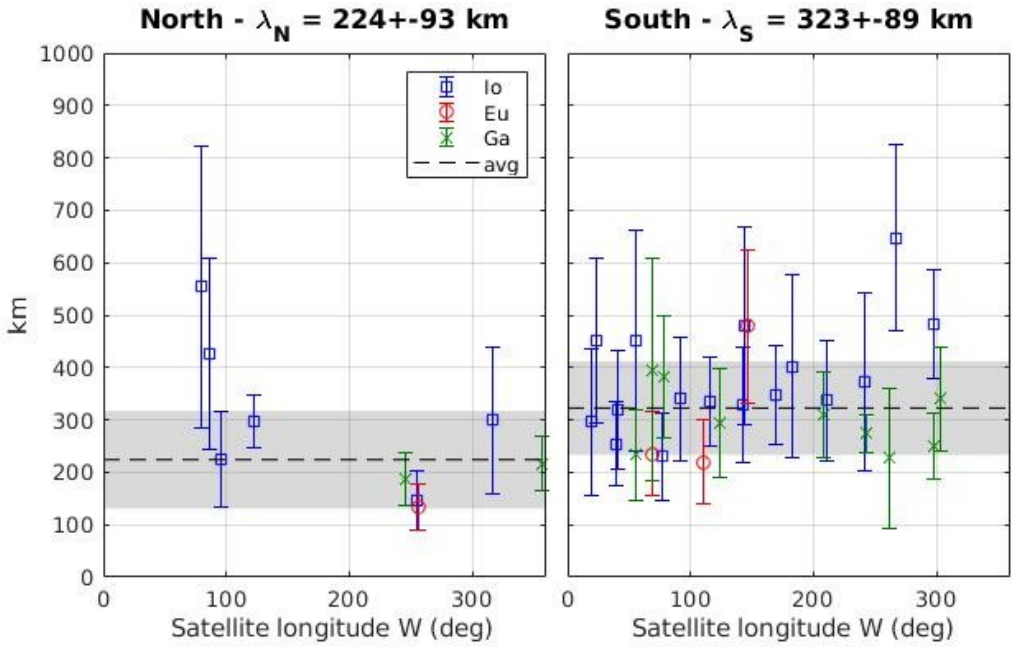

FIGURE 5.2: Average distance between the sub-dots of the footprint of Io, Europa and Ganymede at the northern and southern hemisphere (left and right plot, respectively). The dashed line is the weighted average of the displayed points whose value is reported above each plane, the grey area is the associated standard deviation. Retrieved from Moirano et al. (2021b).

reflection of the Alfvén wings is different among the three moons. Instead, the distance between the sub-dots appears independent of the satellite. Therefore, the uniformity of the sub-dots distance seems to suggests that they do not originate from the same process as the MAW, RAW and TEB spots.

Another characteristic of the sub-dots is their different dynamics compared to the MAW, RAW and TEB spots. JIRAM was able to capture a continuous sequence of image of the IFP at the southern hemisphere during PJ 13 on May 24^{th}, from UTC 07:10:57 to 07:18:33. The images are acquired 30 apart and they are shown in Fig. 5.3 (an animation can be found among the supporting material of the work by Moirano et al. (2021b)). In the sequence, the MAW spot moves by about 3° westwards from 67° to 70° in

about 7.5 minutes, with no displacement in latitude. The white arrow in Fig. 5.3 highlight a specific sub-dot that appears to be in a stable position near 65°. In principle, the sampling frequency of the images can make the substructure of the tail appear static if, coincidentally, the sub-dots moves over the neighboring brightness trough in 30 s, which is the period between two consecutive images. The high resolution of the images allows us to observe and identify each separate sub-dot in different images. For example, the pair of sub-dots highlighted by the blue arrows looks blended together and more extended, while the others between these two and the MAW spot are narrower and well separated from each other. This set of sub-dots was observed from 07:10:57 to 07:16:01 and it remained fixed slightly before 65°. Moreover, if the sub-dots moved to the location of it predecessor (i.e: the next sub-dot towards the MAW spot) in 30 seconds, then its speed in Jupiter's frame would be given by $\lambda_S/30$ s $\approx$10 km s^{-1}: this is higher than the speed of the MAW spot in the same frame, which is between 2.5 and 4 km s^{-1}. We are thus confident that the sub-dots in the tails are actually standing still in Jupiter's frame and that this is not a result of the timing between images.

JIRAM acquired two additional sequences in the southern hemisphere (PJ 14 and 26) which show the same dynamics of the sub-dots, even though the time windows covered were shorter (about 120 and 150 s, respectively). Hence, we believe that the stationary nature of the sub-dots observed during PJ 13 may be a consistent feature of the tail.

A brightness envelope can be observed overlapping the sub-dots structure around 2000 km from the MAW spot along the tail (highlighted by the dotted ellipse in Fig. 5.3). This modulation appears to move alongside the MAW spot, and it is likely caused by the electron precipitation associated with the TEB. This conclusion is also supported by the position of Io within the IPT: at the time of the observations, Io was below the centrifugal equator, hence the TEB spot is expected to occur downstream from the MAWspot (see also Fig. 3.3 and 3.5).

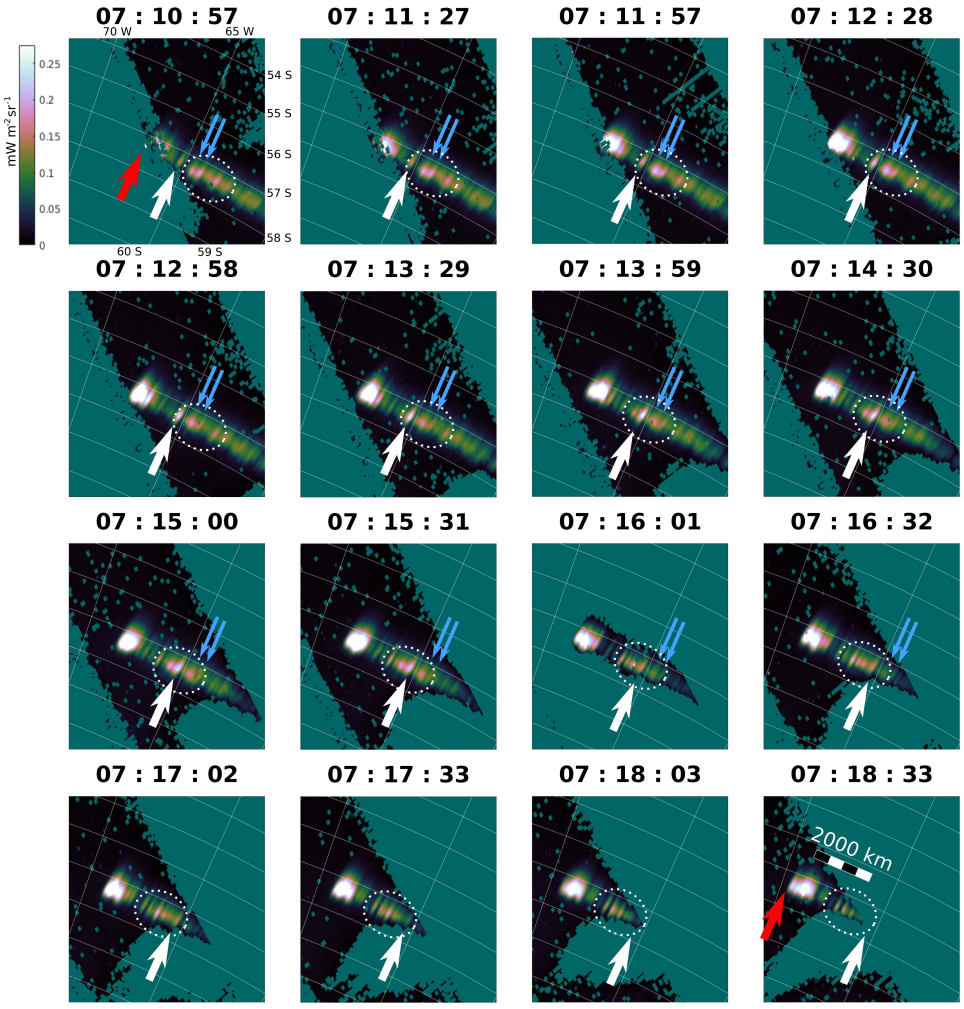

FIGURE 5.3: Sequence of images taken at the southern hemisphere by JIRAM during PJ 13 from UTC 07:10:57 to 07:18:33. The red arrows point out the initial and final positions of the MAW spot of Io, while the white and light blue arrows point out sample sub-dots that stayed near ∼65°. The white dotted ellipses highlight a bright group of several sub-dots following the IFP by about 2000 km, which is likely associated with the TEB. Retrieved from Moirano et al. (2021b).

5.2 A Candidate Driving Mechanism: The Ionospheric Feedback

The sub-dots are hardly explained by the propagation and reflection of Alfvén wave in the Jovian magnetosphere, which create the pattern of the Alfvén wings depicted in Fig. 3.3. Indeed, the Alfvén wings are tied to Io's frame, thus the associated spots move with the satellite, while the sub-dots appears static in Jupiter's frame. Moreover, the typical distance between the MAW, RAW and TEB spots is about 1000-1500 km for Io and up to 3000 km for Europa and Ganymede, while the typical distance between the sub-dots is between 200 and 350 km. Lastly, the shape of the Alfvén wings is determined by the tilt of the centrifugal equator with respect to the rotational equator: this introduces a periodic longitudinal variation of the pattern of wave reflection, which is not observed in the morphology of the sub-dots structure.

In the case of the Io footprint, it was suggested that the sub-dots might originate in the local interaction between the moons and the magnetospheric plasma (Mura et al., 2018). Indeed, in principle, the plasma flow around Io might generate a vortex street resembling the von Kármán vortex shedding in hydrodynamics (von Kármán, 1911). Alternatively, the radial velocity shear in the IPT or between Io's ionosphere and the torus might favour the development the *Kelvin-Helmholtz instability* (KHI) (Chandrasekhar, 1961), which also leads to vortex formation. The idea of this hypotheses is that the sub-dots are then a reflection of the morphology of these vortices. Nevertheless, the formation of vortices represents a theoretical challenge, as the conditions for their formation are unlikely met. In the following, we summarize the potential inconsistencies between the vortices formation and the plasma conditions at Io's orbit.

- In magnetized plasmas, the KHI requires strong velocity shear and low magnetic field along the plasma flow. Assuming a total velocity difference of $\sim$57 km s^{-1} over $\sim$ 200 km - corresponding to the velocity difference between Io and the IPT and the altitude of Io's ionosphere

(McElroy and Yung, 1975) - then the growth rate of the instability is $\gamma \approx 0.01\text{-}0.03$ s^{-1} (Miura and Pritchett, 1982), which implies the formation of fully developed vortices in 150-200 s (Miura, 1997). This is not compatible with the detection of sub-dots immediately after the MAW spot, which would require a faster growth rate (at least half of the one here estimated). Moreover, the KHI vortices can undergo nonlinear processes such as pairing and disruption (Miura, 1997), which ultimately should be reflected in the morphology of the subdots.

- The IPT is not expected to develop the KHI, as the radial velocity shear $dU/dr = \Omega_J$ and the decreasing density are conditions that cannot develop into the instability at Io's orbit (see §103 of Chandrasekhar (1961)). Simulations of the stability of the IPT shows that the plasma can be unstable to azimuthal perturbations, which evolve into the interchange instability (the analogous of the Rayleigh-Taylor instability for centrifugally-dominated systems) Hiraki et al. (2012). Such instability can lead to the formation of vortices with typical size of $\sim$20 R_{Io}. By mapping the sub-dots to Io's orbit, they should correspond to vortices with a size of 2-4 R_{Io}, hence it appears unlikely that the two phenomena are related.

- The development of a von Kármán vortex street in Io's wake occurs only if the Reynolds number[3] is in a certain range (Grenier, 2005). Space plasmas usually have very little to negligible viscosity, hence the Reynolds number is very high: in this regime a turbulent wake is expected instead of a structured trail of vortices.

- The structure and dynamics of the vortices depend on the environmental parameters of each moon, as they determine the size of the shear layer, which in turn affects the most unstable mode. Each of the Galilean moons can interact electromagnetically with its surrounding plasma differently one from another (Saur et al., 2013) and their magnetic fields are different: these two elements potentially affect

[3]That is: the ratio between inertia and viscosity of the plasma.

the size of the shear layer, which is unlikely to be the same for all three moons. So if the KHI triggers, the resulting vortices are likely to exhibit different morphologies, which is not consistent with the observations made by JIRAM.

Although vortices in the low latitude magnetosphere near the orbits of the Galilean moons are unlikely to develop or to exhibit features compatible with our observations (if they form), it is not possible to completely rule out the presence of vortices: further studies are needed to properly assess if vortices can develop as a result of the interaction of the moons with the magnetospheric plasma and what is their precise dynamics.

We suggest that the origin of the sub-dots lies in a ionospheric process known as *ionospheric feedback* (IF): according to such model, the variations in the ionospheric properties caused by the particle precipitation trigger a local perturbation that launches plasma waves from the ionosphere towards the magnetosphere[4]. This process is suggested to ripple the auroral arc on Earth, producing small-scale periodic structures (Hiraki, 2015; Watanabe, 2010) that can explain the formation of the sub-dots at Jupiter. No previous application of the IF to Jupiter have been performed before the present study. Here, a compatibility study between the IF model and JIRAM observations is carried by performing an order-of-magnitude application of the IF theory to Jupiter.

The IF requires two conditions: (a) the presence of currents in the ionosphere and (b) a local variation of the ionospheric electric conductivity (Atkinson, 1970; Sato, 1978). The process can be break down into five steps, as shown in Fig. 5.4:

[4]It's interesting to notice that the IF is conceptually different to the usual approach to auroral studies. Indeed, the auroral emission observed on a planet are often considered a signature of magnetospheric processes, hence the ionosphere is considered as a "photographic plate" which is "exposed" to the phenomena occurring in the magnetosphere. Therefore, as a photo does not affect the subject, the ionosphere is usually considered to not affect the magnetosphere. In contrast, the IF states that ionospheric variations, driven by magnetospheric processes, can in turn produce perturbations that propagate into the magnetosphere, thus the term *feedback*.

1. Electrons are accelerated into the ionosphere by the wave-particle interaction associated with the S-I coupling.

2. The electron precipitation driven by the S-I coupling locally alters the conductivity of the ionosphere at the foot of the MAW.

3. The modified conductivity creates a local polarization, which drives secondary ionospheric currents.

4. The secondary currents are closed by FACs that are carried by Alfvén waves propagating from the ionosphere to the magnetosphere.

5. The waves are reflected at gradients of the Alvén speed such as near the IPT of the ionosphere at the opposite hemisphere. As these waves return near their original source at the ionosphere, they produce additional particle precipitation, thus re-starting the loop.

This process can continue as far as the magnetosphere can supply precipitating material. Watanabe (2010) and Hiraki et al. (2012) shows that the IF process at Earth can evolve into an instability[5] that forms ripples and Kelvin-Helmholtz-like vortices during the nonlinear phase of the process. Although in reality dissipating effects such as light emission and the ionospheric chemistry may limit the growth of the instability, the structuring of the ionospheric currents could still happen, thus forming the sub-dots. Other studies (e.g: Jia and Streltsov (2014); Lysak and Song (2002); Miura and Sato (1980); Streltsov and Mishin (2018)) on the IF at Earth support the ability of this process to structure the auroral arcs into small scale structures.

In order to trigger the IF at Jupiter, the conductivity enhancement can be caused by the electron precipitation associated with the footprints

[5]They refer to the process as *ionospheric feedback instability*. Indeed, the process described here starts with particle precipitation and lead to more particle precipitation, which trigger a positive feedback. Nevertheless, the studies by Watanabe (2010) and Hiraki (2015) do not include any dissipation, such as the ionospheric chemistry and light emission, that can damp the instability. Moreover, the fading nature of the footprint tails seems to be in contrast with the idea of instability, therefore we believe that the term *instability* in the present context may be misleading.

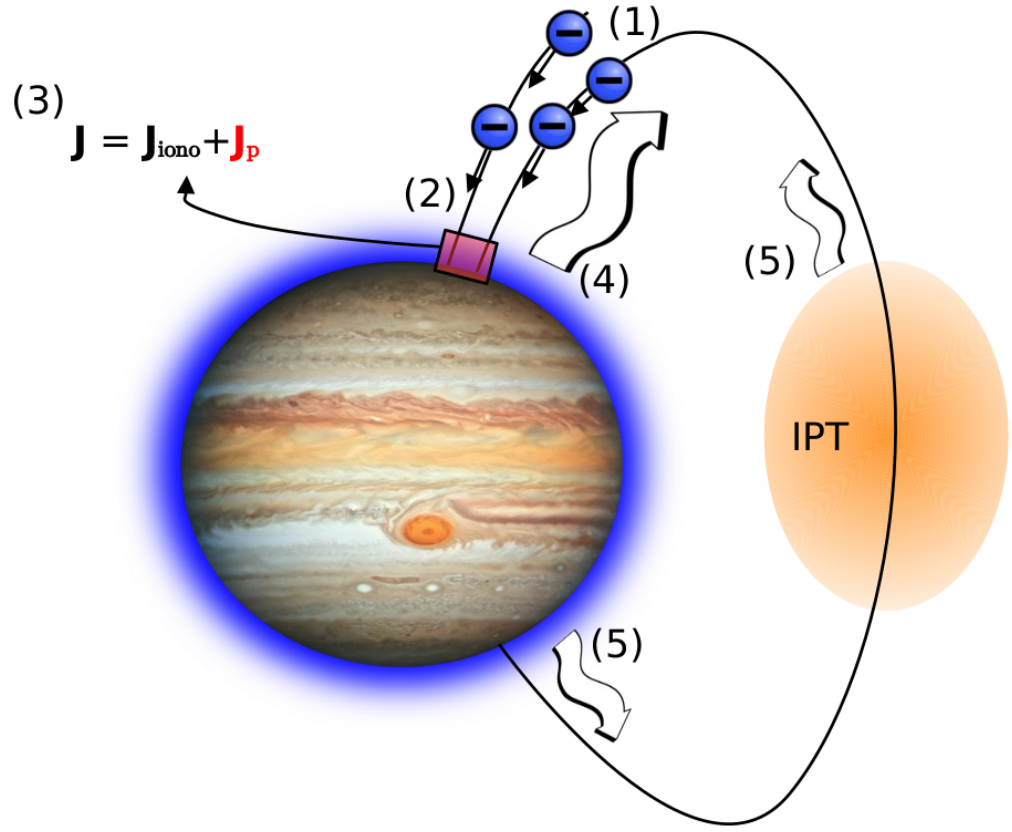

FIGURE 5.4: Sketch of the *ionospheric feedback* (IF). The process can trigger under electron precipitation into the ionosphere (1), which leads to a variation in the ionospheric conductivity (2). The local change in conductivity produces polarization that affects the ionospheric currents (3): this requires additional field aligned currents that propagate from the ionosphere to the magnetosphere as Alfvén waves (4). The waves can be partially reflected at gradients in the Alfvén speed, such as at near the IPT or the ionosphere at the opposite hemisphere (5). The reflected waves then return near their source (the red area in the sketch), where they can further accelerate particles into the ionosphere by wave-particle interaction, closing the loop.

and confirmed by Juno measurements (Allegrini et al., 2020; Szalay et al., 2020a,b). On the other hand, multiple factors can contribute to the ionospheric currents. Generally, such currents can be associated with the electric field provided by the subcorotation in the plasmadisk: this electric field, mapped along the magnetic field into the jovian ionosphere, might provide the background electric field required for the IF. Voyager 1 and Galileo plasma observations are used to determine the azimuthal flow through the plasmasheet, although sometimes with quite large uncertainties. Bagenal et al. (2016) analyze Galileo PLS observations in the plasmasheet between 5 and 30 R_J and they conclude that the plasma flow begins to deviate from corotation near 9 R_J (close to Europa's orbit) and it is between 80% and 100% of corotation out to 25 R_J. Dougherty et al. (2017) re-analyze the Voyager plasma science data and they point out that the azimuthal flow starts to sub-corotate close to Europa, it dips down to 20% below corotation with a localized return to corotation at 17–20 R_J and reaches an asymptotic value of about 225 km s^{-1} further out. The overall increase in the corotation lag with the radial distance from Jupiter is a consequence of the finite conductivity of Jupiter, which limits the currents that mediate the M-I coupling, as introduced in section 2.3. Beyond these general subcorotation trends, significant plasma slowing is also observed near the orbit of Io (Bagenal et al., 1985; Brown, 1983; Thomas et al., 2001). The plasma transport at Io is too small to cause the corotation lag, hence Pontius and Hill (1982) attribute this subcorotation to the ionization of neutral clouds of sulfur and oxygen that extend along Io's orbit (Brown, 1981; Durrance et al., 1983) by electron impact and charge exchange (Delamere and Bagenal, 2003). Ultimately, the ionospheric Pedersen conductance limits the ability of the current to restore the full corotation speed. In addition, dissipation in the magnetosphere-ionosphere coupling currents system may play an important role in the subcorotation near Io's orbit (Coffin et al., 2020). Moreover, at the moons, the magnetospheric plasma is slowed in the wake of the moons by the pickup of newly ionized atmospheric neutrals - at Io and Europa - or by the interaction of the plasma with the intrinsic magnetic field of Ganymede. As a consequence, the magnetic field is stretched in the azimuthal direction

and drives a radial current given by Ampère's Law Eq. A.13 (Ergun et al., 2009). Corotation is then restored by the $\vec{J} \times \vec{B}$ force over time, so the electric field due to the wake is more important near the footprints than far down the tail. Using numerical simulations of the plasma atmosphere interaction at Io and Europa, Saur et al. (1998) estimates that the flow is slowed by 95% at Io and 80% at Europa (see also Saur et al. (2013)), thus the electric field in the wake may depend on the strength of the local interaction between each moon and its environment.

In the last part of the present section, we report three order-of-magnitude arguments in favour of the IF to explain the sub-dots.

1. The shear Alfvén waves carry currents whose perpendicular components are aligned with the perpendicular wavevector [6]. At the ionosphere, these currents can affect the Hall and Pedersen currents, hence the evolution of the IF ultimately depends on the relative direction between the ionospheric electric field $\vec{E}_I$ and the perpendicular wavevector $\vec{k}_\perp$ of the incident Alfvén wave. Most of the theoretical studies of the IF focused on a 2D geometry in which $\vec{k}_\perp \| \vec{E}_I$: in this case, the feedback process could lead to the formation of parallel arcs at different latitudes (see for example the theoretical results by Atkinson (1970); Miura and Sato (1980); Pokhotelov (2003) and the measurements reported by Lynch et al. (2015); Tulegenov and Streltsov (2017)), reminiscent of the Io tail splitting reported in Mura et al. (2018) far down the tail. In order to include an arbitrary direction of $\vec{k}_\perp$ a full 3D geometry have to be considered. Numerical simulations of terrestrial auroral arcs showed that the direction of the most unstable $\vec{k}_\perp$ depends on the Hall and Pedersen background currents and that oblique $\vec{k}_\perp$ can produce ripples along the arc, which resemble the sub-dot structure addressed in this work (Hiraki, 2015; Watanabe, 2010). At Jupiter, the conductivity gradient associated with the IFP is structured in both longitude and latitude, hence modes along the direction of the footprint could be excited and driven unstable. In the nonlinear phase

[6] here "perpendicular" implies "perpendicular to the magnetic field".

of the IF, these ripples form an alternating pattern of upward and downward currents, which may explain the small scale morphology JIRAM is observing in the footprint tails of the Galilean moons.

2. Earth-based simulations of the feedback instability show that the typical distance between spots depends on the most unstable wavevector $\vec{k}_\perp = 2\pi\lambda_\perp^{-1}$ (Hiraki, 2015), whose wavelength $\lambda_\perp$ is related to $\lambda_\parallel$ by $\lambda_\perp = \lambda_\parallel \frac{\delta B_\perp}{B}$. In deriving this equation critical balance was assumed from the magnetohydrodynamics turbulence theory (Saur et al., 2018). The spectrum of the magnetic field measured by MAG and Waves instruments onboard Juno at $\sim$0.4 R_J from the surface revealed that the parallel wavelength of the fluctuations ranges from $\sim$20 to $\sim 10^{-3}$ R_J (Sulaiman et al., 2020). In order to perform an order of magnitude estimate, we assume that this spectrum is the same (or at least very similar) at the altitude where the auroral emission occurs. Taking into account the long-wavelength end of the spectrum (that is, the wavelenghts near $\lambda_\parallel \sim$20 R_J), its amplitude ($\sim$200 nT; Gershman et al. (2019); Sulaiman et al. (2020)) and the magnetic field at Jupiter's surface ($B \sim 10^6$ nT; Connerney et al. (2022)), the perpendicular wavelength is $\sim$280km, which is similar to the value of λ_N and λ_S reported in Fig. 5.2. The dispersion of the Alfvén waves due to inertial effects and mode trapping in the ionospheric cavity may need to be considered in order to better estimate $\lambda_\perp$, but the result from this approximate estimate alone is encouraging.

3. The periodic pattern in the nonlinear phase of the instability moves at a speed given by $\vec{E}_I \times \vec{B}_I$ drift, where the subscript I refers the fiels at the ionoshere (Atkinson, 1970; Hiraki, 2015; Watanabe, 2010). The electric field in the magnetosphere associated with the sub-corotation velocity $\Delta\vec{u}$ is given by $\vec{E}_M = \Delta\vec{u} \times \vec{B}_M$, where B_M is the magnetic field in the equatorial plane. In order to give a quantitative estimate, $\Delta\vec{u}$ is taken from the corotation lag observed from $\sim$10 R_J outward for Europa and Ganymede (Dougherty et al., 2017), while for Io we considered the departure from corotation observed near 5.9 R_J (Brown,

1983). Therefore, for Io, Europa and Ganymede the corotation lag is about 5%, 10% and 20% of the corotation velocity, respectively. As a first approximation, the relationship between ionospheric and magnetospheric field is given by $\vec{E}_I = \xi \vec{E}_M$ if there is no potential drop along magnetic field lines (Ergun et al., 2009). The electric field and the consequent drift can be up to 50% lower if parallel potentials are generated along field lines, depending on the ionospheric and field-aligned conductances (Ergun et al., 2009). The mapping factor ξ stems from the conservation of magnetic flux between the moons and the ionosphere of Jupiter assuming that field lines are equipotentials. Considering a flux tube of radius R_M at the ecliptic and R_I at the ionosphere, the potential drop ΔV across the flux tube must be the same along the tube itself, therefore $\Delta V \approx E_M R_M \approx E_I R_I$ and thus $\xi \approx R_M/R_I$. Taking typical values $\xi \approx 30$ and $B \approx 10^6$ nT, then $E_I \approx$ 0.1 - 0.2 V/m and $v_{drift} \approx 0.1$ - 0.2 km s^{-1} in Jupiter's frame, which is much slower than the speed of the footprints (usually between 2.5 and 4 km s^{-1}). Consequently, the structure of the whole tail would move by about 3–6 km in between consecutive JIRAM images and by 45–90 km during the whole sequence in Fig. 5.3. The resolution of the images was between 70 and 80 km pixel^{-1} at the times in Fig. 5.3, so the sub-dots would move the length of one pixel at maximum because of the drift. Therefore, this velocity is consistent with the apparent stationary nature of the sub-dots in Jupiter's frame observed by JIRAM.

The three above-mentioned arguments suggests that the application of the IF process to Jupiter may explain the formation of the sub-dots. Nevertheless, a few points have to be investigated further:

- As shown in Fig. 5.1, the EFPT often shows a continuous arc instead of a trail of sub-dots. This might be caused by the fact that the conditions for the IF to develop the sub-dots are not always met for the Europa case, meaning that the increase of ionospheric conductivity is too low or that the ionospheric electric field is too weak. The electro-

dynamical interaction at Europa with its surroundings is weaker than at Io and Ganymede (Saur et al., 2013). Indeed, the volcanic activity of Io generates an ionosphere that interacts with the surrounding dense plasma of the IPT, while the intrinsic magnetic field of Ganymede diverts impinging plasma and makes this moon a bigger obstacle than its solid cross section suggests. Thus the weak interaction at Europa can affect the ionospheric electric field at Jupiter and perhaps the conductivity as a consequence of electron precipitation so that the IF cannot be triggered. Nevertheless, JIRAM occasionally observed a trail of sub-dots in the EFPT. This may occur when Europa is in particular environmental conditions such as plasma sheet crossing, water outgassing (Paganini et al., 2020; Roth et al., 2014), or plasma injections (Mauk et al., 1997) so that the interaction becomes temporarily strong enough to trigger the IFI.

- The feedback itself structures the field-aligned currents/Alfvén waves so that they develop the parallel electric field that can accelerate the electrons (Damiano et al., 2019; Hess et al., 2010a; Lysak and Song, 2003). Since this mechanism depends on the ionospheric parameters and not on the moons themselves, this might be the reason that the spot spacing is similar for all three moons. Nevertheless, the relation between the ionospheric current system generated by the IF and the electric field in the acceleration region needs to be addressed quantitatively to estimate the intensity of the auroral emission (Hiraki, 2015).

- Earth-based simulations reveal that the growth rate and the most unstable mode of the IF instability depend on the Pedersen and Hall conductances in the ionosphere (Watanabe, 2010) and on the magnitude of the background electric field (Hiraki, 2015). These two pieces of information are fundamental to carry out a proper quantitative comparison between the observations made by JIRAM and the feedback model, and it will require further analysis to properly determine.

- The role of the *ionospheric Alfvén resonator* (IAR), a resonant cavity caused by the sharp gradient in the Alfvén speed above the ionosphere, can affect the development of the IF. Indeed, the IF can be triggered by eigenmodes of field line resonances extending from one ionosphere to the other (e.g.: Rankin et al. (2005)), as well as by eigenmodes of the IAR (Lysak, 1991; Lysak and Song, 2002; Pokhotelov et al., 2001): the former drives a slow IF with periods of a few minutes while the latter drives a fast IF with periods of a few seconds. There have been no published reports of the application of this feedback mechanism in the Jovian magnetosphere. However, at Jupiter, there is also the possibility of feedback in the cavity formed in the high Alfvén speed region between the ionosphere and the IPT. The interplay of these various cavities may affect the morphology and brightness of the footprint tails due to the different time scales of these cavities.

- Regarding the energy budget of the feedback process, Earth-based simulations reveal that the energy of the Alfvén waves leaving the ionosphere is correlated to the decrease of Joule heating, which results from the increased ionospheric conductivity (Lysak and Song, 2002). In addition, the infrared H_3^+ auroral emission on Jupiter is mostly due to chemical reactions (see section 3.4), which may strongly damp the formation of ripples by the IF (Lysak and Song, 2002). Therefore, the relationship between the energetics of the IF and the intensity of the IR emission is not straightforward and requires further investigation.

CHAPTER 6

Constraining the Io Plasma Torus and Determining its Variability

This chapter illustrates that the position of the Io Footprint (IFP) *can be used to quantitatively constrain the state of the Io Plasma Torus* (IPT). *Although variations of the footprint position and morphology have been qualitatively associated with variations in the plasma conditions at the moon's orbits, the work presented here is the first attempt to derive* quantitative *information on the IPT by using the position of the IFP. The chapter is divided into three main sections: section 6.1 shows how to derive information of the IPT by using the data from the JIRAM L-band imager; section 6.2 reports the full database of JIRAM observations of the footprints, which is used to investigate the IPT over the course of the Juno mission; section 6.3 shows the determination of the state of the IPT obtained by using both the IFP position and the radio occultations of the torus.*

One of the hottest topics of the Jovian magnetosphere physics - and perhaps of the whole Jupiter system - is the effect of the plasma source on the variability of the magnetosphere. As introduced in Chapter 2, the main plasma source near Jupiter is the volcanic activity on Io, which supplies the IPT; then the plasma diffuses from Io's orbit and fills the whole

magnetosphere. Moreover, the M-I coupling mechanism that transfers energy and angular momentum between Jupiter and the Iogenic plasma accelerates the magnetospheric plasma in the azimuthal direction: the fast rotation of the planet is then transmitted to the IPT and the plasmadisk, which are then subject to a strong centrifugal force. As the magnetic field is advected with the plasma, the presence of the centrifugally-accelerated, high-density plasma inflates the Jovian magnetosphere to a size that is almost the double with respect to the size expected by the internal magnetic field of Jupiter: this shows the fundamental relevance of Io's volcanic activity on the system. Moreover, monitoring the volcanic activity on Io and the state of the IPT is fundamental to understand the dynamics of the Jovian magnetosphere and to predict its variations. The variability of the IPT is a long-lasting topic of research (Brown, 1995), with two major questions: (a) how the IPT changes depending on the Iogenic source (e.g., Roth et al. (2020)) and (b) how the Jovian magnetosphere responds to the variability of the torus (e.g.: Bonfond et al. (2013)). To properly address these issues, it is essential to simultaneously and continuously monitor Io, the IPT and the aurorae.

At present day, four major observables are used to inspect the IPT: spectrometry, imaging, particle detections and occultations[1]. The latter two requires a probe inside the Jovian magnetosphere, potentially inside the IPT itself, or behind the IPT as seen from Earth, respectively. Hence, a deep space mission is required to perform those types of observations. On the contrary, spectrometry and imaging can be performed from ground and near Earth, thus it currently represents the most reliable way to continuously monitor the torus - except during solar conjunction. Nevertheless, spectrometry is not without shortcomings of practical nature. The intensity of the spectral lines depends on both the line-of-sight integrated density (also

[1]In the context of the exploration of the Io torus, occultations are usually performed by measuring the frequency shift in the radio signal coming from a spacecraft behind the torus and crossing the torus. For this reason, this type of observation is usually referred to as *radio occultation*. Notice that the occultation technique of the IPT is different from the one usually used for atmospheric radio occultations: in that case, the relevant parameter is the index of refraction of the atmosphere, which bends the path of the radio signal.

called *column density*) and the temperature of the torus plasma, therefore the two quantities are coupled. By inspecting several lines it is possible, in principle, to disentangle the temperature and column density, but the limited wavelength range of real instruments may forbid breaking the degeneracy. Moreover, if multiple lines overlaps or are very close to each other, it may be difficult to separate multiple species. Lastly, compromises have to be made between spatial and spectral resolution. As a rule of thumb, ground-based observations have very high spectral resolution, but lack of spatial resolution. This translate in the difficulty to observe small and faraway structures and in obtaining spectra that contains spectral information from different regions. On the other side, in-situ spectrometry performed onboard deep space spacecraft has worse spectral resolution than ground-based measurements, because of the engineering constrains on the spacecraft payload, but make up for this limitation with a better spatial resolution. Therefore, having new methods to monitor the IPT is crucial to complement spectroscopy, as well as particle measurements and radio occultations, especially if they can be performed from Earth. As it will be (hopefully) clear by the end of this thesis, the position of the footprint of the Galilean moon represents a new observable that can be acquired from in-situ missions and Earth-based campaigns, although these latter usually at a lower spatial resolution than the former.

The remainder of this thesis will illustrate how the footprint of Io can be used as an additional observable to constrain the state of the IPT, provided that sufficient spatial resolution is achieved. Moreover, the position of the footprint is used alongside the radio occultations of the torus performed by Juno to form a multi-instrumental dataset of nearly-simultaneous observations: this helps to determine the properties of the IPT over the Juno mission, which, in turn, supports ground based observations and in-situ measurements in reconstructing the evolution of the IPT and its interplay with Io and the Jovian magnetosphere.

6.1 Determination of the Io Plasma Torus from the Io Footprint Position

[2] As introduced in sec 2.1, the variability of the IPT can be classified into four categories: System III and System IV variations, local time asymmetry and temporal variability. In principle, any variation of the plasma content of the torus affects the speed of the Alfvén waves Eq. 3.5 and its corrections Eq. 3.16, 3.18 and 3.19. In turn, such variations change the Alfvén travel time Eq. 3.32 and the shape of the Alfvén wings Eq. 3.24, thus leading to potential variations in the position of the auroral footprint. A sketch showing the qualitative effect of the IPT variability on the Alfvén wings is presented in Fig. 6.1. System III variations due to Io oscillating up and down within the IPT will not be covered in this section, as they are already broadly documented in the literature (e.g.: Bonfond et al. (2008, 2017a). Instead, the aim is at finding evidence of System IV variations, local time asymmetries and temporal variability. For this purpose, the data acquired over the first 42 orbits of Juno are surveyed, with focus on the images of the IFP showing the MAW and TEB spots, because (a) they can be easily identified, especially when the TEB is located upstream of the MAW and (b) they are less affected by the complex pattern of the reflected Alfvén waves that develops along the footprint tail. Moreover, the JIRAM images must meet three criteria to be selected for the present analysis:

1. the footprint has to be observed during two or more orbits with Io in nearly the same System III longitude: this requirement rules out variability due to System III variations, allowing the detection of the other types of variability.

2. JIRAM performs multiple sequences of images during every flight over the poles and the images are taken 30 s apart. The IFP moves at $\sim$2.5–6 km s^{-1} relative to Jupiter in the North and $\sim$3–4.5 km s^{-1} in the South, which implies that it moves by about 100–150 km between

[2] Section 6.1 reports the results published in Moirano et al. (2023).

two subsequent images. Hence, it is essential to restrict the analysis to single images or - if not possible - to tessellations of 2–3 consecutive images in order to limit the effect of the movement of the emission. Therefore, both the MAW and the TEB spots should be identifiable in the same sequence or, better, in the same image, so that their relative distance can be used to highlight any potential variability.

3. Images showing the TEB leading the MAW are better suited for the retrieval of the position of these spots than observations with the TEB downstream. Indeed, as illustrated in section 5.1 and Fig. 5.3, the brightness of the sub-dots can interfere with the morphology of the TEB, making more difficult the determination of the precise location of TEB spot when it is downstream. The sub-dots show a typical spacing of ∼300 km, which should be taken into account to estimate the position of the TEB.

The meeting of the above-mentioned criteria produces two pairs of observations where it is possible to observe a change in the IFP position: PJ 10–31 (December 16^{th} 2017 at UTC 19:51 and December 30^{th} 2020 at UTC 23:21, respectively) and PJ 11–32 (February 7^{th} 2018 at UTC 15:55 and February 21^{st} 2021 at UTC 19:28, respectively). The difference in Io's longitude between the images in each of these pairs is less than 1.5°.

The altitude of the emission needs to be taken into account in order to accurately determine the coordinates of the emissions. Based on auroral emission models, the peak altitude of the IR emission is expected to occur between 500 and 1000 km for electron energies between 0.1 and 100 keV (Tao et al., 2011). Juno-JADE-E electron measurements reported a broadband electron energy distribution associated with the IFP, with a peak energy between 0.1 and 1 keV (Sulaiman et al., 2020; Szalay et al., 2020b), which implies that the IR emission should peak near 900–1000 km. JIRAM observed the IFP during both PJ 4 and 7 in the northern hemisphere when its longitude was between ∼90° and 120° at two different emission angles. This allows to retrieve the altitude of the footprint by stereoscopy, and it is estimated to peak at 600±100 km. Potentially, this discrepancy stems

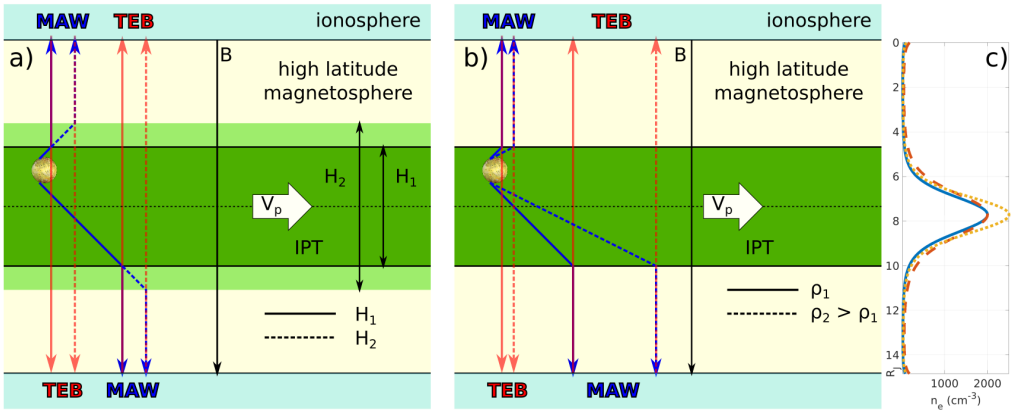

FIGURE 6.1: Sketches of the Alfvén wings in Io's rest frame when the moon is above the centrifugal equator (black dotted line) under different plasma conditions. The plasma in the IPT (green area) flows from left to right. The density of the torus is assumed uniform in both panels. The magnetic field is also uniform and points southwards (black arrow). The light blue areas are the Jovian ionospheres where auroral emissions occur. *(a)*: Alfvén wings for two different sizes of the IPT with the same density. The torus thickness is represented by H_1 (dark green) and $H_2 > H_1$ (light green). The blue solid arrows represent the path of the Alfvén waves when the thickness of the IPT is H_1, while the blue dashed ones the path when the thickness is H_2. The red arrows point out the path of the field-aligned TEB in the two conditions. *(b)*: Alfvén wings for two values of the density (ρ_1 and $\rho_2 > \rho_1$), while the size of the torus is the same. The reflected Alfvén wings are not drawn for sake of clarity. *(c)*: examples of three more realistic electron density distributions, computed using the diffusive equilibrium model described in by Eq. 6.2, 6.3 and 6.4 (Bagenal and Sullivan, 1981). The vertical axis is the distance along the magnetic field line crossing the orbit of Io at 0° longitude, measured from the northern hemisphere. The blue and red dashed lines correspond to the case in panel *(a)*, and the blue and orange dotted lines to panel *(b)*. Retrieved from Moirano et al. (2023).

from the assumption of a Maxwellian distribution for the electrons in the model by Tao et al. (2011), while JADE-E measurements reported a kappa distribution. The difference between the two distributions is stronger at higher energy: the Maxwellian one underestimates the contribution of high-energy electrons, which penetrate deeper into the atmosphere and cause the emission to occur at lower altitudes.

6.1.1 Modelling the Io Plasma Torus: Diffusive Equilibrium

As explained in chapter 3, the position of the IPT depends on the Alfvén speed profile (Eq. 3.5) along the magnetic shell connected to Io's orbit. In order to predict the position of the footprint, it is therefore necessary to model the magnetic field and the plasma distribution. Due to the strong magnetic field of Jupiter, the relativistic correction Eq. 3.16 has to be included. On the contrary, the inertial corrections Eq. 3.19 can be neglected in this study. Indeed, above the ionosphere, the Alfvén speed is nearly the speed of light, thus the Mach-Alfvén angle Eq. 3.27 is very small, and the Alfvén wings are basically aligned with the magnetic field. The inertial effects accelerate the electrons along the magnetic field, therefore their inclusion in the modelling does not affect the predicted position of the auroral footprint. The kinetic correction Eq. 3.18 can also be neglected, as it is less than 1% near the IPT, where it is expected to be most relevant (Jones and Su, 2008). The Alfvén speed can be integrated according to Eq. 3.32: this gives the time needed by the local perturbation to travel from Io to the Jovian ionosphere. During the same time, Io continues its orbital motion, hence it is possible to build a map that relates Io's position with the MAW spot at any given time. Additionally, the position of the TEB spot can be computed by mapping the position of the MAW spot in the opposite hemisphere along the magnetic field (Bonfond et al., 2008; Jacobsen et al., 2010), as its energetic electrons quickly travel along the magnetic field lines between the two hemispheres in less than 30 s (Hess et al., 2013). For comparison, the Alfvén travel time associated with the

MAW spot is between 2 and 12 minutes, depending on the distance of Io from the centrifugal equator (Hinton et al. (2019) and Fig. 6.2).

The *Juno Reference Model through Perijove 33* (JRM33), built from the first 33 Juno orbits (Connerney et al., 2022) is used to compute the internal magnetic field. For consistency with the footprints provided in the supporting information of Connerney et al. (2022), the spherical harmonic expansion of the field is limited at degree 18. We also take into account the magnetic contribution of the current in the plasmadisk by including the magnetodisk formulation of Connerney et al. (2020).

The plasma density in the IPT is computed using a diffusive equilibrium model (Bagenal and Sullivan, 1981; Mei et al., 1995; Thomas, 1992), which takes into account the electron and ion pressures, the centrifugal and gravitational forces, the magnetic mirror force and the ambipolar electric field due to charge separation driven by the centrifugal motion of the plasma. Assuming that the temperature of the ions and electrons is constant along the field lines, the density distribution of the species α along each field line is given by

$$n_\alpha(s) = n_{\alpha 0} exp\Big[\frac{m_\alpha \Omega_J^2(\rho^2-\rho_0^2)}{2k_B T_{\alpha\parallel}} + \frac{m_\alpha}{k_B T_{\alpha\parallel}} GM_J\Big(\frac{1}{r}-\frac{1}{r_0}\Big) + \\ + \Big(1-\frac{T_{\alpha\perp}}{T_{\alpha\parallel}}\Big) ln\Big(\frac{B}{B_0}\Big) - Z_\alpha e \frac{\Delta\phi(s)}{k_B T_{\alpha\parallel}}\Big] \tag{6.1}$$

where m_α is the particle mass, Ω_J the angular rotation of Jupiter, k_B is the Boltzmann constant, $T_{\alpha\parallel}$ and $T_{\alpha\perp}$ are the parallel and perpendicular temperatures respectively, G the gravitational constant, M_J the Jovian mass, r and ρ the distance from the planet center and spin axis respectively, B the magnetic field magnitude, Z_α the atomic number ($Z_\alpha = -1$ for the electrons) , $\Delta\phi = \phi(s) - \phi_0$ the potential drop associated with the ambipolar electric field, s the distance from the centrifugal equator along the field line. The quantities denoted with "0" refer to the centrifugal equator. For the electrons, the centrifugal and gravitational terms (the first two on the rhs of Eq.6.1) can be neglected because of their small mass compared to the mass of the ions. Besides, for species with isotropic temperatures ($T_{\alpha\parallel} = T_{\alpha\perp}$) the mirror force (i.e: the third term on the rhs of

Eq.6.1) can be omitted. The temperature anisotropy of the thermal ions is expected to be $1 \leq T_{\alpha\perp}/T_{\alpha\parallel} < 2$, while the hot ions can exhibit higher values ($3 < T_{\alpha\perp}/T_{\alpha\parallel} < 10$, see Crary et al. (1996, 1998)). Assuming that the electrons have isotropic temperatures, the density of each species can be derived by solving the following system:

$$n_e(s) = n_{e0} exp\Big[e\frac{\Delta\phi(s)}{k_B T_{e\parallel}}\Big] \tag{6.2}$$

$$n_i(s) = n_{i0} exp\Big[\frac{m_i \Omega_J^2(\rho^2 - \rho_0^2)}{2k_B T_{i\parallel}} + \frac{m_i}{k_B T_{i\parallel}} GM_J\Big(\frac{1}{r} - \frac{1}{r_0}\Big) + \\ + \Big(1 - A_\alpha\Big) ln\Big(\frac{B}{B_0}\Big) - Z_i e\frac{\Delta\phi(s)}{k_B T_{i\parallel}}\Big] \tag{6.3}$$

$$n_e(s) = \sum_i Z_i n_i(s) \tag{6.4}$$

where the subscripts e and i stands for electrons and ions respectively and $A_\alpha = T_{\alpha\perp}/T_{\alpha\parallel}$. Eq.6.4 is the condition of charge neutrality, which couples Eq.6.2 and 6.3.

The plasma composition used as reference in the present work is based on the re-analysis of the Voyager 1 data by (Dougherty et al., 2017). The reference value for the electron density n_{e0} at the intersection of the centrifugal equator with the magnetic shell of Io is 2500 cm^{-3}. Eight ion species are included in the model and their densities are computed from the electron density and the ion mixing ratios at 6 R_J: H^+ (1%), O^+(24%), O^{2+}(3%), S^+(7%), S^{2+}(22%), S^{3+}(3%), Na^+(3%) and O^+_{hot}(6%). The electron and ion temperatures are also taken at 6 R_J (5 eV for electrons, 94 eV for protons, 80 eV for O^+, O^{2+}, S^+, S^{2+}, S^{3+} and Na^+, 362 eV for O^+_{hot}). To study different plasma distributions, we compute several electron density distributions derived from equatorial values n_{e0} between 2000 and 3000 cm^{-3} with steps of 250 cm^{-3}. This interval is consistent with previous observations of the IPT (Bagenal and Dols, 2020; Delamere and Bagenal, 2003; Moirano et al., 2021a; Phipps et al., 2021; Thomas et al., 2004), although occasional more extreme cases were detected. The ion density distributions are computed from the above-mentioned mixing ratios, estimated from Voyager 1 (Dougherty et al.,

2017). Past observations of the IPT constrained the ion temperature within a factor 2 (Thomas, 1995); moreover, mass loading events are followed by a temperature increase up to a factor 3 (Delamere et al., 2004). Therefore, we explore different ion temperatures by scaling the Voyager 1 observations at Io's orbit by a factor S_T ranging from 0.50 to 1.50 with 0.25 steps. The thermal ion and electron temperatures are assumed isotropic (Crary et al., 1998), while for the hot oxygen $A_{O^+_{hot}} = 6.5$ (that is: the average of the values reported by Crary et al. (1996)). A summary of the above-mentioned parameters is presented in Table 6.1 (case 1, 2 and 3).

6.1.2 Sensitivity of the Io Footprint Position on the Torus Parameters

The plasma distribution in the Io plasma torus depends on many parameters, according to Eq. 6.2 and 6.3. To properly address the variability of the IFP position, we first need to determine which of these parameters is the most influential. Therefore, in the current section we investigate the sensitivity of the model output to the following parameters: peak electron density n_{e0}, ion temperatures $T_{i\|}$, proton mixing ratio, proton temperature T_{H^+}, temperature anisotropy of the thermal ions, inclusion of the hot oxygen population, temperature anisotropy of the hot oxygen and different mixing ratios of O^+, O^{2+}, S^+, S^{2+}, S^{3+} and Na^+. Additionally, as Io can potentially enter the ribbon region of the IPT when it is near the dawn sector, we test a ribbon-like plasma distribution. The parameters used for the sensitivity test are summarized in Table 6.1 (case 2–11).

In the top panel of Fig. 6.2 we report the one way Alfvén travel time, that is: the time the Alfvén waves take to travel from Io to the North or South hemisphere. The one-way travel time predicted by our reference model (that is: case 1 in Table 6.1) is between 4 and 14 minutes, 1.5 minutes longer than the model of Hinton et al. (2019). This difference may stem from the different magnetic model used in the present work as well as from a different choice for the ion mixing ratios and temperatures. Indeed, the ion temperature shows a sharp drop from 6 R_J inwards: if we use S_T=0.75 in

Table 6.1: Summary of the parameter space investigated with the model described in section 6.1.1. Empty spaces should be referred to case 1.

case	$S_T^{(a)}$	$n_{e0}^{(b)}$	$H^{+(c)}$	$T_{H^+}^{(d)}$	$A_{th}^{(e)}$	$O_h^{+(c)}$	$A_{O_h^+}^{(e)}$	O^+,$S^{+,2+,3+(c)}$	Na^+,$O^{2+(c)}$
1 (*reference*)	1.00	2500	1	94	1	6	6.5	24, 7, 22, 3	3, 3
2*a*	0.50	-	-	-	-	-	-	-	-
b	0.75	-	-	-	-	-	-	-	-
c	1.25	-	-	-	-	-	-	-	-
d	1.50	-	-	-	-	-	-	-	-
3*a*	-	2000	-	-	-	-	-	-	-
b	-	2250	-	-	-	-	-	-	-
c	-	2750	-	-	-	-	-	-	-
d	-	3000	-	-	-	-	-	-	-
4*a*	-	-	0	-	-	-	-	25,-,-,-	-
b	-	-	10	-	-	-	-	21,-,20,-	1,-
5*a*	-	-	-	50	-	-	-	-	-
b	-	-	-	150	-	-	-	-	-
6*a*	-	-	10	50	-	-	-	21,-,20,-	1,-
b	-	-	10	150	-	-	-	21,-,20,-	1,-
7	-	-	-	-	2	-	-	-	-
8	-	-	-	-	-	0	-	30,-,-,-	-
9*a*	-	-	-	-	-	-	1	-	-
b	-	-	-	-	-	-	3	-	-
c	-	-	-	-	-	-	10	-	-
10*a*	-	-	-	-	-	-	-	23,9,23,2	-
b	-	-	-	-	-	-	-	20,11,25,1	-
c	-	-	-	-	-	-	-	25,5,21,4	-
d	-	-	-	-	-	-	-	28,3,19,5	-
11	0.50	3000	0	/	-	0	/	42,26,16,0	0,0

[a] The ion temperatures are reported in term of the scaling factor S_T (see section 6.1.1).
[b] Electron density in cm^{-3}.
[c] The abundance of the ions are in mixing ratio percentage $\frac{n_\alpha}{n_e} \cdot 100$.
[d] Temperature, in eV.
[e] Anisotropy $A_\alpha = T_{\alpha\perp}/T_{\alpha\parallel}$. A_{th} is for the thermal ions, $A_{O_h^+}$ for the hot oxygen.

our model, this improves the agreement with the results from Hinton et al. (2019), the difference between the two models being 0.7 minutes.

The percent difference of the Alfvén travel time obtained from cases 2–10 with respect to the reference Case 1 is reported in the bottom panel of Fig. 6.2. To compute the percentage, we first compute the travel time t_{ref}, with Io at 290° longitude (i.e., approximately in the centrifugal equator) for the reference model, and the travel time t, obtained by changing one parameter at a time. Then the percentage is obtained from $(t_{ref} - t)/t_{ref}$. Hence a positive/ negative percentage represents a faster/slower travel time.

Case 2 *Ion Temperature Scaling*. We scale the ion temperature by a factor S_T between 0.50 and 1.50, which changes the Alfvén travel time between +20% and -15%. Indeed, changes in the temperature affect the size of the Io plasma torus, therefore by increasing/decreasing the temperature at a constant peak density n_{e0}, the total plasma content along the magnetic field lines increases/decreases as well. Consequently, the Alfvén travel time is reduced/increased.

Case 3 *Peak Electron Density*. The electron density at the centrifugal equator n_{e0} is varied between 2000 and 3000 cm^{-3}, which correspond to a time travel variation between +10% and -10%. This is not surprising, as the Alfvén speed depends on the reciprocal of the square root of the ion mass density, which is proportional to the electron density and the ion mixing ratios. Therefore lower/higher density implies faster/slower Alfvén waves.

To understand why changes in S_T and n_{e0} produce a similar effect on the Alfvén travel time t_A, we can estimate t_A from the simple geometry of Fig. 6.1. Assuming uniform magnetic field B_0, mass density $\rho_0 = constant > 0$[3] in the IPT and $\rho_0 = 0$ outside, the travel time is given by

$$t_A = \int_{s_{Io}}^{s_{iono}} \frac{ds}{v_A} = \int_{s_0}^{s_{iono}} \frac{\sqrt{\mu_0 \rho(s)}}{B(s)} ds \approx \frac{\sqrt{\mu_0 \rho_0}}{B_0} \Delta L \qquad (6.5)$$

[3]Not to be confused with the cylindrical radius in Eq. 6.3.

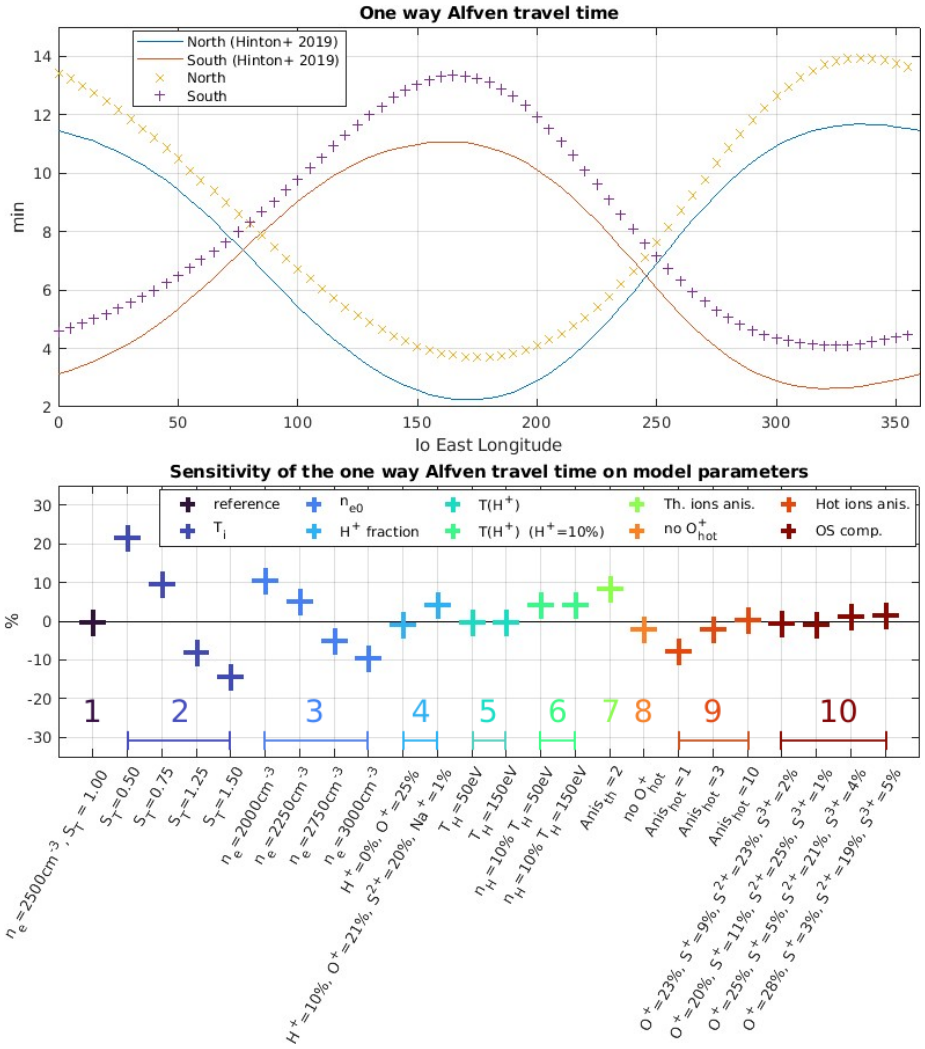

FIGURE 6.2: *Top*: One way Alfvén travel time predicted by the Voyager 1-based case 1 of Table 6.1 from Io to the North (orange crosses) and South hemisphere (purple pluses), respectively. The blue and red lines are the travel times reported by Hinton et al. (2019). *Bottom*: sensitivity of the one way Alfvén travel time calculated when Io is close to the centrifugal equator in the warm torus at System III longitude 290°. The numbering from 1 to 10 points to the cases in Table 6.1 and the labels on the x axis briefly specify the values used for the test. The percentage represents how much faster the Alfvén wave travels compared to the reference, therefore a positive/ negative value implies a shorter/longer travel time. Retrieved from Moirano et al. (2023).

where ΔL is the distance traveled by the Alfvén wave in the region where $\rho_0 > 0$, s_{Io} and s_{iono} are the positions of Io and the planetary ionosphere along a magnetic field line respectively. ΔL can be expressed in terms of the thickness of the IPT (H in Fig. 6.1), which in turn depends roughly on the square root of the ion temperature (Bagenal and Sullivan, 1981), hence: $\Delta L \sim H \sim \sqrt{T_i}$. Therefore we obtain

$$t_A \propto \sqrt{\rho_0 T_i} \tag{6.6}$$

which explains why the travel time increases or decreases with both density and temperature. Because the position of the footprint is determined by t_A, there is a degeneracy between n_{e0} and S_T. This can be seen by looking at the parameter space derived for PJ 10–31 and PJ 11–32 in Fig. 6.3, where we report the values of n_{e0} and S_T that predict the MAW spot position within 250 km from the JIRAM observations (this value is approximately half the longitudinal size of the MAW spot). The regions of the parameter space compatible with the observations have an hyperbolic shape, which agrees with Eq. 6.6.

Case 4 *Proton Mixing Ratio*. Due to the light mass of the protons compared to the sulfur and oxygen masses, protons are not expected to considerably affect the Alfvén speed within the IPT. Nevertheless, at high latitude, where heavy ions are almost absent, protons dominate the plasma density. The proton abundance in the torus is 1%–10% (Bodisch et al., 2017; Delamere et al., 2005; Nerney and Bagenal, 2020), hence we increase their mixing ratio to 10% (case 4b). In order to preserve charge neutrality, we have to decrease the mixing ratios of O^+, S^{2+} and Na^+ (see Table 6.1 and the labels in Fig. 6.2 for the quantitative details). Besides, we also completely remove the protons to investigate the role of their presence (case 4a), although there is no observational evidence of a complete hydrogen depletion in the IPT. By removing the protons from the ion species, t_A decrease by less than 1%, while by increasing their mixing ratio to 10%, t_A increases by about 4%. This changes are not due to the variations of the proton mixing ratio itself,

but rather to the adjustment made to the other mixing ratios. Indeed, the Alfvén speed in the high latitude magnetosphere is still a large fraction of the speed of light even for a 10% proton mixing ratio and the Alfvén waves spend a few tens of seconds in the low density region between the IPT and the Jovian ionosphere.

Case 5 and 6 *Proton Temperature*. To determine the role of the spatial distribution of H^+, we test a proton temperature of 50 and 150 eV, which approximately corresponds to the scaling of the reference value 94 eV by S_T=0.5 and 1.50, respectively. The resulting t_A is the same as the one obtained with the reference temperature of 94 eV within 10^{-5}%. In order to amplify any possible effect on t_A, we also tested the same temperatures with a 10% proton mixing ratio: the travel time changes by only ∼0.05% with respect to the case with the same mixing ratio at T_{H^+}= 94 eV. Indeed, protons are loosely confined by the centrifugal force because of their light mass and thus they spread quite uniformly along the magnetic field lines. Therefore, changes in their temperature affect very little their distributions.

Case 7 *Temperature Anisotropy of the Thermal Ions*. We set A_i= 2 in Eq. 6.1, according to the results reported in Crary et al. (1996), to determine the effect of the magnetic mirror force confinement on the thermal ions. This value reduces t_A by about 9%. Indeed, the confinement reduces the size of the IPT, hence the total plasma content along the field lines decreases as well, reducing the Alfvén travel time.

Case 8 and 9 *Presence of Hot O^+ and its Temperature Anisotropy*. In situ measurement of the IPT revealed the presence of O^+ ions with a temperature of ∼400 eV Dougherty et al. (2017). To probe the effect of such population on the position of the IFP, we compared the reference model against a model with only thermal oxygen (Case 8). This increases t_A by less than 2%. Indeed, the distributions of the hot and thermal oxygen populations have a typical thickness of ∼2 R_J and they peak at about 0.3 R_J from each other along the magnetic field lines, as they

are confined near the magnetic and centrifugal equator, respectively. Therefore, they largely overlap and the case with no hot oxygen has a similar mass distribution as the reference model. To assess the importance of the magnetic mirror force confinement, we test the case $A_{O^+_{hot}} = 1$ (isotropy, case 9a), $A_{O^+_{hot}} = 3$ (low anisotropy, case 9b) and $A_{O^+_{hot}} = 10$ (high anisotropy, case 9c). The first case is used to determine the effect of the inclusion of anisotropy in Eq. 6.1, while the other two test the lower and upper limit on the anisotropy reported by Voyager 1 (Crary et al., 1996). The changes of t_A are -8%, -2% and +0.5%, respectively. In the case of isotropic temperature, the hot oxygen distribution is broadly distributed along the field lines, and it is the dominant species by density at high latitude. Thus, the Alfvén waves are slower at high latitude with respect to the reference case and the travel time is longer. The cases with low and high anisotropy are quite close to the reference, which suggest that the position of the IFP is little sensitive on the precise value of $A_{O^+_{hot}}$. Nevertheless, the inclusion of the temperature anisotropy of the hot oxygen is relevant for proper modeling (i.e., $A_{O^+_{hot}} > 1$ in Eq. 6.3).

Case 10 *Mixing Ratios of O^+, S^+, S^{2+} and S^{3+}*. The azimuthal distribution of O^+ and S^{2+} in the IPT fluctuates by 2%–5%, depending on the relative phase between System III and System IV (Hess et al., 2011b; Steffl et al., 2008), while for S^+ and S^{3+} the fluctuations are 5%-25% (Steffl et al., 2006). Besides, the mixing ratio of S^+ is correlated with the mixing ratio of S^{2+}, while it is anti-correlated with O^+ and S^{3+}. We test two different set of the O^+, S^+, S^{2+} and S^{3+} mixing ratios that are roughly compatible with the amplitude variations associated with System IV (Case 10a and 10c). Besides, we test two arbitrarily large variations of O^+ correlated with S^{3+} and anticorrelated with S^+ and S^{2+}(Case 10b and 10d). These are not supported by observational or modeling evidences and they are included for the sole purpose of the sensitivity test. In all the above-mentioned cases the variation of t_A is smaller than 2%. The most abundant sulfur ion (i.e., S^{2+})

has the same charge-to-mass ratio as the most abundant oxygen ion (i.e., O^+), hence, for the same electron density, the total mass in the IPT changes mostly due to the variation in the S^+ and S^{3+} Therefore, the change of t_A caused by the increase/decrease of the O^+ and S^{3+} mixing ratios is compensated by the decrease/increase of the S^+ and S^{2+} mixing ratios.

Case 11 *Ribbon*. The ribbon exhibits higher electron density and a slightly lower temperature than the warm torus, as well as considerably different mixing ratios. To test the potential effect of the ribbon on the MAW spot position, which might occur when Io is near the dawn sector, we set n_{e0}= 3000 cm^{-3} and S_T= 0.5 (Bagenal and Dols, 2020), while for the mixing ratios of the major ions O^+, S^+ and S^{2+} we used 42%, 26% and 16%, respectively (Bagenal, 1994). The travel time in this case is 5% longer than the reference case (not shown in Fig. 6.2). This suggest that a longer t_A from the IFP observations near the dawn sector could be explained by the ribbon occurring near Io's orbit. In the present study, we do not aim at deriving the plasma parameters at the ribbon, which has its own parameter space to be tested and investigated. Nevertheless, a relatively high density derived near the dawn sector in the present study might be interpreted as the ribbon approaching Io's orbit.

6.1.3 Data-Model Comparison

Following the results of the sensitivity test, the results of the model of section 6.1.1 are compared with the position of the IFP observed by JIRAM. The focus will be on the peak electron density n_{e0} and the ion temperature through the scaling factor S_T, as they are the most sensitive parameters. The temperature anisotropy is also a relevant parameter for both the thermal and hot ion populations. Nevertheless, its value is poorly determined from the literature. Besides, the diffusive equilibrium model give by Eq. 6.2-6.4 is based on the assumption of constant temperature along the field line, while

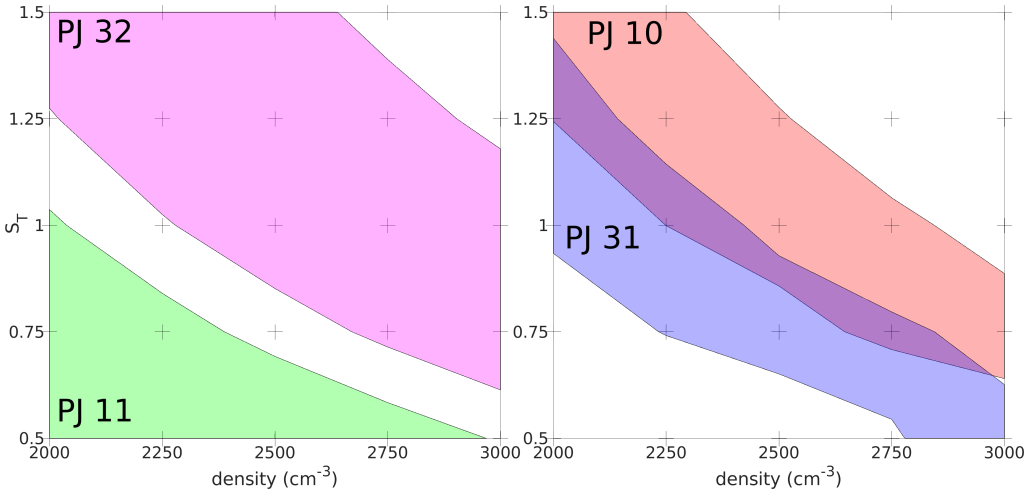

FIGURE 6.3: Parameter space obtained from the JIRAM observations of the IFP during PJ 11 and 32 (left side) and PJ 10 and 31 (right side). The colored areas represent the parameter spaces in agreemen with the MAW spot position within 250 km for each observation. Retrieved from Moirano et al. (2023).

it likely increases at high latitude (Thomas and Lichtenberg, 1997). Thus, the temperature anisotropy may also change along the magnetic field lines. Lastly, including an anisotropy $A_{O^+_{hot}} > 1$ in Eq. 6.3 is more important than a precise value for $A_{O^+_{hot}}$. For these reasons, we decided to postpone an in-depth analysis of the anisotropy effect on the IFP position to a future work, which potentially can include the latitudinal variation of the temperature. Here, we assume that the temperature of the thermal ions is isotropic, while for the hot oxygen $A_{O^+_{hot}} = 6.5$. Each image of the footprint is compared to the location of the footprint calculated from n_{e0}= 2500 cm^{-3} and S_T= 1.00, which serves as the Voyager 1-based reference, and we test different values for the density and for the temperature, as explained at the end of section 6.1.1. In Fig. 6.3 we show the parameter spaces compatible with the observed positions of the MAW spot within 250 km (i.e., the distance between the observed and predicted position of the spot is less than 250 km). In the case of PJ 11-32, the parameter spaces are not compatible, PJ 11 preferring lower temperatures and densities than PJ 32. The parameter space of PJ 10 covers slightly higher temperatures and densities than PJ 31,

but the two spaces are marginally compatible.

Fig. 6.4 shows the JIRAM observations performed during PJ 10–31 (panel a) and 11–32 (panel b), when the TEB spot was upstream of the MAW spot. We superimpose colored pluses and crosses that represent the modeled positions of these two auroral features to the images, according to different values of the electron density and the ion temperature. To highlight the respective role of the density and the temperature, we show the predicted position of the MAW spot by varying only one parameter at a time from the reference case. The position of the MAW and TEB spots predicted by the Voyager 1 values are represented by asterisks. In panel a Io was at the same longitude ϕ_{Io}= 205.2°, but the images show that the MAW spot of PJ 31 was at a higher longitude by ∼1° than PJ 10. This displacement corresponds to about 300 km on the surface of Jupiter. The emission angle was ∼10° in both cases, therefore the error associated with the emission altitude of 6004±100 km translates to an uncertainty on the position of the MAW of less than 20 km along the track of the IFP. Hence, it is unlikely that the displacement between the images results from the uncertainty of the altitude of the emission. By comparing the modeled position of the MAW spot in the left column of panel (a) in Fig. 6.4 (colored pluses), we conclude that the best match corresponds to the ion distribution obtained from an electron density of about 2500-27550 cm^{-3} for PJ 10 and 2000-2250 cm^{-3} for PJ 31, while the best match temperature (right column) is determined by S_T= 1.00–1.25 and 0.75 respectively. During the PJ 11 and 32 observations shown in panel (b) of Fig. 6.4, Io was at 169.4° and 170.8° longitude, respectively. The position of the MAW spot differs by less than 100 km in the two images; besides, it is clear that the distance between the tip of the TEB and the MAW in each image is remarkably different in the two orbits (∼1000 km and ∼1700 km, respectively). The emission angle for PJ 11 was ∼20°, which translates to an uncertainty of less than 40 km on the IFP position, while for PJ 32 the angle was ∼5°, corresponding to an uncertainty smaller than 10 km. This noticeable morphological difference is reflected in the model prediction: the electron density of PJ 11 was likely smaller than 2000 cm^{-3}, while for PJ 32 it is significantly different at $n_{e0} \approx$

Table 6.2: Summary of the best-match electron density and ion temperature for PJ 10, 11, 31 and 32.

PJ	ϕ_{III}(deg)	Io local time (hh:mm)	n^a_{e0} (cm^{-3})	S^b_T
10	205.2	02:07	2500-2750	1.00-1.25
31	205.2	08:17	2000-2250	0.75
11	169.4	22:37	<2000	0.50
32	170.8	04:47	2750	1.25

[a]The ion densities assume $S_T = 1.00$.
[b] The ion temperatures scaling factor assume $n_{e0} = 2500$ cm $^{-3}$.

2750 cm^{-3}. The best fit scaling factor for the temperature during these two orbits is S_T= 0.50 and 1.25 for PJ 11 and 32, respectively. In Table 6.2 we summarize the results of the present section for PJ 10-31 and 11-32.

6.1.4 Comparison with Previous Missions

The density and temperature of the IPT were previously constrained mainly by spectroscopy from both Earth-based facilities (e.g.: Schmidt et al. (2018)) and in-situ missions (e.g.: Steffl et al. (2008)). Additional sources of observations are radioccultations (e.g.:Bird et al. (1993)) and direct particle measurements (e.g.: Bagenal and Sullivan (1981)). In the following, we show how the results obtained from the IFP position compare with those from other measurements.

- *Voyager 1*. The ion plasma composition of the inner magnetosphere of Jupiter measured by the Voyager 1 Plasma Science instrument (PLS) re-analyzed by Dougherty et al. (2017) is the reference point of the present analysis, therefore it is a straightforward comparison with the Juno-JIRAM measurements. The electron density we report in Table 6.2 differs by about ±250 cm^{-3} with respect to the Voyager 1 value of 2450 cm^{-3} at 6 R$_J$, except during PJ 11, when the best fit density was smaller than 2000 cm^{-3}. The temperature measured by Voyager 1 steeply increases from 2-3 eV to ∼80 eV between 5 and 6 R$_J$. The temperature used in the reference model is the one measured by Voyager at 6 R$_J$, which might overestimate the value at 5.9 R$_J$ by

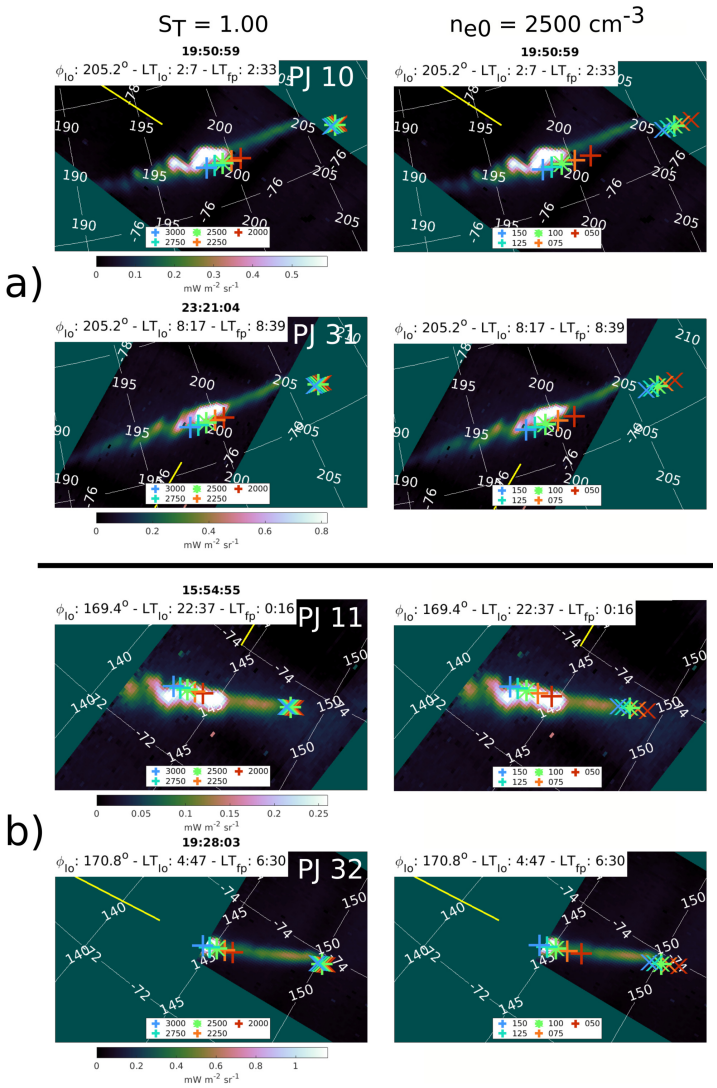

FIGURE 6.4: Comparison between JIRAM data and the model of section 6.1.1 for PJ 10–31 (panel a) and PJ 11–32 (panel b). The pluses and the crosses represent the predicted position of the MAW and TEB, respectively. The position of the MAW and TEB for the reference model (n_{e0}= 2500 cm^{-3} and S_T= 1.00) is represented by asterisks. The yellow line is aligned with the MAW-Sun direction. The left column shows the predicted position of the MAW and TEB spots for n_{e0} between 2000 and 3000 cm^{-3} for constant S_T=1.00, while the right column the prediction for S_T between 0.50 and 1.50 for n_{e0}= 2500 cm^{-3}. UTC time is reported in the titles in the left column, while Io System III longitude and local time of both Io and the IFP are reported in each figure. Retrieved from Moirano et al. (2023).

∼10 eV. The best fit temperature in the present analysis corresponds to a temperature scaling factor S_T between 0.75 and 1.25, except for PJ 11, whose best match is S_T= 0.50. Therefore, the IPT density variations inferred from the IFP position in JIRAM data is about 10% the density measured by Voyager 1, while the temperature changes by about 25%.

- *Voyager 1, Voyager 2 and Cassini*. Delamere and Bagenal (2003) investigated the variability of the IPT using a chemistry model that depends on the radial transport time, the source of neutral particles, the oxygen-to-sulfur ratio and the fraction and temperature of the hot electrons. Their results were then compared with observations of the IPT performed by Voyager 1, Voyager 2 and Cassini. They found remarkable differences in the torus properties between those missions: the electron density was 1800-2200 cm^{-3} for Voyager 1, 2600–3400 cm^{-3} for Voyager 2 and 1700–2000 cm^{-3} for Cassini. The density we derived from PJ 10, 11, 31 and 32 are compatible with these values for the different epochs. The density of PJ 10 and 32 is compatible with the density observed during Voyager 2, the density of PJ 31 with the observations of Voyager 1 and the density of PJ 11 with the measurements of Cassini. It is interesting that the IPT might have lost 25%, and potentially more, of its electron density from PJ 10 to PJ 11 in only ∼50 days. Nerney and Bagenal (2020) used a chemistry model to investigate the plasma properties of the IPT and compared the expected spectral emission with the observations made by Cassini-UVIS. The electron density in that work is ∼1900 cm^{-3}, while the ion temperature is 60-70 eV for S^{2+}, S^{3+}, O^{+} and O^{2+} (corresponding to S_T ∼0.75 in the present model), ∼100 eV for S^{+} (corresponding to S_T ∼1.25) and ∼90 eV for the protons. Therefore, the electron density and temperature we obtained for PJ 11 and 31 suggest that the IPT was in a state similar to that observed during the Cassini epoch rather than during the Voyager 1 and Voyager 2 epochs.

- *Juno*. The Juno spacecraft performed several radio occultations of the IPT and thus it has been able to probe directly the *total electron content* (TEC) between the spacecraft and the ground station (see section 6.3 for more details on the radio occultations), thus they can be used to determine the electron content of the IPT. By analyzing the radio occultations from PJ 1 to 15, Phipps et al. (2021) reported that the maximum TEC of the warm torus is 24 hexem on average (1 hexem = 10^{16} electrons m^{-2}) and varies between 17 and 29 hexem. Moirano et al. (2021a) analyzed the radio occultations from PJ 1 to 25, assuming that the radial density distribution of the warm torus outside 5.5 RJ can be modeled by a Gaussian profile $Nexp\Big[-\frac{(r-R)^2}{W^2}\Big]$, with R = 5.7 R$_J$ and W=1.5 R$_J$, while N is a free parameter for the peak electron density. The electron density reported in that analysis is ∼2500 cm^{-3} on average, with variations between 1400 cm^{-3} and 3400 cm^{-3}. These large variations in electron density based on Juno radio occultations are roughly compatible with the different torus conditions observed during Voyager 1 (∼2000-2500 cm^{-3}), Voyager 2 (∼2600-3400 cm^{-3}) and Cassini (∼1700-2000 cm^{-3}) (Delamere and Bagenal, 2003). The electron density reported in the present study is between less than 2000 cm^{-3} and 2750 cm^{-3}, in agreement with the results from the radio occultations. More specifically, the radio occultation during PJ 11 showed a remarkably low electron density compared to other orbits, while the torus appeared slightly thicker (Moirano et al., 2021a; Phipps et al., 2021). This suggests that the position of the IFP of PJ 11 in panel (b) of Fig. 6.4 may be explained by a density depletion rather than a temperature drop. PJ 11 showed evidence of strong magnetospheric activity, which was detected by the Juno magnetometer as a high number of reconnection events associated with plasmoid ejection in the magnetotail (Vogt et al., 2020). At the same time, both Juno and HST reported a dawn storm (Bonfond et al., 2021; Nichols et al., 2020), which are usually associated with large scale magnetotail reconfigurations, but not the global main auroral brightening typically associated with a solar wind compression

(Yao et al., 2022). On the other side, Huscher et al. (2021) reported particularly low density in the middle magnetosphere during PJ 12, but not during PJ 11, for which they do not record any remarkable feature. A comprehensive analysis of the above-mentioned datasets to determine the timeline of events of PJ 11 is not tackled in this thesis, but the position of the IFP can be used as an additional piece of evidence to pursue that goal.

- *Hisaki and Cassini*. The IPT response to strong mass loading events was studied using the Cassini fly by during the period October 2000 - March 2001 (Delamere et al., 2004) and Hisaki monitoring from 2013 to 2015 (Yoshioka et al., 2018). By using the Cassini-UVIS measurements, Delamere et al. (2004) concluded that the electron density initially decreased from 2500 cm^{-3} to 2200 cm^{-3} in about 25 days, and it increased up to 2700 cm^{-3} in the next ∼75 days. At the same time, the ion temperature increased from ∼50 eV to ∼110-140 eV in about 30 days and then it fell back to the pre-event value in the following 30 days. Yoshioka et al. (2018) compared the Hisaki-EXCEED spectroscopic observations during a low-mass loading period (November 2013) with the measurements of a period of high loading (February 2015). The evolution of the brightness of the torus detected by Hisaki was similar to the one observed by Cassini, so they suggested that there was a similar trigger (that is: a major volcanic outburst) in 2000 and 2015. The electron density estimated during the February 2015 event is 2860±260 cm^{-3}, to be compared with the density of the quiet period in November 2013 of 2350±340 cm^{-3}. The brightness enhancement in 2015 lasted for about 3 months, and then it came back to the quiet period level. The density increases observed by Cassini and Hisaki are similar to the electron density found for PJ 32 and marginally for PJ 10. Major volcanic outbursts such as the ones in 2000 and in 2015 are expected to be quite rare, approximately one every ∼5-10 years, even though our knowledge of the frequency of such events is affected by the impossibility of continuous monitoring

of Io and the torus. Besides, there are no report of such events since the arrival of Juno at Jupiter. Therefore, it appears unlikely that the density reported for PJ 10 and 32 was caused by one of these events.

6.1.5 Source of Variability

As discussed in section 2.1, the IPT exhibits different types of variability, that is, System III and System IV variations, temporal variations and local time variability (Bagenal and Dols, 2020). This classification is rooted in the underlying physical processes that drive each type of variability, but there is a mutual influence. For example, mass loading into the IPT can cause a radial displacement of the torus barycenter (Brown and Bouchez, 1997) - thus increasing the dawn-dusk asymmetry - as well as a change in the System IV periodicity (Tsuchiya et al., 2019). System III and System IV modulations create a beat that can be detected in the UV brightness (Steffl et al., 2006). In this section, we discuss each type of variability separately for sake of clarity - bearing in mind the above-mentioned interplay - to explain how the torus variability can affect the IFP and what types of variations are compatible (or detectable) using footprint position. For the cases presented in Fig. 6.4, System III variability can be ruled out, as the observations were performed within a few degrees longitude.

- *System IV Variability*. System IV variability is difficult to infer from the present data set. In the sensitivity test of section 6.1.2 we tested different ion compositions of the IPT that are correlated with System IV periodicity. The increase of O^+ and S^{3+} at the expense of S^+ and S^{2+} causes a slight decrease of the Alfvén travel time, while t_A increases in the opposite case. Nonetheless, these changes affect the Alfvén travel time by less than 2%, which implies that the position of the IFP in these cases differs by ∼30 km with respect to the position predicted by the reference model. This difference is smaller that the difference in the IFP position observed by JIRAM during PJ 10-31 and 11-32 in Fig. 6.4. Therefore, we suggest that System IV variability has a negligible effect on the position of the IFP.

- *Local Time Asymmetry*. The ribbon region of the torus is located at a radial distance from the spin axis of the planet of 5.56±0.07 R_J on the dusk side and 5.83±0.06 R_J on the dawn side (Schmidt et al., 2018; Schneider and Trauger, 1995; Smyth et al., 2011). The uncertainty represents the System III modulation of the dawn-dusk asymmetry. The ribbon is ∼0.2 R_J wide and has a similar vertical extension as the warm torus, but its density is as high as ∼3000 cm^{-3} and it consists mainly of O^+, S^+ and S^{2+} Bagenal and Dols (2020). As explained in section 2.1, the torus dawn-dusk displacement is usually explained by the presence of a dawn-dusk electric field, which depends on the magnetic field as well as the plasma flow in the magnetotail (Barbosa and Kivelson, 1983) and it might be affected by their dynamics and variability (e.g.: Kennel and Coroniti (1977); Murakami et al. (2016)). Therefore, the dawn-dusk asymmetry could be increased or reduced by changes of the plasma flow in the magnetotail. Moreover, the direction of the electric field appears to be tilted with respect to the dawn-dusk direction by 15-20° (Sandel and Broadfoot, 1982; Smyth et al., 2011), which corresponds to 7-7:20 and 19-19:20 hr in local time, instead of at 6 and 18. For each set of observations in Table 6.2 and Fig. 6.4, one image was acquired near the dawn sector between 04:47 and 08:17 local time (i.e.: PJ 31 and 32). Nevertheless, those observations do not always correspond to a density increase with respect to the corresponding images taken at the same longitude, which might suggest that Io did not entered the ribbon. Indeed, during PJ 31 (08:17 local time) the best fit density was lower compared to PJ 10 (02:07 local time). On the other hand, PJ 32 (04:47 local time) showed a remarkable density increase compared to PJ 11, which occurred at 22:37 local time. Another interpretation of this results might lie in the variability of the ribbon itself. For example, the Plasma Wave Subsystem onboard Galileo reported no signs of the presence of the ribbon along the J0 flyby in December 1995 (Bagenal et al., 1997); instead, the electron density in the same region was only a few hundreds cm^{-3} at the typical location of the ribbon, while the electron density at Io orbit

was surprisingly large (∼4000 cm^{-3}). The hypotheses proposed at that time was that either the ribbon was not present or that Io was located in the ribbon at the time of the J0 flyby. The n_{e0} obtained from PJ 10 and 31 suggests that the ribbon was not present at the time of the PJ 10 observations and that Io was in a transition region between the warm and cold torus. Additionally, the supply of material from the torus to the magnetosphere can affect the plasma flow in the magnetotail and, hence, the dawn-dusk electric field. It was observed that the dawn sector of the IPT shifts dawnward by ∼0.3 R_J during periods of increased IPT mass (Brown and Bouchez, 1997), but the dusk sector remains in place. This effect might have displaced the dawn sector more dawnward during PJ 32 than PJ 31, so that Io was orbiting within the ribbon at that time; nevertheless simultaneous observations of the IPT are needed to confirm any mass loading events. Furthermore, based on brightness observations of the IPT by Hisaki, it was suggested that a solar wind-driven compression of the Jovian magnetosphere can increase the dawn-dusk field, hence shifting the IPT dawnward by ∼0.2 R_J (Murakami et al., 2016), although this shift could not be measured simultaneously by Hisaki itself. The reliability of solar wind propagation models based on near-Earth measurements decreases near solar conjuction (Zieger and Hansen, 2008) and, at the time of the JIRAM observations reported here, the *Jupiter-Sun-Earth* (JSE) angle was -155°, -100°, 145° and 180° for PJ 10, 11, 31 and 32 respectively. Besides, the uncertainty on the timing of compression events from these propagation model is ∼15 hr during opposition, and rapidly increases with the JSE angle. This, with the limited data set used in this work, prevents a statistical analysis to potentially correlate the solar wind variations with the IPT. Lastly, the density does not increase monotonically from the warm torus to the ribbon. For example, in Fig. 6 of Dougherty et al. (2017), the data shows a small dip of a few hundreds cm^{-3} between the two regions (called *"the gap"* (Herbert et al., 2008)), which could be consistent with the results in Table 6.2.

- *Temporal Variability*. If the other types of variability can be quite confidently excluded - such as System III and IV in the previous part of this section - or less confidently - such as local time asymmetries - the only other source of variability may lay in the temporal variability of the IPT and its mass loading. Indeed, in principle any variation in the supply of material into the IPT can affect its density and temperature (e.g.: Delamere et al. (2004); Yoshioka et al. (2018)), which in turn affect t_A in Eq. 3.32 and thus the position the MAW spot. The loading can be caused by internal or external sources. "Internal sources" means that the plasma comes from the local interaction between Io, the neutral cloud along its orbit and the magnetospheric environment, while a driving mechanism that lies outside the plasma torus can be referred to as an "external source". The volcanic activity on Io is the ultimate internal source. The various types of hot spots (Lopes and Williams, 2015) on Io's surface eject material (such as Na, NaCl, SO_2, SO and K) that likely do not directly contribute to plasma loading and scatters in Io atmosphere. SO_2 is the dominant species in the atmosphere of the satellite, and it is sustained by either sublimation from the surface or by direct volcanic input (Roth et al., 2020). Both the atmosphere and the ionosphere interact with the plasma environment, providing S and O atomic neutrals - mainly by impact dissociation - and ions - mainly by electron impacts and by charge-exchange reactions (Bagenal and Dols, 2020). Due to the challenge of a continuous and simultaneous observation of the IPT, the neutral cloud and Io (both its atmosphere and its hot spots), there are still no definitive evidence on the mechanism driving the interplay between the variable volcanic activity observed on Io (e.g.: de Kleer et al. (2019); de Pater et al. (2017)), its atmosphere and the mass loading into the magnetosphere (Roth et al., 2020). More evidence are expected in the future, thanks to Earth-based monitoring (Morgenthaler et al., 2022b) and from Juno dust observations (Jørgensen et al., 2020). As an external source, it was suggested that a global reconfiguration of the Jovian magnetosphere might drive injections of

electrons from the middle and outer magnetosphere toward the inner magnetosphere (Louarn et al., 2014). These injections might affect the temperature and density of the IPT, and thus the local interaction at Io, ultimately determining the neutral supply and eventually the torus plasma loading—at least partially (Morgenthaler et al., 2022a). Unfortunately, no clear evidence or in-depth studies of this process are currently available. Given the complexity and the uncertainty on the above-mentioned processes, relying only on the footprint positions reported in this work to determine mass loading events appears overly ambitious. Nevertheless, the images shown in Fig. 6.4 show evidence of variability in the plasma environment around Io. Therefore the auroral imaging of the IFP can help to reconstruct the timeline of the mass loading (or depletion) events that can occur in the IPT.

6.1.6 Conclusions

The present section represents the first attempt to constrain the plasma distribution along magnetic field lines crossing the *Io Plasma Torus* (IPT) and its variability by analyzing the auroral footprints of Io in the Jovian ionosphere. This is possible thanks to the unique vantage point offered by Juno's polar orbit, together with the high spatial resolution of the JIRAM instrument onboard the spacecraft. Deriving quantitative information on the plasma torus and its variability from the Io footprint position can help complement Earth-based and in-situ observations that aim at understanding the complex interplay between Io, the IPT and the Jovian magnetosphere, especially regarding the changes in plasma supply within the torus. The variations of the properties of the IPT can be classified into four main types, namely: System III and System IV variations, local time asymmetry and temporal variations. In the present work, System III variations are not addressed by choosing images with similar longitudinal position of Io. In order to study the other types of variability, we determine the location of the auroral footprint by calculating the travel time for an alfvénic pertubation produced at Io to reach the Jovian ionospheres. The path traveled by the

alfvénic perturbations and the position of the Io footprint depend on both the geometry and strength of the magnetic field and the plasma distribution along the field lines. Hence, we adopted a reverse approach: using the observed position of the Io footprint to determine the state of the IPT at different epochs. The Alfvén travel time is computed using the recent JRM33 magnetic field model based on Juno's observations (Connerney et al., 2022) and a prescribed plasma density distribution along the field lines (Dougherty et al., 2017). After the sensitivity tests in section 6.1.2, we describe the plasma distribution along the field lines with two main parameters, that is: the ion average temperature and the equatorial electron density. Although density and temperature are degenerate parameters in the present analysis (see Eq. 6.5), the parameter spaces that best match the JIRAM observations shown in Fig. 6.4 do not overlap (see Fig. 6.3): this suggests the plasma environment around Io changes independent of the System III longitude. We tested different mixing ratio of O^+, S^+, S^{2+} and S^{3+} to investigate the sensitivity of the model, and we found that variations of the these mixing ratios correlated with System IV variability have little effect on the position of the footprint. Therefore, it is unlikely that the variability detected in the JIRAM images was caused by the System IV periodicity. Moreover, we are not able to unequivocally determine if the variations of the Io footprint position are caused either by a local time asymmetry or by the temporal variability of the Io torus. Nevertheless, we can constrain the parameter space of the IPT by fitting the position of the Io footprint: this technique can thus be used to support the investigation on the interplay between Io, its torus and the magnetosphere.

6.2 The Tracks of the Io, Europa and Ganymede Footprints

The method explained in section 6.1 is validated by a limited number of JIRAM images, as shown in Fig. 6.4 and Table 6.2. Indeed, the dataset used for the analysis presented in section 6.1 has been selected according to

three criteria (as explained in that section), the most restrictive one being taking the observations with Io at nearly the same System III longitude over different orbits. Therefore, the System III variability of the IFP was ruled out, and the IFP position was used to investigate other, less known variabilities. This approach has proved both the possibility to detect variations in the IFP position with Juno-JIRAM and to derive quantitative results from those data. The next step is gathering the full database of the IFP observations to be used to derive a global monitoring of the IPT during the Juno mission. JIRAM has been able to observe the auroral footprint of Europa and Ganymede as well, which in principle can be used to perform a similar analysis the one presented in section 6.1, hence their position have also been collected. The analysis of the plasma environment at Europa and Ganymede from their footprints has not been performed yet; nevertheless, they are reported in the present section, as the inspection of the database made by the footprint position of the three moons is used for secondary - but fundamental - analyses. Moreover, the present section uses the same analysis method for the three footprints, hence gathering only the IFP data would have represented a probable waste. The availability of the dataset presented in this section is also relevant for complementing the in-situ particle an field measurements that Juno has been performing during the flybys of the satellites, and all the observations that can be used to derive information about the environment of the moons are crucial to support future missions, such as Juice and Europa Clipper, which will focus on the Jovian moons. Moreover, the results here presented will help to test the reliability of magnetic field models by comparing JIRAM observations with the foot of the magnetic shell of Io, Europa and Ganymede predicted by such models. Lastly, the MAW spot can be a reference for calibrating Earth-based observations: this will help to better determine the position of the aurorae observed from near Earth, hence improving the quality of the analysis based on those data.

It's worth mentioning that, despite the six years of data gathered by JIRAM and the multple detection of the Io, Europa and Ganymede footprints, there has been no clear evidence of the Callisto footprint so far. This

is not surprising, as the electron precipitation associated with Callisto is expected to be far weaker than the precipitation due to the other three Galilean moons (Saur et al., 2013); moreover, Callisto footprint would be observed very close or overlapping the main emission, whose brightness likely outshine the auroral emission due to Callisto. For this two reasons, the detection of the Callisto footprint is much more challenging than the other three moons, even with an high-resolution in-situ imager like JIRAM, and at present day we report no observations from the Juno mission.

6.2.1 The JIRAM Database and Fitting Procedure

We survey the observations performed since PJ 1 on August 27^{th} 2016 until PJ 42 on May 23^{rd} 2022, and we used a 2D peak-finder routine (Natan, 2021) to determine the position of the emissions. For the MAW spots, we gathered 259 images for Io (130 north, 129 south), 127 for Europa (54 north, 73 south) and 234 for Ganymede (95 north, 139 south). This initial dataset was then reduced to account for batches of images that show the same MAW spot in the same sequence. Indeed, thanks to the high resolution of JIRAM, these batches do not significantly improve the determination of the footprint position with respect to a single image, but they statistically affect the result of the fitting procedure. Hence, the data points from a single sequence were binned in 500-km-wide bins, and the final dataset includes 115 data points for Io (56 north, 59 south), 55 for Europa (17 north, 38 south) and 83 for Ganymede (32 north, 51 south). Additionally, we survey the position of the *Footprint Tail* (FPT) downstream of the MAW spot to be compared with the MAW spot position. To obtain the position of the footprint tail, we used *sequences* - that is, tessellations of several consecutive images - instead of single images. The *Io Footprint Tail* (IFPT) was observed in 170 sequences (57 north, 113 south), and the *Europa Footprint Tail* (EFPT) and *Ganymede Footprint Tail* (GFPT) in 58 (13 north, 45 south) and 65 (18 north, 47 south), respectively. The numbers of JIRAM observations used in this section is reported in Table 6.3.

Table 6.3: Summary of the dataset used in this work, the footprint characteristics (size and lead angle) and the performance of the reference footprint track obtained from JIRAM dataset. The manuscript reference sections are reported in the first column. For the lead angle: the uncertainty represents the variation due to the wiggling of the moon in the centrifugal frame, while the parentheses contain the accuracy.

	Io	Europa	Ganymede
dataset (sec. 6.2.1)			
MAW - North[a]	130(56)	54(17)	95(32)
MAW - South[a]	129(59)	73(38)	139(51)
Tail - North[b]	57	13	18
Tail - South[b]	113	45	47
MAW spot size (km) (sec. 6.2.1)			
Longitudinal	438±156	538±206	958±120
Transversal	154±16	202±24	200±42
Vertical	382±76	502±360	(400)[c]
Fit residuals (km) (sec. 6.2.2)			
MAW - North	198	65	110
MAW - South	109	85	293
Tail - North	231	62	190
Tail - South	252	150	301
JRM33 residuals (km) (sec. 6.2.2.1)			
ord. 13^{th}	512(424)	449(549)	609(881)
ord. 18^{th}	484(451)	320(325)	441(600)
Lead angle (deg) (sec. 6.2.2.2)			
North	4.2±2.4(0.1)	6.2±2.5(0.6)	13±6(1)
South	4.1±2.0(0.1)	5.7±3.0(0.4)	11.9±3.5(0.4)

[a] Number of single images. The parentheses contain the number of images used in the fit.
[b] Number of sequences.
[c] Estimated.

Similarly to the analysis of section 6.1, the altitude of the peak emission is estimated to occur at 600±100 km above the 1 bar level of Jupiter's

atmosphere. Then, the position of the MAW and the footprint tails are fitted by a Fourier expansion to determine their reference tracks. The fit is performed for each feature (MAW spot or tail) of each moon at both hemispheres separately. For each fit, the best value for the Fourier degree is estimated by computing the *mean weighted sum of squared residuals* (MWSSR) as function of the Fourier degree, that is:

$$MWSSR(N) = \sqrt{\frac{\sum_i W_i D_i^2}{L - (2N+1)}} \tag{6.7}$$

where D_i is the i-th residual (i.e: the distance between the i-th data point and the fitted curve), W_i its normalized weight, L the number of observations and N the degree of the Fourier expansion. The weights in Eq. 6.7 are obtained from

$$w_i = \frac{1}{\Delta_x^2 + \Delta_y^2 + \Delta_z^2} \tag{6.8}$$

and their normalization

$$W_i = \frac{w_i}{\sum_i w_i} \tag{6.9}$$

The denominator of Eq. 6.8 represents the uncertainty on the position of the MAW and footprint position, which includes three contributions: 1) the uncertainty on the altitude of the emission, 2) the physical size of the MAW spot and 3) the resolution of the image. The uncertainty Δ_k (k being an xyz coordinate) on the position of the MAW spots is then computed as

$$\Delta_k = \sqrt{\Delta_{h(k)}^2 + \Delta_{size(k)}^2 + \Delta_{res(k)}^2} \tag{6.10}$$

where the three term on the rhs are the above-mentioned source of uncertainty. The uncertainty $\Delta_{h(k)}$ is computed by using the instrument pointing provided by the *Navigation and Ancillary Information Facility* (NAIF) (Acton et al., 2018; Acton, 1996)) and by referencing the images at surfaces at the different altitudes of 600±100 km. The longitudinal and transversal size of the MAW spots (Δ_{size}) is estimated from images captured at an emission angles <15°, while we selected images at emission angles >70° for the vertical extension. Unluckily, no images of the GFP at high emission angle are available. Nevertheless, the energy distribution of the precipitating

electrons associated with the GFP is similar to the distribution of the EFP and IFP, thus we can assume that the vertical extension of the GFP is also similar to the other two. The longitudinal-transversal-vertical size of the footprints is reported in Table 6.3. The higher longitudinal size of the GFP is due to the presence of two lobes in the MAW spot, which are potentially caused by the geometry of the intrinsic magnetic field of Ganymede. The uncertainty Δ_{size} of the footprint tail in takes into account its transversal and vertical extension.

6.2.2 Results and Discussion

In panel *a* and *b* of Fig. 6.5, we report the position of the MAW spots and the footprint-tail positions respectively, alongside the results of the fitting procedure of the previous section. Each point is color-coded according to its local time and two palettes were used to highlight any potential indication of local time variations. The best value for the Fourier-expansion degree N was determined to be 9 in the north and 5 in the south. In the this work, relative distances on the Jovian surface - such as potential model-observation discrepancies or the distance between two features - are usually reported in kilometers. These can be approximately converted into angular distances with the following formula:

$$\Delta r = R(\theta)\Delta\theta \tag{6.11}$$

where Δr is the distance given in kilometers, $\Delta\theta$ the angular distance corresponding to Δr, and $R(\theta)$ is given by Eq. 5.1.

In panel *(a)* of Fig. 6.5, in the north, only about half of each track is sampled by the JIRAM observations. JIRAM was able to observe IFP and GFP at 60°-120° and around 140° longitude respectively, while there are only a few observations for Europa around 120°. In this region, we observe deviations between the fit and JRM33+Con2020 up to ∼1000 km. Poleward deviations of about 1000 km between the GFP track and the model can also be noticed at 240°-280° longitude. In the southern hemisphere the coverage is almost complete, the largest gap being in the GFP between 0°

and 40° longitude. Between 210° and 320°, the fit to the IFP, EFP and GFP are poleward of JRM33+Con2020 by up to ∼600, ∼400 and ∼200 km, respectively. Between 60° and 120° longitude, the GFP appears displaced poleward when it is observed in the dusk sector, while it is equatorward in the dawn sector. For each fit, we computed the root mean square (rms) of the residuals $R_{fit} = \sqrt{\sum_i D_i^2/L}$, which are 198, 65 and 110 km for Io, Europa and Ganymede in the north respectively, and 109, 85 and 293 km in the south.

In panel *(b)*, we report the same plots as in panel *(a)* showing the position of the footprint tails. The data coverage of the IFPT is almost complete and the only gap is around 150°-160°. This improvement is due to the long extension of the IFPT (Bonfond et al., 2017b; Mura et al., 2017, 2018). All the differences between the MAW spot position and JRM33+Con2020 are also observed in the plots of panel *(b)*, as well as the transversal variability of the GFPT between 60° and 120° longitude. The rms of the residuals R_{fit} obtained from the footprint tails are 231, 62 and 190 km for Io, Europa and Ganymede in the north, respectively, and 252, 150 and 301 km in the south. The rms of the residuals is also reported in Table 6.3.

The fitted footprint tracks of panel *(a)* and *(b)* of Fig. 6.5 are compared Fig. 6.6 and they are largely compatible within the rms of the residuals. Therefore, we suggest that both the MAW spots and the footprint tails can be used interchangeably to determine the reference ovals of the footprint tracks.

To highlight the variability of the position of the footprints, we computed the *lead angle* (Hess et al., 2010b; Hue et al., 2023), which is computed by first tracing the MAW spot position along the magnetic field to the equatorial plane and then computing the angular separation with the corresponding moon at the same epoch. This quantity depends on the Alfvén travel time between the satellites and the Jovian ionosphere, so it contains information about the magnetic field and plasma mass distribution in the magnetosphere. In Fig. 6.7, we report the lead angles relative to the observations of Fig. 6.5. The lead angle is fitted with a periodic function $L_0 + \Delta L cos(\lambda - \phi)$, where L_0, ΔL and ϕ are free parameters and λ is the longitude of the satellites.

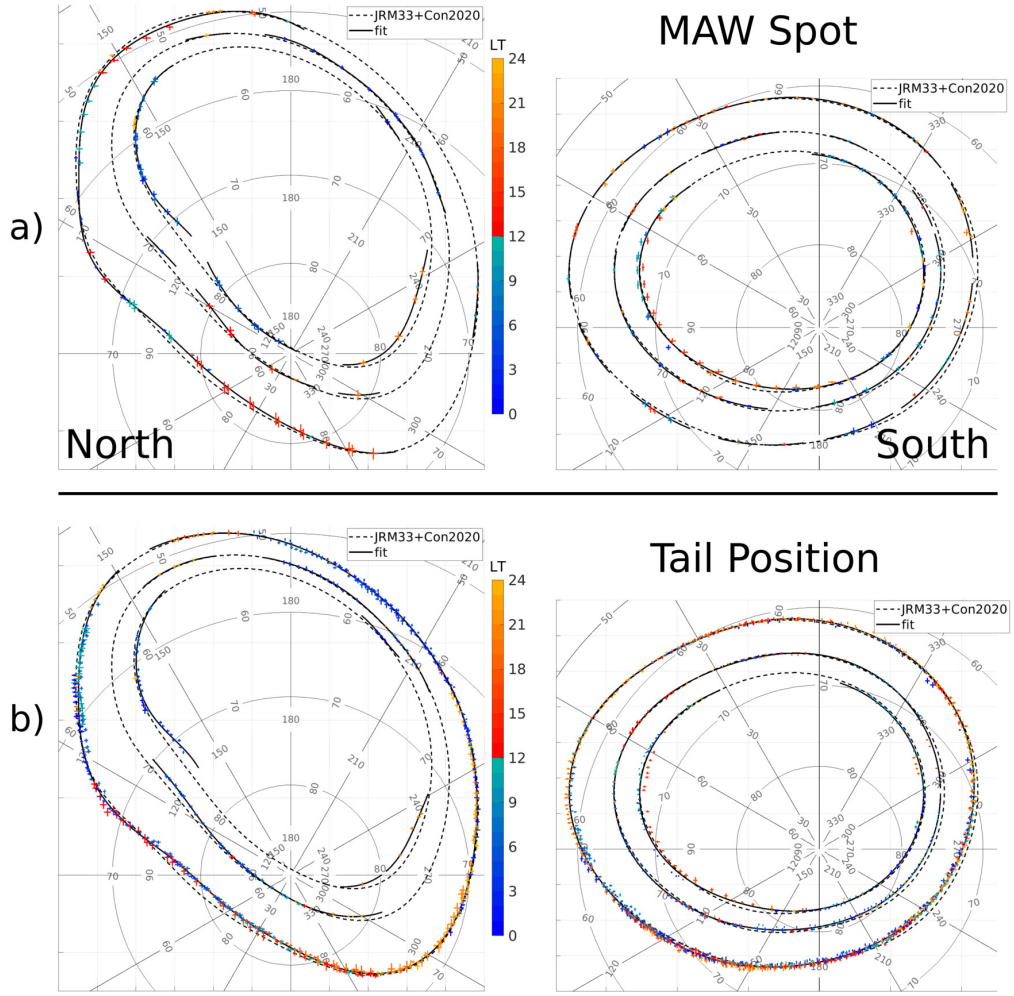

FIGURE 6.5: *(a)* Position of the MAW spot of Io, Europa and Ganymede in the north and south (left and right columns, respectively). The data are color-coded according to the local time of the footprint. The grey continuous line is the fit to the data, the grey dashed line is the footprint track predicted by the JRM33+Con2020 magnetic field model. *(b)* The same as in panel *(a)*, but for the position of the footprint tails.

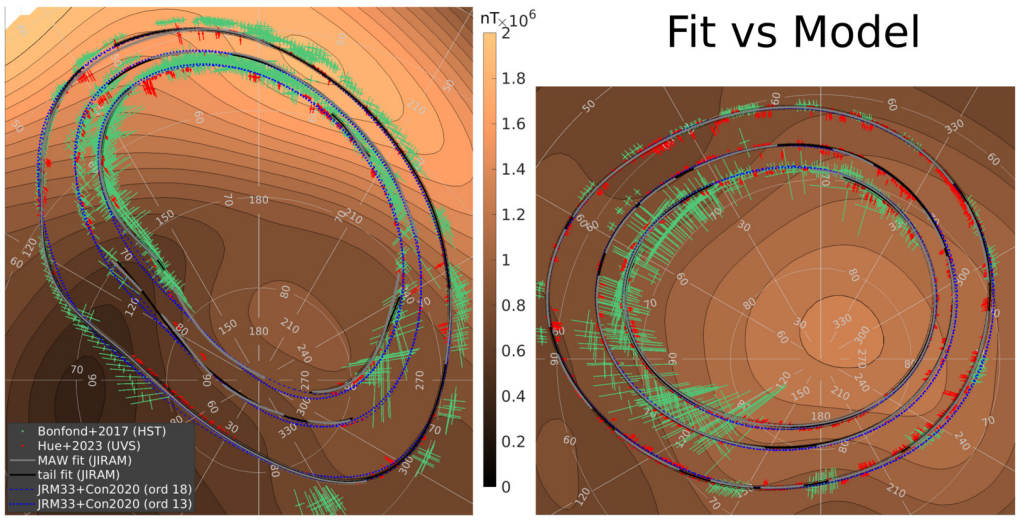

FIGURE 6.6: Comparison among the fits obtained from the MAW spots (grey line) and the footprint tails (black line), the JRM33+Con2020 model expanded up to order 13^{th} and 18^{th} (blue dotted and blue dashed lines, respectively) and the observations performed by HST (green points, from Bonfond et al. (2017b)) and Juno-UVS (red points, from Hue et al. (2023)). The grey and black lines are surrounded by thin dotted lines of the same colors: they represent the confidence of the two fits, respectively. The background contours are the magnetic field magnitude at the surface according to JRM33+Con2020 to order 18^{th}.

The results of these fits are presented alongside the plots of Fig. 6.7 and summarized in Table 6.3.

6.2.2.1 Validation of JRM33+Con2020 Magnetic Field Model

We computed two predictions by expanding the spherical harmonics of JRM33 up to order 13^{th} and 18^{th}, which are the recommendations in the original work by Connerney et al. (2022), depending on the level of confidence of the magnetic field coefficients. In Fig. 6.6, the two expansions show differences in the longitude sector between 270° and 170° in the northern hemisphere. Thus, we compare the rms R_{13} and R_{18} of the distance between JIRAM data and the two JRM33+Con2020 predictions in the northern hemisphere (the two expansions lead to very similar footprint tracks in the southern hemisphere). For Io, we obtain $R_{13} = 512$ km and $R_{18} = 484$ km

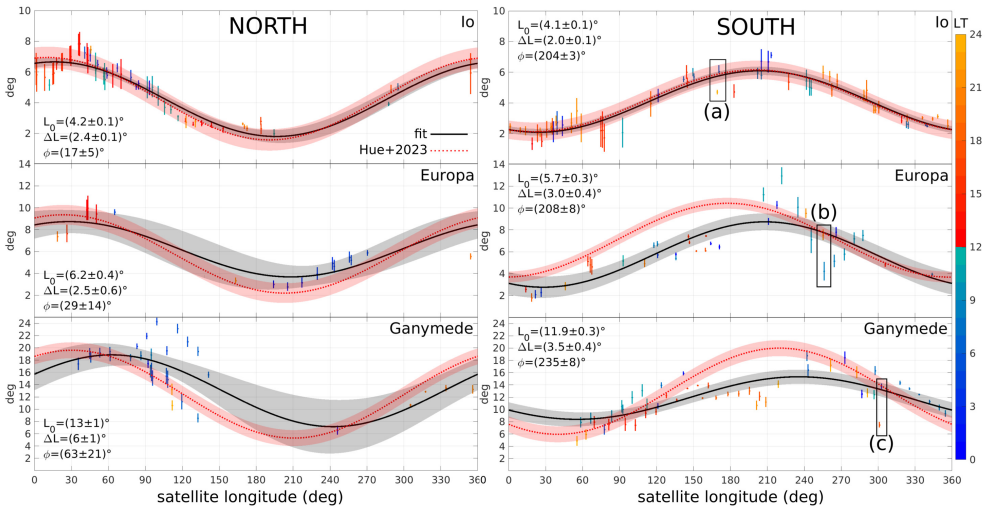

FIGURE 6.7: *Left*: Lead angles of the Io, Europa and Ganymede MAW spots in the northern hemisphere. The data are color-coded according the local time. The black line is the fit with a first-order Fourier expansion, the grey shaded area the associated 95% confidence interval. The red dotted line and the red shaded area are the fit to the lead angle derived from Juno-UVS observations (Hue et al., 2023). In each plot, we report the parameters obtained by fitting $L_0 + \Delta L cos(\lambda - \phi)$ to JIRAM data. *Right*: the same as panel on the left, but for the southern hemisphere. The boxes labelled *a*, *b* and *c* highlight cases of high variability (see also Fig. 6.9).

from the MAW spot position and R_{13} = 424 km and R_{18} = 451 km from the tail position. Indeed, in the longitude sectors 300°-330° and 100°-130°, the order 18^{th} better matches the JIRAM data, while the order 13^{th} is better between 30° and 100°. Instead, for Europa and Ganymede, R_{18} is smaller than R_{13} for both the MAW spot position and the tail positions. For Europa we obtain R_{13} = 449 and 549 km for the two features respectively, and R_{18} = 320 and 325 km, while for Ganymede R_{13} = 609 and 881 km, and R_{18} = 441 and 600 km. The rms of the difference between the fit based on JIRAM data and the predictions based on JRM33+Con2020 is summarized in Table 6.3.

According to the residual analysis presented here, we thus suggest expanding the JRM33 spherical harmonics up to order 18^{th} for mapping the

magnetospheric region from around Europa to Ganymede to the northern hemisphere of Jupiter. For Io, both expansions of JRM33 appear overall equally valid, although the expansion up to order 18^{th} should be preferred in the longitude sectors 300°-330° and 100°-130°. For mapping towards the southern hemisphere, there is no preferred choice of the order expansion, as both order 13^{th} and 18^{th} lead to the same prediction within JIRAM spatial resolution.

6.2.2.2 Variability of the Footprint: Transversal Shift and Lead Angle

As explained in chapter 3, the position of the MAW spots depends on the shape of the Alfvén wings, which, in turn, are determined by the magnetic field and by the plasma distribution in the magnetosphere. Therefore, in principle, any variation in the position of the MAW spots should be attributed to changes in either the plasma environment and/or the magnetic field. Here, the variability of the footprint positions is deduced by inspecting cases of transversal shift (with respect to the direction of the footprint) and the lead angle associated with each MAW spot.

In Fig. 6.5, the GFP exhibits transversal displacements, which is also reported in Figure 6.8 for a better view. JIRAM was able to observe the GFP in both hemispheres during PJ 1, PJ 4 and PJ 7; among these, Ganymede orbited in the same longitude sector during both PJ 1 and PJ 4. These two orbits allowed to sample the GFP track at 140° longitude and 60°-70° latitude north, where no clear evidence of latitudinal displacement is observed. *Local Time* (LT) of the northern MAW spot during PJ 1 and PJ 4 was 4-5 hr and 7-9 hr respectively, thus both observations were in the dawn sector. In the southern hemisphere, the GFP was observed at ∼-66° latitude, between 70° and 80° longitude during both orbits, showing an latitudinal offset of 0.75±0.19°, which corresponds to a transversal displacement of 880±220 km. The LT of those observations was 11-12 hr for PJ 1 (dawn sector, with the footprint equatorward displaced) and 15 hr for PJ 4 (dusk sector, with the footprint poleward displaced). This suggests that the variability of

the GFP position reported here might be due to a local-time asymmetry. Further evidences can be observed in the GFP and the GFPT position in the southern hemisphere at:

- ∼165° longitude, where the MAW emission during PJ 25 (LT = 14 hr) was equatorward with respect to PJ 21 (LT = 2 hr) and 32 (LT = 5 hr) by 0.3±0.1°, or 370±140 km;

- ∼310° longitude, where the tail during PJ 10 (LT = 19) was poleward with respect to PJ 19 (LT = 4) and PJ 33 (LT = 12 hr) by about 0.6±0.3°, or 660±330 km.

We also looked for a potential day-night correlation (not shown), but the transversal shift shows no systematic dependency with this criterion. The transversal displacement of the GFP has already been observed by HST (Grodent et al., 2008) and it have been explained by variations in the plasmadisk mass and/or radial transport (Promfu et al., 2022). Although the observations performed during PJ 1 and PJ 4 suggest local-time variability, we cannot completely rule out a global variation of the plasmadisk. Nevertheless, this change should have occurred over less than 10 hours in order to explain the different north-south displacement observed by JIRAM. Unfortunately, JIRAM did not record the GFP crossing from the dawn to the dusk sector (or vice-versa), which might have represented stronger evidence of its local-time variability.

The lead angle in Fig. 6.7 helps to detect evidence of longitudinal variability between different orbits. In the north, we report a single case for Io at ∼290° between PJ 20 and PJ 34, and one for Ganymede between 90° and 135°, where the lead angle of PJ 1 was larger than the one of PJ 4, 9, 32 and 37. In the south, we identified several cases: for Io there is PJ 11-32 at 170° longitude; for Europa PJ 18-32 at 120°, PJ 8-40 at 135°, PJ 14-29 at 160°, PJ 7-37 at 255° and PJ 7-26 at 265°; for Ganymede PJ 1-4 between 90° and 120°, PJ 4-7 at 160° and PJ 30-33 and PJ 10-19, both around 300°. For each satellite, we select one example pair of observations, labelled *a*, *b* and *c* in Fig. 6.7, and reported in Fig. 6.9. Case *a* shows

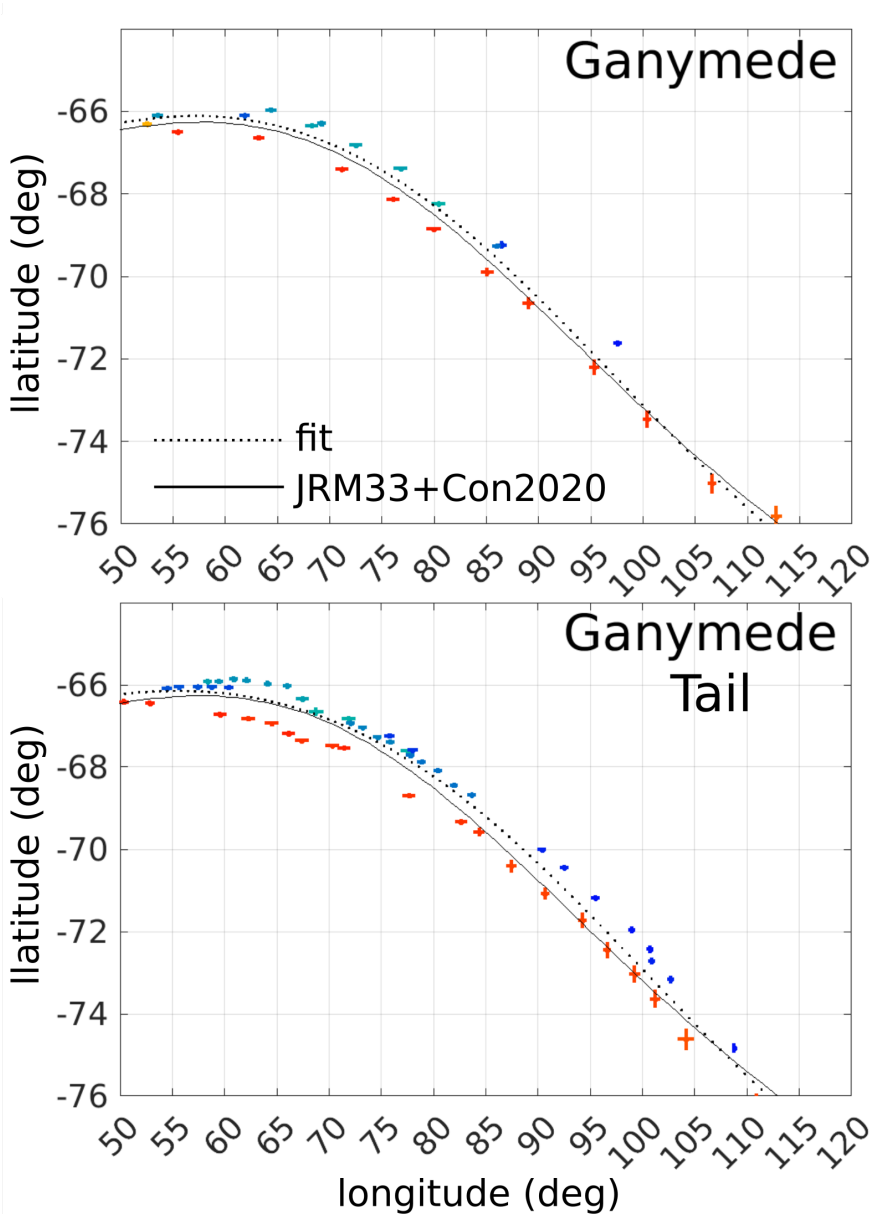

FIGURE 6.8: Longitude-latitude plot of the position of the MAW spot (top) and tail (bottom) of the Ganymede footprint. The warm colors represent observations on the dusk sector (points below the fit dotted line), the cold colors observations on the dawn sector (point above the fit line). The black line is the prediction based on the JRM33+Con2020 model.

the IFP during PJ 11 and PJ 32, with lead angles 4.7±0.2° and 6.0±0.3°, respectively. This pair of observations was analyzed in Moirano et al. (2023) (see section 6.1), where the difference was attributed either to changes in the state of the IPT (Bagenal and Dols, 2020) between the two orbits or to the local-time asymmetry of the plasma torus. Case *b* shows the longitudinal displacement of the EFP by comparing PJ 7 and PJ 37, when the lead angle was 4.3±0.8° and 7.5±0.5° respectively, while Europa was at the same longitude within less than 1°. In case *c*, the GFP exhibits both transversal and longitudinal displacement by comparing PJ 10 and PJ 19 (lead angle 7.5±0.5° and 13.8±0.5°, respectively). The transversal displacement in case *c* can be ascribed to a local time asymmetry as discussed in the previous paragraph, but we found no clear local-time dependency of the lead angle. A summary of the best-fit values of the lead angle is given in Table 6.3.

The longitudinal and the transversal displacements of the footprints can be explained by two different processes. The former can be caused by a change in the Alfvén travel time - which corresponds to a variation in the plasma environment - or to a change in the radial current of the plasmadisk - which causes an azimuthal stretch of the magnetic field lines. On the other hand, a transversal displacement can be explained by the satellites connecting to different magnetic shells, which can be due to variations in the azimuthal component of the magnetodisk current that radially stretches the magnetic field. See also section 2.2 and Fig. 2.4 for a description of the relation between the magnetic field geometry and the plasmadisk currents. In either case, the variation of the footprint position is due to a different mapping between the satellite position and its associated auroral emission. We estimated the longitudinal and transversal displacement by changing the radial current of the Con2020 model $\mu_0 I_R/2\pi$ between 7.7 and 35.2 MA, and the azimuthal current $\mu_0 I_{MD}/2$ between 124.2 and 156.1 nT, according to the Juno magnetometer data (Connerney et al., 2020). The predicted longitudinal shift is approximately 70, 200 and 450 km for Io, Europa and Ganymede respectively, while the transversal shift is about 100, 250 and 650 km. For Io and Europa, these values are similar to or smaller than the footprint size; hence it appears unlikely that the variability observed at

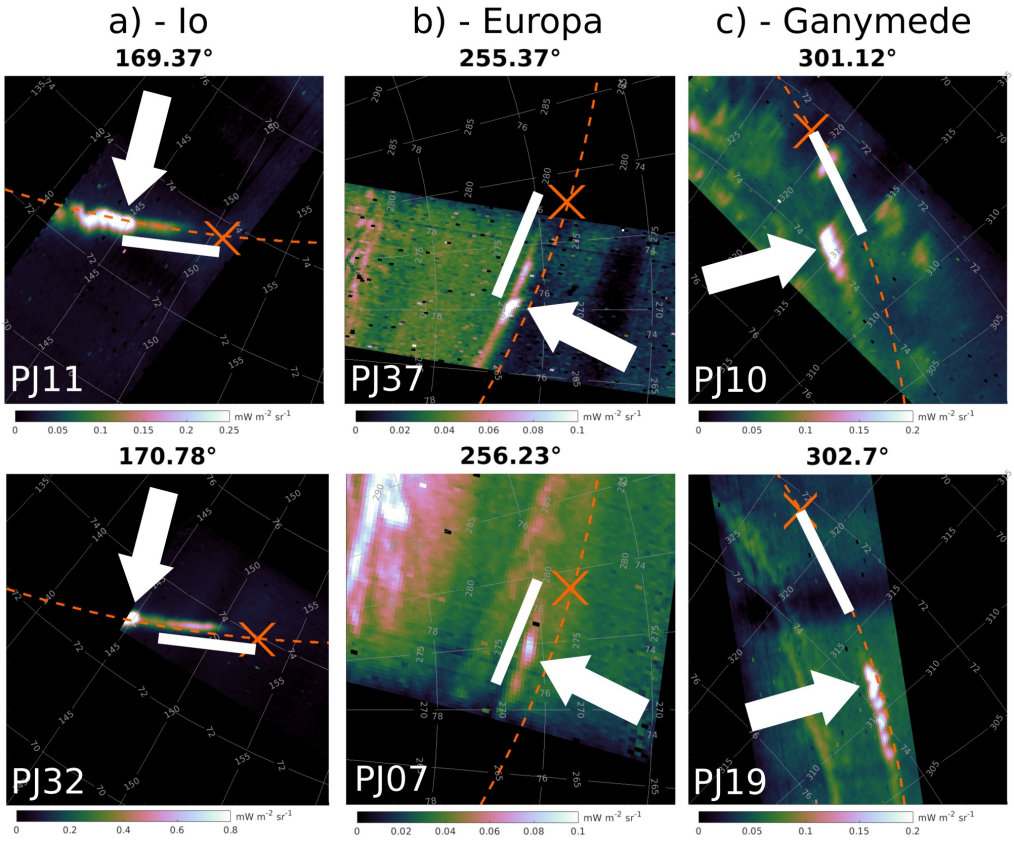

FIGURE 6.9: Examples of variation in the MAW spot position for Io (left), Europa (center) and Ganymede (right). The orange dashed line is the satellite footprint track according to JRM33+Con2020, the cross is the magnetic footprint of each moon at the time of the acquisition of the image. The System III longitude of the satellites is reported above each image. The white arrows point to the MAW spot in each image. The Io case is thoroughly analyzed in section 6.1. Notice how the MAW spot appears at different positions between the two rows despite the similar satellite longitude of each column. To highlight the difference, the white bar in each of the top images has the same size as in the bottom images, and it is aligned with the magnetic footprint. We suggest that the difference between the top and the bottom observations is due to different magnetospheric conditions that affect the propagation of the Alfvén waves. More details are discussed in section 6.2.2.2.

those moons is caused by changes in the plasmadisk currents. Furthermore, both the IFP and EFP exhibited lead angle variations, but no transversal variation, which suggests variations in the plasma environment around the two satellites. On the other hand, the GFP displacement in Fig. 6.5 and 6.8 may be compatible with magnetodisk variations such as the ones detected by the Juno magnetometer. Thus, we suggest that the variations in the GFP position can be caused either by local time asymmetry and temporal variations of the magnetodisk currents or changes in the plasmadisk mass content.

In summary, the GFP position can exhibit latitudinal shifts, which are suggested to be due to a local-time asymmetry of the magnetosphere. This is supported by the observations at the southern hemisphere, where the GFP has been detected at different latitudes by $0.75 \pm 0.19^{\circ}$ while being in different dawn-dusk hemisphere. The same shift was not observed during the same PJs at the northern hemisphere. Moreover, the lead angle associated with Io, Europa and Ganymede shows variability by comparing observation with the satellites at the same System III longitude at different epochs. This implies a variation in the Alfvén travel time, which determines the mapping between the moons and their emission (e.g: Hinton et al. (2019); Moirano et al. (2023)). This might be caused by either a change in the plasma conditions or a transient longitudinal stretching (or contraction) of the magnetic field, which in turn can be due to variations in the radial plasmadisk currents. Only the GFP position shows latitudinal variations, which may be ascribed to the radial stretching of the magnetic field, caused by changes in the azimuthal plasmadisk currents. The JIRAM observations are in agreement with the magnetodisk currents estimated by the Juno-MAG instrument (Connerney et al., 2020).

6.2.2.3 Comparison with Juno-UVS and Hubble Space Telescope

In Fig. 6.6, we compare the fit obtained from the MAW spot and tail positions against the ultraviolet observations performed by HST Bonfond et al. (2017b) and Juno-UVS Hue et al. (2023). For the IFP in the north,

the HST observations are systematically equatorward with respect to both the JIRAM-based fits and UVS data. In the south, the HST observations usually lie equatorward with respect to the Juno measurements roughly between 30° and 120° longitude, while at the other longitudes the data from the two spacecraft agree within the HST uncertainty. The HST data of the GFP between 40° and 60° longitude seems to suggest a transversal shift of the GFP of about 2400 km between September 2009 (poleward) and December 2000, January 2001 and May 2007 (equatorward). We inspected the local-time distribution of these observations, but we found no clear evidence of local-time dependency as in the JIRAM data. Lastly, the lack of observations in the northern hemisphere during September 2009 prevents a north-south comparison of this shift.

The referencing of the HST images onto the Jovian surface is radically different from the one used for Juno. For HST, the inferred position of the footprints relies on the localization of the planetary center, which in turn is determined by fitting the planetary limb in the HST images themselves (Bonfond et al., 2009). On the other hand, Juno-based observations are localized using the spacecraft ephemeris and the instrument pointing, which are provided by the *Navigation and Ancillary Information Facility* (NAIF) (Acton et al., 2018; Acton, 1996). Therefore, the different referencing procedures for HST and Juno might be the root cause of the discrepancy among the observations performed by the two spacecraft. Now, thanks to the fits in Fig. 6.5, it becomes possible to automatically compute the location of Jupiter's center relative to the IFP MAW spot for any HST image in which the Io footprint is visible and use this spot to improve significantly the referencing accuracy. This new method assumes that the location of the MAW spot is stable through time at resolution of HST: both the data shown in Fig. 6.5 and the Io lead angle in Fig. 6.7 suggest that the IFP position varies only occasionally, thus we suggest that its MAW spot is a reliable reference.

The Juno-UVS data in Fig. 6.5 are very consistent with the JIRAM fits. In the north, the UVS observation of the IFP between 60° and 120° longitude performed during PJ 8, PJ 12, PJ 15 and PJ 18 matches very

well the fits in the same region, which was observed by JIRAM during PJ 4, PJ 7, PJ 15 and PJ 18. The UV and IR measurements also agree between 250° and 290° longitude of the GFP, where they both show a poleward displacement with respect to JRM33+Con2020. In the south, UVS data shows the transversal displacement in the GFP at ∼75°-90° longitude, where the GFP was displaced poleward during PJ 7 (LT = 18 hr) with respect to PJ 27 (LT = 8). Unfortunately, no measurements are reported in the northern hemisphere during those PJss for comparison. In Fig. 6.7, the lead angle derived from JIRAM data is compared with the one from UVS data. For Io, the sinusoidal fit to the lead angle appears almost symmetric between the two hemispheres, apart from a phase difference of 187±8°, and it matches the result obtained by UVS. The lead angle phases are consistent with the tilt of the centrifugal equator towards ∼200° longitude (Moirano et al., 2021a; Phipps et al., 2020) and the wiggling up and down of Io within the Io Plasma Torus. The Europa lead angle is also consistent between the two hemisphere, the phase difference being ∼179±22°. The Europa lead angle is also compatible with the position of the centrifugal equator, showing a maximum at 29±14° in the north and 208±8° in the south. The UVS results shows a larger lead angle than JIRAM, and the phase difference between JIRAM and UVS is about 20° in the south. At Ganymede, the amplitude of the lead angle in the northern hemisphere is larger than the amplitude in the south ($\Delta L = 6\pm1°$ and 3.5±0.4°, respectively), and the two fits are out of phase by 172±29°. Unlike the Io and Europa lead angles, the Ganymede lead angle peaks at 63±21° in the north and 235±8° in the south, while UVS data reported ∼30° and ∼220°, respectively. The differences between the JIRAM and UVS lead angles at Europa and Ganymede might be due to the different coverage between the two instrument, combined with the intrinsic variability of these footprints.

To summarize, the Earth-based observations of the footprints from HST do not always agree with the reference footprint track derived in the present study. The most probable cause for such discrepancy is the limb-fitting method used to determine Jupiter's location in HST images Bonfond et al. (2009), which is less accurate than using the instrument pointing from an

in-situ spacecraft such as Juno. On the other hand, the footprint positions from Juno-UVS images (Hue et al., 2023) agrees well with the reference track obtained from JIRAM dataset. As the processing of JIRAM and UVS data are performed independently, their mutual agreement supports the validity of the reference track shown in Fig. 6.5. Nevertheless, the JIRAM and UVS images shows differences in the footprint lead angle of Europa and Ganymede. This difference between the two datasets might be caused by either the intrinsic variability of the footprint positions or the different coverage of the two instrument. A dedicated analysis would be necessary to further address this question.

6.2.3 Conclusions

This section reported the full database of JIRAM observations of the footprint of Io, Europa and Ganymede, from August 2016 to May 2022. The detection of the Callisto footprint is much more challenging than the other three moons, due to the expected weaker precipitation and its overlap with the main emission. Therefore, at the present day, we have not been able to report any observation of the Callisto footprint. The main goal of this section is to provide the reference tracks for the three footprints, which serve a variety of purposes, here summarized:

- The footprint position can be used to test the reliability of magnetic field models. By comparison with the Juno-based magnetic field model JRM33+Con2020 (Connerney et al., 2020, 2022; Wilson et al., 2023), we conclude that the model precisely predict the footprint tracks, although variations up to ∼1000 km are reported in the northern hemisphere, as well as deviations up to ∼600km in the south. We recommend the expansion of the harmonics of the JRM33 internal field up to order 18^{th} for the Europa and Ganymede position. For the Io footprint, the expansion up to order 18^{th} works better in the longitude sectors 300°-330° and 100°-130°, while we suggest the order 13^{th} between 30° and 100°.

- The positions of the MAW spots in JIRAM data agree very well with the Juno-UVS observations, while the positions derived from HST campaigns are occasionally systematically displaced (such as the IFP north). Therefore, we suggest using the reference track reported in the present manuscript to calibrate the localization of Earth-based observations, when the MAW spot of the footprint can be identified. Due to the variability of the Ganymede footprint (and of the Europa footprint, to a lesser extent), we recommend using the Io footprint whenever possible.

- The footprint position can be used to investigate the plasma environment near the moons Moirano et al. (2023) by studying the lead angle associated with the footprints themselves Hue et al. (2023). For this reason, the footprints represent *(a)* a source of information that complements the particle measurements carried by Juno during the satellite flybys in its extended mission, and *(b)* a supporting dataset for the next missions Juice and Europa Clipper, which are dedicated to the Jovian major moons.

- We report the transversal shift of the Ganymede footprint by ∼900 km (corresponding to ∼0.8° in latitude, see Fig. 6.8), which appear to be local-time dependent and it might be explained by variations in the external magnetic field due to the plasmadisk current, that radially stretches the magnetic field.

6.3 The Io Plasma Torus from JIRAM/UVS Observations and Juno Radio Occultations

In this last section, the determination of the IPT conditions from the footprint position described in section 6.1 is complemented by the radio occultations performed by Juno. The goal is to extend the method of section 6.1 to the whole JIRAM dataset presented in section 6.2 and to determine the plasma properties of the IPT over a long period of time (such the duration

of the Juno mission), which is fundamental for both navigation and scientific purposes. For example, the main driver of the Jovian magnetosphere is the fast rotation of the planet and its magnetic field, which permeates the dense Iogenic plasma, while the variability of the solar wind is relevant mostly in the outer magnetosphere, and its effects decrease in the inner regions. Both the plasma source and the solar wind are variable, and the dynamics of the Jovian magnetosphere reflect the same variability, which is usually detected by inspecting the auroral emission (see for example Promfu et al. (2022); Vogt et al. (2019, 2022)). As there are no in-situ measurement of the solar wind conditions at Jupiter[4], the possibility of monitoring the internal plasma source - the IPT - can help to determine if the variability of the Jovian aurorae is related to the variability of the torus or to other, external factor (e.g: the interaction with the variable solar wind, plasma injections from the outer magnetosphere). Moreover, the plasma diffuses from Io's orbit to the whole magnetosphere, therefore, future missions to the Jovian system might take advantage of the knowledge about its plasma variations.

According to the sensitivity test of section 6.1.2, the position of the IFP is mostly sensitive to the the plasma temperature and density. The footprint position depends on the Alfvén travel time, which can be estimated according to Eq. 6.6, therefore density and temperature are degenerate parameters. To break this degeneracy, the parameter space obtained from the JIRAM observations is used to simulate several radio occultations of the IPT by Juno, which are compared with the measurement acquired by the radio science experiment. Indeed, the frequency of the radio communications between the spacecraft and the DSN ground station is affected by the presence of plasma between the transmitter and the receiver. The frequency shift due to the plasma is proportional to the time derivative of the optical path of the radio signal, which in turn is proportional to the *total electron content* (TEC)

[4]As mentioned in section 6.1.3, there are solar wind models that propagate its conditions measured at Earth up to Jupiter. Nevertheless, the uncertainty on the timing of the events is about 15 hours at best - that is: during opposition - and increases with the JSE angle. As Jupiter and Earth are relatively close to opposition only for a short period of the year, this uncertainty is a lower limit, which restricts the time scales of the variability of the Jovian magnetosphere that can be ascribed to solar wind variations.

along the line of sight between Juno and the ground station (more details are presented in section 6.3.1). Thanks to the geometry of the spacecraft orbit, the TEC recorded by Juno have a typical bell shape, whose peak is given by the maximum TEC and the width is due to the vertical extension of the IPT, in the centrifugal frame (see Fig. 6.10, and Moirano et al. (2021a) and Phipps et al. (2021)). The vertical scale of the torus depends on the plasma temperature (see Eq. 6.3), therefore, the ambiguity between plasma density and temperature is solved when using the radio occultations. This section is dedicated to exploring the potential of such analysis.

From PJ 1 to 43, JIRAM has been able to detect the IFP during 31 orbits (13 of which at both hemispheres), while the available radio occultations are 26. At the moment, radio occultations that does not clearly show the IPT signature are not considered. The number of orbits covered by both a radio occultation and the detection of the IFP is 17 (9, if considering the detection at both hemispheres). In order to have a more extended dataset of the IFP position, the Juno-UVS data (Hue et al., 2023) are used to complement the JIRAM ones. There are 9 radio occultations that cannot be compared with JIRAM observations due to the lack of data: these can then be compared with data from UVS, which reports at least one observation for the missing orbits.

6.3.1 Multi-frequency Radio Occultations

A signal sent at a frequency f_0 across a medium and recorded at a later time with a frequency f experiences a fractional frequency y that depends on the optical path Δl according to

$$y = \frac{f - f_0}{f_0} = \frac{1}{c}\frac{d\Delta l}{dt} \tag{6.12}$$

where d/dt is the time derivative. This shift is caused by both dispersive effects - such as the presence of the plasma in the Jovian magnetosphere, the solar wind and the Earth's ionosphere - and non-dispersive effects - Doppler and the tropospheric delay. In general, the optical path is related to the

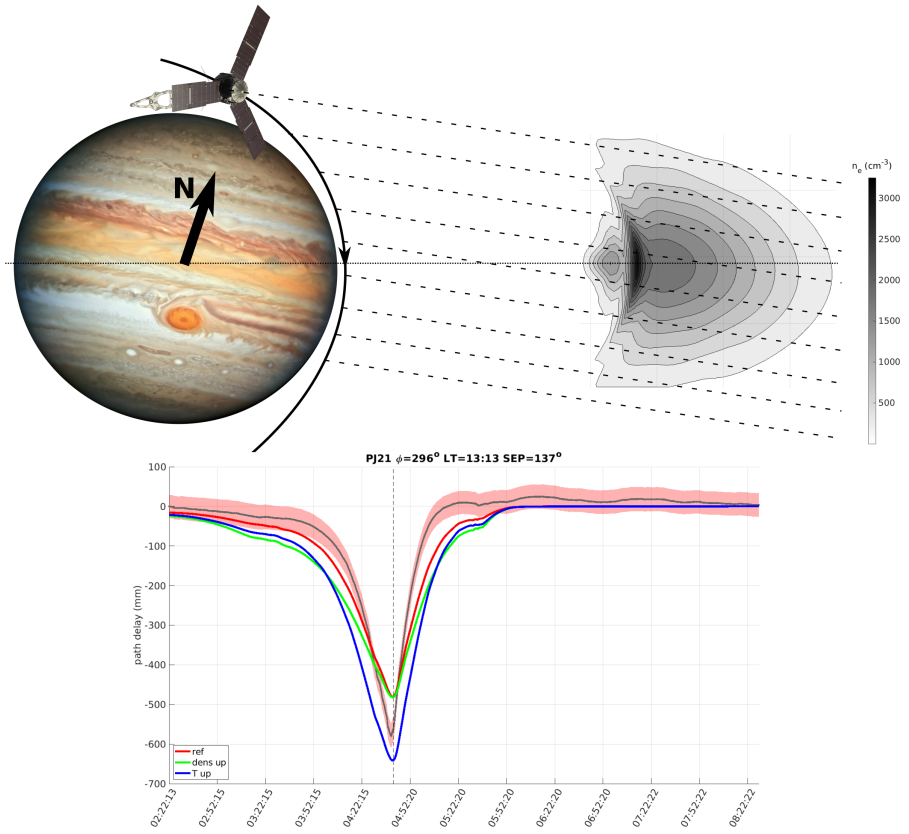

FIGURE 6.10: *Top*: sketch of the meridional projection of Juno trajectory near perijove in the centrifugal frame. The dashed lines that cross the IPT are the path of the radio communications. The dotted horizontal line represents the centrifugal equator. *Bottom*: example of the IPT signature in the path delay (i.e: the optical path difference between two bands of Juno's radio communications) observed during PJ 21. The path delay is proportional to the TEC, with a sign change, and the signature around 04:50 is due to the presence of the IPT. The red area represents the uncertainty due to the Earth's ionosphere and solar wind scintillation. The dashed vertical line is the time of the spacecraft closest approach to Jupiter. The title on top reports the longitude and local time of the location of the torus at 5.9 R_J that intersect the radio link at the time of the closest approach. The Sun-Earth-Probe (SEP) angle is also reported. The three colored lines represent simulations obtained with three IPT conditions. The green one corresponds to a torus whose ion temperature is 1.5 times the temperature of the red line, but with the same peak electron density. On the other hand, the blue line is obtained from the same ion temperature, but 1.5 times higher electron density.

index of refraction n_r of the medium:

$$\Delta l = c \int_{t_0}^{t} [n_r(\gamma(\tau), \tau) - 1] d\tau \tag{6.13}$$

where the integration is carried from the transmission time t_0 and the receiving time t along the line of sight γ (Bertotti et al., 1993). If the medium is a plasma, the index of refraction can be approximated as

$$n_r \approx 1 - \frac{\omega_p^2}{8\pi^2 f_0^2} = 1 - \frac{q_e^2 n_e}{2\pi m_e f_0^2} \tag{6.14}$$

which holds for frequencies higher than the plasma frequency. For the uplink frequency of Juno in the X band (∼7.3 GHz), this approximation is satisfied by electron density below $\sim 6.5{\cdot}10^5$ cm^{-3}. Substituting Eq. 6.14 into Eq. 6.13 the optical path can be related to the TEC between the transmitter and the receiver:

$$\Delta l = -\frac{ce^2}{2\pi m_e f_0^2} \int_{t_0}^{t} n_e(\gamma(\tau), \tau) d\tau = -\kappa \frac{TEC}{f_0^2} \tag{6.15}$$

where $\kappa = \frac{cq_e^2}{2\pi m_e}$ is a constant factor. The TEC is usually measured is *TECU* (TEC units) or *hexems*, which are both equivalent to 10^{16} electrons m^{-2}. As the optical path and the frequency shift are related by Eq. 6.12, it is possible to derive a time series of the TEC by measuring the fractional frequency of the two-way link between Juno and the DSN.

As mentioned in section 4.2, the radio instrumentation is capable of supporting three types of link: X/X, Ka/Ka and X/Ka, where each of the two bands is the uplink and downlink frequency, respectively. Among these, two of them are used for each occultation. Indeed, while the present work takes advantage of the dispersive frequency shift due to the plasma, the gravity measurements aim at isolating the non-dispersive contribution of the Doppler shift caused by the gravity field of Jupiter (e.g: Iess et al. (2018)). To that end, a dual-frequency link is needed (more details are presented in Mariotti and Tortora (2013)). Moreover, only the DSS 25 is capable of a Ka uplink among the DSN stations, thus the need for a X/Ka link. To our ends, it is instead necessary to extract the dispersive contribution from the

radio link. To determine the total fractional frequency of the full two-way link, consider first the two legs (uplink and downlink) separately (see Fig. 4.4 and Moirano et al. (2021a)):

$$y_i^U = \frac{f_{Ri} - f_i}{f_i} \tag{6.16}$$

$$y_{ij}^D = \frac{f_{ij} - f_{Tj}}{f_{Tj}} = \frac{f_{ij} - \alpha_{ij} f_{Ri}}{\alpha_{ij} f_{Ri}} \tag{6.17}$$

where the apices U and D stands for uplink and downlink, f_i and f_{ij} are the frequencies transmitted (in the i-band) and received (in the j band) by the DSN station, f_{Ri} and $f_{Tj} = \alpha_{ij} f_{Ri}$ are the frequency received and transmitted by the spacecraft (again, in the i and j band) and α_{ij} is the turnaround ratio, which ensures that there is no interference between the uplink and the downlink. These two equations can be combined to remove f_{Ri}, which leads to

$$\alpha_{ij} f_i (y_i^U y_{ij}^D + y_i^U + y_{ij}^D + 1) = f_{ij} \tag{6.18}$$

Assuming that the fractional frequency is smaller than one, the term $y_i^U y_{ij}^D$ can be neglected, thus it is possible to define a total fractional frequency

$$Y_{ij} = \frac{f_{ij}}{\alpha_{ij} f_i} - 1 \approx y_i^U + y_{ij}^D = \frac{1}{c}[(\dot{\Delta} l_{ND}^U + \dot{\Delta} l_{Di}^U) + (\dot{\Delta} l_{ND}^D + \dot{\Delta} l_{Dj}^D)] \tag{6.19}$$

where ND points out the non-dispersive contributions and Di (Dj) the dispersive ones, which takes the form of Eq. 6.15. By having two links, it is possible to compute the difference between the respective fractional frequency: this removes the non-dispersive contribution in Eq. 6.19. Juno performs two types of dual-link: X/X-Ka/Ka and X/X-X/Ka, therefore by taking the quantities $Y_{XX} - Y_{KaKa}$ and $Y_{XX} - Y_{XKa}$ is is possible to estimate the path delay (that is: the difference in the optical path between the two links, which is the quantity shown in Fig. 6.10) and thus the TEC between the spacecraft and the ground station. There are three major contributions to the TEC: the IPT, the solar wind and the Earth's ionosphere. The TEC of the Io torus can be considered the same between the uplink and the downlink, as the radio signal takes about 1 s between the inbound and

outbound crossing of the IPT. On the contrary, the uplink and downlink contributions of the solar wind and the ionosphere must be considered separately, as the one-way light time between Juno and Earth is about 40 minutes. Therefore, the path delay of the $Y_{XX} - Y_{KaKa}$ link can be estimated from

$$\begin{aligned} Y_{XX} - Y_{KaKa} = \\ = -\frac{\kappa}{c}\Big[T\dot{E}C^{U}_{SW}\Big(\frac{1}{f_X^2} - \frac{1}{f_{Ka}^2}\Big) + T\dot{E}C^{D}_{SW}\Big(\frac{1}{\alpha_{XX}^2 f_X^2} - \frac{1}{\alpha_{KaKa}^2 f_{Ka}^2}\Big) + \\ + T\dot{E}C^{U}_{iono}\Big(\frac{1}{f_X^2} - \frac{1}{f_{Ka}^2}\Big) + T\dot{E}C^{D}_{iono}\Big(\frac{1}{\alpha_{XX}^2 f_X^2} - \frac{1}{\alpha_{KaKa}^2 f_{Ka}^2}\Big) + \\ + T\dot{E}C_{IPT}\Big(\frac{1}{f_X^2}\frac{\alpha_{XX}^2+1}{\alpha_{XX}^2} - \frac{1}{f_{Ka}^2}\frac{\alpha_{KaKa}^2+1}{\alpha_{KaKa}^2}\Big)\Big] \end{aligned} \tag{6.20}$$

while the $Y_{XX} - Y_{XKa}$ link leads to

$$Y_{XX} - Y_{XKa} - \frac{\kappa}{c}(T\dot{E}C^{D}_{SW+iono} + T\dot{E}C^{D}_{IPT})\frac{1}{\alpha_{XX}^2 f_{XX}^2}\Big(1 - \frac{\alpha_{XX}^2}{\alpha_{XKa}^2}\Big) \tag{6.21}$$

Indeed, the uplink contributions cancel out in the latter case, as the fractional frequencies of the two links are both referred to the X band.

The path delay obtained by integrating either Eq. 6.20 or 6.21 contains contributions of the Earth's ionosphere and the solar wind that should be calibrated and their uncertainties taken into account. The terrestrial ionosphere is calibrated by using GPS data (Thornton and Border, 2000), and its uncertainty is obtained from the archive of the National Centers for Environmental Information of the National Oceanic and Atmospheric Administration (https://www.ngdc.noaa.gov/stp/iono/ustec/products/). The processing of the solar wind contribution is quite challenging, as its high variability (Ebert et al., 2014; Matthaeus et al., 1991) makes the determination of its impact on the path delay difficult. By assuming that the solar wind density is a decreasing function of the distance from the Sun (Köhnlein, 1996), the corresponding delay can be approximated by a linear trend caused by the relative motion between the ground station and Juno. Depending of the *Sun-Earth-Probe* (SEP) angle, the contribution of the solar wind ranges between 1 mm (e.g: PJ 35, SEP = 148°) and 80 mm

(e.g: PJ 17, SEP = 20°). This linear trend is not compatible with the path delay measured by Juno far from the signature of the IPT: indeed, large fluctuations that are not correlated with the static density model of the solar wind are usually detected. An example of such an effect can be seen in the path delay shown in Fig. 6.11. To remove these fluctuations, we first use the model to determine the time windows that are expected to have no contributions from the IPT electrons, within 5% of the minimum path delay (i.e: the peak of the IPT signature). Then, the modeled path delay in those time windows is subtracted to the measured delay. The resulting delay, which should only be caused by the solar wind, is than fitted by a 9^{th} degree polynomial (Phipps et al., 2018) and summed to modeled path delay. The final result can then be compared with the measured path delay. The uncertainty due to scintillation of the solar wind is given by numerical integration of the uncertainty in the Doppler shift in the X-band and it is a function of the SEP angle (Iess et al., 2014).

The estimate of the solar wind path delay is affected by the vertical extension of the IPT, its tilt and rapid rotation, and the geometry of Juno's trajectory. Indeed, during the inbound leg of each PJ, the radio signal can potentially cross the IPT at a high latitude, if the timing with the wiggling motion of the torus is favorable. Consequently, the path delay measured before the occultation is mainly due to the solar wind, but it may also contain a contribution from the IPT. This poses a strong conceptual limit, as it is not possible to decouple the solar wind from the torus at those times, hence the impossibility of retrieving the solar wind calibration. In order to make use of the radio data, we calibrate for the solar wind from the path delay where the IPT model predicts a delay smaller than 5% the minimum value. Therefore, we can select the path delay which is minimally caused by the IPT, while retaining a meaningful time window to compute the solar wind delay.

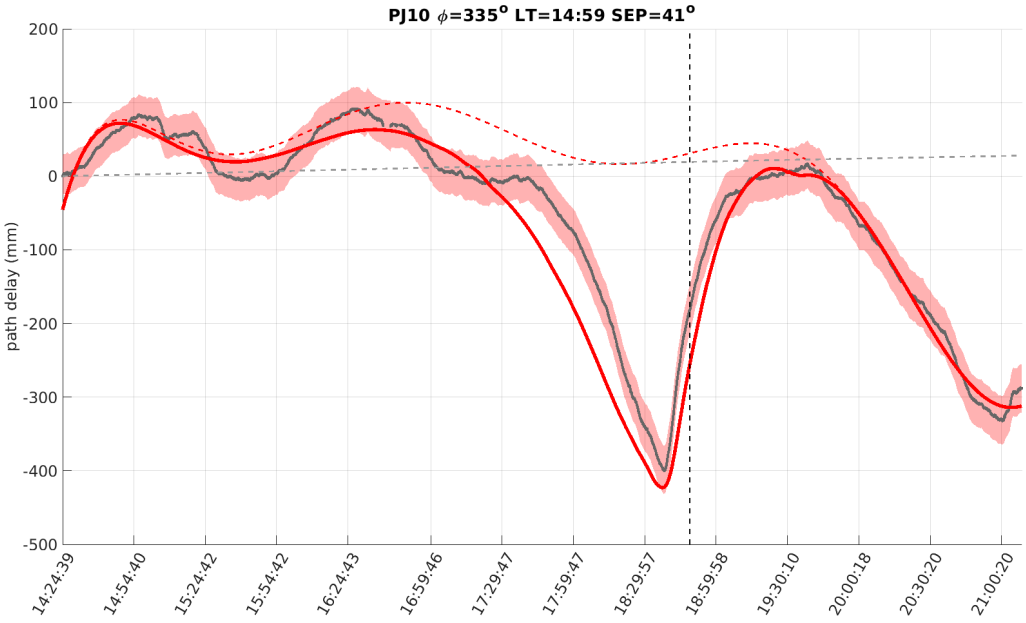

FIGURE 6.11: Path delay derived during PJ 10 (gray line) and example of the solar wind removal. The fluctuations before 17:30 and after 19:30 cannot be physically modeled. The red dashed line represents the empirical background caused by the solar wind and it is obtained from a 9^{th} degree polynomial fit to the *measured* path delay at the times when the *modeled* path delay is less than 5% than the absolute minimum value (i.e: the peak of the modeled signature). The red line is the sum of the empirical solar wind background and the modeled path delay. The gray dashed line is the contribution expected from a static model of the solar wind density. The vertical dash line is the time of the spacecraft closest approach to Jupiter. The longitude and local time reported over the path delay plot are the same as in Fig. 6.10.

6.3.2 Determination of the Io Torus State from the Footprint Position and the Radio Occultations

The model used in section 6.1 to predict the position of the IFP needs to compute the plasma density along the magnetic shell connected to Io's orbit. On the contrary, the simulations of the radio occultations require a full 3D models of the IPT that includes its radial structure. To this end, we assume the Voyager 1 ion mixing ratios and plasma temperature of the IPT reported by Bagenal (1994) and Dougherty et al. (2017) (see Fig. 6.12);

the data presented in those works are then smoothed between 5 and 10 R_J and used as the reference radial profile of the torus. The electron density at the centrifugal equator is also estimated from Voyager 1 data, but it is analytically modeled in four regions, according to the equation:

$$\begin{aligned} n_{e0}(r) = N_1 exp\Big[-\Big(\frac{r-R_1}{W_1}\Big)^2\Big] + \\ + N_2 exp\Big[-\Big(\frac{r-R_2}{W_2}\Big)^2\Big] + \\ + N_3 exp\Big[-\Big(\frac{r-R_3}{W_3}\Big)^2\Big] f_{warm}(r) + \\ + N_4 exp\Big[-\frac{|r-R_4|}{W_4}\Big] f_{disk}(r) \end{aligned} \tag{6.22}$$

where

$$\begin{aligned} f_{warm}(r) = \frac{1}{\pi}\Big(\frac{\pi}{2} + atan\Big(\frac{r-5.8}{0.01}\Big)\Big) \\ f_{disk}(r) = \frac{1}{\pi}\Big(\frac{\pi}{2} + atan\Big(\frac{r-8.5}{0.5}\Big)\Big) \end{aligned} \tag{6.23}$$

The value of r in Eq. 6.23 is in unit of R_J, and the values of N_i, R_i and W_i in Eq. 6.22 corresponding to each IPT region are reported in Table 6.4.

Table 6.4: Parameters of the radial electron density at the centrifugal equator used in Eq. 6.22 to derive the profile in Fig. 6.12.

IPT region	N_i (cm^{-3})	R_i (R_J)	W_i (R_J)
cold disk (1)	1800	5.2	0.3
ribbon (2)	3000	5.7	0.1
warm torus (3)	2000	5.9	1.8
disk trns. (4)	100	8.5	2

The cold disk and the ribbon are hence modeled as Gaussian functions, the warm torus as a half-Gaussian function (to simulate the D-shape of the torus), and the transition into the plasmadisk - that is: the region between 10 and 15 R_J - as a decreasing exponential. The model of this latter region agrees with the plasma density measured at Europa's and Ganymede's orbit ($\sim$150 cm^{-3} and $\sim$10 cm^{-3}, respectively). Outside 10 R_J, the plasma temperature is assumed to increase exponentially, in order

to match the observed values of ∼180 eV and ∼400 eV at Europa's and Ganymede's orbit, respectively. In the same region, the plasma composition is assumed to be frozen, which is consistent with the Voyager 1 observations and with the low collisional rate. Inside about 4.9 R_J, there are little plasma measurements, thus we also assume that the plasma properties are constant. This region contributes little (∼ 1 mm) to the path delay, thus its details are not fundamental. The radial profiles are modulated according to the System III longitudinal variation detected by Cassini (Steffl et al., 2006), which consider a ∼5% variation in electron density and ∼10% in temperature. The radial profiles shown in Fig. 6.12 are used as boundary conditions to solve the diffusive equilibrium Eqs. 6.2-6.4: this generates the density distribution of the IPT, whose cross section is similar to the one shown in Fig. 2.3 and 6.10.

According to the sensitivity test of section 6.1.2, the most sensitive parameters of the model for determining the satellite footprint position are the plasma peak density and temperature. As shown in Fig. 6.10, the signature of the path delay is also affected by the same parameters. But, while the footprint position exhibits a negligible dependence on the proton distribution, the presence of hydrogen in the model affects the path delay on the sides of the occultation signature of the IPT. A comparison between the path delay obtained with and without the protons in the density model is shown in Fig. 6.13. It is clear that the presence of hydrogen is negligible near the peak of the signature, while it greatly increases outside of it. This is not unexpected. Indeed, contrary to the centrifugally confined heavy ions, the protons are more widely spread along the magnetic field. Because of their minor role in determining the total plasma mass of the IPT compared to the oxygen and sulfur, they do not greatly affect the position of the footprint. Nevertheless, they are likely the dominant species at high latitudes, and, because of the charge-neutrality tendency of plasmas, they determine the presence of electrons, which affects the path delay. In order to avoid further complications besides the solar wind calibration mentioned at the end of section 6.3.1, in the present work we use an IPT model without hydrogen.

In order to compare JIRAM and the radio data, we compute the IPT

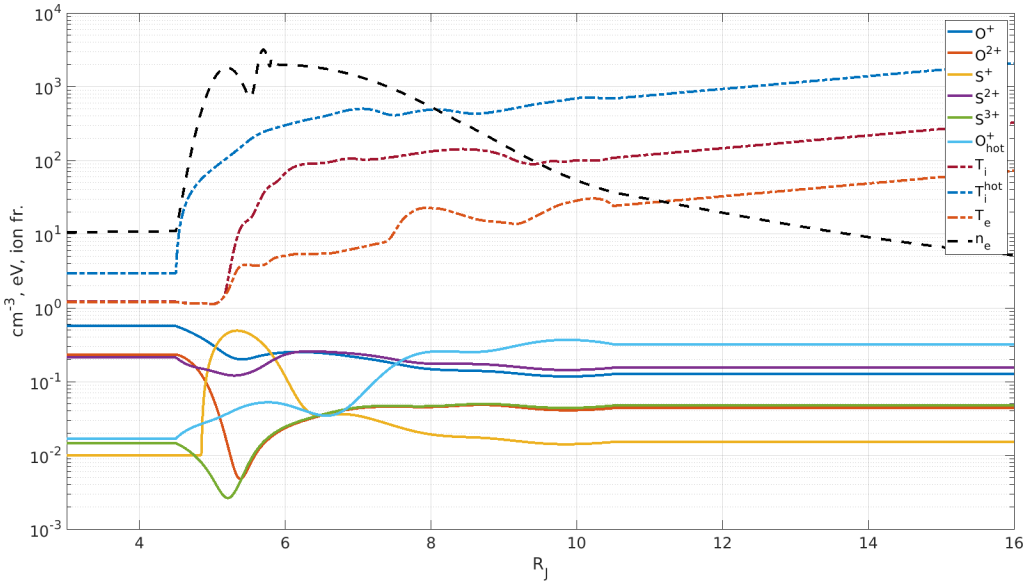

FIGURE 6.12: Radial profile of the IPT used to simulate both the auroral footprint position and the path delay measured by the radio occultations. The continuous lines are the mixing ratios of the major species of the torus, the dot-dashed lines the particles temperatures. The black dashed line is the electron density at the centrifugal equator. The curves are derived by smoothing the data reported by Bagenal (1994) and Dougherty et al. (2017). The composition is assumed frozen outside $\sim$ 10 R_J and inside 4.9 R_J, the latter because of the lack of data. The ion temperature from $\sim$ 10 R_J outwards is assumed to increase exponentially with an e-fold scale-length of 5 R_J, while the density decreases exponentially over a scale-length of 2 R_J. The radial profiles of density and temperature between 10 and 15 R_J are estimated in agreement with the plasma values at Europa's and Ganymede's orbit.

density distribution according to two scaling factor, S_d for the density and S_T for the temperature, respectively. These two factors are used to multiply the electron density and particle temperature profiles shown in Fig. 6.12, while the ion densities are obtained from the electron density and the ion mixing ratios. Therefore, several states of the IPT are computed according to the diffusive equilibrium model Eqs. 6.2-6.4 by changing these two scaling factors. In this section, we explore the range of S_d and S_T between 0.5 and 2, with steps of 0.25, which yields to a total of 49 IPT states. These values are approximately the same parameter space covered in section 6.1.

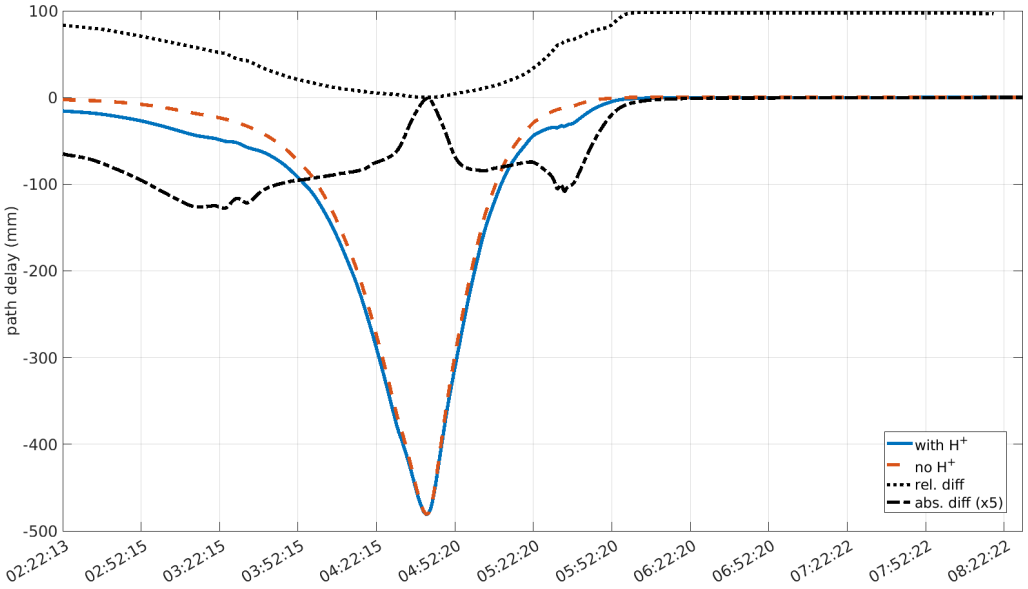

FIGURE 6.13: Comparison of the modeled path delay for PJ 21, with and without the protons (blue and red dashed lines respectively). The dotted line is the relative difference between the two models, while the dot-dashed line is five times the absolute difference.

To determine the conditions of the IPT, we use the footprint position observed by JIRAM to determine the density-temperature parameter space compatible with the observations. To this end, for each combination of S_d and S_T, we compute the distance between the predicted and the observed positions, which gives a contour plot like the one shown in Fig. 6.14. For each value of S_T, we then determine the best-matching value of S_d and simulate the corresponding path delay, which are the plots in Fig. 6.14. Among those plots, we used the widest IPT signature[5] to determine the time windows when the torus contribution to the path delay is less than 5%: these data are used to fit the solar wind path delay, which is then subtracted to the observed path delay and compared with the model.

The peak electron density and the radial extension of the torus are degenerate parameters of the Juno occultations. As shown by Phipps and

[5]That is: the signature corresponding to the largest time window where the IPT contribution to the delay is higher than 5% the minimum of the path delay.

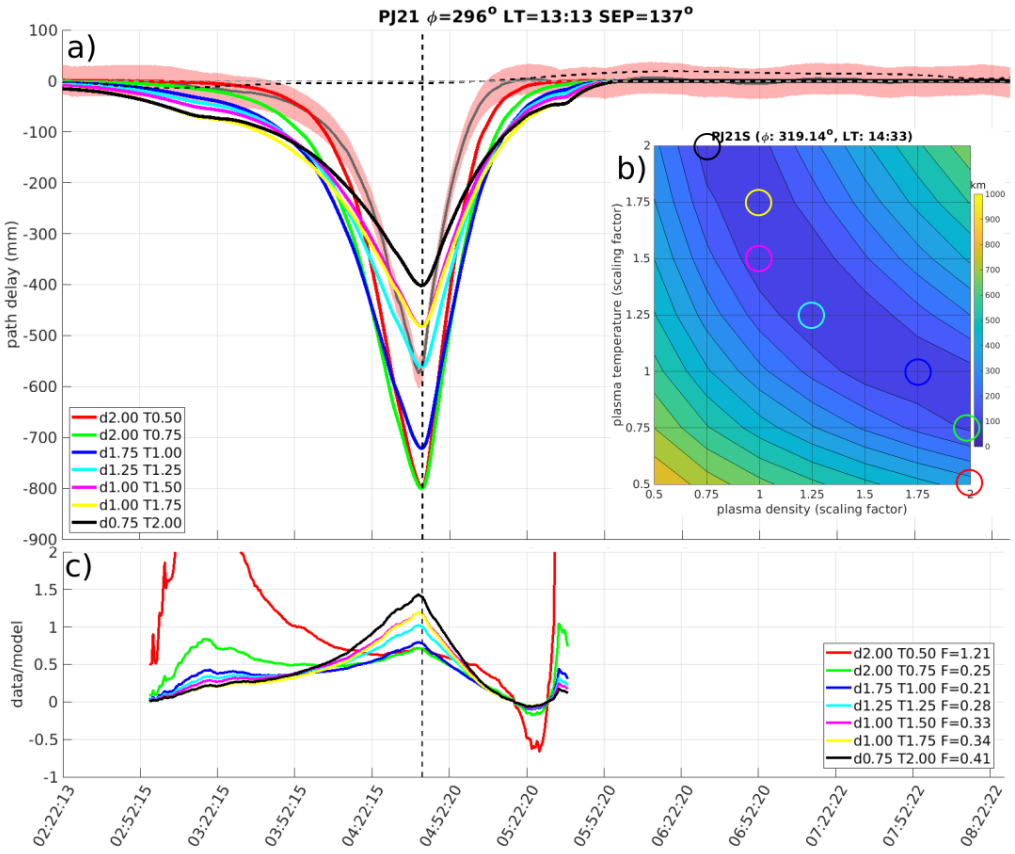

FIGURE 6.14: *(a)*: Observed (grey line) and modeled path delay (coloured lines). The modeled lines are obtained according to the values of S_d and S_T reported in the legend. The dashed lines represents the empirical background caused by the solar wind and they are obtained from a 9^{th} degree polynomial fit to the path delay. The vertical dash line is the time of the closest approach of the spacecraft. The longitude and local time reported over the path delay plot are the same as in Fig. 6.10. *(b)*: contour plot showing the distance between the footprint observed by JIRAM and the one predicted by the IPT model, as a function of the scaling factors S_d and S_T. For each value of S_T, we compute the path delay corresponding to the IPT that minimize the difference between the JIRAM observation and the model. These cases are highlighted by coloured circles, and they correspond to the path delay plots. The longitude and local time reported above the contour plot are relative to Io. *(c)*: ratio between the observed and modeled path delay over the IPT signature. The factor F in the legend corresponds to the sum of the squared residuals between the ratios and their respective average, and it is used to measure the "flatness" of these curves.

Withers (2017) and Moirano et al. (2021a), the path delay signature of the IPT can be approximately fitted by a sum of Gaussian functions of the form

$$delay(t) \propto TEC(t) = \sum_i N_i W_i exp\Big[- \Big(\frac{z(t) - Z_i}{H_i} \Big)^2 \Big] \qquad (6.24)$$

where the summation is over the regions of the IPT, N_i, W_i, Z_i and H_i are the peak electron density, radial extension, offset from the centrifugal equator and vertical scale-height of each region of the torus, and $z(t)$ is the cylindrical z-coordinate of Juno in the centrifugal frame[6]. The torus TEC seen by Juno is roughly equivalent to the radial electron column density of the IPT, as the line of sight to the DSN ground station stretches almost radially, as depicted in Fig. 6.10. Therefore, the peak electron density cannot be directly determined from Juno radio occultations, without assuming the radial structure of the IPT.

According to Eq. 6.24, it is clear how the TEC content of the IPT is a parameter decoupled from its temperature, when using Juno radio occultations. Indeed, the peak TEC $N_i W_i$ is determined by the depth of the path delay signature, while the H_i by its width. In turn, the scale height H_i depends approximately on the plasma temperature (see the sensitivity test in section 6.1.2 and Bagenal and Sullivan (1981)). As the radial size of the torus is not a sensitive parameter for the auroral footprint, it has not been included as a free parameter. Therefore, it is possible that the path delay simulated with the present model either over- or under-estimates the observed delay, due to variations in the radial extension of the IPT. To compare the simulations of the path delay with the observations, we calculated the ratio between the two curves for each model over the time window excluded from the solar wind calibration. Indeed, due to the degeneracy of N_i and W_i - that is: the peak density and the radial structure of the IPT - we expect the best-fit model curve to agree with the data, apart for a constant factor. The plots showing the ratio between data and model are shown in panel *c* of Fig. 6.14. For each curve, we compute the residuals with respect

[6]Eq. 6.24 is obtained by integrating an approximate density profile of the IPT along the radial direction. See Moirano et al. (2021a) for the details of this approximation and for an analytical improvement to Eq. 6.24.

to their respective average, and in the legend we report the value of the "flatness" F of each curve, which is the square root of the sum of the squared residuals, divided by the number of data-points. As the model and the data are expected to agree within a *constant* multiplicative factor, the flatter the curve, the better the match. For example, for PJ 21 in Fig. 6.14, the flattest curve is the one given by $S_d = 1.75$ and $S_T = 1.00$: this means that the width of the path delay obtained with these values is the best match to the width of the observed signature. The uncertainty can be estimated from the next two best matches, which implies that the torus conditions during PJ 21 are described by $S_d = 1.75^{+0.25}_{-0.50}$ and $S_T = 1.00 \pm 0.25$.

The signature of the $S_d = 1.75$ case (blue line in Fig. 6.14) does not match the path delay, which is better estimated from the depth of the signature with $S_d = 1.25$ (light blue line). By chance, both the radio occultations and Io where located at close System III longitudes and local times during PJ 21, which likely rules out any density variations in the IPT content (see section 2.1) between the two observations. We suggest three possibilities to account for different values of S_d: (1) the radial electron distribution of Fig. 6.12 overestimate the width of the warm torus, (2) the presence of the transition region into the plasmadisk, (3) the density of the ribbon was much lower than the one expected from Voyager 1. We tested these three hypotheses by (1) reducing the width of the Gaussian that models the warm torus electron density from 1.8 R_J to 1.44 R_J (i.e: 80% decrease of W_3 in Eq. 6.22), (2) removing the transition region (i.e: $N_4 = 0$ in Eq. 6.22) or (3) reducing the peak density of the ribbon N_2 from 3000 cm^{-3} to 1000 cm^{-3}. The reduction in the warm torus size produces the best agreement with the path delay depth, although a combined result of all three sources is possible. In Fig. 6.15, the model with $S_d = 2.00$ and $S_T = 0.75$ of Fig. 6.14 is compared with the same model, but with the the three above-mentioned modification to the radial profile. The combination of both JIRAM and the radio occultations therefore suggests that, during PJ 21, the IPT peak electron density of the warm torus was ~ 4000 cm^{-3}, while the ion temperature was ~ 40 eV, by converting the radial profiles in Fig. 6.12 with $S_d = 2$ for the electron density and $S_T = 0.75$ for the ion temperature. The ribbon might have been

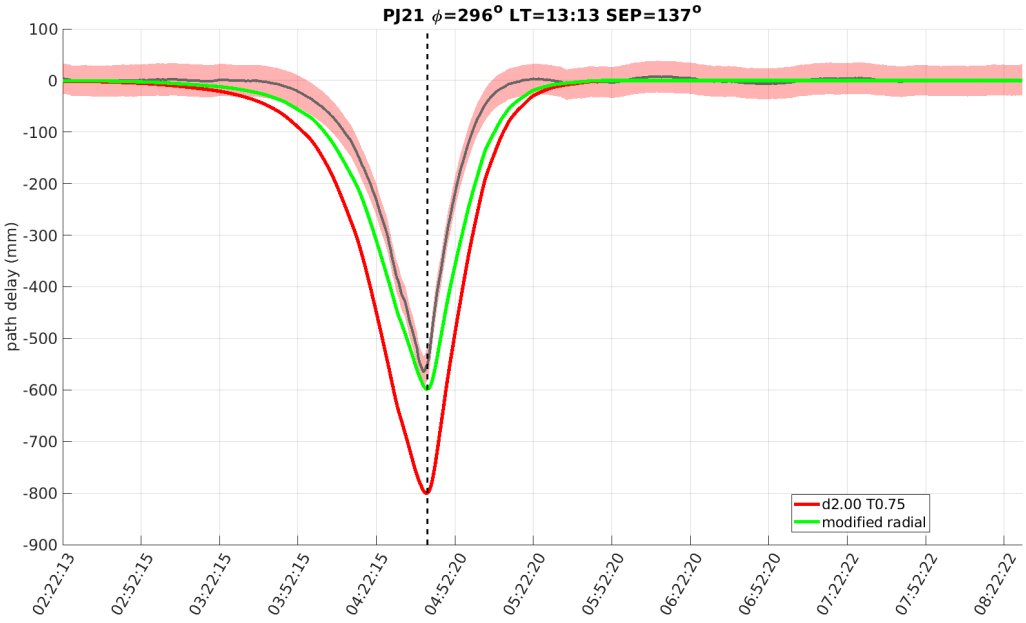

FIGURE 6.15: Comparison of the path delay obtained with $S_d = 2$ and $S_T = 0.75$ (red line) and the path delay obtained with the same model but with a reduced radial extension of the warm torus, a highly depleted ribbon and no plasma between 10 and 15 R_J (green line). The details of the model with the modified radial structure are given in the text.

highly depleted, although the high density retrieved from JIRAM data may suggests that the ribbon actually entered the warm torus, leaving its usual location depleted. This is similar to what observed by Galileo (Bagenal et al., 1997). Moreover, the ion temperature here derived agrees with the lower temperature measured by Galileo with respect to Voyager 1 (Crary et al., 1998).

6.3.3 Results

The method explained in section 6.3.2 is here applied to the whole dataset obtained from the JIRAM+UVS observations and Juno radio occultations. PJ 13, 14, 25, 36 and 37 have not been included yet, either because of the lack of a sufficiently wide time window to determine the solar wind contribution to the path delay, or because of the IPT signature being cut by the time

window of the observation. These orbits require additional processing before representing a reliable source of information. Fig. 6.16 shows the electron density and ion temperature for each PJ, alongside the average derived from the present dataset. Several remarks should be observed. First, The average $S_d \approx 1.3$ and $S_T \approx 1.4$ suggest an overall higher plasma content and temperature compared to the Voyager 1 era. Both quantities show large variations from one PJ to the other: this has already been reported in other Juno-based works (Hue et al., 2023; Moirano et al., 2021a, 2023; Phipps et al., 2021). Furthermore, the density derived by comparing the path delay with the IFP observations at the northern hemisphere are not always the same as the ones derived from the southern pole. In particular, the densities derived from PJ 6, 8, 15, 33 and 35 are only marginally compatible between the two hemispheres. On the contrary, the temperature shown in the bottom plot of Fig. 6.16 is consistent between the two hemispheres. The reason for such north-south discrepancy is still not clear. Lastly, the electron density and ion temperature are anti-correlated, with a correlation factor -0.5±0.2. This is not unexpected if the IPT can be considered a plasma whose density and temperature are related by a polytropic $N \sim T^{-1}$, which relies on the assumption that density and temperature variations take place at constant pressure. Nevertheless, the anticorrelation shouldn't be taken too strictly. Indeed, the variability of the IPT and its plasma source might produce transient states of the torus, during which the anticorrelation between density and temperature is not necessarily satisfied. The anticorrelation should instead hold more strictly when the supply of plasma is steady and the ion composition does not change appreciably.

The density and temperature are reported in Fig. 6.17 as functions of Io longitude and local time at the time of JIRAM observations. The Juno mission has been allowing an overall good coverage of longitudes and local times, although noticeable gaps are present in the dusk sector (LT = 15-21) between 0° and 180°, as well as in the dawn sector (LT = 3-9) between 90° and 270°. The noon sector (LT = 9-15) is the most densely measured; the plots of the plasma properties in this sector are reported in Fig. 6.18. Moreover, we filtered out the results obtained from images of

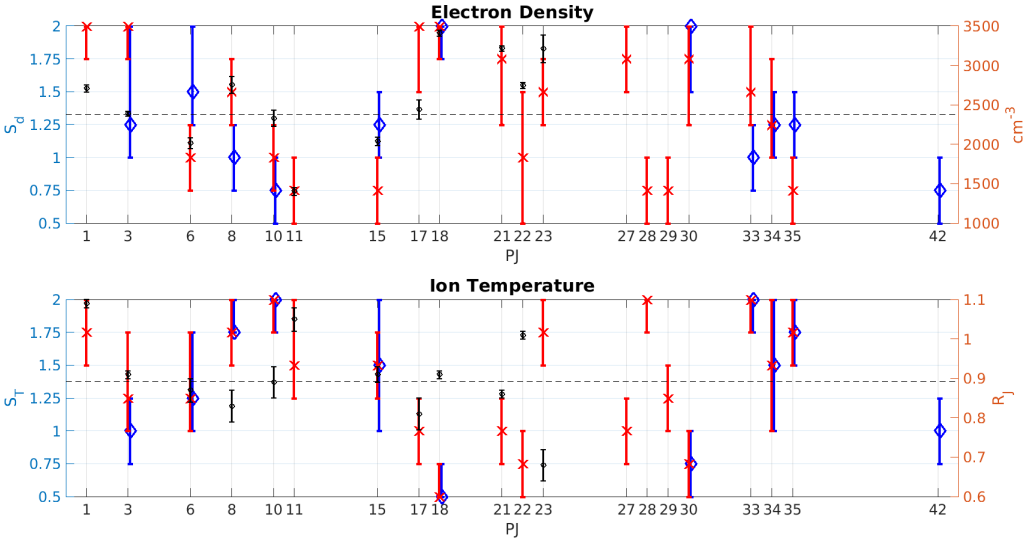

FIGURE 6.16: Plot of the electron density and ion temperature of the IPT derived for each PJ, in terms of the scaling factors S_d and S_T. The blue diamonds are obtained from observations of the the IFP in the northern hemisphere, the red crosses in the southern one. The dashed line is the average value. The black circles are the electron density and scale height of the IPT (axes on the right) derived from Juno radio occultations only (Moirano et al., 2021a).

the northern IFP when Io was between 155° and 245°, and of the southern IFP when Io was between 335° and 65°. Indeed, in those conditions, Io was orbiting at high centrifugal latitudes, hence one of the two Alfvén wings is less sensitive to the presence of the IPT, compared to observations with the satellite at other longitudes. Those observations are thus removed from the dataset, as they are deemed less reliable to determine the IPT state than the remaining. The value of S_d seems to be 0.75 between ∼0° and ∼180°, with the exception of the data point at ∼140°. Instead, the density seems to increase between ∼220° and 320°. The temperature shows a similar variability, anticorrelated with the electron density. Hence, both density and temperature seem to exhibit a longitudinal variation that is not accounted for in the model. A similar result is obtained by plotting the IPT parameters at all local times as functions of the longitude (not shown), although the presence of a longitudinal variation is less clear.

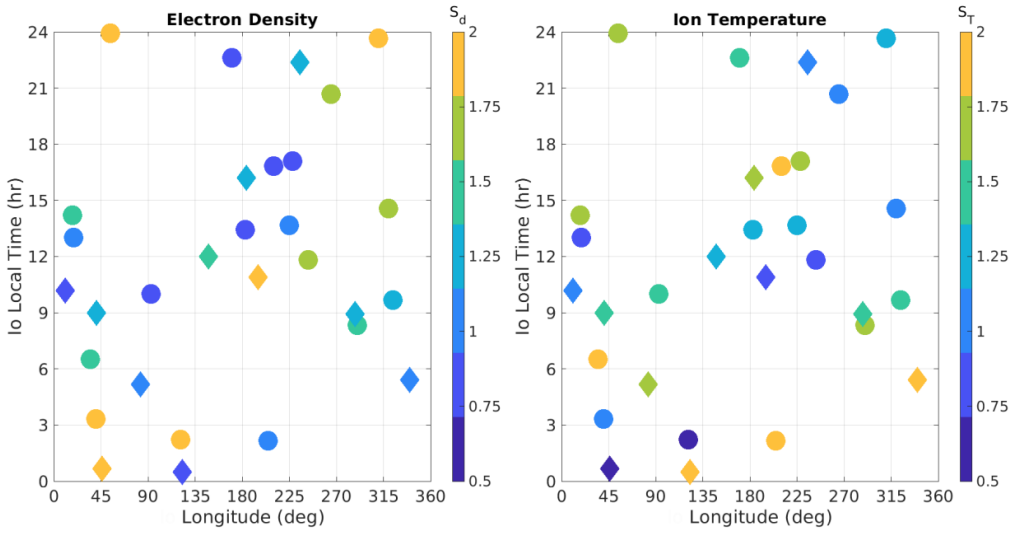

FIGURE 6.17: Scatter plots of the IPT electron density and temperature as functions of the longitude and local time. Each data point is color-coded according to the corresponding value of S_d or S_T. The diamonds are determined from observations of the IFP in the northern hemisphere, the circles in the southern one.

Due to gaps in the plots of Fig. 6.17, we cannot single out a specific longitudinal sector and inspect the local time variations at that longitude. In Fig. 6.19, instead, density and temperature are shown as a function of local time for all longitudes. While the electron density appears to be uncorrelated with local time, the ion temperature suggests the presence of two peaks in the dawn and dusk sectors. According to the data in Fig. 6.17, it is not possible to determine if this is due to a combined effect of local time and longitude variations.

6.3.4 Discussion and Further Developments

The state of the IPT obtained by combining the JIRAM and UVS observations of the IFP with the radio occultations of the IPT performed by Juno appears different with respect to the IPT observed during the Voyager 1 mission, which is used as a reference state in the present work. In particular,

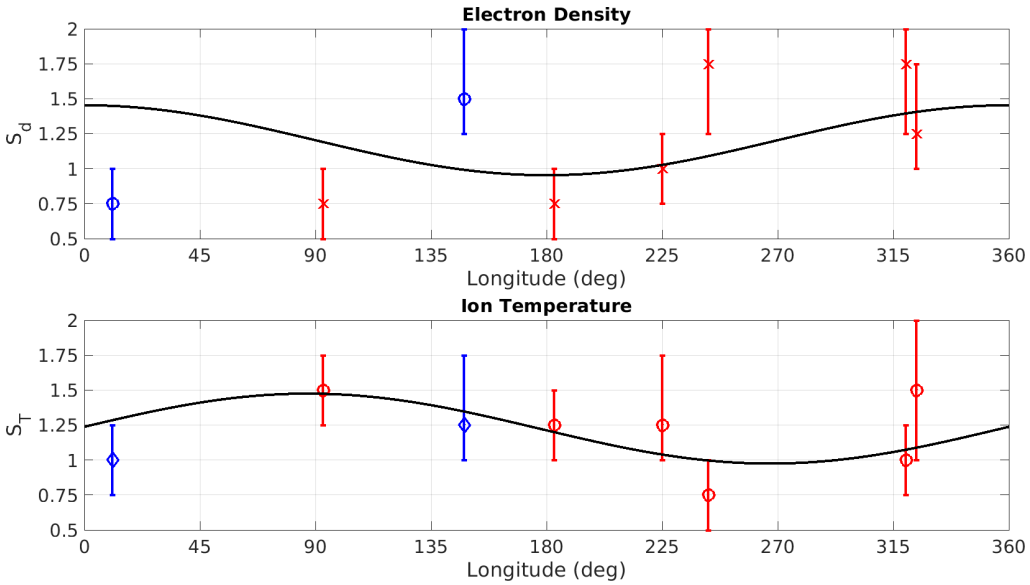

FIGURE 6.18: Plot of the electron density and ion temperature of the IPT as function of Io's longitude at the time of JIRAM observations, in terms of the scaling factors S_d and S_T. The data are acquired in the noon sector, between LT = 9 and 15. The blue diamonds are obtained from observations of the the IFP in the northern hemisphere, the red crosses in the southern one. The black line is the fit obtained with a first-order Fourier series.

both the plasma density and temperature are, on average, ∼30% higher. The peak electron density and scale-height of the IPT derived from Juno radio occultations alone (Moirano et al., 2021a) are shown in Fig. 6.16, alongside the results of the present analysis. The results of the two studies show a good qualitative agreement, which supports their robustness. The average peak electron density derived from the radio occultations is ∼2500 cm^{-3}, which agrees with $S_d \sim 1.3$. Nevertheless, large deviations from the average are reported, both in the present work and in previous analyses of Juno radio occultations (see also Phipps et al. (2019, 2021)). These fluctuations are larger than the System III modulation of electron density and temperature of ∼5% and ∼10%, respectively, although the Cassini observations that led to that estimate shows fluctuations of about 30%. The fluctuations shown in Fig. 6.16 are also more frequent than the occurrence of strong volcanic

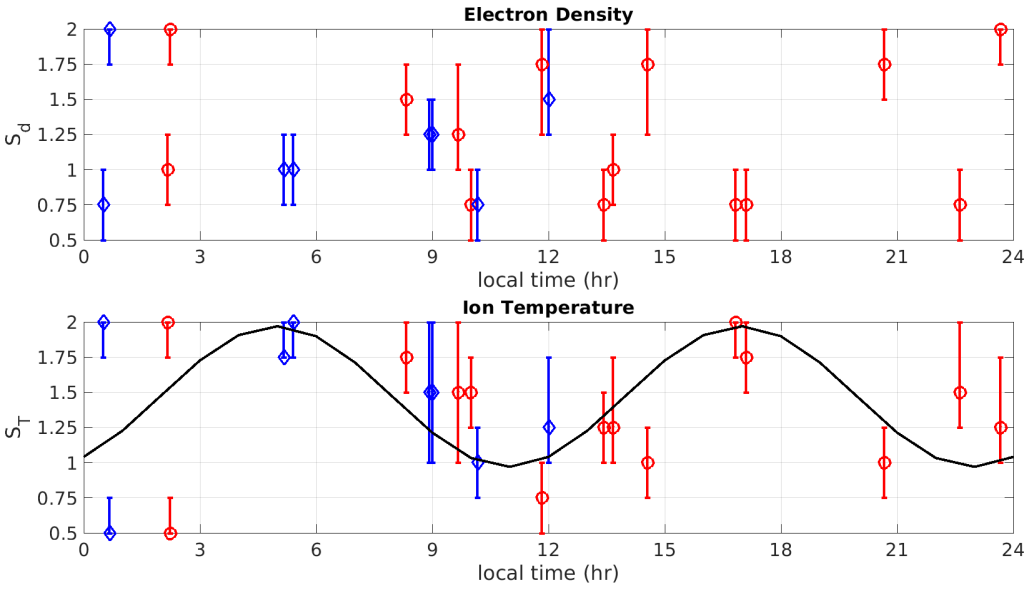

FIGURE 6.19: Plot of the electron density and ion temperature of the IPT as function of Io's local time at the time of JIRAM observations, in terms of the scaling factors S_d and S_T. The blue diamonds are obtained from observations of the IFP in the northern hemisphere, the red crosses in the southern one. The black line is the fit obtained with a second-order Fourier series.

outburst, which are expected to occur every ∼5-10 years. Moirano et al. (2021a) suggests a potential correlation of the electron content of the torus with the periodicity of volcanic activity from September 2013 to June 2018. Nevertheless, the response of the IPT to the time-variable volcanic activity of Io is not straightforward, hence any conclusion should be carefully drawn.

Thomas (1993) classified the variability of the IPT based on their typical time-scale, ranging from tens of minutes to a few years. Among those, the IPT shows typical variations between a few tens of days and several months. For example, the brightness of the S^+ in the ribbon region during March 1991 was much stronger than in December 1989. During the two observations, the ribbon was observed at the same local time and System III longitude, which rules out any longitudinal effect. Similarly, the density reported by Voyager 2 was ∼50% higher than the one recorded by Voyager 1 (Delamere and Bagenal, 2003): the two spacecraft performed their flyby

in March and July 1979, respectively, hence this variation occurred over a few months. Earth-based observations of S^+ have been performed regularly since the '80s (see Fig. 8 of Thomas (1993)), and they show that the IPT brightness varies by a factor 3 over a couple of years, although the time coverage of those observations does not allow to determine a lower limit on the temporal scale for such variations. Observations of the S^+, S^{2+} and O^+ emission lines from ground also revealed density and temperature variations over a few months (Morgan, 1985). As Juno takes about 50 days between two perijoves, we suggest that the variability shown here in Fig. 6.16 and 6.17 may belong to the same type of variability that drove the above-mentioned, direct observations of the torus. At present, the physical mechanism underlying these variations is still not clear. The driver of the IPT variability can lie either in the plasma source - that is: Io and the neutral cloud - or in external factors. In the former case, the dynamics of the torus is determined by the variability of the plasma supply, hence the observed variations might be ascribed to variations in the plasma supply from Io or the plasma cloud. Observations of Io's atmosphere and its hot spots activity have not led to a clear and unambiguous understanding of the response of the IPT to the volcanic activity (e.g: Roth et al. (2020)). Therefore, it is not possible to determine if the variations derived in this work are compatible with changes in the interaction between Io, the torus and the neutral cloud. It is suggested that external factors, such as the solar wind or electron injections from the outer magnetosphere, might be the root cause of the IPT variability (Louarn et al., 2014; Moirano et al., 2023; Morgenthaler et al., 2022a; Roth et al., 2020). Nevertheless, there are no available models to quantitatively compare with the Juno observations presented here. It is difficult to interpret the variability retrieved in the analysis of this last section, as it fit the temporal variability of the IPT over a typical time-scale of a few tens of days, but its underlying driving mechanism is hardly explained by either the current understanding of changes in the plasma source or of any potential external drivers.

Future development of the present study may improve the quality of the data presented in this section:

- The IPT model used in this section and in section 6.1 is computed according to the diffusive equilibrium model Eqs. 6.2-6.4. In turn, those equations are obtained by integrating the momentum equation for each plasma species, *assuming constant temperature along the magnetic field lines*. Measurements of the ion perpendicular temperature shows that the temperature can increase by about 50% outside the IPT (Thomas and Lichtenberg, 1997). This does not necessarily imply a variation in the parallel temperature, but a sensitivity test that explores the effect of the field-aligned distribution of temperature is recommended to properly determine the vertical size of the IPT.

- The discrepancy in the parameter space derived from the observations of the footprint position between the northern and southern hemisphere needs to be further investigated. To this end, the simultaneous observations from both JIRAM and UVS can be compared, which may help to shed light onto the nature of this north-south asymmetry.

- Several radio occultations have not been used in the present study. The occultations performed during PJ 13, 14, 25, 36 and 37 have been excluded because of the additional processing required to correctly estimate the solar wind contribution to the path delay. Other occultations (PJ 31, 32, 39, 40 and 41) have been discarded because the IPT signature was more difficult to identify, due to the high fluctuations in the background delay. Therefore, there are ten more radio occultations that have not been included and that can potentially fill the gaps in the plots of Fig. 6.17.

- The analysis performed in this thesis relies on in-situ, high resolution data, which is fundamental to precisely determine the position of the satellite footprint. In order to apply the same method to Earth-based observations, the instrument must be able to detect variation in the footprint position within a few hundreds kilometres. The application of the method shown in chapter 6 to near-Earth data (such as HST observations) is hoped for a next work.

- Earth-based facilities and spacecraft have been sparsely, but periodically monitoring Io, the IPT and the Jovian aurorae for the last few decades (Thomas, 1993). Recently, the IPT is being investigated as continuously as possible[7] to understand its interaction with Io and the Jovian magnetosphere, as well as to shed light on its variability. The results shown in this last chapter will be hopefully enriched by spectrometry and imaging performed from Earth, in order to carry a proper multi-instrument monitoring of the IPT out.

In conclusion, the IPT shows a remarkable variability, which is still not properly modeled from a theoretical point of view. The torus is located between the middle and inner Jovian magnetosphere, where the role of the solar wind is expected to be negligible, especially compared to the strong centrifugal confinement caused by the strong magnetic field and the fast planetary rotation. The volcanic activity of Io is the ultimate source of plasma in the whole magnetosphere, and its variability has been suggested to be the origin of the variations of the IPT, which in turn can affect the outer regions of the magnetosphere. Although episodes of Iogenic volcanic activity have been associated to noticeable changes in the IPT (e.g: Delamere et al. (2004); Tsuchiya et al. (2018)), variations of the IPT state have also been recorded during periods of low mass loading (Delamere and Bagenal, 2003; Thomas, 1993). This might suggest that the IPT can be affected by external factors, like electron injections, but the physical processes are poorly understood. Both the present work and spectroscopic observations revealed a high variability over a few months, with Juno that have been taking measurements of the IPT every $\sim$ 50 days for about 6 years. Nevertheless, these variations still remain unexplained: we hope that more theoretical models will be developed in the future to compare with the IPT observations and to better understand the interplay between Io, the IPT and the Jovian magnetosphere.

[7]For example, by the Hisaki mission and the Planetary Science Institute's Io Input/Output observatory (IoIO) (Morgenthaler et al., 2022a).

APPENDIX A

Equations

In this appendix all the formulae typically used in magnetohydrodynamics are reported. These equations holds only if the typical timescale of the system is longer than the inverse of the plasma and cyclotron frequencies, and length-scale is larger that the Debye length and the electron and ion skin depth (e.g: Krall and Trivelpiece (1973)).

In the following, an operation $\vec{A}\vec{B} = \mathbf{C}$ represents the outer product between $\vec{A}$ and $\vec{B}$, that is: $C_{ij} = A_i B_j$.

A.1 Multiple-Fluids Equations

The equations below must to be applied to each species s in the plasma. The physical quantities are defined as follow:

n_s : number density of particles.

$\vec{u}_s$: bulk speed of the species s.

S_s,L_s : source and loss of particles of the species s, respectively.

m_s : particle mass.

q_s : particle charge.

$\vec{E}$,$\vec{B}$: electric and magnetic field, respectively.

$\mathbf{P}_s$: pressure tensor.

$\nu_{s,t}$: collision frequency between the spiecies s and t.

$\mathbf{Q}_s$: heat flux tensor.

c : speed of light.

Mass continuity:

$$\frac{\partial n_s}{\partial t} + \nabla \cdot (n_s \vec{u}_s) = S_s - L_s \tag{A.1}$$

Momentum conservation:

$$n_s m_s \frac{\partial \vec{u}_s}{\partial t} + n_s m_s (\vec{u}_s \cdot \nabla)\vec{u}_s = n_s q_s \Big(\vec{E} + \frac{\vec{u}_s \times \vec{B}}{c}\Big) + \nabla \cdot \mathbf{P}_s - \\ - \sum_t n_s m_s (\vec{u}_s - \vec{u}_t)\nu_{s,t} \tag{A.2}$$

where the last term represents the collisions between the s and t species.

Energy conservation:

$$\frac{\partial \mathbf{P}_s}{\partial t} + \mathbf{P}_s(\nabla \cdot \vec{u}_s) + \nabla \cdot \mathbf{Q}_s + \Big[\Big(\mathbf{P}_s \cdot \nabla\Big)\vec{u}_s\Big]_S = \frac{q_s}{m_s c}\Big[\mathbf{P}_s \times \vec{B}\Big]_S \tag{A.3}$$

where

$$\Big[\Big(\mathbf{P}_s \cdot \nabla\Big)\vec{u}_s\Big]_{S,ij} = P_{ik}\frac{\partial u_j}{\partial x_k} + P_{jk}\frac{\partial u_i}{\partial x_k}$$

and

$$\Big[\mathbf{P}_s \times \vec{B}\Big]_{S,ij} = \epsilon_{ikl} P_{jk} B_l + \epsilon_{jkl} P_{ik} B_l$$

A.2 Single-Fluids Equations

These equations are obtained from the set of equations in section A.1 with the trasformations

$$n = \sum_s \frac{m_s n_s}{m_s} \tag{A.4}$$
$$\rho_c = \sum_s q_s n_s$$
$$\vec{U} = \sum_s \frac{m_s n_s \vec{u}_s}{m_s n_s}$$
$$\vec{J} = \sum_s q_s n_s \vec{u}_s$$

Mass continuity:

$$\frac{\partial n}{\partial t} + \nabla \cdot (n\vec{U}) = S - L \tag{A.5}$$

Charge continuity:

$$\frac{\partial \rho_c}{\partial t} + \nabla \cdot \vec{J} = 0 \tag{A.6}$$

Momentum conservation:

$$n\frac{\partial \vec{U}}{\partial t} + n(\vec{U} \cdot \nabla)\vec{U} = -\frac{\nabla \cdot \mathbf{P}}{m_i} + \frac{\vec{J} \times \vec{B}}{m_i c} \tag{A.7}$$

The last term on the rhs can be re-written as $\vec{J} \times \vec{B} = \frac{1}{4\pi}(\nabla \times \vec{B}) \times \vec{B} = \frac{1}{4\pi}[\vec{B} \cdot \nabla)\vec{B} - \frac{1}{2}\nabla B^2] = \frac{1}{4\pi}\nabla \cdot (\vec{B}\vec{B} - \frac{1}{2}B^2\mathbf{I})$, where $\mathbf{I}$ is the identity matrix. The quantity $(\vec{B}\vec{B} - \frac{1}{2}B^2\mathbf{I})$ is known as *Maxwell magnetic stress tensor*.

Generalized Ohm's law

$$C_1\vec{E} + C_2\frac{\vec{U} \times \vec{B}}{c} + \frac{4\pi}{\omega_{pe}^2}\frac{\partial \vec{J}}{\partial t} = \tag{A.8}$$
$$= C_3\frac{\vec{J} \times \vec{B}}{enc} - \frac{1}{en}\nabla \cdot \left(\mathbf{P}_e - \frac{m_e}{m_i}\mathbf{P}_i\right) -$$
$$-\frac{4\pi}{\omega_{pe}^2}\nabla \cdot \left[C_4 en\vec{U}\vec{U} + C_5(\vec{U}\vec{J} + \vec{J}\vec{U}) - \frac{C_6}{en}\vec{J}\vec{J}\right]$$

(the coefficients C_1-C_6 are detailed in Cerri (2012)).

Ideal Ohm's law

$$\vec{E} + \frac{\vec{U} \times \vec{B}}{c} = 0 \tag{A.9}$$

A.3 Maxwell's Equations

$$\nabla \cdot \vec{E} = 4\pi\rho_c \tag{A.10}$$

$$\nabla \cdot \vec{B} = 0 \tag{A.11}$$

Faraday's Law

$$\nabla \times \vec{E} = -\frac{1}{c}\frac{\partial \vec{B}}{\partial t} \tag{A.12}$$

Ampère's Law

$$\nabla \times \vec{B} = \frac{1}{c}\Big(4\pi\vec{J} + \frac{\partial \vec{E}}{\partial t}\Big) \tag{A.13}$$

In MHD, the displacement current $\partial_t \vec{E}$ is usually neglected for non-relativistic processes. Indeed, from Eq. A.12 and the estimates $\partial_t \sim 1/\tau$ and $\nabla \sim 1/L$ (τ being the typical timescales and L the typical length scale), one obtains $E/B \sim U/c$, where U is the typical speed of the system and c the speed of light. By comparing the displacement current with $\nabla \times \vec{B}$, one obtains $\partial_t \vec{E}/\nabla \times \vec{B} \sim (E/B)(U/c) \sim U^2/c^2 \ll 1$ in the non-relativistic case.

A.4 Conductivity in a Magnetized Plasma

In a magnetized plasma, the conductivity is not isotropic, as the presence of magnetic and electric fields breaks the symmetry. Here there are the

definition of "parallel", Pedersen and Hall conductivities:

$$\sigma_{\parallel} = \frac{n_i q}{|\vec{B}|}\Big(\frac{\Omega_i}{\nu_i} + \frac{\Omega_e}{\nu_e}\Big) \tag{A.14}$$

$$\sigma_P = \frac{n_i q}{|\vec{B}|}\Big(\frac{\Omega_i \nu_i}{\Omega_i^2 + \nu_i^2} + \frac{\Omega_e \nu_e}{\Omega_e^2 + \nu_e^2}\Big)$$

$$\sigma_H = \frac{n_i q}{|\vec{B}|}\Big(\frac{\Omega_i^2}{\Omega_i^2 + \nu_i^2} - \frac{\Omega_e^2}{\Omega_e^2 + \nu_e^2}\Big)$$

where $\Omega_{i,e} = \frac{q_{i,e}B}{m_{i,e}c}$ are the ion and electron gyrofrequency, respectively, while $\nu_{i,e}$ are the ion-neutral and electron-neutral frequencies. The ionospheric currents are determined by

$$\vec{J} = \sigma_{\parallel}\vec{E}_{\parallel} + \sigma_P \vec{E}_{\perp} + \sigma_H \frac{\vec{E}_{\perp} \times \vec{B}}{|\vec{B}|} \tag{A.15}$$

where $\parallel$ and $\perp$ (parallel and perpendicular, respectively) are referred to the local direction of the magnetic field.

APPENDIX B

Short Glossary

- **Centrifugal equator** Plasmas tend to be confined by magnetic fields, so that any motion perpendicular to the field is strongly inhibited. Instead, the plasma is free to move along the field lines, therefore the dynamics of a magnetized plasma can be assimilated to an ensemble of beads sliding along wires (that is: the magnetic field lines). In a fast rotating magnetosphere, where the plasma experiences a strong centrifugal acceleration, the plasma is thus confined near the farthest point from the rotation axis along the magnetic field lines (Hill et al., 1974). The plane passing through these points is called *centrifugal equator* (Fig. 2.2), and, in a tilted dipolar-like magnetic field, it can be estimated as two-third between the spin equator and the magnetic equator.

- **Dispersion relation**: an equation that describe the relation between the wavelength λ and frequency ν of a wave in a medium. The quantity ω/k is known as *phase velocity*, where $\omega = 2\pi\nu$ and $k = 2\pi\lambda^{-1}$, while $\partial\omega/\partial k$ is the *group velocity*. A wave packet is considered non-dispersive when its group velocity is zero, which means that the speed of the waves is not dependent on their frequency.

- **Emission Angle**: angle between the normal to a body surface at

a given point and the line of sight from an instrument/observed to the same point. Hence, an emission angle near 0° corresponds to *nadir* observations, while an angle of close to 90° is used for *limb* observations.

- **Homopause**: it describes the transition region between the atmosphere whose composition is homogeneous, as it is determined by vertical mixing, and the one that is stratified and whose structure is mainly determined by gravitational settling.

- **Jupiter's surface**: being a gaseous planet, Jupiter does not have a defined surface like rocky planets. Nevertheless, the 1-bar pressure level is conventionally assumed as *the* Jovian surface. It can be approximated by an ellipsoid with equatorial radius $R_J = 71492$ km and polar radius $R_{Jp} = 66854$ km.

- **McIlwain L-parameter, L-shell, L-value**: it is the parameter used to refer to a specific set of magnetic field lines. For a dipole magnetic field, it represents all the field lines that cross the magnetic equator at a distance given by L times the planetary radius. For example, $L = 5$ represents all the field lines that cross the magnetic equator at 5 planetary radii.

- **Mixing ratio**: the ratio of the number density n_s of a given particle of species s over the electron number density n_e.

- **Mirror ratio**: the ratio of the magnitude of the magnetic field at two different points along the same field line. The importance of such parameter can be understand by considering the confining property of a magnetic field. Indeed, a charged particle in a magnetic field orbits in a gyromotion, which results in a current and thus in a magnetic moment. If the magnetic field changes slower than the gyroperiod of the charged particle, than the magnetic moment of the particle is an adiabatic invariant, i.e: it is constant. When the particle moves toward a region where the magnetic field increases, than

the conservation of both the particle magnetic moment and energy implies that the field-aligned component of the velocity must decrease, while the perpendicular component must increase. It is possible for the magnetic field to completely confine the particle (i.e: there is no field-aligned component of the velocity), if the field become strong enough. The mirror ratio therefore allows to estimate the degree of confinement of a plasma.

- **Poynting vector, flux**: mathematically, the Poynting vector is defined as

$$\vec{S} = \frac{\vec{E} \times \vec{B}}{\mu_0} \tag{B.1}$$

where μ_0 is the magnetic permeability, $\vec{E}$ and $\vec{B}$ are the electric and magnetic field, respectively. The flux of the Poynting vector represents the electromagnetic energy streaming across a given surface, while the vector itself represent the direction of such flow.

Bibliography

C. Acton, N. Bachman, B. Semenov, and E. Wright. A look towards the future in the handling of space science mission geometry. *Planetary and Space Science*, 150, Jan. 2018. doi: 10.1016/j.pss.2017.02.013.

C. H. Acton. Ancillary data services of NASA's Navigation and Ancillary Information Facility. *Planetary and Space Science*, 44(1), Jan. 1996. doi: 10.1016/0032-0633(95)00107-7.

A. Adriani, G. Filacchione, T. Di Iorio, D. Turrini, R. Noschese, A. Cicchetti, D. Grassi, A. Mura, G. Sindoni, M. Zambelli, G. Piccioni, M. T. Capria, F. Tosi, R. Orosei, B. M. Dinelli, M. L. Moriconi, E. Roncon, J. I. Lunine, H. N. Becker, A. Bini, A. Barbis, L. Calamai, C. Pasqui, S. Nencioni, M. Rossi, M. Lastri, R. Formaro, and A. Olivieri. JIRAM, the Jovian Infrared Auroral Mapper. *Space Sci Rev*, 213(1-4), Nov. 2017. doi: 10.1007/s11214-014-0094-y.

A. Adriani, A. Mura, G. Orton, C. Hansen, F. Altieri, M. L. Moriconi, J. Rogers, G. Eichstädt, T. Momary, A. P. Ingersoll, G. Filacchione, G. Sindoni, F. Tabataba-Vakili, B. M. Dinelli, F. Fabiano, S. J. Bolton, J. E. P. Connerney, S. K. Atreya, J. I. Lunine, F. Tosi, A. Migliorini, D. Grassi, G. Piccioni, R. Noschese, A. Cicchetti, C. Plainaki, A. Olivieri, M. E. O'Neill, D. Turrini, S. Stefani, R. Sordini, and M. Amoroso. Clusters of cyclones encircling Jupiter's poles. *Nature*, 555(7695), Mar. 2018. doi: 10.1038/nature25491.

H. Alfvén. Existence of Electromagnetic-Hydrodynamic Waves. *Nature*, 150 (3805), Oct. 1942. doi: 10.1038/150405d0.

H. Alfvén. On the Existence of Electromagnetic-Hydrodynamic Waves. *Arkiv for Matematik, Astronomi och Fysik*, 29B, Jan. 1943.

F. Allegrini, G. R. Gladstone, V. Hue, G. Clark, J. R. Szalay, W. S. Kurth, F. Bagenal, S. Bolton, J. E. P. Connerney, R. W. Ebert, T. K. Greathouse, G. B. Hospodarsky, M. Imai, P. Louarn, B. H. Mauk, D. J. McComas, J. Saur, A. H. Sulaiman, P. W. Valek, and R. J. Wilson. First Report of Electron Measurements During a Europa Footprint Tail Crossing by Juno. *Geophys. Res. Lett.*, 47(18), Sept. 2020. doi: 10.1029/2020GL089732.

S. W. Asmar, S. J. Bolton, D. R. Buccino, T. P. Cornish, W. M. Folkner, R. Formaro, L. Iess, A. P. Jongeling, D. K. Lewis, A. P. Mittskus, R. Mukai, and L. Simone. The Juno Gravity Science Instrument. *Space Sci Rev*, 213 (1-4), Nov. 2017. doi: 10.1007/s11214-017-0428-7.

G. Atkinson. Auroral arcs: Result of the interaction of a dynamic magnetosphere with the ionosphere. *J. Geophys. Res.*, 75(25), Sept. 1970. doi: 10.1029/JA075i025p04746.

S. V. Badman, G. Branduardi-Raymont, M. Galand, S. L. G. Hess, N. Krupp, L. Lamy, H. Melin, and C. Tao. Auroral Processes at the Giant Planets: Energy Deposition, Emission Mechanisms, Morphology and Spectra. *Space Science Reviews*, 187(1), Apr. 2015. doi: 10.1007/s11214-014-0042-x.

F. Bagenal. Empirical model of the Io plasma torus: Voyager measurements. *J. Geophys. Res.*, 99(A6), 1994. doi: 10.1029/93JA02908.

F. Bagenal and P. A. Delamere. Flow of mass and energy in the magnetospheres of Jupiter and Saturn. *Journal of Geophysical Research: Space Physics*, 116(A5), 2011. doi: 10.1029/2010JA016294.

F. Bagenal and V. Dols. The Space Environment of Io and Europa. *J. Geophys. Res. Space Physics*, 125(5), May 2020. doi: 10.1029/2019JA027485.

F. Bagenal and M. Kivelson. Radial Transport in the Io Plasma Torus: Flux Tube Interchange or Not? In *AGU Fall Meeting 2019*, volume 2019, Dec. 2019.

F. Bagenal and J. D. Sullivan. Direct plasma measurements in the Io torus and inner magnetosphere of Jupiter. *J. Geophys. Res.*, 86(A10), Sept. 1981. doi: 10.1029/JA086iA10p08447.

F. Bagenal, R. L. McNutt, J. W. Belcher, H. S. Bridge, and J. D. Sullivan. Revised ion temperatures for Voyager plasma measurements in the Io plasma torus. *J. Geophys. Res.*, 90(A2), 1985. doi: 10.1029/JA090iA02p01755.

F. Bagenal, F. J. Crary, A. I. F. Stewart, N. M. Schneider, D. A. Gurnett, W. S. Kurth, L. A. Frank, and W. R. Paterson. Galileo measurements of plasma density in the Io torus. *Geophys. Res. Lett.*, 24(17), Sept. 1997. doi: 10.1029/97GL01254.

F. Bagenal, R. J. Wilson, S. Siler, W. R. Paterson, and W. S. Kurth. Survey of Galileo plasma observations in Jupiter's plasma sheet. *Journal of Geophysical Research: Planets*, 121(5), 2016. doi: 10.1002/2016JE005009.

F. Bagenal, A. Adriani, F. Allegrini, S. J. Bolton, B. Bonfond, E. J. Bunce, J. E. P. Connerney, S. W. H. Cowley, R. W. Ebert, G. R. Gladstone, C. J. Hansen, W. S. Kurth, S. M. Levin, B. H. Mauk, D. J. McComas, C. P. Paranicas, D. Santos-Costa, R. M. Thorne, P. Valek, J. H. Waite, and P. Zarka. Magnetospheric Science Objectives of the Juno Mission. *Space Sci Rev*, 213(1-4), Nov. 2017. doi: 10.1007/s11214-014-0036-8.

F. Bagenal, R. J. Wilson, E. Huscher, F. Allegrini, J. E. P. Connerney, and L. Spalsbury. Radial Transport in Jupiter's Magnetosphere. In *AGU Fall Meeting 2018*, volume 2018, Dec. 2018.

D. D. Barbosa and M. G. Kivelson. Dawn-dusk electric field asymmetry of the Io plasma torus. *Geophysical Research Letters*, 10(3), 1983. doi: 10.1029/GL010i003p00210.

B. Bertotti, G. Comoretto, and L. Iess. Doppler tracking of spacecraft with multi-frequency links. *Astron. Astrophys.*, 269(1-2), 1993.

A. Bhardwaj and G. R. Gladstone. Auroral emissions of the giant planets. *Reviews of Geophysics*, 38(3), 2000. doi: 10.1029/1998RG000046.

D. Bhattacharyya, J. T. Clarke, J. Montgomery, B. Bonfond, J. Gérard, and D. Grodent. Evidence for Auroral Emissions From Callisto's Footprint in HST UV Images. *J. Geophys. Res. Space Physics*, 123(1), Jan. 2018. doi: 10.1002/2017JA024791.

E. K. Bigg. Influence of the Satellite Io on Jupiter's Decametric Emission. *Nature*, 203(4949), Sept. 1964. doi: 10.1038/2031008a0.

M. Bird, S. Asmar, P. Edenhofer, O. Funke, M. Pätzold, and H. Volland. The structure of Jupiter's Io plasma torus inferred from Ulysses radio occultation observations. *Planetary and Space Science*, 41(11-12), Nov. 1993. doi: 10.1016/0032-0633(93)90104-A.

K. M. Bodisch, L. P. Dougherty, and F. Bagenal. Survey of Voyager plasma science ions at Jupiter: 3. Protons and minor ions. *Journal of Geophysical Research: Space Physics*, 122(8), 2017. doi: 10.1002/2017JA024148.

S. J. Bolton, M. Janssen, R. Thorne, S. Levin, M. Klein, S. Gulkis, T. Bastian, R. Sault, C. Elachi, M. Hofstadter, A. Bunker, G. Dulk, E. Gudim, G. Hamilton, W. T. K. Johnson, Y. Leblanc, O. Liepack, R. McLeod, J. Roller, L. Roth, and R. West. Ultra-relativistic electrons in Jupiter's radiation belts. *Nature*, 415(6875), Feb. 2002. doi: 10.1038/415987a.

S. J. Bolton, J. Lunine, D. Stevenson, J. E. P. Connerney, S. Levin, T. C. Owen, F. Bagenal, D. Gautier, A. P. Ingersoll, G. S. Orton, T. Guillot, W. Hubbard, J. Bloxham, A. Coradini, S. K. Stephens, P. Mokashi, R. Thorne, and R. Thorpe. The Juno Mission. *Space Science Reviews*, 213(1), Nov. 2017. doi: 10.1007/s11214-017-0429-6.

B. Bonfond, D. Grodent, J.-C. Gérard, A. Radioti, J. Saur, and S. Jacobsen. UV Io footprint leading spot: A key feature for understanding the UV Io footprint multiplicity? *Geophys. Res. Lett.*, 35(5), Mar. 2008. doi: 10.1029/2007GL032418.

B. Bonfond, D. Grodent, J.-C. Gérard, A. Radioti, V. Dols, P. A. Delamere, and J. T. Clarke. The Io UV footprint: Location, inter-spot distances

and tail vertical extent. *J. Geophys. Res.*, 114(A7), July 2009. doi: 10.1029/2009JA014312.

B. Bonfond, S. Hess, F. Bagenal, J.-C. Gérard, D. Grodent, A. Radioti, J. Gustin, and J. T. Clarke. The multiple spots of the Ganymede auroral footprint. *Geophysical Research Letters*, 40(19), 2013. doi: https://doi.org/10.1002/grl.50989.

B. Bonfond, D. Grodent, S. V. Badman, J. Saur, J. C. Gérard, and A. Radioti. Similarity of the Jovian satellite footprints: Spots multiplicity and dynamics. *Icarus*, 292, Aug. 2017a. doi: 10.1016/j.icarus.2017.01.009.

B. Bonfond, J. Saur, D. Grodent, S. V. Badman, D. Bisikalo, V. Shematovich, J.-C. Gérard, and A. Radioti. The tails of the satellite auroral footprints at Jupiter. *J. Geophys. Res. Space Physics*, 122(8), Aug. 2017b. doi: 10.1002/2017JA024370.

B. Bonfond, Z. H. Yao, G. R. Gladstone, D. Grodent, J.-C. Gérard, J. Matar, B. Palmaerts, T. K. Greathouse, V. Hue, M. H. Versteeg, J. A. Kammer, R. S. Giles, C. Tao, M. F. Vogt, A. Mura, A. Adriani, B. H. Mauk, W. S. Kurth, and S. J. Bolton. Are Dawn Storms Jupiter's Auroral Substorms? *AGU Advances*, 2(1), 2021. doi: 10.1029/2020AV000275.

L. Brillouin. La mécanique ondulatoire de Schrödinger: une méthode générale de resolution par approximations successives. *Comptes rendus hebdomadaires des séances de l'Académie des sciences*, 183, July 1926.

A. L. Broadfoot, M. J. S. Belton, P. Z. Takacs, B. R. Sandel, D. E. Shemansky, J. B. Holberg, J. M. Ajello, S. K. Atreya, T. M. Donahue, H. W. Moos, J. L. Bertaux, J. E. Blamont, D. F. Strobel, J. C. Mcconnell, A. Dalgarno, R. Goody, and M. B. Mcelroy. Extreme Ultraviolet Observations from Voyager 1 Encounter with Jupiter. *Science*, 204(4396), June 1979. doi: 10.1126/science.204.4396.979.

M. E. Brown. Periodicities in the Io plasma torus. *J. Geophys. Res.*, 100 (A11), Nov. 1995. doi: 10.1029/95JA01988.

M. E. Brown and A. H. Bouchez. The Response of Jupiter's Magnetosphere to an Outburst on Io. *Science*, 278(5336), Oct. 1997. doi: 10.1126/science.278.5336.268.

R. A. Brown. The Jupiter hot plasma torus - Observed electron temperature and energy flows. *The Astrophysical Journal*, 244, Mar. 1981. doi: 10.1086/158777.

R. A. Brown. Observed departure of the Io plasma torus from rigid corotation with Jupiter. *Astrophys. J.*, 268, May 1983. doi: 10.1086/184027.

M. H. Burger, R. Wagner, R. Jaumann, and T. A. Cassidy. Effects of the External Environment on Icy Satellites. *Space Science Reviews*, 153(1), June 2010. doi: 10.1007/s11214-010-9645-z.

B. F. Burke and K. L. Franklin. Observations of a variable radio source associated with the planet Jupiter. *Journal of Geophysical Research (1896-1977)*, 60(2), 1955. doi: 10.1029/JZ060i002p00213.

G. Caudal. A self-consistent model of Jupiter's magnetodisc including the effects of centrifugal force and pressure. *Journal of Geophysical Research: Space Physics*, 91(A4), 1986. doi: 10.1029/JA091iA04p04201.

S. Cerri. Fluid Modeling of Kinetic Effects in Collisionless Magnetized Plasmas and Application to Solar Wind-Magnetosphere Interactions. Master's thesis, University of Pisa, Pisa, 2012.

S. Chandrasekhar. *Hydrodynamic and hydromagnetic stability*. Dover Publications, New York, 1961. ISBN 978-0-19-851237-0.

D. L. Chenette, T. F. Conlon, and J. A. Simpson. Bursts of relativistic electrons from Jupiter observed in interplanetary space with the time variation of the planetary rotation period. *Journal of Geophysical Research (1896-1977)*, 79(25), 1974. doi: 10.1029/JA079i025p03551.

G. F. Chew, M. L. Goldberger, F. E. Low, and S. Chandrasekhar. The Boltzmann equation an d the one-fluid hydromagnetic equations in the

absence of particle collisions. *Proceedings of the Royal Society of London. Series A. Mathematical and Physical Sciences*, 236(1204), Jan. 1997. doi: 10.1098/rspa.1956.0116.

J. T. Clarke, G. E. Ballester, J. Trauger, R. Evans, J. E. P. Connerney, K. Stapelfeldt, D. Crisp, P. D. Feldman, C. J. Burrows, S. Casertano, J. S. Gallagher, R. E. Griffiths, J. J. Hester, J. G. Hoessel, J. A. Holtzman, J. E. Krist, V. Meadows, J. R. Mould, P. A. Scowen, A. M. Watson, and J. A. Westphal. Far-Ultraviolet Imaging of Jupiter's Aurora and the Io "Footprint". *Science*, 274(5286), Oct. 1996. doi: 10.1126/science.274.5286.404.

J. T. Clarke, J. Ajello, G. Ballester, L. Ben Jaffel, J. Connerney, J.-C. Gérard, G. R. Gladstone, D. Grodent, W. Pryor, J. Trauger, and J. H. Waite. Ultraviolet emissions from the magnetic footprints of Io, Ganymede and Europa on Jupiter. *Nature*, 415(6875), Feb. 2002. doi: 10.1038/415997a.

D. Coffin, P. Delamere, and P. Damiano. Implications for Magnetosphere-Ionosphere Coupling From Jupiter's System IV Quasi-Period. *Journal of Geophysical Research: Space Physics*, 125(5), 2020. doi: 10.1029/2019JA027347.

J. Connerney, S. Timmins, J. Jorgensen, S. Kotsiaros, P. Jorgensen, M. Herceg, J. Bloxham, S. Bolton, and S. Levin. Jovimagnetic Secular Variation and Jupiter's Rotation Period. Technical Report EGU23-10373, Copernicus Meetings, Feb. 2023.

J. E. P. Connerney, M. H. Acuña, and N. F. Ness. Modeling the Jovian current sheet and inner magnetosphere. *Journal of Geophysical Research: Space Physics*, 86(A10), 1981. doi: https://doi.org/10.1029/JA086iA10p08370.

J. E. P. Connerney, R. Baron, T. Satoh, and T. Owen. Images of Excited H3+ at the Foot of the lo Flux Tube in Jupiter's Atmosphere. *Science*, 262(5136), Nov. 1993. doi: 10.1126/science.262.5136.1035.

J. E. P. Connerney, M. Benn, J. B. Bjarno, T. Denver, J. Espley, J. L. Jorgensen, P. S. Jorgensen, P. Lawton, A. Malinnikova, J. M. Merayo, S. Murphy, J. Odom, R. Oliversen, R. Schnurr, D. Sheppard, and E. J. Smith. The Juno Magnetic Field Investigation. *Space Science Reviews*, 213(1), Nov. 2017. doi: 10.1007/s11214-017-0334-z.

J. E. P. Connerney, S. Kotsiaros, R. J. Oliversen, J. R. Espley, J. L. Joergensen, P. S. Joergensen, J. M. G. Merayo, M. Herceg, J. Bloxham, K. M. Moore, S. J. Bolton, and S. M. Levin. A New Model of Jupiter's Magnetic Field From Juno's First Nine Orbits. *Geophys. Res. Lett.*, 45(6), Mar. 2018. doi: 10.1002/2018GL077312.

J. E. P. Connerney, S. Timmins, M. Herceg, and J. L. Joergensen. A Jovian Magnetodisc Model for the Juno Era. *Journal of Geophysical Research: Space Physics*, 125(10), 2020. doi: 10.1029/2020JA028138.

J. E. P. Connerney, S. Timmins, R. J. Oliversen, J. R. Espley, J. L. Joergensen, S. Kotsiaros, P. S. Joergensen, J. M. G. Merayo, M. Herceg, J. Bloxham, K. M. Moore, A. Mura, A. Moirano, S. J. Bolton, and S. M. Levin. A New Model of Jupiter's Magnetic Field at the Completion of Juno's Prime Mission. *Journal of Geophysical Research: Planets*, 127(2), 2022. doi: 10.1029/2021JE007055.

M. Copper, P. A. Delamere, and K. Overcast-Howe. Modeling physical chemistry of the Io plasma torus in two dimensions. *Journal of Geophysical Research: Space Physics*, 121(7), 2016. doi: 10.1002/2016JA022767.

M. M. Cowee, C. T. Russell, Y. L. Wang, and D. A. Gurnett. On the possibility of fast neutral production of the inner Io torus. *Journal of Geophysical Research: Space Physics*, 110(A9), 2005. doi: 10.1029/2004JA010678.

F. J. Crary, F. Bagenal, J. A. Ansher, D. A. Gurnett, and W. S. Kurth. Anisotropy and proton density in the Io plasma torus derived from whistler wave dispersion. *Journal of Geophysical Research: Space Physics*, 101 (A2), 1996. doi: 10.1029/95JA02212.

F. J. Crary, F. Bagenal, L. A. Frank, and W. R. Paterson. Galileo plasma spectrometer measurements of composition and temperature in the Io plasma torus. *Journal of Geophysical Research: Space Physics*, 103(A12), 1998. doi: 10.1029/1998JA900003.

P. A. Damiano, P. A. Delamere, B. Stauffer, C.-S. Ng, and J. R. Johnson. Kinetic Simulations of Electron Acceleration by Dispersive Scale Alfvén Waves in Jupiter's Magnetosphere. *Geophysical Research Letters*, 46(6), 2019. doi: 10.1029/2018GL081219.

K. de Kleer, F. Nimmo, and E. Kite. Variability in Io's Volcanism on Timescales of Periodic Orbital Changes. *Geophys. Res. Lett.*, 46(12), June 2019. doi: 10.1029/2019GL082691.

I. de Pater, K. de Kleer, A. G. Davies, and M. Ádámkovics. Three decades of Loki Patera observations. *Icarus*, 297, Nov. 2017. doi: 10.1016/j.icarus.2017.03.016.

P. A. Delamere and F. Bagenal. Modeling variability of plasma conditions in the Io torus. *Journal of Geophysical Research: Space Physics*, 108(A7), 2003. doi: 10.1029/2002JA009706.

P. A. Delamere, F. Bagenal, R. Ergun, and Y.-J. Su. Momentum transfer between the Io plasma wake and Jupiter's ionosphere. *Journal of Geophysical Research: Space Physics*, 108(A6), 2003. doi: 10.1029/2002JA009530.

P. A. Delamere, A. Steffl, and F. Bagenal. Modeling temporal variability of plasma conditions in the Io torus during the Cassini era. *Journal of Geophysical Research: Space Physics*, 109(A10), 2004. doi: https://doi.org/10.1029/2003JA010354.

P. A. Delamere, F. Bagenal, and A. Steffl. Radial variations in the Io plasma torus during the Cassini era. *Journal of Geophysical Research: Space Physics*, 110(A12), 2005. doi: 10.1029/2005JA011251.

A. J. Dessler, editor. *Physics of the Jovian Magnetosphere*. Cambridge University Press, 1 edition, Jan. 1983. ISBN 978-0-521-24558-6 978-0-521-52006-5 978-0-511-56457-4. doi: 10.1017/CBO9780511564574.

B. M. Dinelli, F. Fabiano, A. Adriani, F. Altieri, M. L. Moriconi, A. Mura, G. Sindoni, G. Filacchione, F. Tosi, A. Migliorini, D. Grassi, G. Piccioni, R. Noschese, A. Cicchetti, S. J. Bolton, J. E. P. Connerney, S. K. Atreya, F. Bagenal, G. R. Gladstone, C. J. Hansen, W. S. Kurth, S. M. Levin, B. H. Mauk, D. J. McComas, J.-C. Gèrard, D. Turrini, S. Stefani, M. Amoroso, and A. Olivieri. Preliminary JIRAM results from Juno polar observations: 1. Methodology and analysis applied to the Jovian northern polar region. *Geophysical Research Letters*, 44(10), 2017. doi: 10.1002/2017GL072929.

L. P. Dougherty, K. M. Bodisch, and F. Bagenal. Survey of Voyager plasma science ions at Jupiter: 2. Heavy ions. *J. Geophys. Res. Space Physics*, 122(8), Aug. 2017. doi: 10.1002/2017JA024053.

S. D. Drell, H. M. Foley, and M. A. Ruderman. Drag and Propulsion of Large Satellites in the Ionosphere; An Alfv\'en Propulsion Engine in Space. *Physical Review Letters*, 14(6), Feb. 1965. doi: 10.1103/PhysRevLett.14.171.

P. Drossart, J. Maillard, J. Caldwell, S. Kim, J. Watson, W. Majewski, J. Tennyson, S. Miller, S. Atreya, J. Clarke, J. Waite, and R. Wagener. Detection of H3+ on Jupiter. *Nature*, 340, Aug. 1989. doi: 10.1038/340539a0.

S. T. Durrance, P. D. Feldman, and H. A. Weaver. Rocket detection of ultraviolet emission from neutral oxygen and sulfur in the IO Torus. *The Astrophysical Journal*, 267, Apr. 1983. doi: 10.1086/184016.

R. W. Ebert, F. Bagenal, D. J. McComas, and C. M. Fowler. A survey of solar wind conditions at 5 AU: a tool for interpreting solar wind-magnetosphere interactions at Jupiter. *Front. Astron. Space Sci.*, 1, Sept. 2014. doi: 10.3389/fspas.2014.00004.

T. M. Edwards, E. J. Bunce, and S. W. H. Cowley. A note on the vector potential of Connerney et al.'s model of the equatorial current sheet in Jupiter's magnetosphere. *Planetary and Space Science*, 49(10), Aug. 2001. doi: 10.1016/S0032-0633(00)00164-1.

W. M. Elsasser. The Hydromagnetic Equations. *Physical Review*, 79(1), July 1950. doi: 10.1103/PhysRev.79.183.

R. E. Ergun, L. Ray, P. A. Delamere, F. Bagenal, V. Dols, and Y.-J. Su. Generation of parallel electric fields in the Jupiter-Io torus wake region. *J. Geophys. Res.*, 114(A5), May 2009. doi: 10.1029/2008JA013968.

P. D. Feldman, D. F. Strobel, H. W. Moos, and H. A. Weaver. The Far-Ultraviolet Spectrum of the Io Plasma Torus. *The Astrophysical Journal*, 601(1), Jan. 2004. doi: 10.1086/380302.

V. C. A. Ferraro. The Non-uniform Rotation of the Sun and its Magnetic Field. *Monthly Notices of the Royal Astronomical Society*, 97(6), Apr. 1937. doi: 10.1093/mnras/97.6.458.

L. A. Frank and W. R. Paterson. Intense electron beams observed at Io with the Galileo spacecraft. *Journal of Geophysical Research: Space Physics*, 104(A12), 1999. doi: 10.1029/1999JA900402.

B. D. Fried and S. D. Conte. *The Plasma Dispersion Function.* Academic Press, New York, Jan. 1961. doi: 10.1016/C2013-0-12176-9.

D. J. Gershman, J. E. P. Connerney, S. Kotsiaros, G. A. DiBraccio, Y. M. Martos, A. F. -Viñas, V. Hue, G. Clark, F. Bagenal, S. Levin, and S. J. Bolton. Alfvénic Fluctuations Associated With Jupiter's Auroral Emissions. *Geophys. Res. Lett.*, 46(13), July 2019. doi: 10.1029/2019GL082951.

G. R. Gladstone, S. A. Stern, D. C. Slater, M. Versteeg, M. W. Davis, K. D. Retherford, L. A. Young, A. J. Steffl, H. Throop, J. W. Parker, H. A. Weaver, A. F. Cheng, G. S. Orton, J. T. Clarke, and J. D. Nichols. Jupiter's Nightside Airglow and Aurora. *Science*, 318(5848), Oct. 2007. doi: 10.1126/science.1147613.

G. R. Gladstone, S. C. Persyn, J. S. Eterno, B. C. Walther, D. C. Slater, M. W. Davis, M. H. Versteeg, K. B. Persson, M. K. Young, G. J. Dirks, A. O. Sawka, J. Tumlinson, H. Sykes, J. Beshears, C. L. Rhoad, J. P. Cravens, G. S. Winters, R. A. Klar, W. Lockhart, B. M. Piepgrass, T. K. Greathouse, B. J. Trantham, P. M. Wilcox, M. W. Jackson, O. H. W. Siegmund, J. V. Vallerga, R. Raffanti, A. Martin, J.-C. Gérard, D. C. Grodent, B. Bonfond, B. Marquet, and F. Denis. The Ultraviolet Spectrograph on NASA's Juno Mission. *Space Science Reviews*, 213(1), Nov. 2017. doi: 10.1007/s11214-014-0040-z.

D. A. Godfrey. A hexagonal feature around Saturn's north pole. *Icarus*, 76 (2), Nov. 1988. doi: 10.1016/0019-1035(88)90075-9.

C. Goertz. Io's interaction with the plasma torus. *Journal of Geophysical Research: Space Physics*, 85(A6), 1980. doi: 10.1029/JA085iA06p02949.

P. Goldreich and D. Lynden-Bell. Io, a jovian unipolar inductor. *The Astrophysical Journal*, 156, Apr. 1969. doi: 10.1086/149947.

E. Grenier. Chapter 4 - Boundary Layers. In S. Friedlander and D. Serre, editors, *Handbook of Mathematical Fluid Dynamics*, volume 3. North-Holland, Jan. 2005. doi: 10.1016/S1874-5792(05)80007-2.

D. Grodent. A Brief Review of Ultraviolet Auroral Emissions on Giant Planets. *Space Sci Rev*, 187(1-4), Apr. 2015. doi: 10.1007/s11214-014-0052-8.

D. Grodent, J.-C. Gérard, A. Radioti, B. Bonfond, and A. Saglam. Jupiter's changing auroral location. *Journal of Geophysical Research: Space Physics*, 113(A1), 2008. doi: 10.1029/2007JA012601.

D. A. Gurnett and C. K. Goertz. Multiple Alfven wave reflections excited by Io: Origin of the Jovian decametric arcs. *Journal of Geophysical Research: Space Physics*, 86(A2), 1981. doi: 10.1029/JA086iA02p00717.

J.-C. Gérard, A. Saglam, D. Grodent, and J. T. Clarke. Morphology of the ultraviolet Io footprint emission and its control by Io's location.

Journal of Geophysical Research: Space Physics, 111(A4), 2006. doi: https://doi.org/10.1029/2005JA011327.

F. Herbert, N. M. Schneider, and A. J. Dessler. New description of Io's cold plasma torus. *Journal of Geophysical Research: Space Physics*, 113(A1), 2008. doi: 10.1029/2007JA012555.

S. Hess, F. Mottez, and P. Zarka. Jovian S burst generation by Alfvén waves. *Journal of Geophysical Research: Space Physics*, 112(A11), 2007. doi: 10.1029/2006JA012191.

S. Hess, B. Bonfond, P. Zarka, and D. Grodent. Model of the Jovian magnetic field topology constrained by the Io auroral emissions. *Journal of Geophysical Research (Space Physics)*, 116, May 2011a. doi: 10.1029/2010JA016262.

S. L. G. Hess, P. Delamere, V. Dols, B. Bonfond, and D. Swift. Power transmission and particle acceleration along the Io flux tube. *J. Geophys. Res.*, 115(A6), June 2010a. doi: 10.1029/2009JA014928.

S. L. G. Hess, A. Pétin, P. Zarka, B. Bonfond, and B. Cecconi. Lead angles and emitting electron energies of Io-controlled decameter radio arcs. *Planetary and Space Science*, 58(10), Aug. 2010b. doi: 10.1016/j.pss.2010.04.011.

S. L. G. Hess, P. A. Delamere, F. Bagenal, N. Schneider, and A. J. Steffl. Longitudinal modulation of hot electrons in the Io plasma torus. *J. Geophys. Res.*, 116(A11), Nov. 2011b. doi: 10.1029/2011JA016918.

S. L. G. Hess, B. Bonfond, V. Chantry, J. C. Gérard, D. Grodent, S. Jacobsen, and A. Radioti. Evolution of the Io footprint brightness II: Modeling. *Planetary and Space Science*, 88, Nov. 2013. doi: 10.1016/j.pss.2013.08.005.

T. W. Hill and V. M. Vasyliūnas. Jovian auroral signature of Io's corotational wake. *Journal of Geophysical Research: Space Physics*, 107(A12), 2002. doi: 10.1029/2002JA009514.

T. W. Hill, A. J. Dessler, and F. C. Michel. Configuration of the Jovian magnetosphere. *Geophys. Res. Lett.*, 1(1), May 1974. doi: 10.1029/GL001i001p00003.

T. W. Hill, A. J. Dessler, and L. J. Maher. Corotating magnetospheric convection. *Journal of Geophysical Research: Space Physics*, 86(A11), 1981. doi: 10.1029/JA086iA11p09020.

P. C. Hinton, F. Bagenal, and B. Bonfond. Alfvén Wave Propagation in the Io Plasma Torus. *Geophysical Research Letters*, 46(3), 2019. doi: 10.1029/2018GL081472.

Y. Hiraki. Auroral vortex street formed by the magnetosphere–ionosphere coupling instability. *Annales Geophysicae*, 33(2), 2015. doi: 10.5194/angeo-33-217-2015.

Y. Hiraki, F. Tsuchiya, and Y. Katoh. Io torus plasma transport under interchange instability and flow shears. *Planetary and Space Science*, 62 (1), Mar. 2012. doi: 10.1016/j.pss.2011.11.014.

V. Hue, G. R. Gladstone, C. K. Louis, T. K. Greathouse, B. Bonfond, J. R. Szalay, A. Moirano, R. S. Giles, J. A. Kammer, M. Imai, A. Mura, M. H. Versteeg, G. Clark, J.-C. Gérard, D. C. Grodent, J. Rabia, A. H. Sulaiman, S. J. Bolton, and J. Connerney. The Io, Europa and Ganymede auroral footprints at Jupiter in the ultraviolet: Positions and equatorial lead angles. *Journal of Geophysical Research: Space Physics*, n/a(n/a), 2023. doi: 10.1029/2023JA031363.

E. Huscher, F. Bagenal, R. J. Wilson, F. Allegrini, R. W. Ebert, P. W. Valek, J. R. Szalay, D. J. McComas, J. E. P. Connerney, S. Bolton, and S. M. Levin. Survey of Juno Observations in Jupiter's Plasma Disk: Density. *Journal of Geophysical Research: Space Physics*, 126(8), 2021. doi: 10.1029/2021JA029446.

L. Iess, M. Di Benedetto, N. James, M. Mercolino, L. Simone, and P. Tortora. Astra: Interdisciplinary study on enhancement of the end-to-end accuracy

for spacecraft tracking techniques. *Acta Astronautica*, 94(2), Feb. 2014. doi: 10.1016/j.actaastro.2013.06.011.

L. Iess, W. M. Folkner, D. Durante, M. Parisi, Y. Kaspi, E. Galanti, T. Guillot, W. B. Hubbard, D. J. Stevenson, J. D. Anderson, D. R. Buccino, L. G. Casajus, A. Milani, R. Park, P. Racioppa, D. Serra, P. Tortora, M. Zannoni, H. Cao, R. Helled, J. I. Lunine, Y. Miguel, B. Militzer, S. Wahl, J. E. P. Connerney, S. M. Levin, and S. J. Bolton. Measurement of Jupiter's asymmetric gravity field. *Nature*, 555(7695), Mar. 2018. doi: 10.1038/nature25776.

S. Jacobsen, F. M. Neubauer, J. Saur, and N. Schilling. Io's nonlinear MHD-wave field in the heterogeneous Jovian magnetosphere. *Geophys. Res. Lett.*, 34(10), May 2007. doi: 10.1029/2006GL029187.

S. Jacobsen, J. Saur, F. M. Neubauer, B. Bonfond, J.-C. Gérard, and D. Grodent. Location and spatial shape of electron beams in Io's wake. *Journal of Geophysical Research: Space Physics*, 115(A4), 2010. doi: 10.1029/2009JA014753.

H. Jeffreys. On Certain Approximate Solutions of Lineae Differential Equations of the Second Order. *Proceedings of the London Mathematical Society*, s2-23(1), 1925. doi: 10.1112/plms/s2-23.1.428.

N. Jia and A. V. Streltsov. Ionospheric feedback instability and active discrete auroral forms. *Journal of Geophysical Research: Space Physics*, 119(3), 2014. doi: 10.1002/2013JA019217.

S. T. Jones and Y.-J. Su. Role of dispersive Alfvén waves in generating parallel electric fields along the Io-Jupiter fluxtube. *Journal of Geophysical Research: Space Physics*, 113(A12), 2008. doi: https://doi.org/10.1029/2008JA013512.

J. L. Jørgensen, T. Denver, M. Benn, P. S. Jørgensen, M. Herceg, J. M. G. Merayo, and J. E. P. Connerney. A profile of the Io dust cloud and

plasma torus as observed from Juno. Technical Report EGU2020-18093, Copernicus Meetings, Mar. 2020.

M. L. Kaiser and M. D. Desch. Narrow-band Jovian kilometric radiation: A new radio component. *Geophysical Research Letters*, 7(5), 1980. doi: 10.1029/GL007i005p00389.

C. F. Kennel and F. V. Coroniti. Possible origins of time variability in Jupiter's outer magnetosphere, 2. Variations in solar wind magnetic field. *Geophysical Research Letters*, 4(6), 1977. doi: 10.1029/GL004i006p00215.

K. K. Khurana, M. G. Kivelson, V. M. Vasyliunas, N. Krupp, J. Woch, A. Lagg, B. H. Mauk, and W. S. Kurth. The Configuration of Jupiter's Magnetosphere. In *Jupiter: The Planet, Satellites and Magnetosphere*, volume 1 of *Cambridge planetary science*. Cambridge University Press, Cambridge UK, 2004. ISBN 978-0-521-03545-3.

M. G. Kivelson, F. Bagenal, W. S. Kurth, F. M. Neubauer, C. Paranicas, and J. Saur. Magnetospheric Interactions with Satellites. In *Jupiter: The Planet, Satellites and Magnetosphere*, volume 21. Cambridge Univ. Press, Cambridge UK, f. bagenal edition, 2004.

N. A. Krall and A. W. Trivelpiece. *Principles of plasma physics*. International series in pure and applied physics. McGraw-Hill, New York, 1973. ISBN 978-0-07-035346-6.

H. A. Kramers. Wellenmechanik und halbzahlige Quantisierung. *Zeitschrift für Physik*, 39(10), Oct. 1926. doi: 10.1007/BF01451751.

H. Krüger, P. Geissler, M. Horányi, A. L. Graps, S. Kempf, R. Srama, G. Moragas-Klostermeyer, R. Moissl, T. V. Johnson, and E. Grün. Jovian dust streams: A monitor of Io's volcanic plume activity. *Geophysical Research Letters*, 30(21), 2003. doi: 10.1029/2003GL017827.

I. Kupo, Y. Mekler, and A. Eviatar. Detection of ionized sulfur in the Jovian magnetosphere. *ApJ*, 205, Apr. 1976. doi: 10.1086/182088.

W. S. Kurth, G. B. Hospodarsky, D. L. Kirchner, B. T. Mokrzycki, T. F. Averkamp, W. T. Robison, C. W. Piker, M. Sampl, and P. Zarka. The Juno Waves Investigation. *Space Science Reviews*, 213(1), Nov. 2017. doi: 10.1007/s11214-017-0396-y.

W. Köhnlein. Radial dependence of solar wind parameters in the ecliptic (1.1 R - 61 AU). *Sol Phys*, 169(1), Nov. 1996. doi: 10.1007/BF00153841.

M. Küppers and N. M. Schneider. Discovery of chlorine in the Io torus. *Geophysical Research Letters*, 27(4), 2000. doi: 10.1029/1999GL010718.

L. D. Landau and E. M. Lifschitz. *Fluid mechanics*. Number v. 6 in Course of theoretical physics. Pergamon Press, Oxford, England ; New York, 2nd ed., 2nd english ed., rev edition, 1987. ISBN 978-0-08-033933-7 978-0-08-033932-0.

R. M. Lopes and D. A. Williams. Volcanism on Io. In *The Encyclopedia of Volcanoes*. Elsevier, 2015. ISBN 978-0-12-385938-9. doi: 10.1016/B978-0-12-385938-9.00043-2.

R. M. C. Lopes, K. De Kleer, and J. Tuttle Keane, editors. *Io: A New View of Jupiter's Moon*, volume 468 of *Astrophysics and Space Science Library*. Springer International Publishing, Cham, 2023. ISBN 978-3-031-25669-1 978-3-031-25670-7. doi: 10.1007/978-3-031-25670-7.

P. Louarn, C. P. Paranicas, and W. S. Kurth. Global magnetodisk disturbances and energetic particle injections at Jupiter. *Journal of Geophysical Research: Space Physics*, 119(6), 2014. doi: 10.1002/2014JA019846.

C. K. Louis, R. Prangé, L. Lamy, P. Zarka, M. Imai, W. S. Kurth, and J. E. P. Connerney. Jovian Auroral Radio Sources Detected In Situ by Juno/Waves: Comparisons With Model Auroral Ovals and Simultaneous HST FUV Images. *Geophysical Research Letters*, 46(21), 2019. doi: 10.1029/2019GL084799.

K. A. Lynch, D. L. Hampton, M. Zettergren, T. A. Bekkeng, M. Conde, P. A. Fernandes, P. Horak, M. Lessard, R. Miceli, R. Michell, J. Moen,

M. Nicolls, S. P. Powell, and M. Samara. MICA sounding rocket observations of conductivity-gradient-generated auroral ionospheric responses: Small-scale structure with large-scale drivers. *Journal of Geophysical Research: Space Physics*, 120(11), 2015. doi: 10.1002/2014JA020860.

R. L. Lysak. Feedback instability of the ionospheric resonant cavity. *J. Geophys. Res.*, 96(A2), Feb. 1991. doi: 10.1029/90JA02154.

R. L. Lysak. The relationship between electrostatic shocks and kinetic Alfvén waves. *Geophysical Research Letters*, 25(12), 1998. doi: 10.1029/98GL00065.

R. L. Lysak and W. Lotko. On the kinetic dispersion for shear Alfven waves. *Journal of Geophysical Research*, 101(A3), Mar. 1996. doi: 10.1029/95JA03712.

R. L. Lysak and Y. Song. Energetics of the ionospheric feedback interaction. *J. Geophys. Res.*, 107(A8), Aug. 2002. doi: 10.1029/2001JA000308.

R. L. Lysak and Y. Song. Kinetic theory of the Alfvén wave acceleration of auroral electrons. *J. Geophys. Res.*, 108(A4), 2003. doi: 10.1029/2002JA009406.

N. Magyar, T. V. Doorsselaere, and M. Goossens. The Nature of Elsässer Variables in Compressible MHD. *The Astrophysical Journal*, 873(1), Mar. 2019. doi: 10.3847/1538-4357/ab04a7.

G. Mariotti and P. Tortora. Experimental validation of a dual uplink multifrequency dispersive noise calibration scheme for Deep Space tracking: DUAL UPLINK INCOMPLETE LINK. *Radio Sci.*, 48(2), Mar. 2013. doi: 10.1002/rds.20024.

L. Marshall and W. F. Libby. Stimulation of Jupiter's Radio Emission by Io. *Nature*, 214(5084), Apr. 1967. doi: 10.1038/214126a0.

W. H. Matthaeus, L. W. Klein, S. Ghosh, and M. R. Brown. Nearly incompressible magnetohydrodynamics, pseudosound, and solar wind fluctuations. *J. Geophys. Res.*, 96(A4), 1991. doi: 10.1029/90JA02609.

B. H. Mauk, D. J. Williams, and R. W. McEntire. Energy-time dispersed charged particle signatures of dynamic injections in Jupiter's inner magnetosphere. *Geophysical Research Letters*, 24(23), 1997. doi: https://doi.org/10.1029/97GL03026.

B. H. Mauk, D. K. Haggerty, S. E. Jaskulek, C. E. Schlemm, L. E. Brown, S. A. Cooper, R. S. Gurnee, C. M. Hammock, J. R. Hayes, G. C. Ho, J. C. Hutcheson, A. D. Jacques, S. Kerem, C. K. Kim, D. G. Mitchell, K. S. Nelson, C. P. Paranicas, N. Paschalidis, E. Rossano, and M. R. Stokes. The Jupiter Energetic Particle Detector Instrument (JEDI) Investigation for the Juno Mission. *Space Science Reviews*, 213(1), Nov. 2017. doi: 10.1007/s11214-013-0025-3.

B. H. Mauk, G. Clark, G. R. Gladstone, S. Kotsiaros, A. Adriani, F. Allegrini, F. Bagenal, S. J. Bolton, B. Bonfond, J. E. P. Connerney, R. W. Ebert, D. K. Haggerty, P. Kollmann, W. S. Kurth, S. M. Levin, C. P. Paranicas, and A. M. Rymer. Energetic Particles and Acceleration Regions Over Jupiter's Polar Cap and Main Aurora: A Broad Overview. *Journal of Geophysical Research: Space Physics*, 125(3), Mar. 2020. doi: 10.1029/2019JA027699.

D. J. McComas, N. Alexander, F. Allegrini, F. Bagenal, C. Beebe, G. Clark, F. Crary, M. I. Desai, A. De Los Santos, D. Demkee, J. Dickinson, D. Everett, T. Finley, A. Gribanova, R. Hill, J. Johnson, C. Kofoed, C. Loeffler, P. Louarn, M. Maple, W. Mills, C. Pollock, M. Reno, B. Rodriguez, J. Rouzaud, D. Santos-Costa, P. Valek, S. Weidner, P. Wilson, R. J. Wilson, and D. White. The Jovian Auroral Distributions Experiment (JADE) on the Juno Mission to Jupiter. *Space Science Reviews*, 213(1), Nov. 2017. doi: 10.1007/s11214-013-9990-9.

W. J. McDoniel, D. B. Goldstein, P. L. Varghese, and L. M. Trafton. Simulation of Io's plumes and Jupiter's plasma torus. *Physics of Fluids*, 31(7), July 2019. doi: 10.1063/1.5097961.

M. B. McElroy and Y. L. Yung. The atmosphere and ionosphere of Io. *The Astrophysical Journal*, 196, Feb. 1975. doi: 10.1086/153408.

M. A. McGrath, E. Lellouch, D. F. Strobel, P. D. Feldman, and R. E. Johnson. Satellite Atmospheres. In *Jupiter: The Planet, Satellites and Magnetosphere*, volume 19. Cambridge Univ. Press, Cambridge, UK, 2004.

Y. Mei, R. M. Thorne, and F. Bagenal. Analytical model for the density distribution in the Io plasma torus. *Journal of Geophysical Research: Space Physics*, 100(A2), 1995. doi: 10.1029/94JA02359.

M. Mendillo, J. Baumgardner, B. Flynn, and W. J. Hughes. The extended sodium nebula of Jupiter. *Nature*, 348(6299), Nov. 1990. doi: 10.1038/348312a0.

M. Mendillo, C. Narvaez, L. Moore, and P. Withers. Jupiter's Enigmatic Ionosphere: Electron Density Profiles From the Pioneer, Voyager, and Galileo Radio Occultation Experiments. *Journal of Geophysical Research: Planets*, 127(3), 2022. doi: 10.1029/2021JE007169.

M. P. Milazzo, L. P. Keszthelyi, J. Radebaugh, A. G. Davies, E. P. Turtle, P. Geissler, K. P. Klaasen, J. A. Rathbun, and A. S. McEwen. Volcanic activity at Tvashtar Catena, Io. *Icarus*, 179(1), Dec. 2005. doi: 10.1016/j.icarus.2005.05.013.

S. Miller, J. Tennyson, T. R. Geballe, and T. Stallard. Thirty years of H 3 + astronomy. *Rev. Mod. Phys.*, 92(3), Aug. 2020. doi: 10.1103/RevModPhys.92.035003.

A. Miura. Compressible magnetohydrodynamic Kelvin–Helmholtz instability with vortex pairing in the two-dimensional transverse configuration. *Physics of Plasmas*, 4(8), Aug. 1997. doi: 10.1063/1.872419.

A. Miura and P. L. Pritchett. Nonlocal stability analysis of the MHD Kelvin-Helmholtz instability in a compressible plasma. *Journal of Geophysical Research: Space Physics*, 87(A9), 1982. doi: 10.1029/JA087iA09p07431.

A. Miura and T. Sato. Numerical simulation of global formation of auroral arcs. *J. Geophys. Res.*, 85(A1), Jan. 1980. doi: 10.1029/JA085iA01p00073.

A. Moirano, L. Gomez Casajus, M. Zannoni, D. Durante, and P. Tortora. Morphology of the Io Plasma Torus From Juno Radio Occultations. *Journal of Geophysical Research: Space Physics*, 126(10), 2021a. doi: 10.1029/2021JA029190.

A. Moirano, A. Mura, A. Adriani, V. Dols, B. Bonfond, J. H. Waite, V. Hue, J. R. Szalay, A. H. Sulaiman, B. M. Dinelli, F. Tosi, F. Altieri, A. Cicchetti, G. Filacchione, D. Grassi, A. Migliorini, M. L. Moriconi, R. Noschese, G. Piccioni, R. Sordini, D. Turrini, C. Plainaki, G. Sindoni, S. Massetti, R. L. Lysak, S. L. Ivanovski, and S. J. Bolton. Morphology of the Auroral Tail of Io, Europa, and Ganymede From JIRAM L-Band Imager. *Journal of Geophysical Research: Space Physics*, 126(9), 2021b. doi: 10.1029/2021JA029450.

A. Moirano, A. Mura, B. Bonfond, J. E. P. Connerney, V. Dols, D. Grodent, V. Hue, J.-C. Gérard, F. Tosi, A. Migliorini, A. Adriani, F. Altieri, C. Castagnoli, A. Cicchetti, B. M. Dinelli, D. Grassi, M. L. Moriconi, R. Noschese, G. Piccioni, C. Plainaki, P. Scarica, G. Sindoni, R. Sordini, D. Turrini, and F. Zambon. Variability of the Auroral Footprint of Io Detected by Juno-JIRAM and Modeling of the Io Plasma Torus. *Journal of Geophysical Research: Space Physics*, 128(8), 2023. doi: 10.1029/2023JA031288.

K. M. Moore, H. Cao, J. Bloxham, D. J. Stevenson, J. E. P. Connerney, and S. J. Bolton. Time variation of Jupiter's internal magnetic field consistent with zonal wind advection. *Nature Astronomy*, 3(8), Aug. 2019. doi: 10.1038/s41550-019-0772-5.

J. S. Morgan. Temporal and spatial variations in the Io torus. *Icarus*, 62(3), June 1985. doi: 10.1016/0019-1035(85)90183-6.

J. P. Morgenthaler, C. Schmidt, M. Marconi, M. Vogt, and N. Schneider. Using Io Input/Output observatory (IoIO) observations to determine

if mass flow in Jupiter's magnetosphere driven by internal or external processes. In *MOP meeting 2023 booklet*, Liege, Belgium, July 2022a.

J. P. Morgenthaler, C. Schmidt, M. Marconi, M. F. Vogt, and N. M. Schneider. Find Your Favorite Io Volcanic Enhancement! A Global View of the Jovian Magnetosphere During the Juno Mission as Recorded by PSI's Io Input/Output Observatory (IoIO). In *AGU poster*, Chicago, Dec. 2022b.

A. Mura, A. Adriani, F. Altieri, J. E. P. Connerney, S. J. Bolton, M. L. Moriconi, J.-C. Gérard, W. S. Kurth, B. M. Dinelli, F. Fabiano, F. Tosi, S. K. Atreya, F. Bagenal, G. R. Gladstone, C. Hansen, S. M. Levin, B. H. Mauk, D. J. McComas, G. Sindoni, G. Filacchione, A. Migliorini, D. Grassi, G. Piccioni, R. Noschese, A. Cicchetti, D. Turrini, S. Stefani, M. Amoroso, and A. Olivieri. Infrared observations of Jovian aurora from Juno's first orbits: Main oval and satellite footprints: Jovian Aurora IR Observations From Juno. *Geophys. Res. Lett.*, 44(11), June 2017. doi: 10.1002/2017GL072954.

A. Mura, A. Adriani, J. E. P. Connerney, S. Bolton, F. Altieri, F. Bagenal, B. Bonfond, B. M. Dinelli, J.-C. Gérard, T. Greathouse, D. Grodent, S. Levin, B. Mauk, M. L. Moriconi, J. Saur, J. H. Waite, M. Amoroso, A. Cicchetti, F. Fabiano, G. Filacchione, D. Grassi, A. Migliorini, R. Noschese, A. Olivieri, G. Piccioni, C. Plainaki, G. Sindoni, R. Sordini, F. Tosi, and D. Turrini. Juno observations of spot structures and a split tail in Io-induced aurorae on Jupiter. *Science*, 361(6404), Aug. 2018. doi: 10.1126/science.aat1450.

G. Murakami, K. Yoshioka, A. Yamazaki, F. Tsuchiya, T. Kimura, C. Tao, H. Kita, M. Kagitani, T. Sakanoi, K. Uemizu, Y. Kasaba, I. Yoshikawa, and M. Fujimoto. Response of Jupiter's inner magnetosphere to the solar wind derived from extreme ultraviolet monitoring of the Io plasma torus. *Geophysical Research Letters*, 43(24), 2016. doi: 10.1002/2016GL071675.

A. Natan. Fast 2D Peak Finder [Software], 2021.

E. G. Nerney and F. Bagenal. Combining UV Spectra and Physical Chemistry to Constrain the Hot Electron Fraction in the Io Plasma Torus. *Journal of Geophysical Research: Space Physics*, 125(4), 2020. doi: 10.1029/2019JA027458.

E. G. Nerney, F. Bagenal, and A. J. Steffl. Io plasma torus ion composition: Voyager, Galileo, and Cassini. *J. Geophys. Res. Space Physics*, 122(1), Jan. 2017. doi: 10.1002/2016JA023306.

F. M. Neubauer. Nonlinear standing Alfven wave current system at Io: Theory. *J. Geophys. Res.*, 85:A3, Mar. 1980. doi: 10.1029/JA085iA03p01171.

C. S. Ng, P. A. Delamere, V. Kaminker, and P. A. Damiano. Radial Transport and Plasma Heating in Jupiter's Magnetodisc. *Journal of Geophysical Research: Space Physics*, 123(8), 2018. doi: 10.1029/2018JA025345.

J. D. Nichols. Magnetosphere-ionosphere coupling in Jupiter's middle magnetosphere: Computations including a self-consistent current sheet magnetic field model. *Journal of Geophysical Research: Space Physics*, 116(A10), 2011. doi: 10.1029/2011JA016922.

J. D. Nichols, N. Achilleos, and S. W. H. Cowley. A model of force balance in Jupiter's magnetodisc including hot plasma pressure anisotropy. *Journal of Geophysical Research: Space Physics*, 120(12), 2015. doi: 10.1002/2015JA021807.

J. D. Nichols, F. Allegrini, F. Bagenal, E. J. Bunce, S. W. H. Cowley, R. W. Ebert, D. Grodent, E. Huscher, A. Kamran, W. S. Kurth, R. J. Wilson, and Z. Yao. An Enhancement of Jupiter's Main Auroral Emission and Magnetospheric Currents. *Journal of Geophysical Research: Space Physics*, 125(8), 2020. doi: 10.1029/2020JA027904.

L. Paganini, G. L. Villanueva, L. Roth, A. M. Mandell, T. A. Hurford, K. D. Retherford, and M. J. Mumma. A measurement of water vapour amid a largely quiescent environment on Europa. *Nature Astronomy*, 4(3), Mar. 2020. doi: 10.1038/s41550-019-0933-6.

S. J. Peale, P. Cassen, and R. T. Reynolds. Melting of Io by Tidal Dissipation. *Science*, 203(4383), Mar. 1979. doi: 10.1126/science.203.4383.892.

P. H. Phipps and P. Withers. Radio occultations of the Io plasma torus by *Juno* are feasible. *J. Geophys. Res. Space Physics*, 122(2), Feb. 2017. doi: 10.1002/2016JA023447.

P. H. Phipps, P. Withers, D. R. Buccino, and Y.-M. Yang. Distribution of Plasma in the Io Plasma Torus as Seen by Radio Occultation During *Juno* Perijove 1. *J. Geophys. Res. Space Physics*, 123(8), Aug. 2018. doi: 10.1029/2017JA025113.

P. H. Phipps, P. Withers, D. R. Buccino, Y. Yang, and M. Parisi. Variations in the Density Distribution of the Io Plasma Torus as Seen by Radio Occultations on Juno Perijoves 3, 6, and 8. *J. Geophys. Res. Space Physics*, 124(7), July 2019. doi: 10.1029/2018JA026297.

P. H. Phipps, P. Withers, M. F. Vogt, D. R. Buccino, Y. Yang, M. Parisi, D. Ranquist, P. Kollmann, and S. Bolton. Where Is the Io Plasma Torus? A Comparison of Observations by Juno Radio Occultations to Predictions From Jovian Magnetic Field Models. *J. Geophys. Res. Space Physics*, 125 (8), Aug. 2020. doi: 10.1029/2019JA027633.

P. H. Phipps, P. Withers, D. R. Buccino, Y.-M. Yang, and M. Parisi. Two Years of Observations of the Io Plasma Torus by Juno Radio Occultations: Results From Perijoves 1 to 15. *Journal of Geophysical Research: Space Physics*, 126(3), 2021. doi: https://doi.org/10.1029/2020JA028710.

J. H. Piddington and J. F. Drake. Electrodynamic Effects of Jupiter's Satellite Io. *Nature*, 217(5132), Mar. 1968. doi: 10.1038/217935a0.

C. Plainaki, T. A. Cassidy, V. I. Shematovich, A. Milillo, P. Wurz, A. Vorburger, L. Roth, A. Galli, M. Rubin, A. Blöcker, P. C. Brandt, F. Crary, I. Dandouras, X. Jia, D. Grassi, P. Hartogh, A. Lucchetti, M. McGrath, V. Mangano, A. Mura, S. Orsini, C. Paranicas, A. Radioti, K. D. Retherford, J. Saur, and B. Teolis. Towards a Global Unified Model of Europa's

Tenuous Atmosphere. *Space Science Reviews*, 214(1), Jan. 2018. doi: 10.1007/s11214-018-0469-6.

D. Pokhotelov. Effects of the active auroral ionosphere on magnetosphere - ionosphere coupling. *Thesis (Ph.D.), Dartmouth College, 2002*, Sept. 2003. doi: 10.1349/ddlp.3332.

O. A. Pokhotelov, V. Khruschev, M. Parrot, S. Senchenkov, and V. P. Pavlenko. Ionospheric Alfvén resonator revisited: Feedback instability. *J. Geophys. Res.*, 106(A11), Nov. 2001. doi: 10.1029/2000JA000450.

D. H. Pontius and T. W. Hill. Departure from corotation of the Io plasma torus: Local plasma production. *Geophys. Res. Lett.*, 9(12), Dec. 1982. doi: 10.1029/GL009i012p01321.

R. Prangé, D. Rego, D. Southwood, P. Zarka, S. Miller, and W. Ip. Rapid energy dissipation and variability of the lo–Jupiter electrodynamic circuit. *Nature*, 379(6563), Jan. 1996. doi: 10.1038/379323a0.

T. Promfu, J. D. Nichols, S. Wannawichian, J. T. Clarke, M. F. Vogt, and B. Bonfond. Ganymede's Auroral Footprint Latitude: Comparison With Magnetodisc Model. *Journal of Geophysical Research: Space Physics*, 127 (12), 2022. doi: 10.1029/2022JA030712.

G. Pucelle and S. E. Segre. *Fisica dei plasmi*. Tipografia Babina for Zanichelli editore S.p.A, Bologna, 5th edition, 2014. ISBN 978-88-08-06383-0.

R. Rankin, K. Kabin, J. Y. Lu, I. R. Mann, R. Marchand, I. J. Rae, V. T. Tikhonchuk, and E. F. Donovan. Magnetospheric field-line resonances: Ground-based observations and modeling. *Journal of Geophysical Research: Space Physics*, 110(A10), 2005. doi: 10.1029/2004JA010919.

L. Roth, J. Saur, K. D. Retherford, D. F. Strobel, P. D. Feldman, M. A. McGrath, and F. Nimmo. Transient Water Vapor at Europa's South Pole. *Science*, 343(6167), Jan. 2014. doi: 10.1126/science.1247051.

L. Roth, J. Boissier, A. Moullet, A. Sánchez-Monge, K. de Kleer, M. Yoneda, R. Hikida, H. Kita, F. Tsuchiya, A. Blöcker, G. R. Gladstone, D. Grodent, N. Ivchenko, E. Lellouch, K. D. Retherford, J. Saur, P. Schilke, D. Strobel, and S. Thorwirth. An attempt to detect transient changes in Io's SO 2 and NaCl atmosphere. *Icarus*, 350, Nov. 2020. doi: 10.1016/j.icarus.2020.113925.

C. T. Russell. Planetary magnetospheres. *Reports on Progress in Physics*, 56(6), June 1993. doi: 10.1088/0034-4885/56/6/001.

B. R. Sandel and A. L. Broadfoot. Io's hot plasma torus—A synoptic view from Voyager. *Journal of Geophysical Research: Space Physics*, 87(A1), 1982. doi: 10.1029/JA087iA01p00212.

T. Sato. A theory of quiet auroral arcs. *J. Geophys. Res.*, 83(A3), 1978. doi: 10.1029/JA083iA03p01042.

J. Saur. A model of Io's local electric field for a combined Alfvénic and unipolar inductor far-field coupling. *Journal of Geophysical Research: Space Physics*, 109(A1), 2004a. doi: 10.1029/2002JA009354.

J. Saur. Turbulent Heating of Jupiter's Middle Magnetosphere. *The Astrophysical Journal*, 602(2), Feb. 2004b. doi: 10.1086/382588.

J. Saur, D. F. Strobel, and F. M. Neubauer. Interaction of the Jovian magnetosphere with Europa: Constraints on the neutral atmosphere. *Journal of Geophysical Research: Planets*, 103(E9), 1998. doi: https://doi.org/10.1029/97JE03556.

J. Saur, F. M. Neubauer, D. F. Strobel, and M. E. Summers. Interpretation of Galileo's Io plasma and field observations: I0, I24, and I27 flybys and close polar passes. *Journal of Geophysical Research: Space Physics*, 107 (A12), 2002. doi: 10.1029/2001JA005067.

J. Saur, F. M. Neubauer, J. E. P. Connerney, P. Zarka, and M. G. Kivelson. Plasma Interaction of Io with its Plasma Torus. In *Jupiter: The Planet,*

Satellites and Magnetosphere. Cambridge Univ. Press, Cambridge UK, 2004.

J. Saur, T. Grambusch, S. Duling, F. M. Neubauer, and S. Simon. Magnetic energy fluxes in sub-Alfvénic planet star and moon planet interactions. *A&A*, 552, Apr. 2013. doi: 10.1051/0004-6361/201118179.

J. Saur, S. Janser, A. Schreiner, G. Clark, B. H. Mauk, P. Kollmann, R. W. Ebert, F. Allegrini, J. R. Szalay, and S. Kotsiaros. Wave-Particle Interaction of Alfvén Waves in Jupiter's Magnetosphere: Auroral and Magnetospheric Particle Acceleration. *J. Geophys. Res. Space Physics*, 123(11), Nov. 2018. doi: 10.1029/2018JA025948.

C. Schmidt, N. Schneider, F. Leblanc, C. Gray, J. Morgenthaler, J. Turner, and C. Grava. A Survey of Visible S+ Emission in Io's Plasma Torus During the Hisaki Epoch. *Journal of Geophysical Research: Space Physics*, 123(7), 2018. doi: 10.1029/2018JA025296.

N. M. Schneider and J. T. Trauger. The Structure of the Io Torus. *ApJ*, 450, Sept. 1995. doi: 10.1086/176155.

J. A. Sinclair, T. K. Greathouse, R. S. Giles, A. Antuñano, J. I. Moses, T. Fouchet, B. Bézard, C. Tao, J. Martín-Torres, G. B. Clark, D. Grodent, G. S. Orton, V. Hue, L. N. Fletcher, and P. G. J. Irwin. Spatial Variations in the Altitude of the CH4 Homopause at Jupiter's Mid-to-high Latitudes, as Constrained from IRTF-TEXES Spectra. *The Planetary Science Journal*, 1(3), Dec. 2020. doi: 10.3847/PSJ/abc887.

G. L. Siscoe. Solar System Magnetohydrodynamics. In R. L. Carovillano and J. M. Forbes, editors, *Solar-Terrestrial Physics*, volume 104. Springer Netherlands, Dordrecht, 1983. ISBN 978-94-009-7196-7 978-94-009-7194-3. doi: 10.1007/978-94-009-7194-3_2.

C. G. A. Smith. Periodic modulation of gas giant magnetospheres by the neutral upper atmosphere. *Annales Geophysicae*, 24(10), Oct. 2006. doi: 10.5194/angeo-24-2709-2006.

W. H. Smyth, C. A. Peterson, and M. L. Marconi. A consistent understanding of the ribbon structure for the Io plasma torus at the Voyager 1, 1991 ground-based, and Galileo J0 epochs. *Journal of Geophysical Research: Space Physics*, 116(A7), 2011. doi: 10.1029/2010JA016094.

P. Sprangle, V. Granatstein, and A. Drobot. The Electron Cyclotron Maser Instability. *Journal de Physique Colloques*, 38(C6), 1977. doi: 10.1051/jphyscol:1977613.

A. Steffl. Cassini UVIS observations of the Io plasma torus.II. Radial variations. *Icarus*, 172(1), Nov. 2004. doi: 10.1016/j.icarus.2004.04.016.

A. Steffl, P. Delamere, and F. Bagenal. Cassini UVIS observations of the Io plasma torusIII. Observations of temporal and azimuthal variability. *Icarus*, 180(1), Jan. 2006. doi: 10.1016/j.icarus.2005.07.013.

A. Steffl, P. Delamere, and F. Bagenal. Cassini UVIS observations of the Io plasma torus. *Icarus*, 194(1), Mar. 2008. doi: 10.1016/j.icarus.2007.09.019.

A. V. Streltsov and E. V. Mishin. On the Existence of Ionospheric Feedback Instability in the Earth's Magnetosphere-Ionosphere System. *Journal of Geophysical Research: Space Physics*, 123(11), 2018. doi: https://doi.org/10.1029/2018JA025942.

Y.-J. Su, S. T. Jones, R. E. Ergun, F. Bagenal, S. E. Parker, P. A. Delamere, and R. L. Lysak. Io-Jupiter interaction: Alfvén wave propagation and ionospheric Alfvén resonator. *Journal of Geophysical Research*, 111(A6), 2006. doi: 10.1029/2005JA011252.

A. H. Sulaiman, G. B. Hospodarsky, S. S. Elliott, W. S. Kurth, D. A. Gurnett, M. Imai, F. Allegrini, B. Bonfond, G. Clark, J. E. P. Connerney, R. W. Ebert, D. J. Gershman, V. Hue, S. Janser, S. Kotsiaros, C. Paranicas, O. Santolík, J. Saur, J. R. Szalay, and S. J. Bolton. Wave-Particle Interactions Associated With Io's Auroral Footprint: Evidence of Alfvén, Ion Cyclotron, and Whistler Modes. *Geophysical Research Letters*, 47(22), 2020. doi: 10.1029/2020GL088432.

A. H. Sulaiman, J. R. Szalay, G. Clark, F. Allegrini, F. Bagenal, M. J. Brennan, J. E. P. Connerney, V. Hue, W. S. Kurth, R. L. Lysak, J. D. Nichols, J. Saur, and S. J. Bolton. Poynting Fluxes, Field-Aligned Current Densities, and the Efficiency of the Io-Jupiter Electrodynamic Interaction. *Geophysical Research Letters*, 50(10), 2023. doi: 10.1029/2023GL103456.

G. Sundström, J. R. Mowat, H. Danared, S. Datz, L. Broström, A. Filevich, A. Källberg, S. Mannervik, K. G. Rensfelt, P. Sigray, M. A. Ugglas, and M. Larsson. Destruction rate of h3+ by low-energy electrons measured in a storage-ring experiment. *Science*, 263(5148), Feb. 1994. doi: 10.1126/science.263.5148.785.

J. R. Szalay, F. Allegrini, F. Bagenal, S. J. Bolton, B. Bonfond, G. Clark, J. E. P. Connerney, R. W. Ebert, D. J. Gershman, R. S. Giles, G. R. Gladstone, T. Greathouse, G. B. Hospodarsky, M. Imai, W. S. Kurth, S. Kotsiaros, P. Louarn, D. J. McComas, J. Saur, A. H. Sulaiman, and R. J. Wilson. Alfvénic Acceleration Sustains Ganymede's Footprint Tail Aurora. *Geophys. Res. Lett.*, 47(3), Feb. 2020a. doi: 10.1029/2019GL086527.

J. R. Szalay, F. Allegrini, F. Bagenal, S. J. Bolton, B. Bonfond, G. Clark, J. E. P. Connerney, R. W. Ebert, V. Hue, D. J. McComas, J. Saur, A. H. Sulaiman, and R. J. Wilson. A New Framework to Explain Changes in Io's Footprint Tail Electron Fluxes. *Geophys. Res. Lett.*, 47(18), Sept. 2020b. doi: 10.1029/2020GL089267.

C. Tao, S. V. Badman, and M. Fujimoto. UV and IR auroral emission model for the outer planets: Jupiter and Saturn comparison. *Icarus*, 213(2), June 2011. doi: 10.1016/j.icarus.2011.04.001.

N. Thomas. Optical observations of Io's neutral clouds and plasma torus. *Surv Geophys*, 13(2), Mar. 1992. doi: 10.1007/BF01903525.

N. Thomas. The variability of the Io plasma torus. *J. Geophys. Res.*, 98 (E10), 1993. doi: 10.1029/93JE01461.

N. Thomas. Ion temperatures in the Io plasma torus. *Journal of Geophysical Research: Space Physics*, 100(A5), 1995. doi: 10.1029/94JA03143.

N. Thomas and G. Lichtenberg. The latitudinal dependence of ion temperature in the Io plasma torus. *Geophysical Research Letters*, 24(10), 1997. doi: 10.1029/97GL01133.

N. Thomas, G. Lichtenberg, and M. Scotto. High-resolution spectroscopy of the Io plasma torus during the Galileo mission. *Journal of Geophysical Research: Space Physics*, 106(A11), 2001. doi: 10.1029/2000JA002504.

N. Thomas, F. Bagenal, T. W. Hill, and J. K. Wilson. The Io neutral clouds and plasma torus. In F. Bagenal, T. E. Dowling, and W. B. McKinnon, editors, *Jupiter. The Planet, Satellites and Magnetosphere*, volume 1. Cambridge Univ. Press, 2004.

C. L. Thornton and J. S. Border. *Radiometric Tracking Techniques for Deep-Space Navigation*, volume 1 of *Deep-Space Communications and Navigation Series*. J. Yuen, Jet Propulsion Lab., California Inst. of Technol., Hoboken, N. J., 2000.

F. Tsuchiya, K. Yoshioka, T. Kimura, R. Koga, G. Murakami, A. Yamazaki, M. Kagitani, C. Tao, F. Suzuki, R. Hikida, I. Yoshikawa, Y. Kasaba, H. Kita, H. Misawa, and T. Sakanoi. Enhancement of the Jovian Magnetospheric Plasma Circulation Caused by the Change in Plasma Supply From the Satellite Io. *J. Geophys. Res. Space Physics*, 123(8), Aug. 2018. doi: 10.1029/2018JA025316.

F. Tsuchiya, R. Arakawa, H. Misawa, M. Kagitani, R. Koga, F. Suzuki, R. Hikida, K. Yoshioka, A. Steffl, F. Bagenal, P. Delamere, T. Kimura, Y. Kasaba, G. Murakami, I. Yoshikawa, A. Yamazaki, and M. Yoneda. Azimuthal Variation in the Io Plasma Torus Observed by the Hisaki Satellite From 2013 to 2016. *Journal of Geophysical Research: Space Physics*, 124(5), 2019. doi: https://doi.org/10.1029/2018JA026038.

B. Tulegenov and A. V. Streltsov. Ionospheric Alfvén resonator and aurora: Modeling of MICA observations. *Journal of Geophysical Research: Space Physics*, 122(7), 2017. doi: 10.1002/2017JA024181.

M. F. Vogt, S. Gyalay, E. A. Kronberg, E. J. Bunce, W. S. Kurth, B. Zieger, and C. Tao. Solar Wind Interaction With Jupiter's Magnetosphere: A Statistical Study of Galileo In Situ Data and Modeled Upstream Solar Wind Conditions. *Journal of Geophysical Research: Space Physics*, 124 (12), 2019. doi: 10.1029/2019JA026950.

M. F. Vogt, J. E. Connerney, G. A. DiBraccio, R. J. Wilson, M. F. Thomsen, R. W. Ebert, G. B. Clark, C. Paranicas, W. S. Kurth, F. Allegrini, P. W. Valek, and S. J. Bolton. Magnetotail Reconnection at Jupiter: A Survey of Juno Magnetic Field Observations. *Journal of Geophysical Research: Space Physics*, 125(3), 2020. doi: 10.1029/2019JA027486.

M. F. Vogt, M. Rutala, B. Bonfond, J. T. Clarke, L. Moore, and J. D. Nichols. Variability of Jupiter's Main Auroral Emission and Satellite Footprints Observed With HST During the Galileo Era. *Journal of Geophysical Research: Space Physics*, 127(2), 2022. doi: 10.1029/2021JA030011.

T. von Kármán. Ueber den Mechanismus des Widerstandes, den ein bewegter Körper in einer Flüssigkeit erfährt. *Nachrichten von der Gesellschaft der Wissenschaften zu Göttingen, Mathematisch-Physikalische Klasse*, 1911, 1911.

J. Warnecke, M. G. Kivelson, K. K. Khurana, D. E. Huddleston, and C. T. Russell. Ion cyclotron waves observed at Galileo's Io encounter: Implications for neutral cloud distribution and plasma composition. *Geophysical Research Letters*, 24(17), 1997. doi: 10.1029/97GL01129.

H. Watanabe, H. Kita, C. Tao, M. Kagitani, T. Sakanoi, and Y. Kasaba. Pulsation Characteristics of Jovian Infrared Northern Aurora Observed by the Subaru IRCS with Adaptive Optics. *Geophysical Research Letters*, 45(21), 2018. doi: https://doi.org/10.1029/2018GL079411.

T.-H. Watanabe. Feedback instability in the magnetosphere-ionosphere coupling system: Revisited. *Physics of Plasmas*, 17(2), Feb. 2010. doi: 10.1063/1.3304237.

G. Wentzel. Eine Verallgemeinerung der Quantenbedingungen für die Zwecke der Wellenmechanik. *Zeitschrift für Physik*, 38(6), June 1926. doi: 10.1007/BF01397171.

R. J. Wilson, M. F. Vogt, G. Provan, A. Kamran, M. K. James, M. Brennan, and S. W. H. Cowley. Internal and External Jovian Magnetic Fields: Community Code to Serve the Magnetospheres of the Outer Planets Community. *Space Science Reviews*, 219(1), Feb. 2023. doi: 10.1007/s11214-023-00961-3.

C. S. Wu. Kinetic cyclotron and synchrotron maser instabilities: Radio emission processes by direct amplification of radiation. *Space Science Reviews*, 41(3), Aug. 1985. doi: 10.1007/BF00190653.

Z. H. Yao, B. Bonfond, D. Grodent, E. Chané, W. R. Dunn, W. S. Kurth, J. E. P. Connerney, J. D. Nichols, B. Palmaerts, R. L. Guo, G. B. Hospodarsky, B. H. Mauk, T. Kimura, and S. J. Bolton. On the Relation Between Auroral Morphologies and Compression Conditions of Jupiter's Magnetopause: Observations From Juno and the Hubble Space Telescope. *Journal of Geophysical Research: Space Physics*, 127(10), 2022. doi: 10.1029/2021JA029894.

M. Yoneda, H. Nozawa, H. Misawa, M. Kagitani, and S. Okano. Jupiter's magnetospheric change by Io's volcanoes. *Geophysical Research Letters*, 37(11), 2010. doi: 10.1029/2010GL043656.

K. Yoshioka, F. Tsuchiya, M. Kagitani, T. Kimura, G. Murakami, D. Fukuyama, A. Yamazaki, I. Yoshikawa, and M. Fujimoto. The Influence of Io's 2015 Volcanic Activity on Jupiter's Magnetospheric Dynamics. *Geophys. Res. Lett.*, 45(19), Oct. 2018. doi: 10.1029/2018GL079264.

B. Zieger and K. C. Hansen. Statistical validation of a solar wind propagation model from 1 to 10 AU. *Journal of Geophysical Research: Space Physics*, 113(A8), 2008. doi: 10.1029/2008JA013046.